Polymer and Ion Dynamics by *In Situ* Nanodielectric Spectroscopy

Dissertation zur Erlangung des Grades

'Doktor der Naturwissenschaften (Dr. rer. nat)'

im Promotionsfach Physikalische Chemie

am Fachbereich Chemie, Pharmazie, und Geowissenschaften

der Johannes Gutenberg-Universität, Mainz

vorgelegt von

Chien-Hua Tu

Geboren in Tainan, Taiwan

Mainz 2021

This thesis was carried out from July 2018 until October 2021 in the department of Prof. Dr. Hans-Jürgen Butt in the group of Prof. Dr. George Floudas at the Max Planck Institute for Polymer Research, Mainz.

Dekan: Prof. Dr. Dirk Schneider
Prodekan: Prof. Dr. Katja Heinze

Gutachter 1: Prof. Dr. Hans-Jürgen Butt
Gutachter 2: Prof. Dr. Holger Frey
Gutachter 3: Prof. Dr. Wolfgang Tremel
Gutachter 4: Prof. Dr. George Floudas

Date of oral examination: 15. 11. 2021

I hereby declare that I wrote the dissertation submitted without any unauthorized external assistance and used only sources acknowledged in this work. All textual passages which are appropriate verbatim or paraphrases from published and unpublished text, as well as all information obtained from oral sources are duly indicated and listed in accordance with bibliographical rules. In carrying out this research, I complied with the rules of standard scientific practice as formulated in the statutes of Johannes Gutenberg University Mainz to ensure standard scientific practice.

_____ _____

(Place, Date) (Signature)

Abstract

Understanding the way that polymers penetrate in narrow pores is important in applications including the separation of proteins with relevance in cell biology and the development of inkjet printing for commercial xerography. In this Thesis we employ a nanofluidic approach that is based on nanodielectric spectroscopy to investigate three important topics in polymer physics. In the first topic we employ a polar polymer poly(*n*-butyl methacrylate) with a convenient liquid-to-glass temperature ($T_g \sim$ RT) and investigate *if* and *how* the segmental dynamics are affected during flow. It was shown that the segmental dynamics are largely unaffected by flow except at early stages where a speed-up is observed.

In a second area we investigate *if* and *how* the chain dynamics are affected during flow. For this purpose, we employ the typical type-A polymer *cis*-1,4-polyisoprene (*cis*-1,4-PI) that possesses dipoles both perpendicular and along the polymer chain. Results show that the imbibition proceeds in two time-regimes both with higher effective viscosity than in the bulk. This finding is discussed by a microscopic picture that considers the competition from an increasing number of chains entering the pores and a decreasing number of fluctuating chain-ends. The latter is a direct manifestation of increasing adsorption sites during flow. The adsorption kinetics of *cis*-1,4-PI was further investigated as a function of molar mass, nanopore diameter and surface functionalization. For a given pore diameter the characteristic adsorption times are some 8 orders of magnitude slower than the terminal relaxation times and more than 12 orders of magnitude slower than the segmental times. The extremely slow kinetics reflect the fact that exchanging chains with the pore surface have to pass through several unfavorable configurations (*e.g.*, trains, loops). The molar mass dependence of the characteristic adsorption times ($\tau_{ads} \sim N^{2.6}$, N is the number of repeat units) is in good agreement with a scaling theory proposed by de Gennes and later refined by Semenov and Joanny. Subsequently, the imbibition of miscible PI blends was investigated by taking advantage of the difference in imbibition speeds of the respective homopolymers. The shorter chains penetrate first the nanopores whereas the longer chains enter only at the late stages of the filling process. Moreover, the long-time adsorption is dominated by an exchange mechanism involving primarily the shorter chains.

In a third area we investigate *if* and *how* the ionic conductivity and chain mobility of a polymer electrolyte is affected during imbibition in the same nanopores. To this end, the archetypal polymer electrolyte poly(ethylene oxide)/LiTFSI was employed. Two distinct stages of imbibition could be seen. At early stages of imbibition and up to the complete pore filling the effective viscosity is reduced below the bulk value. At later stages, polymer adsorption takes place. The time scale of adsorption is very long—much longer than chain diffusion and the segmental relaxation. Adsorption involves several unfavorable configurations of the polymer chains that inevitably affect the ion dynamics by (i) increasing the effective viscosity (higher T_g) and (ii) by reducing the number of mobile ions.

Lastly, we explore a possibility that a semicrystalline polymer can be infiltrated in nanopores below its melting temperature. The results show that the capillary force can be strong that can drive the polymer chains into the nanopores.

Zusammenfassung

Das Verständnis der Art und Weise, wie Polymere in enge Poren eindringen, ist wichtig für Anwendungen wie die Trennung von Proteinen, die in der Zellbiologie von Bedeutung sind, und für die Entwicklung des Tintenstrahldrucks für die kommerzielle Xerographie. In dieser Arbeit verwenden wir einen Ansatz aus der Nanofluidik, welcher auf nanodielektrischer Spektroskopie basiert, um drei wichtige Themen der Polymerphysik zu untersuchen. Beim ersten Thema verwenden wir ein polares Polymer, Poly(n-butylmethacrylat), mit einer günstigen Flüssigkeits-zu-Glas Übergangstemperatur (T_g ~ RT) und untersuchen, ob und wie die Segmentdynamik während des Flusses beeinflusst wird. Es wurde gezeigt, dass die Segmentdynamik weitgehend unbeeinflusst von der Strömung ist, außer in frühen Stadien, in denen eine Beschleunigung beobachtet wird.

In einem zweiten Bereich untersuchen wir, ob und wie die Kettendynamik während der Strömung beeinflusst wird. Zu diesem Zweck verwenden wir das typische Typ-A (dielektrisch) Polymer cis-1,4-Polyisopren (cis-1,4-PI), das Dipole sowohl senkrecht als auch entlang der Polymerkette besitzt. Die Ergebnisse zeigen, dass die Imbibition in zwei Zeitregimen abläuft, die beide eine höhere effektive Viskosität als in der Masse aufweisen. Dieses Ergebnis wird anhand eines mikroskopischen Bildes diskutiert, das die Konkurrenz zwischen einer zunehmenden Anzahl von Ketten, die in die Poren eindringen, und einer abnehmenden Anzahl von fluktuierenden Kettenenden berücksichtigt. Letzteres ist ein direkter Ausdruck der zunehmenden Anzahl an Adsorptionsstellen während des Fließens. Die Adsorptionskinetik von cis-1,4-PI wurde als Funktion der molaren Masse, des Nanoporendurchmessers und der Oberflächenfunktionalisierung weiter untersucht. Bei einem gegebenen Porendurchmesser sind die charakteristischen Adsorptionszeiten um etwa 8 Größenordnungen langsamer als die terminalen Relaxationszeiten und um mehr als 12 Größenordnungen langsamer als die segmentalen Zeiten. Diese extrem langsame Kinetik spiegelt die Tatsache wider, dass der Austausch von Ketten mit der Porenoberfläche mehrere ungünstige Konfigurationen (z. B. Schleifen) durchlaufen muss. Die Molmassenabhängigkeit der charakteristischen Adsorptionszeiten ($\tau_{ads} \sim N^{2,6}$, N ist die Anzahl der Wiederholungseinheiten) steht in guter Übereinstimmung mit einer von de Gennes vorgeschlagenen und später von Semenov und Joanny verfeinerten Skalierungstheorie. Anschließend wurde das Aufsaugen von mischbaren PI-Mischungen unter Ausnutzung der unterschiedlichen Aufsauggeschwindigkeiten der jeweiligen Homopolymere untersucht. Die

kürzeren Ketten dringen zuerst in die Nanoporen ein, während die längeren Ketten erst in den späten Stadien des Füllvorgangs eindringen. Außerdem wird die Langzeitadsorption von einem Austauschmechanismus dominiert, an dem vor allem die kürzeren Ketten beteiligt sind.

In einem dritten Bereich untersuchen wir, ob und wie die Ionenleitfähigkeit und die Kettenbeweglichkeit eines Polymerelektrolyten während des Einschlusses in dieselben Nanoporen beeinflusst wird. Zu diesem Zweck wurde der archetypische Polymerelektrolyt Poly(ethylenoxid)/LiTFSI verwendet. Es konnten zwei unterschiedliche Phasen des Aufsaugens beobachtet werden. In frühen Stadien des Aufsaugens und bis zur vollständigen Porenfüllung sinkt die effektive Viskosität unter den Bulk-Wert. In späteren Stadien findet die Polymeradsorption statt. Die Zeitskala der Adsorption ist sehr lang - viel länger als die Kettendiffusion und die segmentale Relaxation. Die Adsorption umfasst mehrere ungünstige Konfigurationen der Polymerketten, die sich unweigerlich auf die Ionendynamik auswirken, indem sie (i) die effektive Viskosität erhöhen (und damit höheres Tg) und (ii) die Anzahl der mobilen Ionen verringern.

Schließlich untersuchten wir die Möglichkeit, dass ein teilkristallines Polymer in Nanoporen unterhalb seiner Schmelztemperatur infiltriert werden kann. Die Ergebnisse zeigen, dass die Kapillarkraft so stark sein kann, dass die Polymerketten in die Nanoporen getrieben werden können.

Contents

Chapter 1. Introduction

Polymer properties may deviate from bulk when the polymer is confined into sizes close to or even below the radius of gyration. Most of these deviations originate from the interactions between the polymer and the confining medium at the vicinity of the interface. Discerning these effects can bring forth certain advantages in the design and eventually fabrication of nanostructured devices. Several confining geometries (1D, 2D, and 3D) have been employed to address the issue of confinement. A relatively recent development in this direction has been the construction of model 2D confining tubes based on self-ordered nanoporous anodic aluminum oxide, better known as AAO. AAO templates contain arrays of parallel cylindrical nanopores, uniform in length and diameter, where polymers can be infiltrated by capillary action. Understanding the way that polymers penetrate in narrow pores is important in applications including the separation of proteins with relevance in cell biology and the development of inkjet printing for commercial xerography.

In this Thesis a nanofluidic method based on nanodielectric spectroscopy is employed to investigate the effect of 2D confinement on a variety of macromolecules including amorphous polymers, and solid polymer electrolytes *during* imbibition. In first area we address the question of how the segmental and chain dynamics are affected *during imbibition*. We are interested in particular in the effective viscosity that a polymer experiences *during imbibition*. Two amorphous polymers are employed: poly(*n*-butyl methacrylate) (PnBMA) for the segmental process and *cis*-1,4-polyisoprene (PI) for the chain dynamics. In second area we investigate how ions and polymer segments of a polymer electrolyte migrate in nanopores *during imbibition*. To this end, a solid polymer electrolyte based on the archetypal system poly(ethylene oxide) (PEO)/LiTFSI, are employed. In third area we explore the possibility that a semicrystalline polymer can penetrate into narrow pores from its crystalline state. Despite this might sound paradoxical – due to the very high viscosity of a crystalline polymer – earlier measurements from our group revealed the possibility to infiltrate a block copolymer directly into nanopores from an ordered state where the viscosity is also very high. Should this part be successful it will be a demonstration that a crystal can flow by capillary action.

1.1. Polymer dynamics: time- and length-scales?

1.1.1. Segmental dynamics

Because of the chain-like structure, the time-scales and length-scales of polymer dynamics can span several decades (**Figure 1**). The relaxation process of few repeat units is associated with the *segmental relaxation*, or the *segmental dynamics*. The dynamics at the segmental level controls the main structural relaxation of the polymer. Moreover, the transition from the rubbery to the glassy state is reflected in the freezing of the segmental process. The characteristic temperature specifying such transition is called the glass temperature, T_g. It is conventionally defined as the temperature where the viscosity is nearly 10^{12} (Pa·s) and the segmental relaxation time ~100 s. The segmental dynamics follows the empirical Vogel-Fulcher-Tammann (VFT) equation: $\tau = \tau_0 exp\left(\frac{B}{T-T_0}\right)$, where τ_o is the relaxation time at very high temperatures, B is the activation parameter and T_o is the "ideal" glass temperature located below the conventional glass temperature. At temperatures below T_g, there exist local dynamics related to faster motions in the glassy state such as the rotation of side groups. The latter reflect local reorientations of side groups in a frozen environment. Local processes below T_g follow an Arrhenius temperature dependence: $\tau = \tau_0 exp\left(\frac{E}{RT}\right)$ where τ_o (= 10^{-14} s) is the relaxation time in the limit of very high temperatures and E is the activation energy.

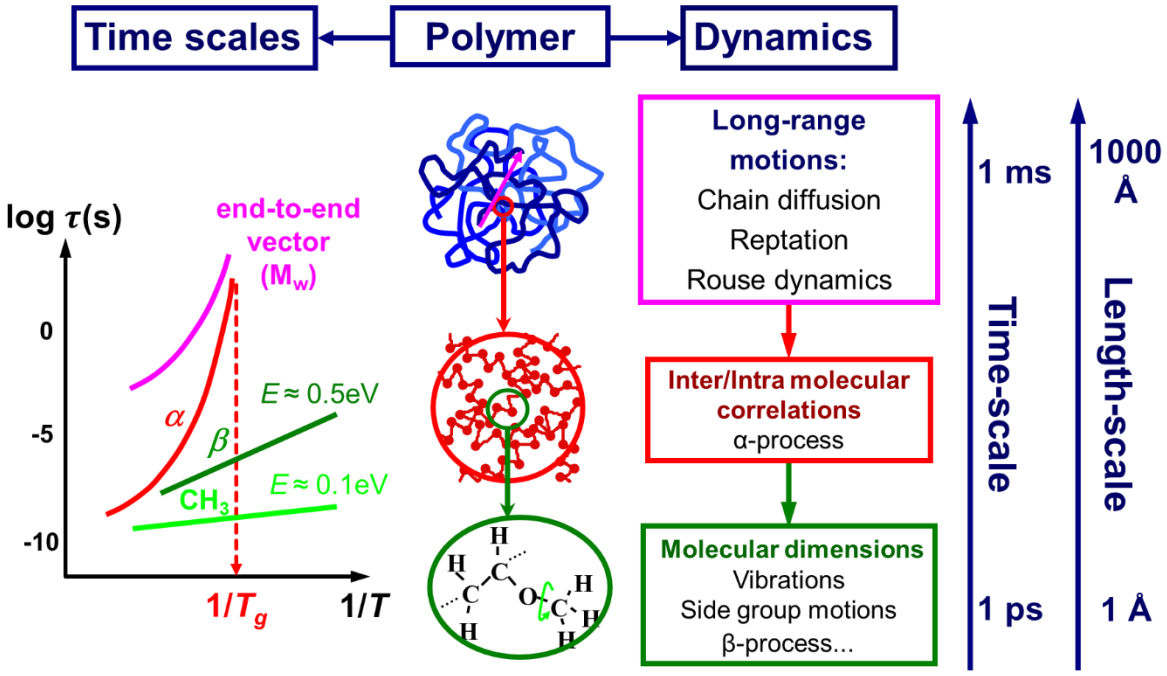

Figure 1. Time-scales and length-scales of polymer dynamics. The activation plot in the left shows the temperature dependence of relaxation times for the different processes: VFT behavior for chain relaxation (magenta) and α-process (red); Arrhenius dependence for local processes (olive/green) below T_g. The glass temperature (T_g) is defined as the temperature where the segmental relaxation time is ~100 s.

1.1.2. Unentangled polymer dynamics: The Rouse model

Longer scale dynamics involving the entire chain determine important macroscopic properties of polymers like viscoelasticity. In the case of unentangled polymer melts with short chains, the dynamics is interpreted by the Rouse model.[2, 3] The idea is to divide a single polymer chain into N "submolecules" comprising individual beads with their own friction coefficient, ζ. The beads are connected by springs, with a spring constant, k. Hence, the Rouse model is called the bead-spring model (**Figure 2**).

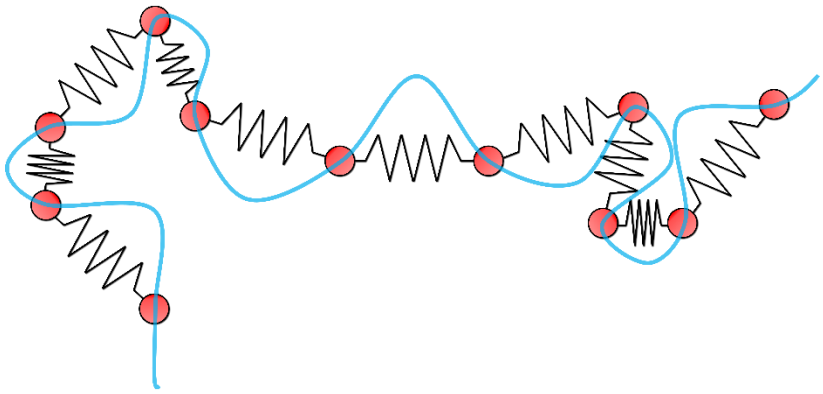

Figure 2. Schematic illustrating a Gaussian polymer chain (blue line) described by the Rouse model as beads (red circles) and springs (black kinks).

The movement of beads follow Brownian dynamics. Consequently, the equation of motion of a Rouse chain can be represented by the Langevin equation as:

$$\zeta \frac{d\boldsymbol{R}_n}{dt} = -k(2\boldsymbol{R}_n - \boldsymbol{R}_{n+1} - \boldsymbol{R}_{n-1}) + \boldsymbol{f}_n \qquad (1)$$

where $\boldsymbol{R}_n$ (n=0, 1, 2, …, N) is the position of beads, ζ the friction coefficient of beads, k $\left(=\frac{3k_BT}{b^2}\right)$ the "spring" constant, and the $\boldsymbol{f}_n$ is the random force representing the total forces induced by the incessant collision of the fluid molecules composed of Brownian beads. The first and second term of equation (1) describes, respectively, the frictional force and the entropic spring force experienced during the movement of Rouse chains. The diffusion coefficient of Rouse chains, D_R, can be derived from equation (1) as:

$$D_{cm} = \lim_{t\to\infty} \frac{1}{6t} \langle \left(\boldsymbol{R}_{cm}(t) - \boldsymbol{R}_{cm}(0)\right)^2 \rangle = D_R = \frac{k_BT}{N\zeta} \qquad (2)$$

The time needed for a Rouse chain to diffuse its own dimension (given by the radius of gyration, R_g) can be calculated from equation (2) as:

$$\tau_R \approx \frac{R^2}{D_R} \approx \frac{R^2}{\left(\frac{k_B T}{N\zeta}\right)} = \frac{\zeta(NR^2)}{k_B T} \tag{3}$$

The relaxation time, τ_R, is the longest relaxation time of a Rouse chain. On the other hand, the shortest relaxation time in the Rouse model is associated with the relaxation of a Kuhn segment as:

$$\tau_{Kuhn} = \tau_0 \approx \frac{\zeta b}{k_B T} \tag{4}$$

where the b is the Kuhn length. Combine the equation (3) and (4), we obtain a simple relation between τ_R and τ_0 as following:

$$\tau_R \approx \tau_0 N^2 \tag{5}$$

with $R \approx bN^{\nu}$ (ν = ½, for the ideal linear chain). For the relaxation of internal subchains, we can divide a Rouse chain into p sections comprising N/p segments (**Figure 3**). The characteristic relaxation time for the N/p segments of a Rouse chain is given by:

$$\tau_p = \frac{\zeta_p}{k_p} = \frac{\zeta N^2 b^2}{3\pi^2 k_B T p^2} \quad (for\ p = 1, 2, \dots, N) \tag{6}$$

Evidently, the relaxation time of the first mode (p = 1) is the longest being 4-times and 9-times longer than the second and third modes, *i.e.* $\tau_p = \frac{\tau_1}{p^2}$. The relaxation time, τ_1, is exactly the longest Rouse time τ_R. Overall, the Rouse model manifests two important scaling laws for unentangled polymer chains:

$$\tau_R \sim N^2 \quad and \quad D_R \sim N^{-1} \tag{7}$$

Since N is proportional to the molar mass:

$$\tau_R \sim M^2 \quad and \quad D_R \sim M^{-1} \tag{8}$$

The Rouse model assumes the absence of any hydrodynamic interactions between the polymer chain and the solvent molecules. In the presence of hydrodynamic interactions (Zimm model) the relaxation times scales as: $\tau \sim M^{3/2}$ instead.

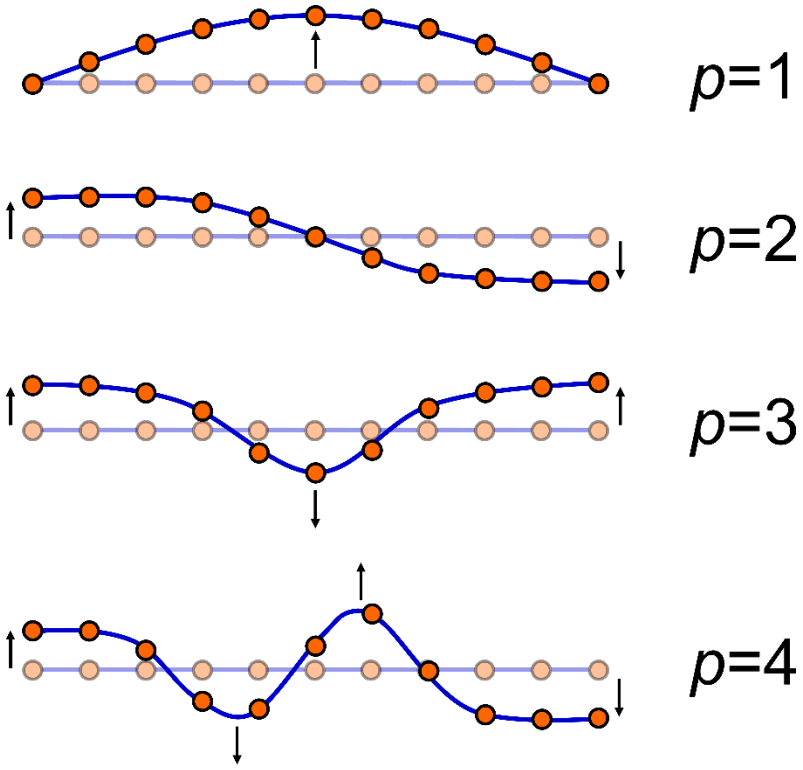

Figure 3. Scheme showing the *p*-mode relaxation of a Rouse chain.

1.1.3. Entangled polymer dynamics: The Reptation model

The Rouse model describes rather short polymer chains without frequent intermolecular contacts. As polymer chains become much longer (*i.e.*, higher molar masses), the chains will start to interpenetrate each other. Due to the forbidden crossing of polymer chains, the interpenetration will impose topological constraints known as entanglements (**Figure 4**).

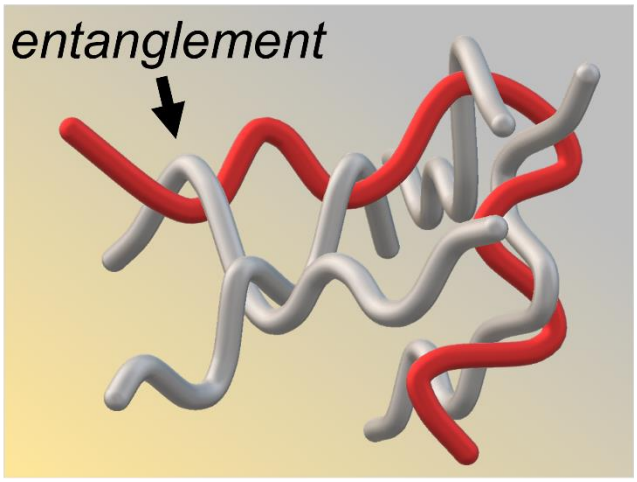

Figure 4. Schematic showing topological constraints (entanglements) on an observed polymer chain (red) imposed by the surrounding chains (silver) in a polymer melt.

The *reptation* model (introduced by de Gennes[4] and later refined by Doi and Edwards[2]) is an insightful theoretical approach to replace a many-body problem with a tractable single-body problem in an effective field. Within this model the dynamics of entangled polymer chains are treated as a collective behavior of a single chain moves in a confined "tube" region created by the topological constraints from surrounding chains. Inside the "tube" the polymer chain moves in a curvilinear pattern. Fluctuations of the polymer chain are strongly suppressed in the direction perpendicular to the chain path. By contrast, the movement parallel to the chain path is not restricted. The tube confinement range is characterized as the tube diameter a_0 (**Figure 5**). The shortest curvilinear path connecting the two ends of the tube is called the *primitive* chain contour length, L_p. The step length of the primitive chain a is also defined as:

$$\langle \big(\boldsymbol{R}(s,t) - \boldsymbol{R}(s',t) \big)^2 \rangle = a\,|s - s'| \tag{9}$$

Here, the $\boldsymbol{R}(s,t)$ and $\boldsymbol{R}(s',t)$ represent the position vector of the two primitive segments, and $|s - s'| \gg a$. The tube diameter a_0 is of the same order as a. Notice that the motion of the

primitive chain can be viewed as a translation of the Rouse chain inside the tube. The corresponding diffusion coefficient is thus defined as $D_c = \frac{k_B T}{N\zeta}$. The mean-square end-to-end vector of the primitive chain ($L_p a$) is equivalent to the Rouse chain (Nb^2), hence the primitive chain contour length is $L_p = \frac{Nb^2}{a}$.

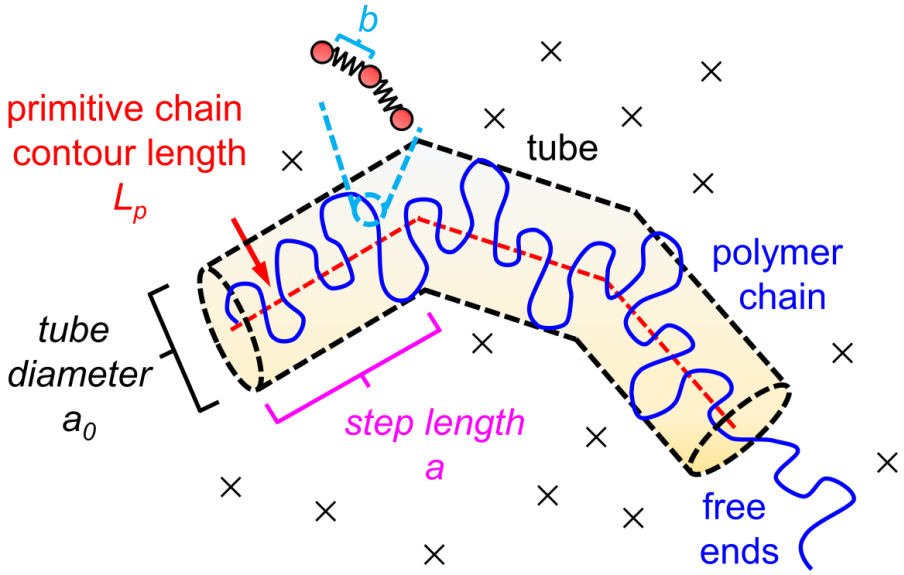

Figure 5. Scheme showing an entangled polymer chain confined into a tube-like region due to the surrounding chains (small crosses). The characteristic lengths are indicated: primitive chain contour length L_p, step length of the primitive chain a, tube diameter a_0, and effective bond length b.[2]

The tube formation is not permanent. After a while, part of chains are leaving the original tube by exploring a new position and form a new tube. The former tubes to which these leaving chains once belonged become empty and disappear. This type of motion of polymer chains is called *Reptation* (**Figure 6**).[2] Given an entangled polymer chain following the reptation behavior, the time correlation of end-to-end vector can be derived with the aid of **Figure 6**. The end-to-end vector is defined as $\boldsymbol{P}(t) \equiv \boldsymbol{R}(L,t) - \boldsymbol{R}(0,t)$ with $\boldsymbol{P}(0) = \overrightarrow{\alpha_0\gamma} + \overrightarrow{\gamma\gamma'} + \overrightarrow{\gamma'\beta_0}$ and $\boldsymbol{P}(t) = \overrightarrow{\alpha\gamma} + \overrightarrow{\gamma\gamma'} + \overrightarrow{\gamma'\beta}$. The time correlation of end-to-end vectors $\langle \boldsymbol{P}(t) \cdot \boldsymbol{P}(0) \rangle$ can be obtained as following:

$$\langle \boldsymbol{P}(t) \cdot \boldsymbol{P}(0) \rangle = Nb^2 \sum_{p;odd} \frac{8}{p^2\pi^2} exp\left(\frac{-p^2 t}{\tau_d}\right) \qquad (10)$$

and with $D_c = \frac{k_B T}{N\zeta}$ and $L = \frac{Nb^2}{a}$, the reptation or disengagement time of a polymer chain is given by:

$$\tau_d = \frac{L^2}{D_c \pi^2} = \frac{\zeta N^3 b^4}{\pi^2 k_B T a^2} \tag{11}$$

Evidently, the entanglement effect makes the relaxation of long polymer chains become much slower than the corresponding unentangled chains (*i.e.*, $\tau_d \propto N^3 >> \tau_R \propto N^2$).

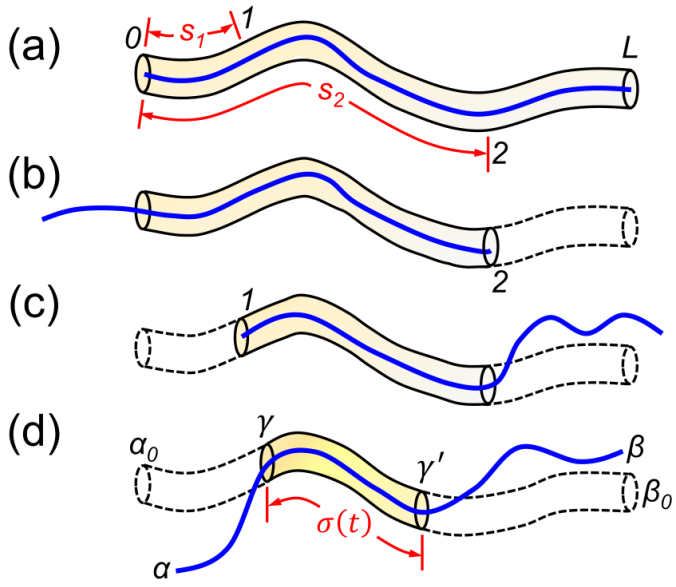

Figure 6. Scheme illustrating the reptation behavior of a polymer chain within a tube. (a) The original tube comprising an initial primitive chain. (b, c) The primitive chain moves left or right with repsect to the initial position. As a result part of the original tube becomes empty (indicated by dashed lines). (d) The tube conformation after a certain time *t*. $\sigma(t)$ represents the contour length between position γ and γ'.[5]

Although the *reptation* model has successfully captured many fundamental features of entangled linear polymer dynamics, quantitative discrepancies between theoretical predictions and experiments still remained. Specifically, the zero-shear viscosity, η_0, and the longest relaxation time (*i.e.*, model prediction $\eta_0 \sim M^3$ and $\tau_d \sim M^3$ against the experimental results suggesting $\eta_0 \sim M^{3.4}$ and $\tau_d \sim M^{3.4}$). Two additional processes were proposed to account for the discrepancy: (i) *contour length fluctuations* (CLF) and (ii) *tube reorganiztion* (TR).[5] According to the CLF model, the contour length of the primitive chain fluctuates with time rather than being constant as

assumed in the original reptation model. During the back-and-forth motions of the chain in the tube, the segments near the ends of the polymer chain are renewed to have random orientation. On the other hand, TR proposed that the topological constraints can be released (or re-created) by the *reptation* of some of the surrounding polymer chains. The two additional models (CLF and TR) can successfully predict the molar mass exponent (3.4).

Overall, the *Rouse* and *Reptation* models together predict five distinctive regimes for polymer dynamics (**Figure 7**)[2]: (I) for $t < \tau_0$, segments can move at very short times, *e.g.*, rotation of bonds or functional groups; (II) for $\tau_0 < t < \tau_e$ (entangled time, *i.e.*, the time when the segmental displacements become comparable to tube diameter), the chain behaves as a *Rouse* chain in free space; (III) for $\tau_e < t < \tau_R$ (*Rouse* relaxation time), chains start to feel the constraints imposed by the tube (restricted motions with directions perpendicular to the primitive path, but free for the curvilinear path along the tube contour); (IV) for $\tau_R < t < \tau_d$ (the *reptation* time or disengagement time), *reptation* process is dominant; (V) for $t > \tau_d$, the polymer chains are completely free. Note that the mean-square displacement $\langle(\boldsymbol{R}(t) - \boldsymbol{R}(0))^2\rangle$ of a chain is proportional to $t^{\frac{1}{4}}$ in the time range $\tau_e < t < \tau_R$. The unique diffusion behavior is the combining effects of Rouse chain behavior along the tube contour and tube-confined diffusion perpendicular to the curvilinear path.

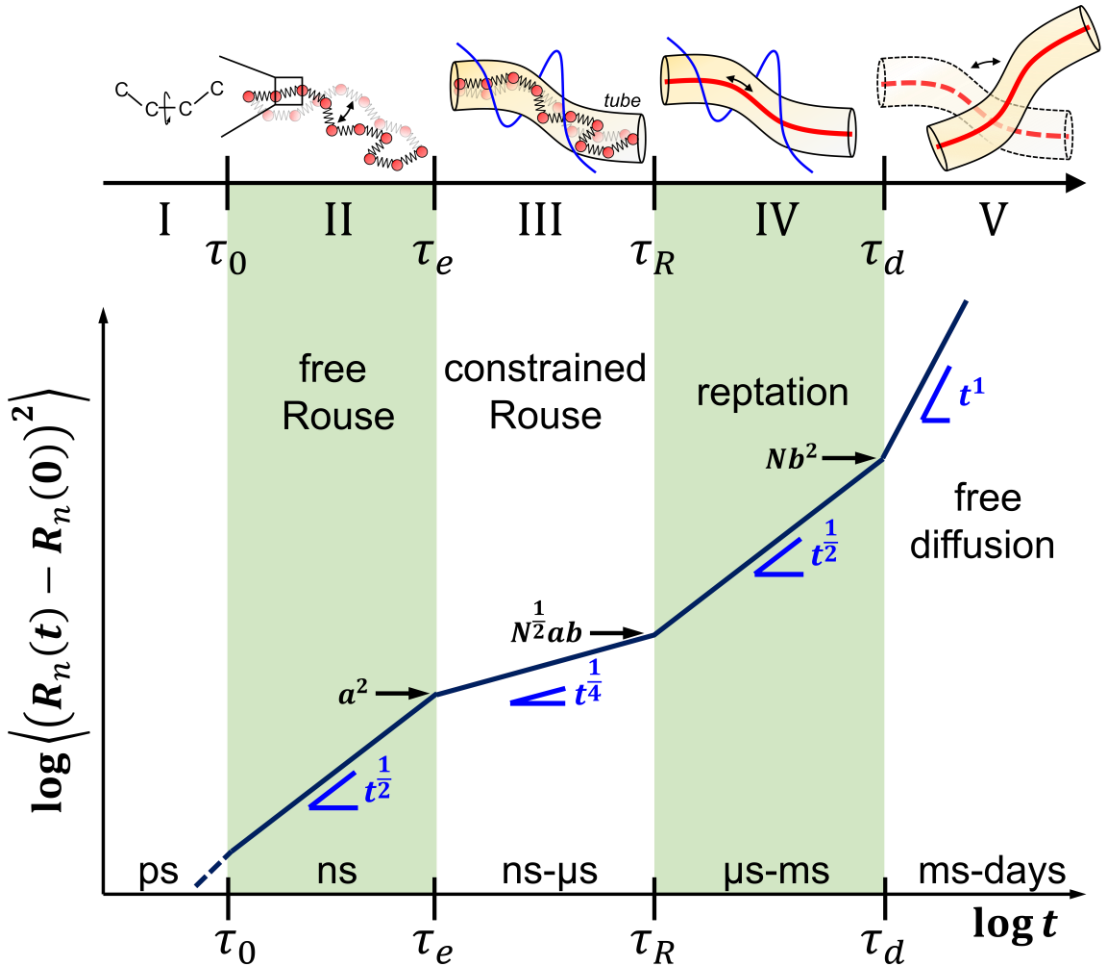

Figure 7. Five regimes of mean-square displacement of entangled polymer chains in a logarithmic time scale: (regime I) sub-segmental dynamics, (regime II) free Rouse dynamics, (regime III) constrained Rouse dynamics, (regime IV) reptation dynamics, and (V) free diffusion. The characteristic time τ_0 means the Kuhn segmental relaxation time, τ_e the entangled time, τ_R the Rouse relaxation time, and τ_d means the disengagement time. The parameter a and b indicates the step length of the primitive chain and the effective bond length, respectively. The schematics on the top describe the chain motions for each regime. Adapted by ref [5].

1.1.4. Signatures of polymer dynamics in rheology and dielectric spectroscopy

1.1.4.1 Rheology

Rheology and dielectric spectroscopy are two major techniques to determine the polymer dynamics. In rheology, either a stress or a strain is applied onto the polymer sample, and the resultant response is recorded (**Figure 8a**)[6]. The strain-controlled rheology is mainly discussed here. An oscillatory shear is applied to determine the viscoelastic behavior of the polymer melt:

$$\gamma(t) = \gamma_0 cos(\omega t) = \gamma_0 \mathbf{Re}\left(e^{i\omega t}\right) \tag{12}$$

where $\omega = 2\pi f$ is the angular frequency and γ_0 is the amplitude of the applied shear. The shear rate is usually small enough (*i.e.*, the velocity gradient is small) to ensure linear viscoelasticity. The response (*i.e.*, the shear stress) under such oscillatory shear is given as:

$$\sigma_s(t) = \gamma_0 \mathbf{Re}\left(G^*(\omega)e^{i\omega t}\right) = \gamma_0 (G'(\omega)\cos(\omega t) - G''(\omega)\sin(\omega t)) \tag{13}$$

and

$$G^*(\omega) = G'(\omega) + iG''(\omega) = i\omega \int_0^\infty G(t)e^{-i\omega t}\, dt \tag{14}$$

$$G'(\omega) = \omega \int_0^\infty G(t)\sin(\omega t)\, dt \tag{15}$$

$$G''(\omega) = \omega \int_0^\infty G(t)\cos(\omega t)\, dt \tag{16}$$

Here, $G^*(\omega)$ is the complex modulus, $G'(\omega)$ is the storage modulus, and $G''(\omega)$ is the loss modulus. The viscoelastic behavior of polymer melts under a small strain is subsequently discussed for two cases: unentangled and entangled polymers. For unentangled polymer melts composed of short chains, the relaxation modulus $G(t)$ is given as:

$$G(t) = ck_BT \sum_{p=1}^{N} exp\left(\frac{-t}{\tau_p}\right) (p = 1, 2, \dots N) = ck_BT \sum_{p=1}^{N} exp\left(\frac{-tp^2}{\tau_R}\right) \tag{17}$$

where $\tau_R (= \frac{\zeta N^2 b^2}{3\pi^2 k_B T})$ is the longest Rouse time (see also eq.6). Hence, the zero-shear viscosity can be obtained as:

$$\eta_0 = \lim_{\omega \to 0} \frac{G''(\omega)}{\omega} = \int_0^\infty G(t)\, dt = \frac{c\zeta}{36} N b^2 \tag{18}$$

The zero-shear viscosity for unentangled polymer melts is proportional to *N*. For entangled polymer melts with long chains, two time-regimes need to be considered: $t \leq \tau_e$ and $t \geq \tau_e$. For

$t \leq \tau_e \ll \tau_R$, the polymer dynamics is described also by the Rouse model. Therefore, the relaxation modulus is given as the approximation of equation (17):

$$G(t) = \frac{c}{2\sqrt{2}N} k_B T \left(\frac{\tau_R}{t}\right)^{\frac{1}{2}} \tag{19}$$

For $t \geq \tau_e$, the free Rouse behavior starts to feel the constraints from the tube. According to the reptation behavior (**Figure 6**), the parts of the polymer chain near the ends will disengage from the original tube and further create new tubes. By contrast, those in the middle will maintain the original tube. Note that only those segments staying in the deformed original tube can contribute to the shear stress. Therefore, the relaxation modulus at $t \geq \tau_e$ is given by:

$$G(t) = G_N^{(0)} \psi(s,t) \tag{20}$$

where $G_N^{(0)}$ is the plateau modulus, and $\psi(s,t)$ is the fraction of the tube that remains in the original tube at time *t*. At the transition from Rouse to the reptation, *i.e.*, $t = \tau_e$, $G_N^{(0)}$ can be represented in terms of equation (19) as:

$$G_N^{(0)} \cong G(\tau_e) \cong \frac{c}{N} k_B T \left(\frac{\tau_R}{\tau_e}\right)^{\frac{1}{2}} \tag{21}$$

Hence, the relaxation modulus expressed by equation (19) for $t \leq \tau_e$ is rewritten as:

$$G(t) \cong \frac{\frac{1}{2\sqrt{2}N}\left(\frac{\tau_R}{t}\right)^{\frac{1}{2}}}{\frac{1}{N}\left(\frac{\tau_R}{\tau_e}\right)^{\frac{1}{2}}} \cong G_N^{(0)} \left(\frac{\tau_e}{t}\right)^{\frac{1}{2}} \tag{22}$$

Equations (20) and (22) define the relaxation modulus for entangled polymer melts. Through equations (15), (20) and (22), the storage modulus $G'$is obtained as:

$$G'(\omega) = G_N^{(0)} \left(\frac{\pi}{2}\omega\tau_e\right)^{\frac{1}{2}} \quad for\ \omega \geq \frac{1}{\tau_e} \tag{23a}$$

and

$$G'(\omega) = G_N^{(0)} \sum_{p;odd} \frac{8}{\pi^2}\frac{1}{p^2}\frac{(\omega\tau_d/p^2)^2}{1+(\omega\tau_d/p^2)^2} \quad for\ \omega \leq \frac{1}{\tau_e} \tag{23b}$$

Evidently, the storage modulus shows a long plateau in a wide frequency range: $\frac{1}{\tau_d} \leq \omega \leq \frac{1}{\tau_e}$, which can be seen in the master curve of entangled *cis*-1,4-polyisoprene (**Figure 8c**). The zero-shear viscosity for the entangled polymer melts is calculated in terms of equation (20):

$$\eta_0 = \int_0^\infty G(t)\,dt = \int_0^\infty G_N^{(0)}\psi(s,t)\,dt = \frac{\pi^2}{12}G_N^{(0)}\tau_d \tag{24}$$

Due to $\tau_d \propto N^3$, the zero-shear viscosity of entangled polymers is $\eta_0 \sim N^3$ as well, which shows stronger molar mass dependence than for unentangled polymers ($\eta_0 \sim N$). In addition, by combining equations (15), (16) and (17), the storage and loss modulus can be represented as:

$$G'(\omega) \sim \omega^2 \sum_{p=1}^{N} \left(\frac{\tau_p^2}{1+\omega^2\tau_p^2}\right) \tag{25}$$

$$G''(\omega) \sim \omega \sum_{p=1}^{N} \left(\frac{\tau_p}{1+\omega^2\tau_p^2}\right) \tag{26}$$

The $G'(\omega)$ and $G''(\omega)$ display distinctly different frequency dependencies especially at low frequencies ($\omega \ll \frac{1}{\tau_d}$) as $G'(\omega) \propto \omega^2$ and $G''(\omega) \propto \omega$, respectively. In other words, the storage modulus is more sensitive to slower viscoelastic modes as compared to the loss modulus. Lastly, the plateau modulus also defines the entanglement molar mass M_e :

$$M_e = \frac{\rho RT}{G_N^{(0)}} \tag{27}$$

Here ρ is the density of the polymer and R is the gas constant. M_e specifies the molecular weight between entanglements, corresponding to N_e Kuhn segments ($M_e = N_e \cdot M_0$).

1.1.4.2 Dielectric spectroscopy

Dielectric spectroscopy can probe the orientation polarization of molecular dipoles under an external electric field (**Figure 8b**)[7]. For the dielectric measurements, a nonzero dipole moment for the examined material is a requirement (this requirement is fulfilled for the vast majority of molecules/polymers). The orientational polarization, $\mathbf{P}(t)$, is defined as the summation of all dipoles in a unit volume, $\boldsymbol{\mu}_i(t)$:

$$\mathbf{P}(t) = \sum_i \boldsymbol{\mu}_i(t) \tag{28}$$

and the dielectric relaxation function $\Phi(t)$ at equilibrium is represented in terms of the auto correlation of polarization:

$$\Phi(t) = \frac{\langle \mathbf{P}(t) \cdot \mathbf{P}(0) \rangle}{\langle \mathbf{P}^2 \rangle} \tag{29}$$

The obtained complex dielectric function, ε^*, measured under an alternating electric field is represented as:

$$\varepsilon^*(\omega) \equiv \varepsilon'(\omega) - i\varepsilon'(\omega) = \varepsilon_\infty - \Delta\varepsilon \int_0^\infty \frac{d\Phi(t)}{dt} exp(-i\omega t)dt \tag{30}$$

where $\varepsilon'(\omega)$ and $\varepsilon'(\omega)$ are, respectively, the real and imaginary part of complex dielectric function, ε_∞, is the dielectric permittivity value at very high frequencies, and $\Delta\varepsilon$ is the dielectric strength.

The dielectric relaxation behavior of linear type-A polymer chains under a small oscillatory electric field is subsequently discussed. According to the Stockmayer classification, type-A polymers possess two types of dipoles, one parallel and one perpendicular to the polymer chain contour. In other words, local segmental dynamics and global chain dynamics can be simultaneously determined by dielectric spectroscopy with type-A polymers. For polymers lacking dipoles parallel to the chain backbone, only information about segmental dynamics can be obtained. The dielectric relaxation along the chain backbone of type-A polymer can be described by the rewritten form of equation (29) in terms of bond vectors **u**:[8]

$$\Phi(t) = \frac{1}{N}\sum_{n=1}^{N}\sum_{n'=1}^{N} \vartheta(n)\vartheta(n')C(n,t;\, n') \tag{31}$$

where $C(n,t;\, n') = \frac{1}{b^2}\langle \mathbf{u}(n,t)\cdot\mathbf{u}(n',0)\rangle$ is the local correlation function manifesting the orientation correlation of two molecules in the same chain at times 0 and *t*. The parameter $\vartheta(n)$ indicate the direction of total dipole moment $\boldsymbol{\mu}_{sum}$: equal to 1 (or -1) for the direction of $\boldsymbol{\mu}_{sum}$ parallel (or anti-parallel) to the bond vector **u**. The dielectric relaxation function, $\Phi(t)$, with Rouse modes is given as:

$$\Phi(t) = \sum_p g_p exp\left(\frac{-t}{\tau_p}\right) \tag{32}$$

where g_p and τ_p are the normalized intensity and characteristic time for the p^{th} dielectric mode, respectively. Combining equations (30) and (32), the real and imaginary part of complex dielectric function can be expressed as:

$$\frac{\varepsilon_0 - \varepsilon'(\omega)}{\Delta\varepsilon} = \omega^2 \sum_p g_p \frac{{\tau_p}^2}{1+\omega^2{\tau_p}^2} \tag{33a}$$

$$\frac{\varepsilon''(\omega)}{\Delta\varepsilon} = \omega \sum_{p} g_p \frac{\tau_p}{1+\omega^2 {\tau_p}^2} \qquad (33b)$$

Notice the similarity with equations (25) and (26) from rheology, *i.e.*, real (imaginary) part of complex dielectric function is proportional to ω^2 (ω). The dielectric relaxation time for the first mode τ_1 is nearly identical to the peak position in the measured dielectric curves of monodisperse type-A polymer chains. Take a linear entangled *cis*-1,4-polyisoprene (a well-known type-A polymer) with a narrow polydispersity (**Figure 8c**, bottom). The sharp peak corresponds to the longest normal mode. To the left side of the peak, *i.e.*, at lower-frequencies region, an asymptote is observed; on the right side corresponding to higher frequencies, a long tail is seen. Given an unentangled (entangled) type-A polymer, the local correlation function $C(n,t;\, n')$ can be expressed via the Rouse model (tube model) as:

$$C(n,t;\, n') = \frac{2}{N}\sum_{p=1}^{N} \sin\left(\frac{p\pi n}{N}\right) \sin\left(\frac{p\pi n'}{N}\right) exp\left(\frac{-tp^2}{\tau_R}\right) \quad for\ unentangled \quad (34)$$

where $\tau_R = \frac{\zeta N^2 b^2}{3\pi^2 k_B T}$ indicates the Rouse time as defined by equation (6) with p=1.

$$C(n,t;\, n') = \frac{2}{N}\sum_{p=1}^{N} \sin\left(\frac{p\pi n}{N}\right) \sin\left(\frac{p\pi n'}{N}\right) exp\left(\frac{-tp^2}{\tau_d}\right) \quad for\ entangled \quad (35)$$

where $\tau_d = \frac{\zeta N^3 b^4}{\pi^2 k_B T a^2}$ indicates the reptation or disengagement time as defined by equation (11). With these local correlation functions (given by equation (34) and (35)), the normalized intensity g_p and characteristic time τ_p for the p^{th} dielectric mode is thus obtained as:

$$\tau_p = \frac{\tau_R}{p^2}\ and\ g_p = \frac{2}{N^2}\left[\int_0^N \vartheta(n) \sin\left(\frac{p\pi n}{N}\right) dn\right]^2 \quad for\ unentangled \quad (36)$$

and

$$\tau_p = \frac{\tau_d}{p^2}\ and\ g_p = \frac{2}{N^2}\left[\int_0^N \vartheta(n) \sin\left(\frac{p\pi n}{N}\right) dn\right]^2 \quad for\ entangled \quad (37)$$

Due to $g_p = \frac{8}{p^2\pi^2}$ (for p = odd) and $g_p = 0$ (for p = even), the dielectric relaxation of the internal Rouse chains are only affected by the odd-modes.

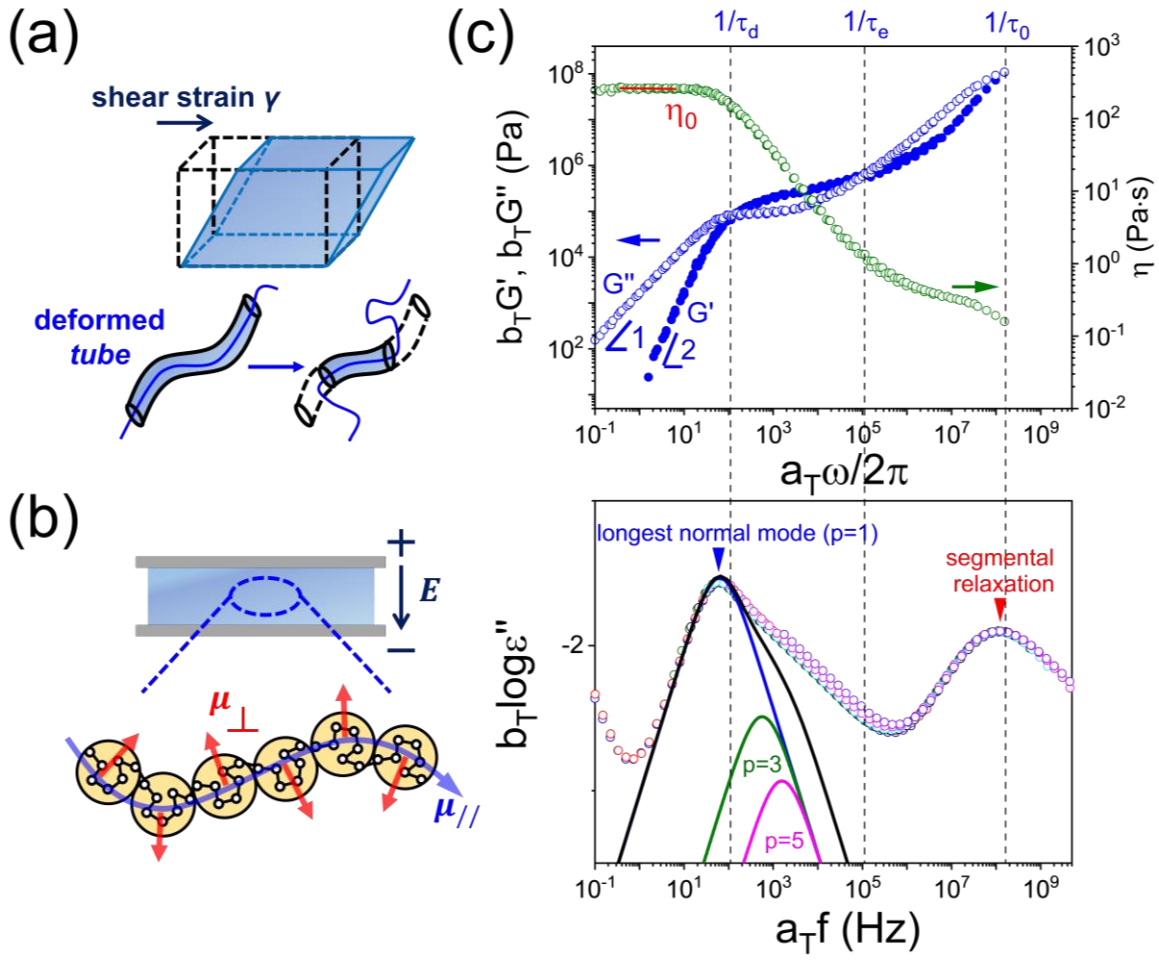

Figure 8. Schematics showing the operational principles of rheology (a) and of dielectric spectroscopy (b) to determine the polymer chain dynamics in a type-A polymer. (c) The time-temperature superposition (master curve) for the viscoelastic (top) and dielectric loss curves (bottom) of entangled *cis*-1,4-polyisoprene with M_w=42 kg·mol^{-1} at reference temperature of 303K. The characteristic relaxation times are specified on top as: τ_0 (Kuhn segmental relaxation time), τ_e (the time for the onset of entanglement), τ_d (the reptation time or disengagement time). Single peaks under the dielectric curve are simulated peaks corresponding to the individual p^{th} mode relaxation modes: (blue) p=1, longest normal mode, (olive) p=3, and (magenta) p=5. The black line gives the summation of the first three Rouse mode.

1.2. Effect of two-dimensional (2D) confinement on polymer dynamics

1.2.1 What is known

Polymer configurations near a surface differ from the bulk. They are usually described in terms of tails, loops, and trains (**Figure 9a**).[9] *Tails* refer to the segments with one end tethered to the surface, and the other end is free; *loops* are formed when a chain has two anchoring points onto the surface; *trains* refer to a sequence of repeat units adsorbed onto the surface. Several challenging problems concerning the polymer dynamics of an adsorbed polymer layer exist: (i) how the density of entanglements and the associated relaxation times are affected near the surface? (ii) How the segmental mobility and the associated glass temperature (T_g) is affected? (iii) How the polymer chains "pack" themselves onto the surface? (iv) How long and what condition do the chain configurations find towards the equilibration? (v) How does an adsorbed layer respond when driven away from equilibrium?

To answer some of the above questions a hypothetical picture of polymer chains in the vinicity of the interface has been proposed (**Figure 9b**).[10] Within this picture, loops of various lengths are created. Polymer chains experience more severe topological constraints (*i.e.*, entanglements) in a tighter loop (*position I*) than in a looser loop (*positions II* and *III*). Furthermore, surface-enhanced entanglements can propagate in the direction normal to the surface. At the same time, the polymer segments within the trains or in the tighter loops can experience a stronger monomeric friction than those segments located in the loops dangling away from the surface. This picture may rationalize the experimental findings of retarded polymer dynamics and higher T_g (in some cases) near the surface. In addition, there is a "parking" problem created by the adsorption of polymer chains (**Figure 9c**). Within this "footprint" model, the first-arrived chains try to maximize the contact area on the initially bare surface, *i.e.*, they have larger footprint size. On the other hand, the late-arrived chains leave a smaller footprint due to reduced adsorption sites. The different chain conformations and configurations adopted in the vinicity of the surface are expected, and indeed have a large impact on the segmental and chain dynamics.

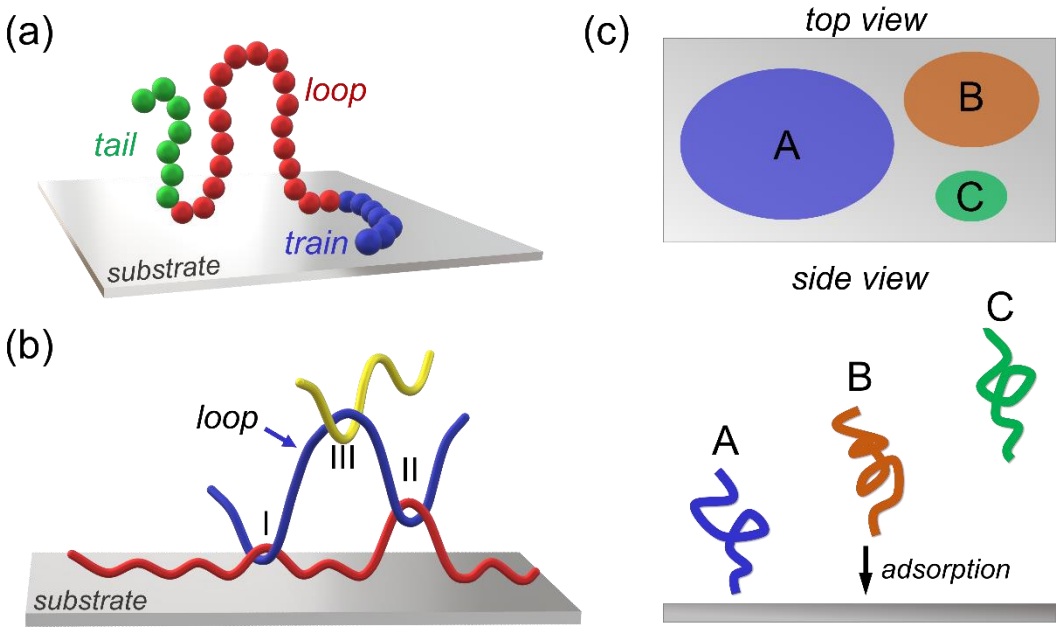

Figure 9. (a) Schematics showing a polymer chain with different configurations (tail, loop, and train) at the polymer/substrate interface. (b) Hypothetical picture showing surface gradient in the polymer chain conformations. (c) Schematic showing the larger footprints for the first-arrived chains (A), and the smaller footprints for the late-arrived chains (B and C) due to reduced adsorption sites. Adapted by ref [10].

Effect of confinement on the segmental dynamics

In general, the segmental relaxation of confined polymers in nanopores displays two features: (i) the broadening of the relaxation peak, *i.e.*, the dynamics become very heterogeneous, and (ii) the faster (slower) dynamics, which is reflected in the lower (higher) T_g.[11] The origin of the different segmental dynamics under confinement has been the explored phenomena. A systematic study was made by Alexandris et al.[12] using dielectric spectroscopy for the segmental dynamics and additional contanct angle and surface tension measurements to explore the origins of deviated segmental dynamics and associated T_g changes. Several amorphous polymers were studied within AAO nanopores of diameters from 25 nm to 65 nm (**Figure 10**). The studied polymers included poly(phenylmethyl siloxane) (PMPS), poly(vinyl acetate) (PVAc), *cis*-1,4-polyisoprene (PI), 1,4-polybutadiene (PB), oligostyrene (PS), and poly(dimethyl siloxane) (PDMS). A trend for decreasing T_g relative to the bulk with increasing interfacial energy was found. The authors concluded that interfacial energy is a key parameter in controlling the segmental dynamics of

polymers under confinement. Later, Talik et al.[13] examined the above trend of T_g versus interfacial energy by infiltrating chemically modified poly(propylene glycol) (PPG) into the same AAO nanopores, *i.e.*, PPG-OH, PPG-NH_2, and PPG-OCH_3. It was found that the reduction in T_g followed the trend obtained by Alexandris et al.[11]

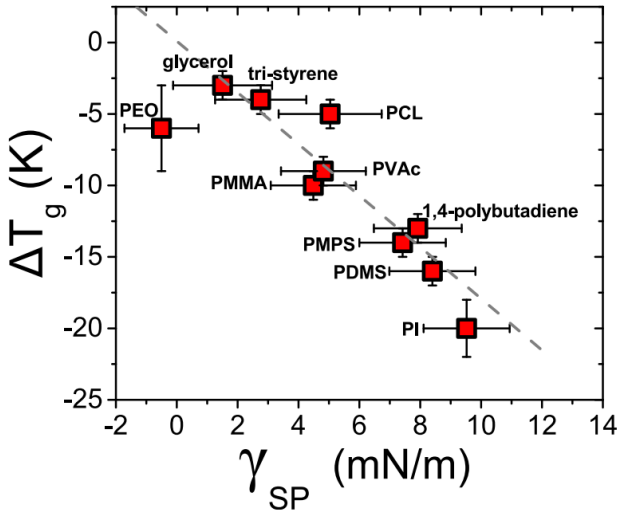

Figure 10. Dependence of $\Delta T_g (= T_g^{AAO} - T_g^{bulk})$ on interfacial energy (at T = 290 K) for several polymers exhibiting different polymer/surface interactions. The data do not refer to the same pore diameter nor to identical degree of confinement ($2R_g/d$; R_g means radius of gyration and d means the pore diameter).[12]

An intriguing observation has been the existence of two (or even three) glass temperatures for 2D-confined polymers. Politidis et al.[14] found a hysteresis in the temperature dependence of the segmental relaxation times for the confined entangled *cis*-1,4-polyisoprene (PI) by DS (**Figure 11b**). Two glass temepratures were found: a lower T_g from the cooling scan and a higher T_g (close to bulk value) from the subsequent heating scan. It was noticed that no hysteresis could be observed if the lower T_g was not crossed in the previous cooling scan. Hence only a lower T_g could be determined, implying that the high T_g is conditional. This observation agreed with measurement results from temperature-modulated differential scanning calorimetry (TM-DSC) following an analogous thermal protocol (**Figure 11a**). A physical interpretation was given: the higher T_g associates with a bulk-like behavior, which is restored by the desorption of segments from the pore walls. On the other hand, the lower T_g is the one closer to the equilibrium.

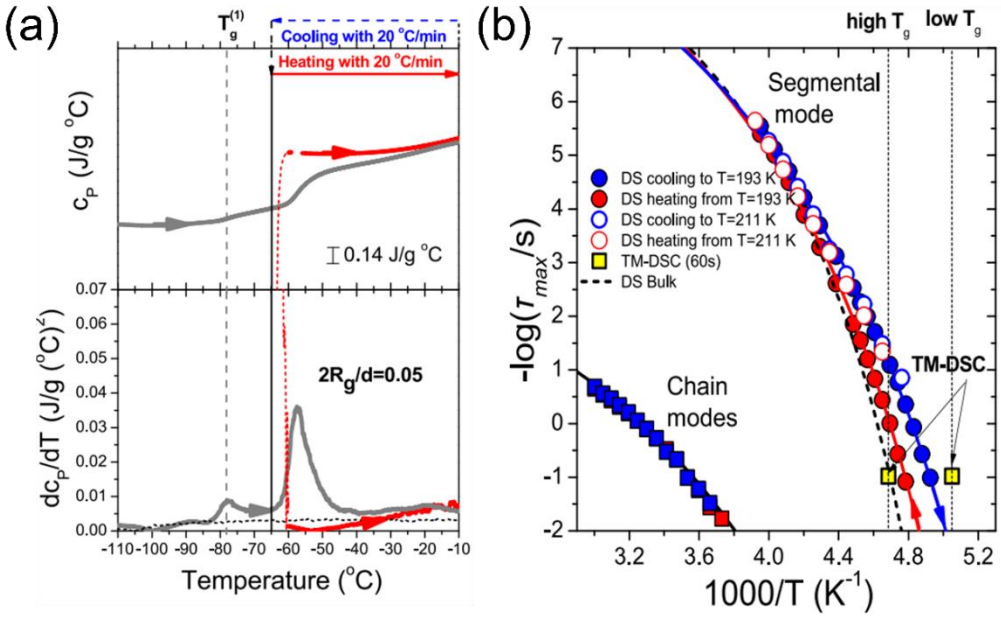

Figure 11. (a) DSC heating traces (rate of 20 °C/min) for the heat capacity (c_p) and the associated derivative (dc_p/dT) with respect to temperature for the entangled *cis*-1,4-polyisoprene with a molar mass of 100 kg/mol confined within AAO 400nm pores. Gray line (red line) represents the heating scan from -120 °C (-65 °C). (b) Arrhenius relaxation map showing the temperature dependence of segmental and normal mode relaxation times of confined PI obtained with different thermal protocols: the first is by cooling to 191 K (filled blue) and subsequent heating (filled red). The second is by cooling to 211 K (empty blue) followed by a heating scan (empty red). The lines represent VFT fits. The yellow squares represent the low and high glass temperatures (T_g) obtained from TM-DSC measurements under isochronal condition ($\tau \sim 10\ s$).[14]

In addition to the studies above some calorimetric and dielectric studies of 2D-confined polymers report a much higher T_g. An interesting feature was shown in these dielectric studies—a kink in the temperature dependence of segmental relaxation times $\tau_\alpha(T)$.[16-20] At temperatures higher than T_{kink}, the $\tau_\alpha(T)$ of the confined polymer followed the same VFT behavior as in bulk. However, at $T < T_{kink}$ a departure of $\tau_\alpha(T)$ from the bulk VFT dependence took place. At T_{kink} crossover from VFT to Arrhenius law was shown, and the segmental dynamics became faster than the bulk. In addition, the characteristic temperature, T_{kink}, shifted to the higher temperature region within the smaller pores. These experimental findings were partially explained with a two-layer model[21] (**Figure 12a**). The two-layer model separates the confined polymer into two subsets with different dynamics: (I) the core segments in the center show the faster dynamics, hence a lower T_g ($T_{g,core} < T_{g,\ bulk}$), and (II) the segments near the pore surface show slower dynamics, and thus a higher T_g ($T_{g,interfacial} > T_{g,\ bulk}$). In some cases, in pores with dimensions much larger than the radius

of gyration, more than two calorimetric T_g's could be observed.[22] A three-layer model (**Figure 12b**) with an additional layer between the core and interfacial area, *i.e.*, the *interlayer*, was considered. The latter was attributed to polymer segments trapped in a nonequilibrium state (*i.e.*, strong cooling rate dependence) with an intermediate glass temperature $T_{g,\,intermediate}$, *i.e.*, $T_{g,\,core} < T_{g,\,intermediate} < T_{g,\,interfacial}$. These intriguing results on the presence of 3 T_g's corresponding to 3 distinct layers of the confined polymers should be seen with some skepticism. The reason is that the author did not discuss/show the corresponding cooling curves where the sample-by definition-is closer to the equilibrium.

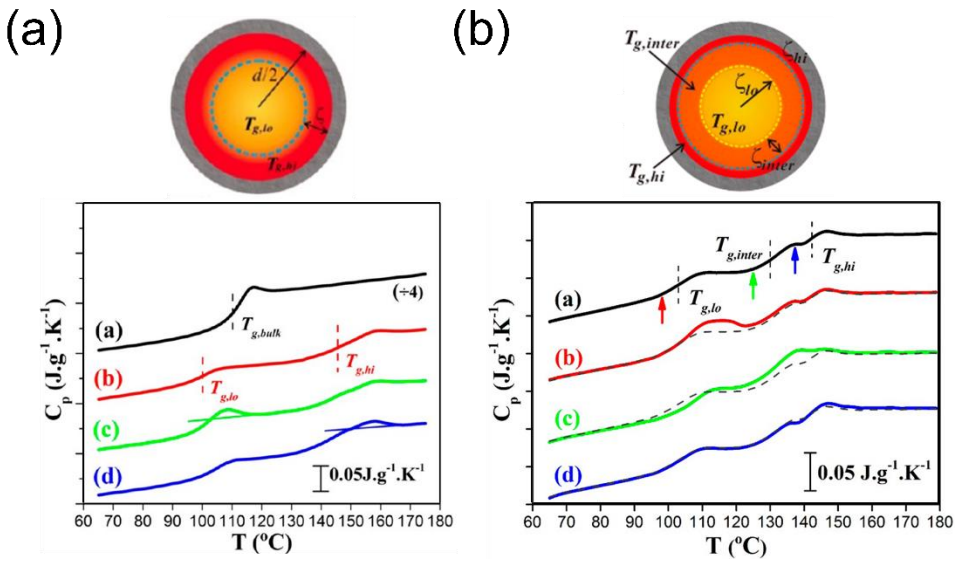

Figure 12. Normalized DSC heating traces (rate of 10 K/min) for bulk and confined $PMMA_{6K}$ within AAO nanopores with diameter of (a) 80 nm and (b) 300 nm. The possible T_g distribution inside the pores are plotted in the top as (a) two-layer and (b) three-layer model. The color codes of (a) are following: (black) bulk $PMMA_{6K}$, (red) confined $PMMA_{6K}$, and $PMMA_{6K}$-filled AAO samples annealed at (green) $T_{g,low} - 10$ K and (blue) at $T_{g,high} - 10$ K for 2 hours. The color codes of (b) are the following: $PMMA_{6K}$-filled AAO samples without aging (black), and annealed at $T_{g,low} - 5$ K (red), $T_{g,intermediate} - 5$ K (green), and $T_{g,high} - 5$ K (blue) for 5 hours. The dashed lines in (b) are heating curves of confined samples without aging. The arrows in (b) indicate the annealing temperatures.[21,22]

Annealing was also employed to understand the origin of the different T_g's. Li et al.[21] designed a series of isothermal annealing protocols on AAO-confined poly(methyl methacrylate) (PMMA) using DSC to examine the influence of annealing temperatures and annealing time on the $T_{g,interfacial}$ and $T_{g,core}$ (**Figure 13**). It was found that the enhancement of either the annealing

temperature or the annealing time increased the glass temperature of the interfacial layer ($T_{g,\ interfacial}$) but reduced the T_g for the core polymer ($T_{g,\ core}$). Interestingly, the three glass temperatures ($T_{g,\ core}$, $T_{g,\ intermediate}$, and $T_{g,\ interfacial}$) could only appear with an intermediate cooling rate like 10 K/min; instead, only a single T_g appeared with a fast cooling rate.

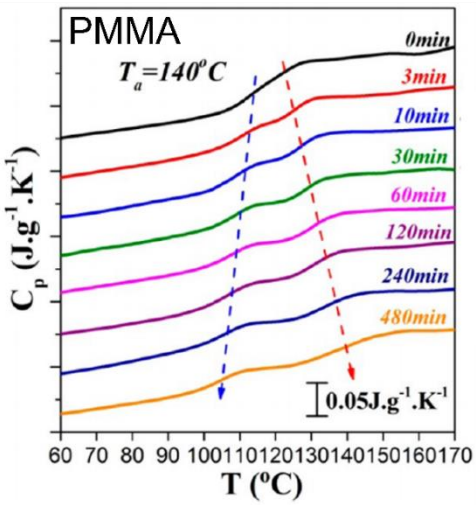

Figure 13. Normlaized DSC traces of hperquenched PMMA6k-filled AAO samples annealed at T=140 °C for different times from 0 min to 480 min.[21]

Effect of confinement on the chain dynamics

As discussed earlier, the polymer chain dynamics can be described by the Rouse model and the Reptation models, respectively, for unentangled and entangled polymers. Both the Rouse and the Reptation dynamics can be perturbed when the dimensions of the confining nanopore is of the order of the polymer radius of gyration ($D \sim R_g$).

Beared with the capability to measure simultaneously the structure and dynamics of polymer chains, the neutron spin echo (NSE) method was exploited to study the polymer behavior within nanopores.[23-25] Krutyeva et al.[24] employed NSE to study the dynamics of unentangled poly(dimethyl siloxane) (PDMS) confined within the AAO nanopores with attractive pore walls (**Figure 14**). The evolution of dynamic structure factor, $S_{chain}(Q,t)$, was descibed by a two-phase model comprising a bulk-like and a confined "phases". Interestingly, the volume fraction of confined phase was found to be larger than the size of a PDMS subchain between the anchoring points, which suggested an interphase between the inner bulk-like phase and the adsorbed chains

(**Figure 14b**). Within this interphase, the surrounding chains interpenetrate the loops at the adsorbed chains. These interpenetrating chains can only diffuse by reptation.

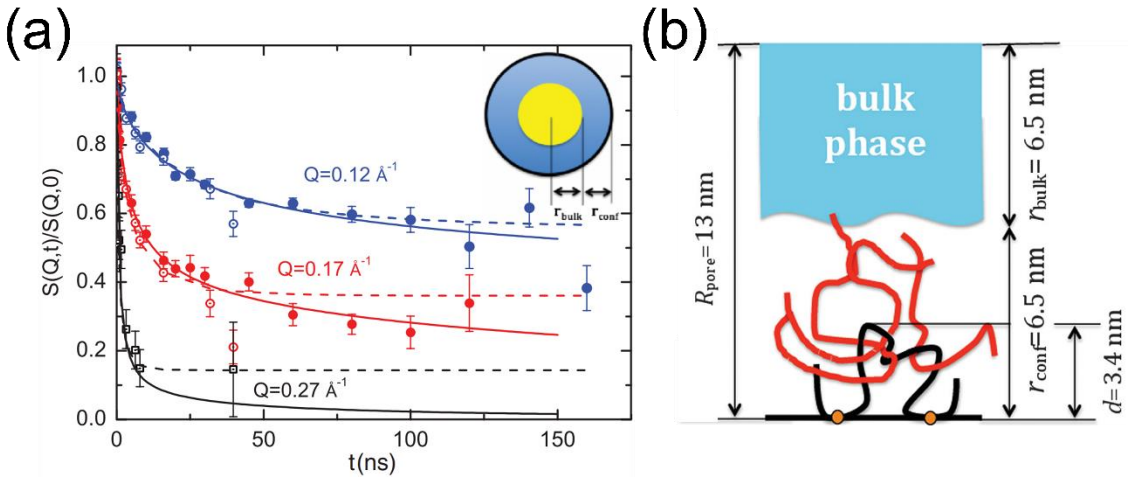

Figure 14. (a) The measured coherent single chain dynamic structure factor (*S(Q, t)*) from neutron spin echo (NSE) for confined PDMS within AAO 26 nm pores. The solid (empty) symbols represent the data obtained from different instruments. The dashed lines represent fits to the Rouse model. The solid lines represent fits using a continuous transition region from the suppressed to free Rouse model. The inset shows a two-phase model. (b) Schematic showing the two-phase model for the cylindrical-confined polymer melts. The black lines represent the adsorbed chains on the pore walls with a loop structure. The red lines show entangled chains in the interphase interpenetrating the loops formed by the adsorbed chains.[24]

The majority of studies of the effect of confinement on the chain dynamics refers to type-A polymer investigated by DS. Two well-known examples are *cis*-1,4-polyisoprene (PI) and poly(propylene glycol) (PPG). With respect to the former (PI), Alexandris et al.[15] studied the dynamics of unentangled PI confined within the AAO nanopores as a function of molecular weight (300 - 5000 g/mol) and pore size (25 - 400 nm). The peak positions of the normal mode and segmental mode were approximately as in the bulk. They claimed that such observation does not necessarily imply the identical global chain dynamics of bulk and confined sample. This argument was supported by two additional findings: (I) a pronounced broadening to the relaxation peaks in the smaller pores, and (II) the low-frequency slope (*m*) of global chain relaxation peak remained below 1 under confinement. The latter implied the retarded chain dynamics due to adsorption. Similar results were revealed by Politidis, C. et al[14] for entangled PI. Interestingly, a new process located between the segmental and longest normal modes was found, the so called “intermediate”

process (**Figure 15**). They discussed the new mode in terms of the adsoption/desorption kinetics of segments in the vicinity of the pore walls.

The broadening of the normal mode relaxation was also reported in 2D-confined PPG independently of molecular weight and end-group.[16-19] In addition, Tarnacka et al.[16-19] observed a crossover from VFT to Arrhenius behavior in the normal mode as in the segmental mode (described before): the normal mode of confined PPG was faster than in bulk below a characteristic temperature (called T_c or $T_{g,interface}$). However, the deviation from bulk behavior was less pronounced in normal mode. They attributed it to the different sensivity of segmental and normal mode dynamics to the density variation induced by the vitrification of adsorbed molecules. An interfacial process slower than normal mode was revealed in smaller pores, although being hardly visible in measured dielectric loss spectra. This interfacial process was discussed in terms of the reorientation motions of adsorbed molecules at the pore walls.

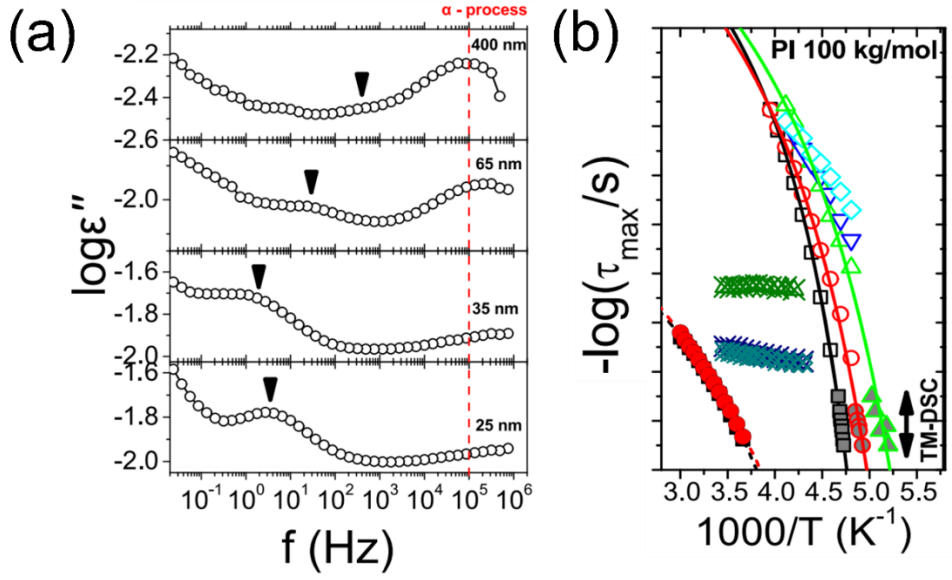

Figure 15. (a) The dielectric loss curve (black empty circles) of confined PI 50 kg/mol within AAO pores (with pore diameters of 400, 65, 35, and 25 nm) obtained at T = 248 K. Black arrows indicate the intermediate process. (b) Arrhenius relaxation map showing the temperature dependence of relaxation times of segmental (empty symbols), most intense chain mode (filled symbols), and intermediate process (crossed symbols) for the confined PI 100 kg/mol within AAO pores with diameters of 400 nm (circles), 65 nm (up triangles), 35 nm (down triangles), and 25 nm (rhombi). The dielectric data were obtained on cooling from higher temperatures. The gray-filled symbols were acquired from the cooling scans in TM-DSC measurements. The lines represent the VFT fits.[13]

The exchange of polymer dynamics within the AAO pores were discovered by Franz et al.[26] using nuclear magnetic resonance (NMR). They studied poly(butadiene) (PB) confined in the same AAO. They reported heterogeneous dynamics with a fast exchange and oriented dipolar tensors parallel to the pore axis for low molar masses. For higher molar masses (M_w > 100 kg/mol) they found an interfacial region with dipolar tensor oriented normal to the pore walls coexisting with a core region where dipolar tensor had an isotropic distribution (**Figure 16**).

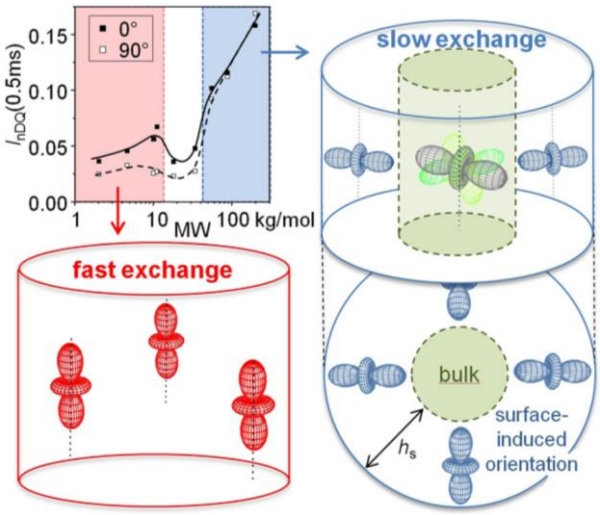

Figure 16. A model explaining the two-regime molecular weight (M_w) and angular dependence of short-time (τ_{DQ} =0.5 ms) single-point nDQ intensities. At low-M_w regimes with fast-exchange dynamics, the orientation of time-averaged residual dipolar tensors was uniaxial and parallel to the pore axis. For high-M_w, a core region was found with an isotropic distribution for both tube segments and associated residual dipolar tensor that coexisted with an interfacial region (a layer thickness of 2.5 nm was obtained) with residual dipolar tensor were oriented normal to the pore walls.[26]

Capillary imbibition of polymer melts in nanopores

The polymer imbibition is intrinsically correlated to the polymer dynamics. Hence, the imbibition kinetics of polymers is not trivial as in simple liquids (*e.g.*, alcohols). For simple liquids, the imbibition behavior is well described by the Lucas-Washburn equation (LWE)[27],

$$h(t) = \left(\frac{\gamma R cos\theta}{2\eta}\right)^{1/2} \sqrt{t} \tag{38}$$

Here, γ is the surface tension of the liquid, R is the pore radius, θ is the contact angle, η is the viscosity, t is the imbibition time, and $h(t)$ represents the imbibition length of the fluids inside the

nanopores. The LWE is the consequence of the balance between the capillary force and the viscous force, which are represented as $2\pi R(\gamma_{SV} - \gamma_{SL})$ and $8\pi\eta h\left({dh}/{dt}\right)$, respectively. The γ_{SV} and γ_{SL} are the interfacial tension between solid/vapor and solid/liquid, individually. The applicability of LWE to the imbibition of polymer melts has been reported. The first report was by Shin et al.[28] They used time-resolved small-angle X-ray scattering to monitor the imbibition of highly entangled polystyrene (PS). Although the imbibition length of PS followed the square-root-of-time behavior ($t^{1/2}$), enhanced mobility and hence a lower effective viscosity were revealed within nanopores. A recent study explored a broader range of pore sizes and polymer dimensions. A reversal in imbibition kinetics of PEO was observed: a *slower* capillary rise than theoretically predicted by LWE was revealed for shorter chains and a *faster* capillary rise for chains with more entanglements.[29] Subsequently, a unified theory was established by the same group to describe the imbibition kinetics of polymer melts.[30] The theory described the process of polymer imbibition as a competition between two mechanisms: the dead-zone effect (**Figure 17a**) and the reptation under confinement (**Figure 17b**). The former originates from the adsorption of polymer chains onto the pore walls. A layer of immobile chains is subsequently formed, thus giving rise to a smaller effective pore radius. Because of the fourth-power relationship between viscosity and pore radius, as $\frac{\eta_{effective}}{\eta} = \left(\frac{R}{R_{effective}}\right)^4$, a slight decrease of pore radius can bring a huge increase to the effective viscosity. This was not realized by the earlier study.[28] Hence, the dead-zone effect is the main reason for the slowing down of the imbibition dynamics for the shorter chains. As the effective pore radius decreases to a value comparable to the thickness of dead-zone, the macroscopic flow can be stopped. Under such strong confinement the transport of polymers can only be achieved by the reptation of free polymer chains in a network driven by pressure gradient. The pressure gradient is the result of the capillary force. The theory was evidenced to be in qualitatively agreement with the experimental results of imbibition of a series of PEO melts (**Figure 17c**).[30] Most importantly, the non-monotonic variation in effective viscosity was successfully captured. Subsequently, the imbibition behavior of polymer mixtures containing short and long chains was investigated.[31] Interestingly, they found a faster penetration into nanopores for the shorter chains. Moreover, the enrichment of the pore surface was mostly by the shorter

chains. It was suggested that an efficient separation of long and short chains in the bulk can be made by the different imbibition speeds through narrow pores.

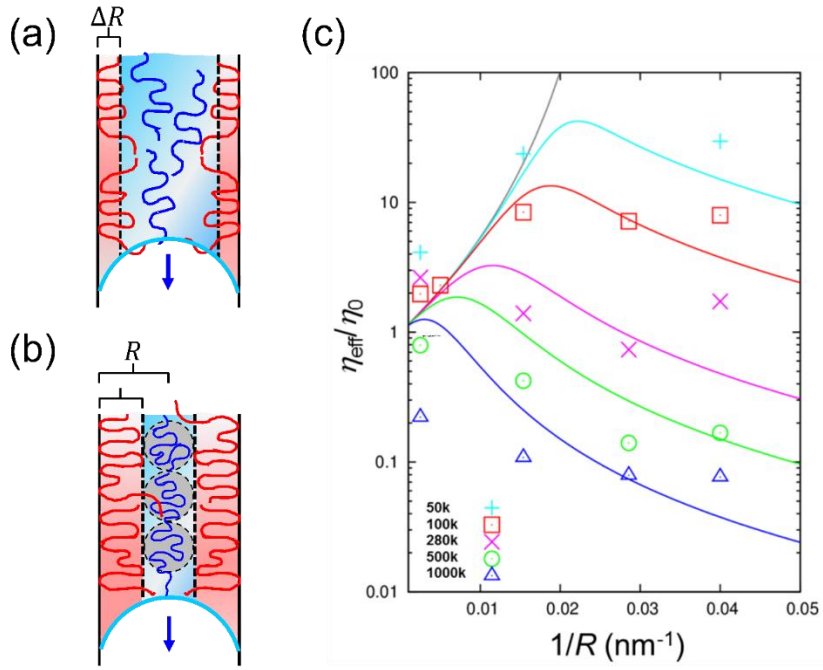

Figure 17. (a, b) Schematics showing the two mechanisms controlling the imbibition of polymer melts within nanopores: parabolic flow with dead-layer effects and reptation under pressure gradient, respectively. The red (blue) lines represent the adsorbed (free) chains. The red labelled region indicates the dead-layer with thickness ΔR. The cyan curved line indicates the meniscus of the growth front. R is pore radius. (c) A comparison of the pore size dependence ($1/R$) of the effective viscosity obtained from the experiment (empty symbols) and the theoretical predictions (lines) for different molecular weights of PEO: (cyan) 50 kg/mol, (red) 100 kg/mol, (magneta) 280 kg/mol, (green) 500 kg/mol, and (blue) 1000 kg/mol.[30]

1.2.2 What is not known

So far, the changes in polymer dynamics under cylindrical confinement were solely determined following the complete imbibition. Although much evidence for confinement effects on the polymer dynamics has been collected, information about the dynamics of polymers at the segmental and chain length scales *during* imbibition is still missing. A recent advancement in studying polymer imbibition *in situ* has been through the development of the *nanofluidic* method.[32-35] The method employs the same AAO templates sputtered with a thin gold layer to transform the membranes into capacitors where an ac-field can be applied along the pore axes. The method offers simultaneous access to (i) the molecular dynamics during flow at the segmental and possibly the chain length scales, and (ii) to the kinetics of imbibition. The first report on polymer imbibition by the nanofluidic method concerned the segmental dynamics of a polar polymer in AAO pores. It was found that the segmental dynamics during imbibition were identical to bulk. This observation is certainly not in line with literature showing moderate to larger shifts in the glass temperature due to the variable polymer/AAO wall interfacial energy. Evidently, this point needs to be clarified. A second point relates to the chain dynamics. Pratically, nothing is known about the polymer dynamics at the chain length level during imbibition. Do chains interact with the pore walls, and if so, how the entanglements are distributed during flow? In addition, the kinetics of capillary imbibition into AAO nanopores were much less investigated by the nanofluidic approach. Although the imbibition lengths were found to scale as $t^{1/2}$, the effective viscosity experienced by the polymer during flow was not extracted, and this precluded a stringent test of the applicability of the LWE at the nanoscale. Lastly, nothing is known about how polymer electrolytes penetrate narrow pores. Do the polymer segments carry the ions during imbibition or there are strong polarization effects that are created?

1.3. The scope of the Thesis

In this Thesis I am concentrating on the effect of 2D confinement on a variety of macromolecules including amorphous polymers, and solid polymer electrolytes during imbibition (**Figure 18**). For each area different important questions are addressed (**Table 1**).

In first area we address the question of how nanoconfinement affects the segmental dynamics and chain dynamics *during imbibition*. Two **amorphous polymers** are employed: poly(*n*-butyl methacrylate) (PnBMA) for the segmental process and *cis*-1,4-polyisoprene (PI) for the chain dynamics. A nanofluidic method, the so-called nanodielectric spectroscopy, is employed to obtain simultaneous access to the imbibition length and the associated polymer dynamics (segmental and chain scales) as a function of imbibition time. Despite many works on confined polymers within nanopores this issue was not discussed before. This part builds on earlier experimental and theoretical work in our group[30] where imbibition was followed *ex situ* by optical microscopy[29]. The present work goes much beyond since it is made *in situ* and, in addition, it provides access to the polymer dynamics during flow.

In second area we investigate how ions and polymer segments migrate in a polymer electrolyte *during imbibition*. To this end **solid polymer electrolytes** based on the archetypal system poly(ethylene oxide) (PEO)/LiTFSI are employed. The system is well known for its high ionic conductivity and its role as potential replacement materials for liquid electrolytes in Li-ion batteries has been explained. In this topic we are interested in the evolution of ionic conductivity as a function of polymer molar mass, ion concentration and pore size.

In third area we explore the possibility that a **semicrystalline polymer** can penetrate into narrow pores from its crystal state. Despite this might sound paradoxical – due to the very high viscosity of a crystalline polymer – earlier measurements from our group revealed the possibility to infiltrate a block copolymer directly into nanopores from an ordered state where the viscosity is also very high. Should this part be successful it will be a demonstration that a crystal can flow by capillary action.

Table 1. Areas of interest to be studied by the nanodielectric spectroscopy method.

Area of research	Problems of interest	Systems to be investigated
In situ imbibition of amorphous polymers	How the segmental and chain dynamics are affected during imbibition? What is the effective viscosity that a polymer experiences?	poly(*n*-butyl methacrylate) (PnBMA), *cis*-1,4-polyisoprene (PI) including blends of PIs
In situ imbibition of solid polymer electrolytes	How ions migrate in a polymer electrolyte during imbibition? What is the effective viscosity?	PEO/LiTFSI
In situ imbibition of semicrystalline polymers	Can the capillary force drag a semicrystalline polymer in nanopore? Can we make a crystal to flow, and if so, what is the effective viscosity?	poly(ethylene oxide) (PEO) poly(ε-caprolactone) (PCL)

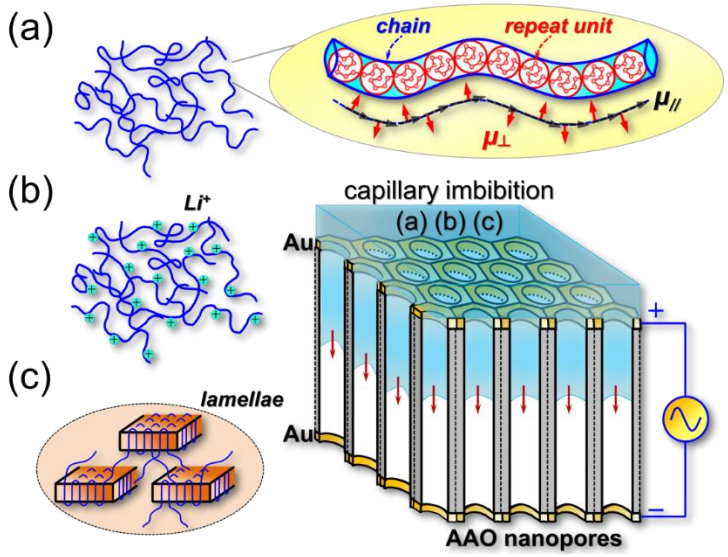

Figure 18. Schematic demonstrating the in-situ imbibition of three different materials to be employed in this Thesis: (a) amorphous polymers with the detailed single chain structure showing

dipole moments perpendicular and parallel to the polymer backbone. (b) The archetypal solid polymer electrolyte PEO/LiTFSI, and (c) lamellar morphology for a semicrystalline polymer (at $T < T_m$).

1.3.1 AAO (anodic aluminum oxide)

Two types of AAO templates are used: (i) the self-ordered AAO (pore diameters of 25 nm, 35 nm, 65 nm and 400 nm; pore depth about 100 μm) with *closed ends* prepared following previously reported procedures. In addition, the templates were characterized for conicity. Experiments using the Focused Ion Beam method revealed a small decrease in pore diameter from the top to the bottom. (ii) AAO templates with *both-ends open* purchased from InRedox (Longmont, USA). Pore diameters and corresponding porosities are 100 nm (24±3%), 40 nm (12±2%) and 20 nm (11±2%) respectively. Prior to infiltration, all AAO templates were placed in an oven under vacuum at a temperature of 423 K for 8-10 h. This procedure is essential here as it removes the majority of OH groups from the AAO surface. **Figure 19** shows representative SEM pictures from the top surface and cross section of AAO pores with/without etching.

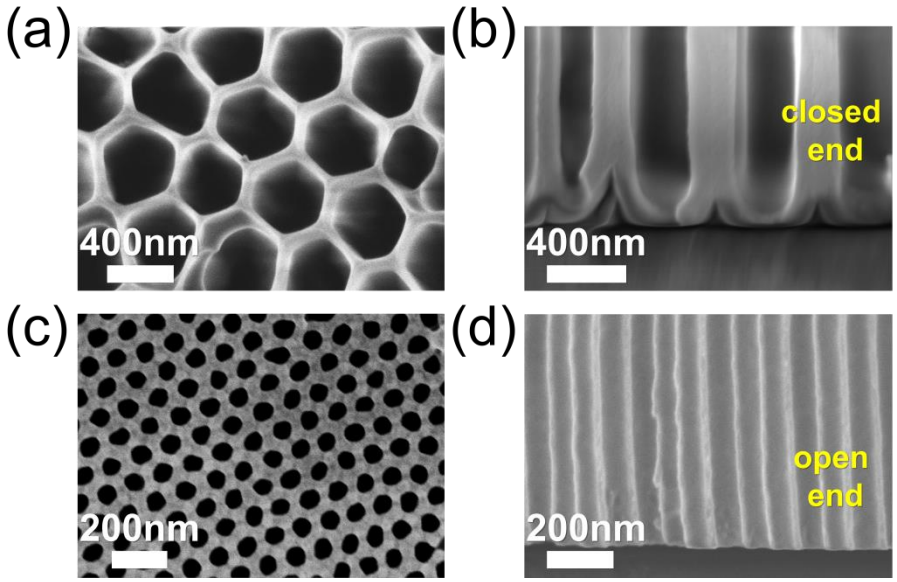

Figure 19. SEM figures showing top surfaces (a) (c) and cross sections (b) (d) of AAO nanopores: 400 nm pores without a closed end (top column) and 65 nm pores with both-ends open (bottom column). Both (b) and (d) represent the regions near the bottom of pores.

1.3.2 The Method—Nanodielectric Spectroscopy

Dielectric spectroscopy (DS) is employed to determine the dynamics of bulk and confined polymers and polymer electrolytes. The instrument is equipped with a Novocontrol Alpha

frequency analyzer composed of a broadband dielectric converter and an active sample head. For bulk samples, the polymer samples are embedded between two stainless steel electrodes with a diameter of 20 mm accompanied with a Teflon spacer of 50 μm to maintain the thickness. The sample preparation for *in situ* nanodieletric spectroscopy is more complicated (**Figure 20**). First, the AAO templates are sputtered with a gold layer with a thickness of 35 nm on the top side (or even rear side for templates from InRedox templates). The aim of the sputtered Au layers is to serve as electrodes, which can build a complete circuit across the template. Sputtering was made under high vacuum (better than 2×10^{-5} Pa) by Bal-tec MED 020 with a current density of 40 mA. The high vacuum environment is to ensure the uniformity of the sputtered Au layer. The current density is optimized to produce Au grains with appropriate size (too big will block the AAO pores; too small will hinder the current transport). Following sputtering, scanning electron microscopy (SEM) is used to determine the distribution of Au grains on the inner surface of the AAO templates (**Figure 20**). In addition to a uniform film deposited on top of AAO templates, Au particles are inevitably to fall within the pores (depth of about 380 nm). However, given the high aspect ratio ($> 10^3$) of nanopores, any inhomogeneities in the field lines can be neglected. Subsequently, a thin film or a drop of polymer is deposited on the top of the template. The frequency range also needs to be selected. A broad frequency range from $10^{-2} - 10^7$ Hz is normally used in bulk DS measurements. In contrast, a narrower frequency range, from $10 - 10^6$ Hz, is applied to probe the faster imbibition kinetics since a shorter time is needed. Typically, the applied voltage is below 1 Volt. The dielectric function depends on frequency, temperature and time. At a given time and temperature, it can be fitted by the empirical equation of Havriliak and Negami (HN):

$$\varepsilon^*_{HN}(\omega,T,t) = \varepsilon_\infty(T,t) + \sum_{k=1}^{2} \frac{\Delta\varepsilon_k(T,t)}{\left[1+\left(i\omega\tau_{HN,k}(T,t)\right)^{\alpha(t)}\right]^{\gamma(t)}} + \frac{\sigma_0(T,t)}{i\varepsilon_0\omega} \qquad (39)$$

Here, k indicates the process under investigation, $\Delta\varepsilon_k(T,t)$ is the relaxation strength, $\tau_{HN,k}$ is the Havriliak-Negami relaxation time, α, γ ($0 < \alpha$, $\alpha\gamma \leq 1$) are shape parameters describing the symmetric and asymmetric broadening of dielectric function (with the high frequency slope in a log-log representation being $\alpha\gamma$), and ε_∞ is the dielectric permittivity at the limit of high frequencies. At lower frequencies, ε'' rises due to the conductivity ($\varepsilon'' = \sigma_0/(\omega\varepsilon_0)$, where σ_0 is the dc conductivity and ε_0 the vacuum permittivity). There are also certain *limitations* in following the imbibition kinetics by Nanodielectric Spectroscopy. It requires a judicious choice of a polymer

with a suitable glass temperature, T_g, and with a bulk viscosity that is neither too low nor too high at the imbibition temperature, so that, the process falls within the experimental frequency window. The frequency window may also be limited by fast kinetics. These are parameters that need to be considered in designing any experiment.

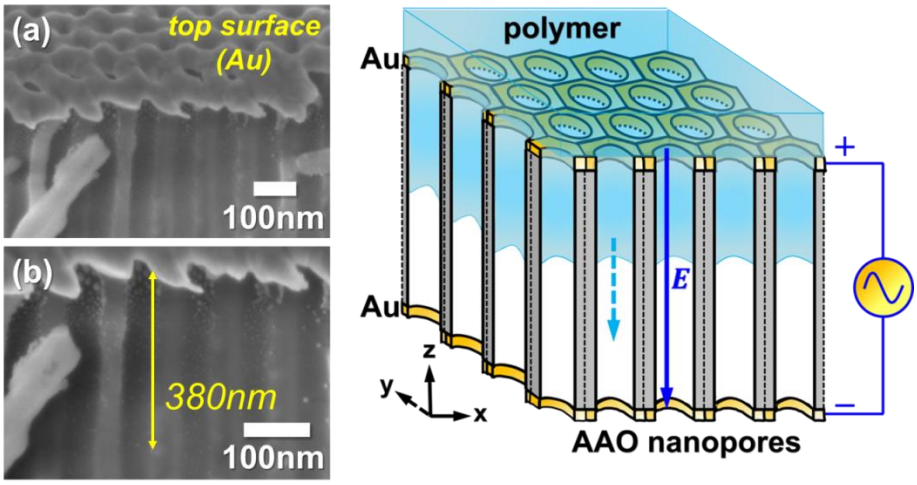

Figure 20. (Left top and bottom) SEM figures showing the top surface and cross section of AAO pores with a diameter of 65 nm following Au sputtering. The bottom left figure is a zoom-in picture. Au particles are distributed at the top of the nanopores within a distance of ~380 nm. (Right) Schematic of the experimental setup of *in situ* nanodielectric spectroscopy. The blue arrow indicates the direction of the applied electric field, E (along the nanopores, z-axis). The cyan dashed arrow indicates the flow direction of the polymer meniscus within the AAO nanopores. The xyz coordinate represents the laboratory axis.

Interestingly, the experimental set-up offers two ways of extracting the imbibition length, L. The first one is based on the growing dielectric strength of the segmental process. As an example, **Figure 21** shows the evolution of the dielectric loss curves and the associated Havriliak-Negami parameters (shape parameters, relaxation time at maximum loss and dielectric strength, all associated with the segmental process) when a PnBMA 5.5k film is placed on top of an empty AAO template. Here the dielectric loss curve of the empty template is used as a background and is subtracted from all other curves. Applying a single HN function to the dielectric loss curves results to the parameters plotted in the **Figure 21**. The dielectric strength increases fast in the beginning and later slow-down typically as $t^{1/2}$. Subsequently, values of $\Delta\varepsilon$ are converted into imbibition lengths by *ex situ* measurement of the capillary height by reflection optical microscopy. This is conceivable as the dielectric strength is proportional to the number density of dipoles that

is increasing with imbibition time ($\Delta\varepsilon = \varepsilon'_S - \varepsilon_\infty \sim \frac{1}{3\varepsilon_o}\frac{\mu^2}{k_B T}\frac{N_0}{V}$, where N_o/V is the number density of dipoles and μ is the dipole moment).

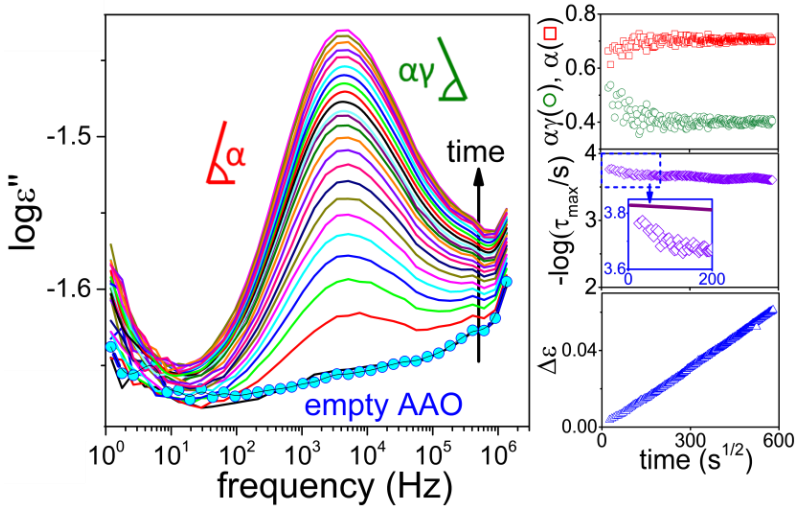

Figure 21. (Left) Evolution of the dielectric loss curves for PnBMA 5.5k entering AAO nanopores with pore diameter of 65 nm at 333 K. The signal from the empty AAO template is shown under the same conditions. The vertical arrow indicates increasing time of imbibition. (Right) Evolution of the HN shape parameters (top), of the relaxation time at maximum loss (middle) and of the dielectric strength (bottom) during the experiment plotted as a function of the square root of imbibition time.

The second method is based on the equivalent circuit. The geometry shown in **Figure 20** can be treated equivalently as an electric circuit composed of three layers (**Figure 23a**): polymer, air and AAO layers, each with its own permittivity, capacitance and length. Moreover, the polymer layer (indicated as C_1) is connected with the air layer (indicated as C_2) in series, and this composite layer (polymer-air, C_{12}) is arranged in parallel to the AAO (C_3). In terms of the equivalent circuit, we acquire the following expressions used to derive the imbibition length of the polymer as a function of time:

$$\varepsilon'_{123} - i\varepsilon''_{123} = \left\{\left[\frac{D\varepsilon'_1 d_1 + Dd_2[(\varepsilon'_1)^2 + (\varepsilon''_1)^2]}{(d_1 + d_2\varepsilon'_1)^2 + (d_2\varepsilon''_1)^2}\right]\varphi_{12} + \varepsilon'_3\varphi_3\right\} - i\left[\frac{Dd_1\varepsilon''_1\varphi_{12}}{(d_1 + d_2\varepsilon'_1)^2 + (d_2\varepsilon''_1)^2} + \varepsilon''_3\varphi_3\right] \quad (40)$$

and

$$d_1 = D\left(\frac{\varphi_{12} b}{(a)^2 + (b)^2}\right)\left(\frac{(\varepsilon'_1)^2 + (\varepsilon''_1)^2}{\varepsilon''_1}\right) \quad (41)$$

$$\text{with } a = \varepsilon'_{123} - (\varepsilon'_3)\varphi_3, \quad \text{and} \quad b = \varepsilon''_{123} - (\varepsilon''_3)\varphi_3.$$

The above equation provides the polymer imbibition length, d_1, as a function of the dielectric properties of the bulk polymer (ε_1^*), the pure AAO (ε_3^*), the measured dielectric function of the composite cell (ε_{123}^*) and the porosity. The method is sensitive to the presence of a background in the pure AAO. Some simplification can result by subtracting the background contribution and subsequently employing the properties of alumina ($\varepsilon_3' = 2.6$; $\varepsilon_3'' = 0$). As for the porosity, φ_{12} ($\varphi_3 = 1 - \varphi_{12}$), we use the values obtained earlier for the self-made AAOs with one open end as 0.375 (400 nm), 0.175 (65 nm), 0.0073 (35 nm) and 0.111 (25 nm). The second method does not need a calibration measurement but requires knowledge of porosities. In general, a good agreement can be found by extracting the imbibition lengths with the two methods provided that the background contribution is subtracted and the porosities are known independently, as shown in **Figure 22**.

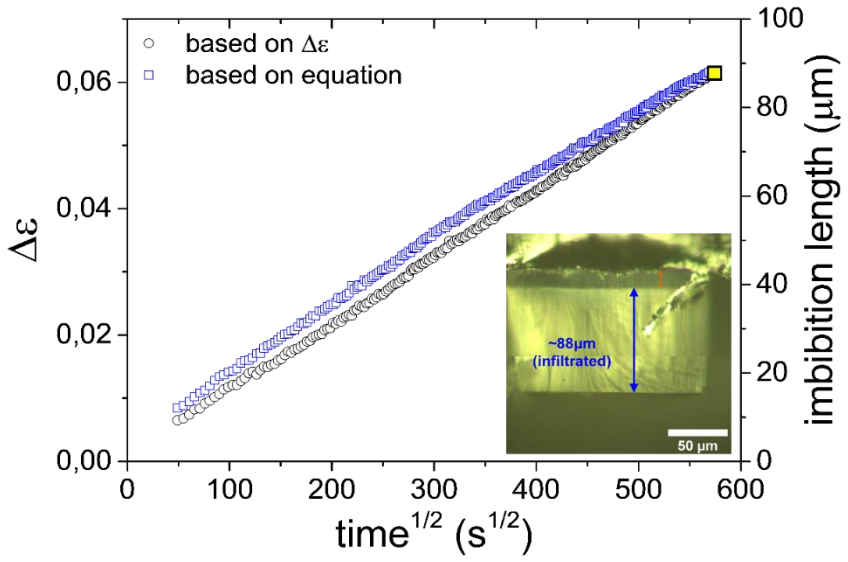

Figure 22. Imbibition lengths extracted by the two differed methods: (circles) from the evolution of the dielectric strength, (squares) from the equivalent circuit. The polymer is PnBMA 5.5 k, the templates have a diameter of 65 nm and the imbibition temperature is at 333 K. The image from reflection optical microscopy (inset) is obtained at the end of the imbibition process (corresponding yellow square point at 88 μm).

1.3.3 Simulation of the imbibition process

1.3.3.1 Homopolymers in the absence of ions

Despite the simplicity of the method several factors need to be considered, including the porosity of the templates, the presence or absence of closed ends and the possibility of entrapped air, the background signal from the AAO, the polarity of the polymer and the interactions between the polymer and the AAO walls. The Debye model function is used to simulate the frequency dependence of complex dielectric permittivity ($\varepsilon^* = \varepsilon' - i\varepsilon''$) of a polar and a nonpolar polymer:

$$\varepsilon^*_{polymer} = \Delta\varepsilon_{polymer}\ \frac{1}{1 + i\omega\tau_D} + \varepsilon_{polymer,\infty} \tag{42}$$

with real (ε') and imaginary (ε") parts

$$\varepsilon'_{polymer} = \frac{\Delta\varepsilon_{polymer}}{1 + (\omega\tau_D)^2} + \varepsilon_{polymer,\infty} \tag{43}$$

$$\varepsilon''_{polymer} = \Delta\varepsilon_{polymer}\ \frac{\omega\tau_D}{1 + (\omega\tau_D)^2} \tag{44}$$

Here, $\Delta\varepsilon_{polymer}$ is the dielectric strength of the polymer, $\varepsilon_{polymer,\infty}$ is the dielectric permittivity at very high frequencies, and τ_D is a characteristic relaxation time (here set to 1s). For the polar (nonpolar) polymer cases, the following exemplary values were employed: $\Delta\varepsilon_{polymer}$ = 1 (0.1), and $\varepsilon^*_{polymer,\infty}$ = 2.25 for both cases. To provide a comprehensive analysis, the equivalent capacitance representation is necessary. Here, two models are considered with respect to the interaction of the polymer/AAO (*e.g.*, by "interaction" we mean the area of contact and the strength of polymer/AAO interaction at the interface): (i) a parallel model with weak interactions in the horizontal direction (*e.g.*, the direction perpendicular to the nanotubes), and (ii) a series model with strong interactions in the horizontal direction. In the parallel model, the capacitance of the polymer (C_1) and air (C_2) are connected in series, and the combinational capacitance of polymer/air (C_{12}) connects in parallel with AAO (C_3) (**Figure 23a**). In the series model, the combinatorial capacitance of the polymer (C_1) and AAO (C_3), C_{13} connect in series with the combined air/AAO capacitance (C_{23}) (**Figure 23b**).

Parallel Model: Weak Interaction between Polymer and AAO in the Horizontal Direction

In terms of the equivalent circuit, we have the following equations,

$$\frac{1}{C_{12}} = \frac{1}{C_1} + \frac{1}{C_2} \tag{45}$$

$$C_{123} = C_{12} + C_3 \tag{46}$$

From the definition of capacitance (*i.e.*, $C = \varepsilon A/d$) it follows that,

$$\varepsilon_{12}^* = \frac{D\varepsilon_1^*}{d_1 + d_2\varepsilon_1^*} \tag{47}$$

$$\varepsilon_{123}^* = \varepsilon_{12}^*\varphi_{12} + \varepsilon_3^*\varphi_3 \tag{48}$$

φ_{12} represents the porosity of AAO templates, $\varphi_3 (= 1 - \varphi_{12})$ is the remaining area of the template, and *D* is the full length of AAO nanopores. After some arrangements, we can obtain the following equation for the complex dielectric permittivity:

$$\varepsilon_{123}^* = \left[\frac{D\varepsilon_1^*}{d_1 + d_2\varepsilon_1^*}\right]\varphi_{12} + \varepsilon_3^*\varphi_3 \tag{49}$$

Therefore, the imaginary part is

$$\varepsilon_{123}'' = \frac{d_1\varepsilon_1''\varphi_{12}}{(d_1 + d_2\varepsilon_1')^2 + (\varepsilon_1''d_2)^2} \tag{50}$$

Series Model: Strong Interaction between Polymer and AAO in the Horizontal Direction

In terms of the equivalent circuit,

$$\frac{1}{C_{123}} = \frac{1}{C_{13}} + \frac{1}{C_{23}} \tag{51}$$

$$C_{13} = C_1 + C_3 \tag{52}$$

$$C_{23} = C_2 + C_3 \tag{53}$$

From the definition of capacitance (*i.e.*, $C = \varepsilon A/d$),

$$\frac{D}{\varepsilon_{123}^*} = \frac{d_1}{\varepsilon_{13}^*} + \frac{d_2}{\varepsilon_{23}^*} \tag{54}$$

$$\varepsilon_{13}^* = \varepsilon_1^*\varphi + \varepsilon_3^*(1 - \varphi) \tag{55}$$

$$\varepsilon_{23}^* = \varepsilon_2^*\varphi + \varepsilon_3^*(1 - \varphi) \tag{56}$$

After some arrangements, we can obtain the following equation for the complex dielectric permittivity:

$$\varepsilon_{123}^* = \frac{[\varepsilon_1^*\varphi + \varepsilon_3^*(1 - \varphi)][\varepsilon_2^*\varphi + \varepsilon_3^*(1 - \varphi)]}{[\varepsilon_1^*\varphi + \varepsilon_3^*(1 - \varphi)] + x\varphi(\varepsilon_2^* - \varepsilon_1^*)} \tag{57}$$

Here, $x = d_1$ (imbibition length of polymer). The imaginary part is

$$\varepsilon''_{123} = \frac{BC - AG}{C^2 + G^2} \tag{58}$$

$$B \to \varepsilon''_1 \varphi^2 + a\varphi\varepsilon''_1 \tag{59}$$

$$C \to \varepsilon'_1 \varphi(1-x) + a + x\varphi \tag{60}$$

$$A \to \varepsilon'_1 \varphi^2 + a\varphi(\varepsilon'_1 + 1) + a^2 \tag{61}$$

$$G \to \varepsilon''_1 \varphi(1-x) \tag{62}$$

$$a \to \varepsilon^*_3(1-\varphi) \tag{63}$$

For the real and imaginary parts of dielectric constant of AAO we have employed typical values $\varepsilon'_3 = \varepsilon'_{AAO} = 2.6$ and $\varepsilon''_3 = \varepsilon''_{AAO} = 0$. The latter involves the subtraction of the empty cell (*e.g.*, the background signal).

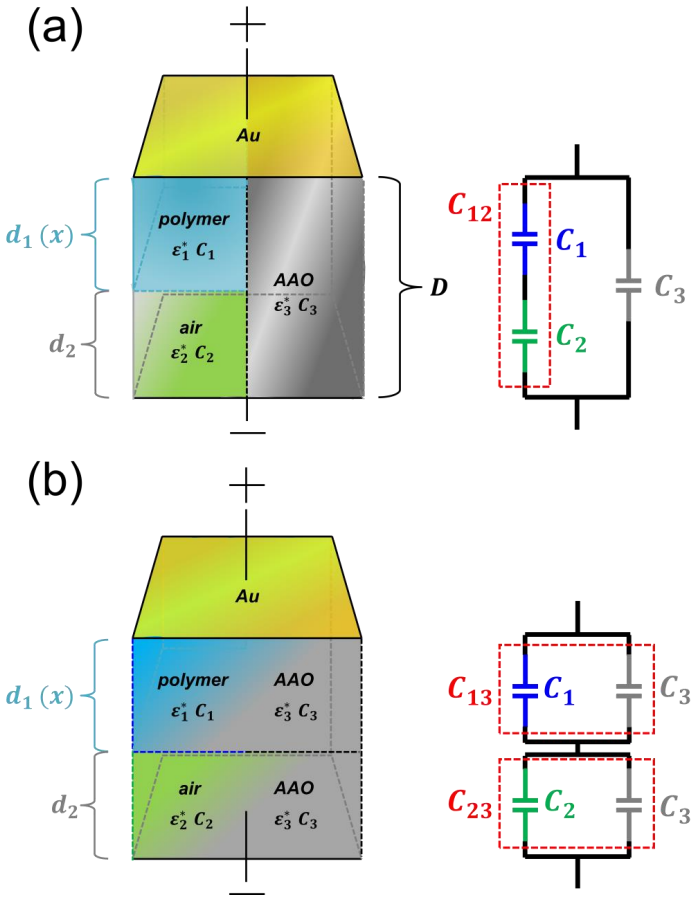

Figure 23. Illustration the equivalent capacitance of the (a) parallel and (b) series models. Parameters are defined as follows: ε_1^*, ε_2^*, ε_3^*, ε_{12}^*, ε_{13}^*, and ε_{23}^* are, respectively, the complex dielectric function of the polymer layer, air, AAO, polymer/air composite, the polymer/AAO composite, and air/AAO composite; C_1, C_2, C_3, C_{12}, C_{13}, and C_{23} are the respective capacitances;

d_1, and d_2 are the lengths of the pores comprising the polymer and air. *D* is the full length of nanopores.

Three issues are addressed for two polymers (polar and apolar): (i) the effect of porosity (φ) on the evolution of ε", (ii) the variation of the dielectric strength ($\Delta\varepsilon$) with the imbibition length (d_1 or x), and (iii) the variation of the relaxation time during imbibition. The results of the parallel and the series model for a nonpolar (**Figures 24**) and a polar (**Figures 25**) polymer are discussed with respect to the growing dielectric loss. Independent of polarity, at low porosities (*i.e.*, $\varphi = 0.1$), $\Delta\varepsilon$ shows a linear increase with d_1 in the series model (**Figure 24b** and **25b**). In contrast, within the parallel model a linearity applies only at the initial stages of the imbibition process. At intermediate (*i.e.*, $\varphi = 0.5$), and high (*i.e.*, $\varphi = 0.9$) porosities even the series model (**Fig. 30, 31**) deviates from linearity.

On the other hand, polarity affects mainly the relaxation times *during* imbibition. For the nonpolar polymer (*e.g.*, *cis*-1,4-polyisoprene), the position of the relaxation peak stays nearly constant during imbibition and this is independent from the model; by contrast, for the polar polymer (*e.g.*, poly(*n*-butyl methacrylate)) a faster relaxation process at shorter imbibition lengths is followed by a gradual slowing-down at longer imbibition lengths (**Figure 26**). Notice that the molecular dynamics obtained from the series model are always slower than the parallel model and closer to the bulk behavior. This phenomenon reflects on the extensive interactions between polymer and AAO in the series model. More realistic applications of the models can be made for the two particular polymers to be examined here: PI and PnBMA. The results of the two models for the actual experimental porosities are provided in **Figure 27**. The figure depicts a minor effect on the PI relaxation times and some effect (faster dynamics at the initial stages of imbibition) for the more polar PnBMA.

Overall, simulation results show stronger effects on the evolution of the characteristic times and the dielectric strength for the polar polymers and nearly no effect for nonpolar polymers. Hence, such effects should be considered at the initial stages of imbibition for polar polymers.

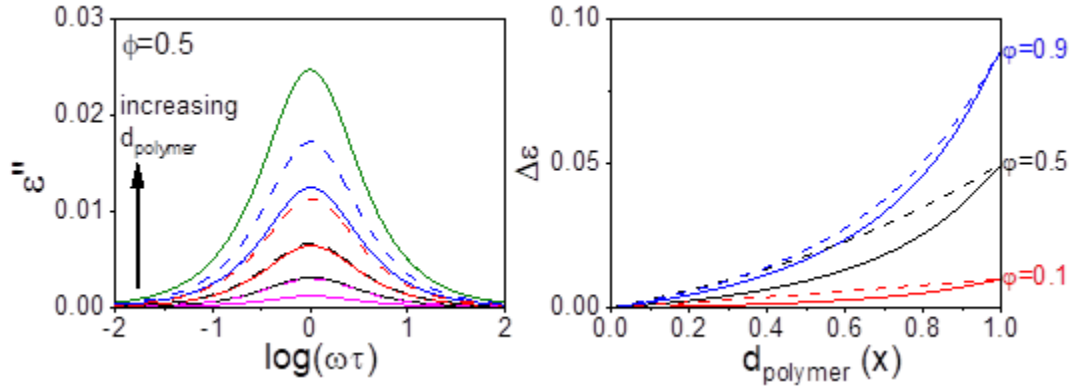

Figure 24. (Left) Comparison in simulated dielectric loss curves, ε'', of a nonpolar polymer ($\Delta\varepsilon$ = 0.1) as a function of imbibition length (x) via two different models (solid lines: parallel model; dashed lines: series model) for porosity (φ) equal to 0.5. Color codes are as following: (magenta) x = 0.2, (black) x = 0.4, (red) x = 0.6, (blue) x = 0.8, and (olive) x = 1. (Right) Comparison in extracted dielectric intensity ($\Delta\varepsilon$) as a function of x for different porosity: (red) φ = 0.1, (black) φ = 0.5, and (blue) φ = 0.9. Solid (dashed) lines represent the parallel (series) model.

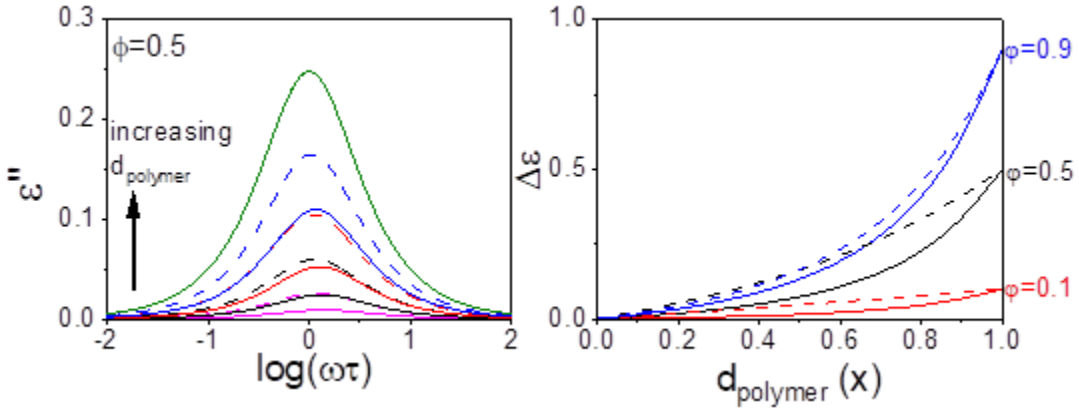

Figure 25. (Left) Simulated ε'' of a polar polymer ($\Delta\varepsilon$ = 1) as a function of imbibition length (x) via two different models (solid lines: parallel model; dashed lines: series model) for porosity (φ) equal to 0.5. Color codes are as following: (magenta) x = 0.2, (black) x = 0.4, (red) x = 0.6, (blue) x = 0.8, and (olive) x = 1. (Right) Comparison in extracted dielectric intensity ($\Delta\varepsilon$) as a function of x for different porosity: (red) φ = 0.1, (black) φ = 0.5, and (blue) φ = 0.9. Solid (dashed) lines represent the parallel (series) model.

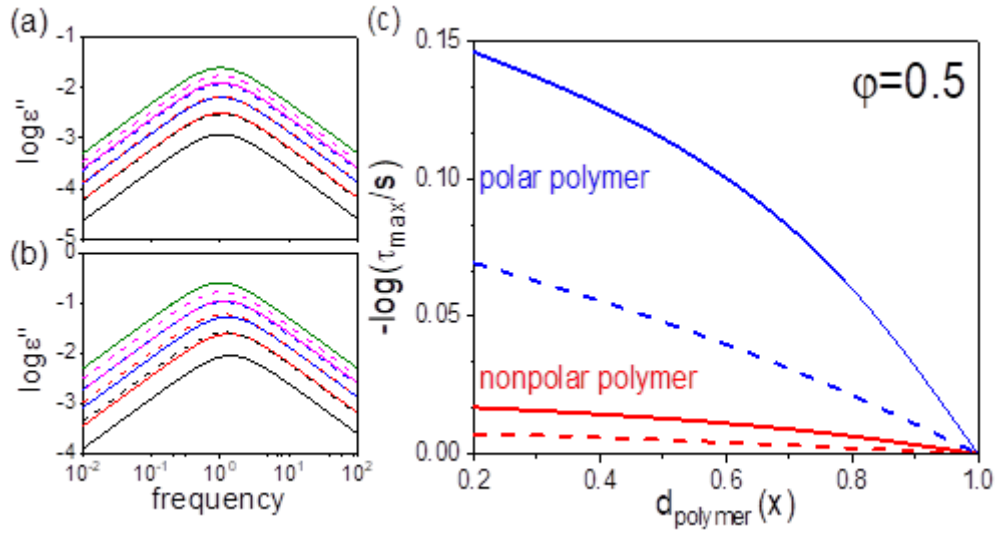

Figure 26. Representative simulated DS loss curves during imbibition for (a) a nonpolar and (b) a polar polymer. (c) Comparison of the extracted relaxation times as a function of imbibition length (x). Solid (dashed) lines represent the parallel (series) model. Color codes in (a) and (b): (black) x = 0.2, (red) x= 0.4, (blue) x = 0.6, (magenta) x = 0.8, and (olive) x = 1.0. Color codes in (c): (blue) polar polymer and (red) nonpolar polymer. The selected porosity (φ) for all cases here is 0.5.

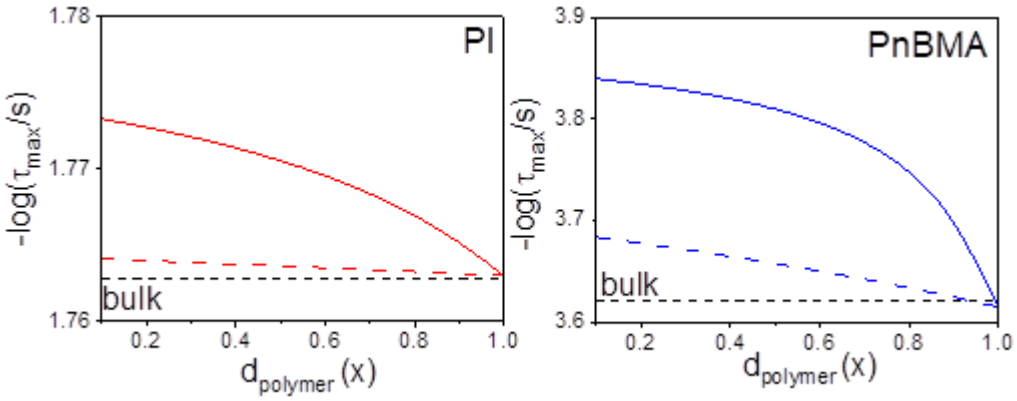

Figure 27. Comparison of the relaxation times of (left) polyisoprene (PI) and (right) poly(*n*-butyl methacrylate) (PnBMA) during imbibition at temperatures of 303 K and 333 K, respectively. Simulation models: (dashed lines) series model and (solid lines) parallel model. Porosity: 0.12 (Left, AAO with pore dimeter of 40 nm) and 0.175 (Right, AAO with pore diameter of 65 nm). Black dashed line in the left (right) plot indicates the longest normal mode relaxation (α-relaxation) time in bulk polymers.

1.3.3.2 Ionic system—Imbibition of a polymer electrolyte

The Debye model function including the conductivity term is used to simulate the frequency dependence of complex conductivity ($\sigma^* = \sigma' + i\sigma''$) of a polymer electrolyte as:

$$\varepsilon^* = \varepsilon \ + \frac{\Delta\varepsilon}{1 + i\omega\tau_D} + \frac{\sigma_{dc}}{i\omega\varepsilon_0} \tag{64}$$

with real (ε') and imaginary (ε'') parts

$$\varepsilon' = \varepsilon_\infty + \frac{\Delta\varepsilon}{1 + (\omega\tau_D)^2} \tag{65}$$

$$\varepsilon'' = \Delta\varepsilon \ \frac{\omega\tau_D}{1 + (\omega\tau_D)^2} + \frac{\sigma_{dc}}{\omega\varepsilon_0} \tag{66}$$

because $\sigma^*(\omega) = \sigma'(\omega) + i\sigma''(\omega) = i\omega\varepsilon_0\varepsilon^*(\omega)$,

$$\sigma'(\omega) = \omega\varepsilon_0\varepsilon''(\omega) = \sigma_{dc} + \frac{\omega^2\tau\varepsilon_0\Delta\varepsilon}{1 + (\omega\tau_D)^2} \tag{67}$$

$$\sigma''(\omega) = \omega\varepsilon_0\varepsilon'(\omega) = \omega\varepsilon_0\left(\varepsilon_\infty + \frac{\Delta\varepsilon}{1 + (\omega\tau_D)^2}\right) \tag{68}$$

Here, $\Delta\varepsilon$ is the dielectric strength of a polymer electrolyte (set to 1×10^3), ε_∞ is the dielectric permittivity at very high frequencies (set to 10), τ_D is a characteristic relaxation time (set to 0.1), and σ_{dc} is the conductivity of polymer electrolyte (set to 1×10^{-4} S/cm). To provide a comprehensive analysis for the imbibition of a polymer electrolyte within nanopores, the equivalent capacitance representation was employed. Here, the abovementioned parallel model is considered. Through the equation (49) and the definition $\sigma^*_{123} = i\omega\varepsilon_0\varepsilon^*$ after some arrangements,

$$\sigma^*_{123} = \sigma' + i\sigma'' = \left\{\left[\frac{Dd_1\sigma_1'(\omega\varepsilon_0)^2}{(d_2\sigma_1')^2 + (d_1\omega\varepsilon_0 + d_2\sigma_1'')^2}\right]\varphi_{12} + \sigma_3'\varphi_3\right\} + i\left\{\left[\frac{D[d_2\left[(\sigma_1')^2 + (\sigma_1'')^2\right]\omega\varepsilon_0 + \sigma_1''(\omega\varepsilon_0)^2 d_1]}{(d_2\sigma_1')^2 + (d_1\omega\varepsilon_0 + d_2\sigma_1'')^2}\right]\varphi_{12} + \sigma_3''\varphi_3\right\} \tag{69}$$

For the real and imaginary parts of complex conductivity of AAO we have employed values $\sigma_3' = \sigma_{AAO}' = 10^{-14}$ and $\sigma_3'' = \sigma_{AAO}'' = 0$. The evolution of dielectric curves of the complex conductivity during imbibition is shown in **Figure 28**.

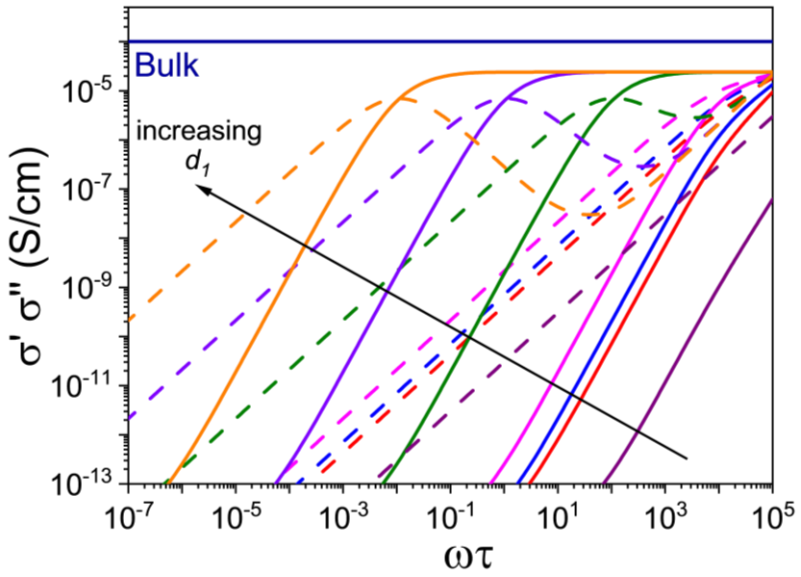

Figure 28. Simulated growing of real (solid lines) and imaginary parts (dashed lines) of complex conductivity as a function of imbibition length (d_1) calculated via the parallel model. Simulation parameters are as following: $\Delta\varepsilon = 1\times10^{3}$, $\varepsilon_0 = 8.854\times10^{-12}$, $\varepsilon_\infty = 10$, $\sigma_{dc} = 10^{-4}$ S/cm, $\tau = 0.1$, φ_{12} $(= 1 - \varphi_3) = 0.24$, $D = 100$ μm, $\sigma_3' = \sigma_{AAO}' = 10^{-14}$ S/cm, and $\sigma_{AAO}'' = 0$ S/cm. Color codes are as following: (purple) $d_1 = 30$ μm, (red) $d_1 = 95$ μm, (blue) $d_1 = 97$ μm, (magenta) $d_1 = 99$ μm, (olive) $d_1 = 99.99$ μm, (violet) $d_1 = 99.9999$ μm, and (orange) $d_1 \sim 100$ μm. Solid lines and dashed lines represent the real (σ') and imaginary (σ'') parts of complex ionic conductivity.

1.3.4. Segmental dynamics during imbibition of the amorphous poly(*n*-butyl methacrylate)

Poly(*n*-butyl methacrylate) (PnBMA) homopolymers with narrow dispersities, *Đ*, were purchased from PSS Polymer Standards Service GmbH and used without further purification. Their molecular characteristics as obtained by GPC/SEC are shown in **Table 2**. Blends of the two homopolymers as PnBMA 5.5k/PnBMA 100k, with compositions B1 (75/25), B2 (50/50), B3 (25/75), were prepared and investigated in the second part of this study.

Table 2. Molecular characteristics of the poly(*n*-butyl methacrylate) samples.

Sample	$\overline{M_n}$ (g mol^{-1})	$\overline{M_w}$ (g mol^{-1})	*Đ*
PnBMA 5.5k	4950	5490	1.11
PnBMA 100k	104000	110000	1.06

Main Findings

The results of the imbibition experiments for the homopolymer PnBMA 5.5k can be discussed with the help of **Figure 21**. The Figure shows low- and high-frequency shape parameters as well as relaxation times at longer times nearly identical to the bulk polymer. This effect, *e.g.*, the faster relaxation times at the beginning of the imbibition process, is anticipated by the equivalent circuit model. The predictions of the model (eq. 40) is included in **Figure 21** by a solid line and compared to the experimental times. Evidently, the measured segmental relaxation times exhibit a steeper dependence at short imbibition times than the theoretically predicted by the equivalent circuit. The fact that at the end of the process the segmental relaxation times are identical to the bulk might lead to the erroneous conclusion that there is little or even no effect of confinement on the polymer dynamics at the segmental level. Such a conclusion would not be in line with several experiments that have shown a speed-up of dynamics under confinement or even a bimodal glass temperature. Here this result is not unexpected as the imbibition temperature is located far above (typically 30-50 K) the glass temperature. On the other hand, imbibition at temperatures in the vicinity of T_g is extremely slow.

The evolution of the imbibition lengths for PnBMA 5.5k are shown for different temperatures at two pore diameters in **Figure 29** and for different pore diameters at two temperatures in **Figure 30**. At early times, the rise of the imbibition length, d_1, is linear with the square root of time. At

longer times, however, deviations from linearity are observed. It is confirmed that the origin of the non-linear dependence at long times is the pressure exerted by the trapped air at the bottom of nanotubes. Imbibition lengths based on the LWE are calculated based on the $<\cos\theta_d>$ (= $(\cos\theta_{d,i}+\cos\theta_{d,f})/2$; $\theta_{d,i}$ and $\theta_{d,f}$ are initial and final dynamic contact angle, respectively) values and are shown by the solid lines. The deviations from LWE are more pronounced at lower temperatures and for the smaller pore diameters. The experimental data suggest a higher effective viscosity for PnBMA 5.5k within the smaller pores. According to a recent theory,[30] the dead-layer effect is proven to be dominant for this molecular weight.

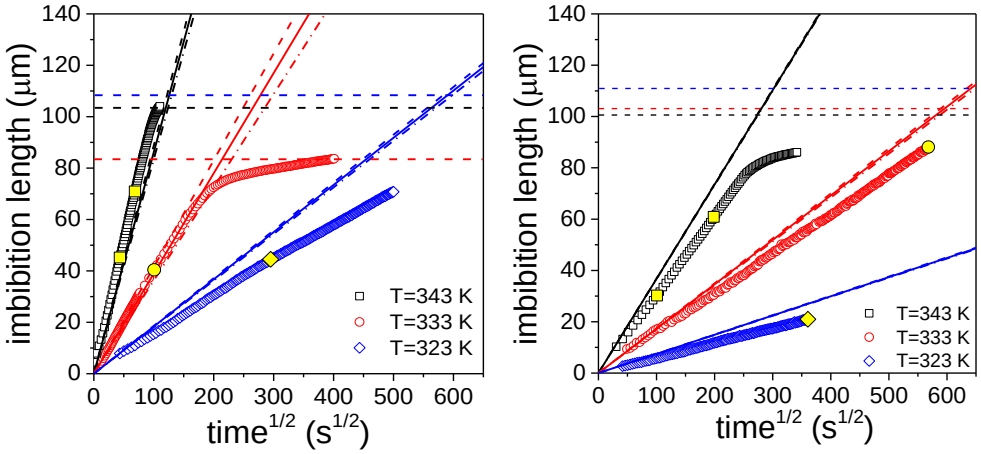

Figure 29. Imbibition length d_1, as a function of $t^{1/2}$ for the PnBMA 5.5k at different temperatures T = 343 K (squares); T = 333 K (circles); T = 323 K (rhombi) and for two AAO pore diameters; 400 nm (left) and 65 nm (right). Symbols in yellow indicate the calibration points used from reflection optical microscopy. The solid lines gives the predictions of the LWE equation using $<\cos\theta_d>$ ($\cos\theta_{id}$ and $\cos\theta_{fd}$ values were also used in the LWE and plotted with dashed and dash-dotted lines, respectively). The horizontal dashed lines provide the template thickness (different for each template).

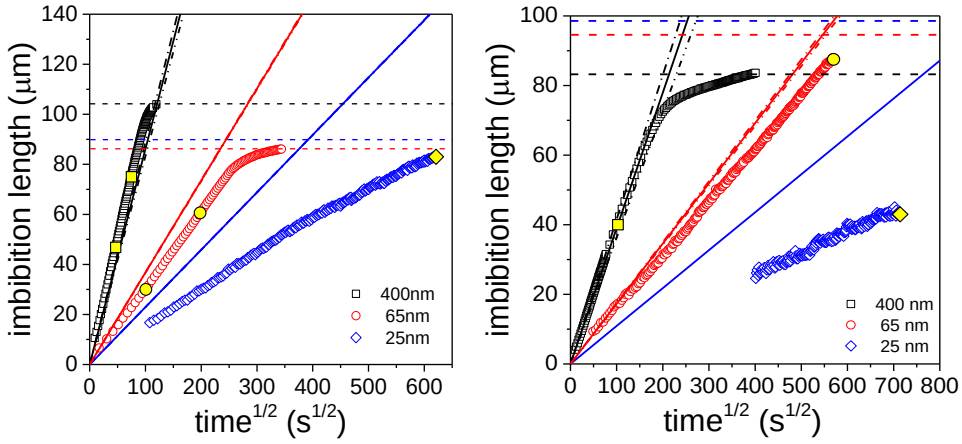

Figure 30. Imbibition length d_1, as a function of $t^{1/2}$ for the PnBMA 5.5k for different AAO pore diameters; 400 nm (squares), 65 nm (circles) and 25 nm (rhombi) at two temperatures; (left) T = 343 K and (right) T = 333 K. The solid lines give the predictions of the LWE equation using $\langle\cos\theta_d\rangle$, whereas $\cos\theta_{id}$ and $\cos\theta_{fd}$ values were also used in the LWE and plotted with dashed and dash-dotted lines, respectively. The horizontal dashed lines provide the template thickness (different for each template).

DS is further applied to follow the imbibition kinetics *in situ* for three PnBMA blends (B1, B2 and B3) by following the evolution of the segmental process. The dynamics of the three blends were first studied in the bulk as a function of temperature. **Figure 31a** compares the dielectric loss curves of the homopolymers and the blends in the bulk at the imbibition temperature (343 K). The relaxation times at maximum loss in the bulk follows a linear concentration dependence (**Fig. 31c**). This is to be contrasted with the segmental dynamics at the end of the imbibition process (**Fig. 31b,c**); the segmental process does not follow the same linear dependence. The segmental process of B2 (50/50) and of B3 (25/75) deviate (are faster) from the expected bulk relaxation times. Evidently, the B2 and B3 blend composition inside AAO is enriched by segments from the shorter chains (PnBMA 5.5k) and hence become faster. By projecting isochronally the relaxation times in confinement to the composition dependence in the bulk we estimate an effective composition of 55/45 instead of 25/75 for B3. Similarly, for B2 the estimated blend composition is 63/37 instead of 50/50. Because the segmental relaxation times in the blends is independent of imbibition time (**Fig. 31b**) this suggests that already at short time scales polymer chains entering the nanopores are enriched by PnBMA 5.5k. This enrichment by segments of the shorter chains should alter the imbibition dynamics at longer length scales as probed by the evolution of the dielectric strength

and the associated imbibition length. Overall, the blend study confirmed the potential of the method to fractionate polymers with different molecular weights.

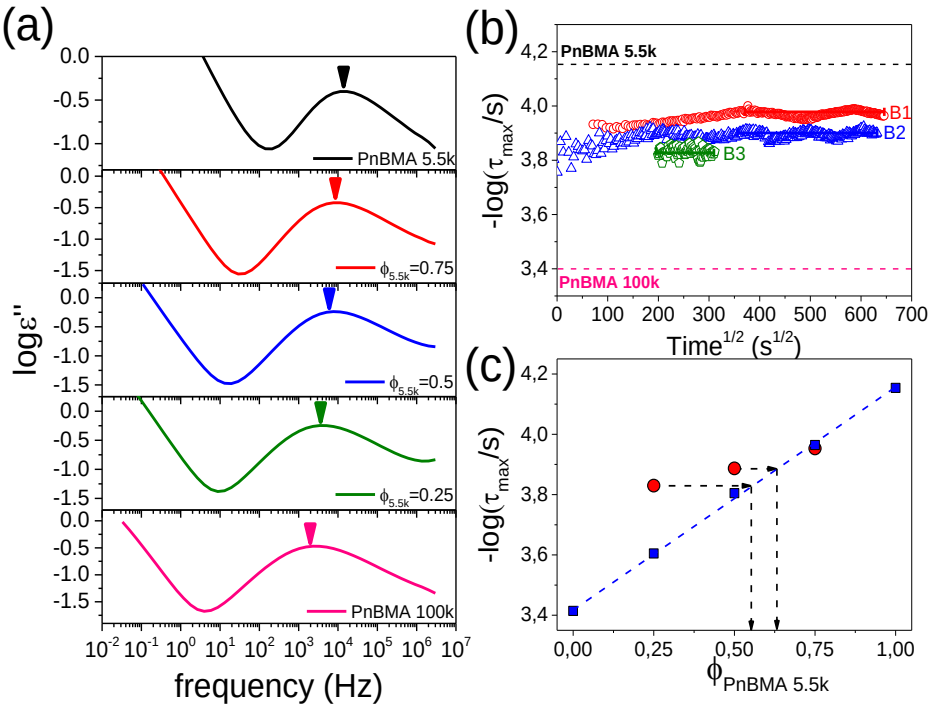

Figure 31. (a) Dielectric loss spectra of the homopolymers and their blends at 343 K. Arrows indicate the frequency of maximum loss. (b) Evolution of the relaxation time at maximum loss for the three blends (circles): B1, (squares): B2 and (up triangles) B3 during their imbibition within AAO with a pore diameter of 65 nm at 343 K. Dashed and dash-dotted lines give the respective times for the PnBMA 5.5k and PnBMA 100k homopolymers. (c) Relaxation times at maximum loss as a function of blend composition (squares) at 343 K. The corresponding times for the blends are also shown (circles). Dashed lines with arrows indicate projections to the composition in the bulk that provides estimates of the effective blend composition within the nanopores.

1.3.5. Chain dynamics during imbibition of the amorphous *cis*-1,4-polyisoprene

Four *cis*-1,4-polyisoprene (PI) homopolymers with narrow dispersities, *Đ*, were employed in the present study (**Table 3**). PI 12k and PI 21k were purchased from PSS Polymer Standards Service GmbH and used without further purification. PI 5k and PI 42k were synthesized in house (MPI-P). Two symmetric blends (composition 50/50 wt%) of PI 5k with PI 21k and of PI 5k with PI 42k (designated as B1 and B2, respectively) were prepared and investigated in the second part of this study.

Table 3. Molecular characteristics of the *cis*-1,4-polyisoprene homopolymers and their blends.

Sample	$\overline{M_n}$ (g·mol^{-1})	$\overline{M_w}$ (g·mol^{-1})	*Đ*	R_g (nm)[a]	η_o (Pa·s)
PI 5k	4840	5116	1.06	2.3	2.0
PI 12k	5366	9723	1.81	56	72
PI 21k	23300	23600	1.01	5.1	
PI 42k	42412	43997	1.04	6.9	259.0
B1 (5k/21k)					-
B2 (5k/42k)					50.0

[a]The radius of gyration, R_g, was calculated according to $\langle R_g^2 \rangle = \frac{\langle R_0^2 \rangle}{6}$ using $\frac{\langle R_0^2 \rangle}{M} = 0.679$ (Å^2 mol/g).

Main findings

The *in situ* measurement of PI was first made for the entangled PI 42k. **Figure 32a** provides fitting examples for bulk PI using a summation of two Havriliak and Negami (HN) functions following imbibition. The slower one corresponds to the longest normal mode whereas the faster to the summation of all higher (shorter) modes. We first note that the higher normal modes seem to approach the longest normal mode and second, the longest normal mode is longer than in the bulk.

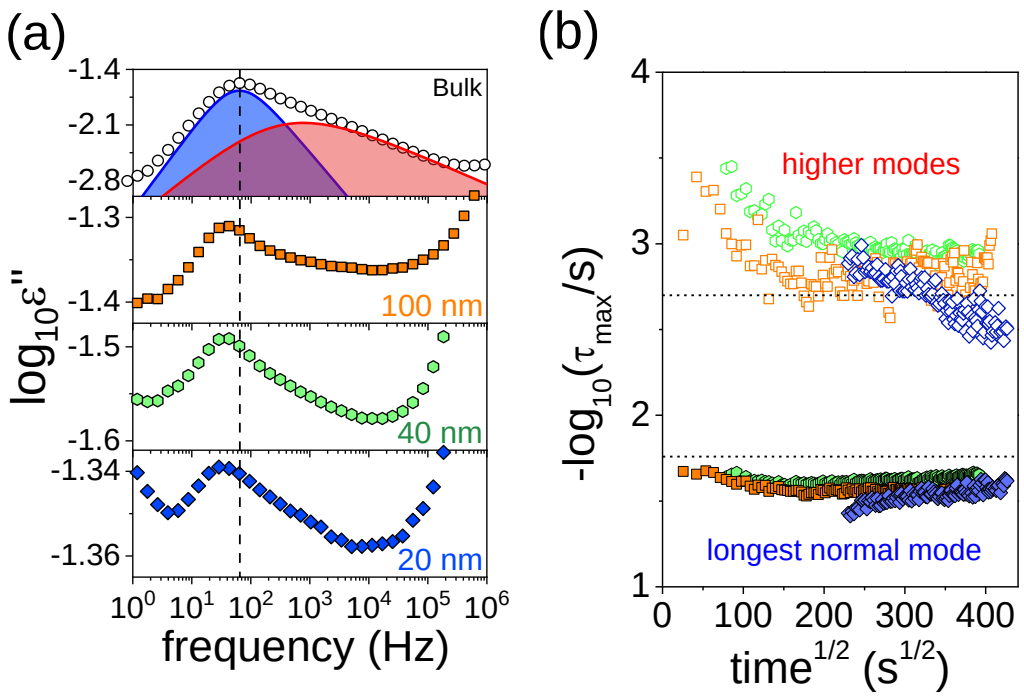

Figure 32. (a) Dielectric loss curves of bulk and confined PI 42k within AAO pores with pore diameters of 100 nm, 40 nm, and 20 nm at T = 303 K. The black dashed line indicates the peak position of the longest normal mode in bulk PI. Representative fit of the dielectric loss curve for the bulk PI 42k with a summation of two HN functions corresponding to the longest normal mode (blue shaded area) and the summation of shorter normal modes (red shaded area). (b) Evolution of the relaxation times for PI 42k during imbibition inside AAO nanopores as a function of the square-root of time. Same color codes as in (a): 100 nm (orange circles), 40 nm (green squares), and 20 nm (blue rhombi). The short dash lines give the position of the longest normal mode and of the internal modes in the bulk polymer at the same imbibition temperature.

The evolution of the dielectric loss curves at the length scale of the normal modes is depicted in **Figure 33a** for AAO pores with diameter of 40 nm. The radius of gyration of the polymer, R_g, is smaller than the diameter of the pore, d, ($2R_g/d$ = 0.35). The analysis of the dielectric loss curves provides the dielectric strength of the slower (longest normal mode) and faster (higher normal modes) (**Figure 33b**). It shows an initially increasing dielectric strength for both modes, scaling as $t^{1/2}$, up to 17000 s. This increase is followed by a plateau at longer times (for the slower mode) or even a decrease (for the higher normal modes). In parallel, the imbibition lengths, L, was measured *ex situ* by optical reflection microscopy and the result is shown in **Figure 40c**. Based on the LWE with the bulk viscosity η_0 = 285 Pa·s (from rheology measurements), the measured surface tension γ_L = 30.1 mN/m and the measured advancing contact angle, θ = 28° we obtain the

solid line in **Figure 33c**. The experimental results deviate from the LWE predictions. The *L*-versus-$t^{1/2}$ plots (**Fig. 33c**) also show the two regimes. Up to t = 17000 s the polymer melt imbibes like a liquid with the effective viscosities of 4660 Pa·s. For longer times the imbibition can be described by an effective viscosity of 910 Pa·s. This suggests that the polymer penetrates the pores with a 16-fold and 3-fold higher viscosity than in the bulk. At the same time, the characteristic relaxation time corresponding to the longest normal mode (**Figure 32b**) is slightly *longer* than in the bulk.

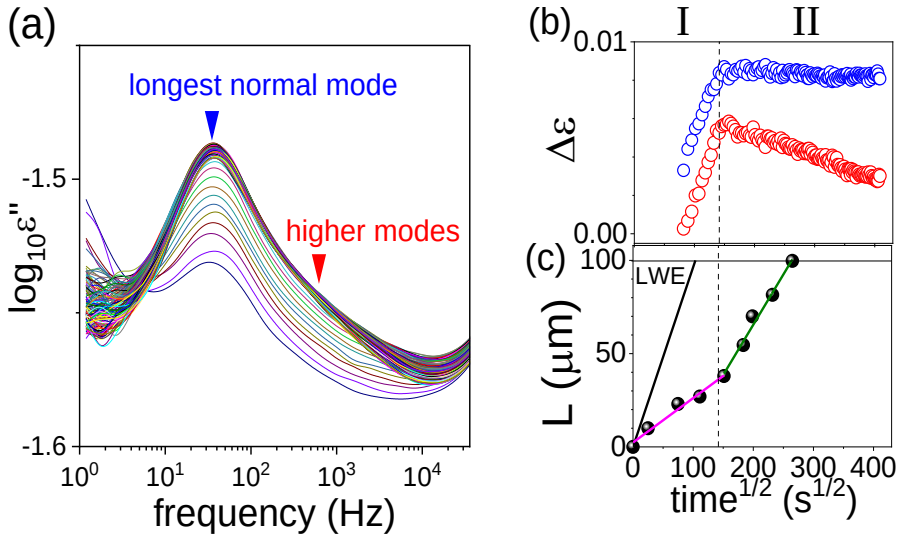

Figure 33. (a) Evolution of the dielectric loss spectra of PI 42k during imbibition within AAO nanopores with pore diameter of 40 nm at 303 K. (b) The extracted dielectric intensity as a function of the square root of imbibition time. (c) Imbibition lengths extracted via the optical reflection method at selected times. The dashed line is a guide for the eye. The extracted effective viscosity, η_{eff}, in the two regimes is 4660 Pa·s (magenta) and 910 Pa·s (green) for regimes I and II, respectively. The solid black line is the prediction of LWE. The calculation is based on the bulk viscosity η_0(bulk) = 285 Pa·s; γ_L = 30.1 mN/m; cosθ = 0.88; R = 20 nm.

By contrasting the growing imbibition lengths (**Figure 33c**) with the evolution of dielectric loss (**Figure 33b**) we come to – at a first site – surprising finding: Although in regime I the polymer advances within the pores following the LWE (albeit with a higher effective viscosity), in regime II, the polymer continues to advance under a *constant* (or even slightly decreasing) dielectric strength. To better understand this result we need to comment on the microscopic factors that influence the dielectric strength for the segmental and normal mode processes. The corresponding $\Delta\varepsilon$'s for the segmental and normal mode processes are[36-43]:

$$\Delta\varepsilon_{segmental} = \frac{1}{3\varepsilon_0} F g \frac{\mu_s^2}{k_B T} \frac{N_A}{V} \quad (70)$$

$$\Delta\varepsilon_{longest\ n.m.} = \frac{4\pi N_A \mu_{NM}^2}{3k_B T} \frac{\langle r^2 \rangle}{M_{PI}} \quad (71)$$

In Eq. 70, for the segmental relaxation, F is the local field, g the Kirkwood/Fröhlich correlation factor, μ_s the dipole moment per molecule and N_A Avogadro's number. Evidently, the dielectric strength for the segmental mode being proportional to the number density of dipoles, is an increasing function of imbibition time up to the complete pore filling. This has been confirmed by following the evolution of the segmental process in PI (at a lower temperature) and in poly(*n*-butyl methacrylate). Hence, the evolution of the segmental process follows approximately the predictions from Eq. 70. In contrast, the dielectric strength of the chain modes relates to the relaxation of the end-to-end vector, $\langle r^2 \rangle$, the dipole moment per contour length, μ_{NM}, and the chain molecular weight, M_{PI}. The former is prone to chain configurations next to the pore wall (**Figure 34**).

Below we provide a plausible *microscopic* scenario (with the help of **Figure 34**) that attempts to reconcile all experimental findings. The figure depicts only few chains and shows the imbibition process at the beginning (corresponding to regime I) and at later stages (regime II). At the beginning, only a small portion of chains are in contact with the pore walls forming trains, loops and some tails (*e.g.*, chain in red). Despite the small fraction of adsorbed segments, the effective pore diameter is reduced and the overall viscosity is increased reflecting the effect of the dead-layer. However, the majority of chains are not in contact with the pore walls and hence there exist fluctuations of the end-to-end vector (*e.g.*, chains in green, blue and yellow). As time progresses within regime I ($t^{1/2} < 150$ s$^{1/2}$) more polymer chains enter the pores and the dielectric strength increases (Eq. 71). At longer times, within regime II, more segments are adsorbed at the pore walls creating more train and longer loop configurations that have as an effect the reduction in the dielectric strength for the normal modes (**Figure 33**).

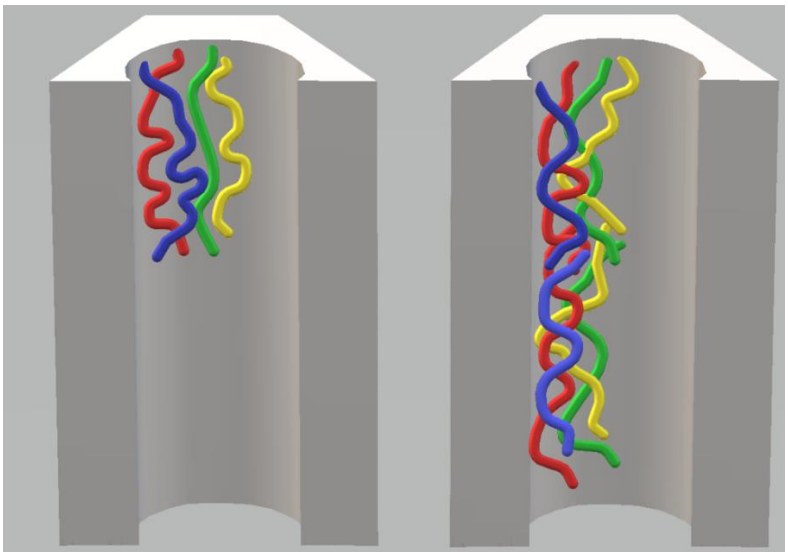

Figure 34. Schematic of PI imbibition in native nanopores. Four colored chains are shown at initial (left) and additional chains at later stages (right). Initially only a small number of segments corresponding to the red chain are adsorbed to the walls forming some trains, loops and tails. At latter stages, additional chains have segments in the vicinity of the pore walls and inner chains (*e.g.*, yellow chain) are more entangled with the loops of the adsorbed chains (red/blue chains).

In the present case of PI 42k, the near constancy of the dielectric strength is a composite effect owing to an increasing number of chains within the pores and a decreasing number of fluctuating chains (**Figure 33b**). Interestingly, the crossover time from **Fig. 33b** corresponds to a time scale much longer than the terminal relaxation time of the bulk polymer. This provides additional support to the fact that other – longer – times scales are involved in the adsorption process. Adsorption, apart from chain diffusion towards the interphase, it involves continuous conformational pathways of the chains towards minimizing their free energy. The existence of a somewhat slower longest normal mode (**Figure 32**) within regime II in the native AAO nanopores is more difficult to explain. It could associate with an increasing density of topological constraints (entanglements). New chains entering the pores (*e.g.*, yellow chains in **Figure 34**) are topologically constrained by the increased numbers of longer loops. This can explain the longer characteristic time for the normal modes during polymer flow (**Fig. 32**). Notably, this effect is absent in the case of silanized AAO. In the absence of adsorption sites long loops are not formed, the chains do not experience extra topological constraints and imbibe with the same time scale as in bulk.

To gain a deeper understanding for the adsorption of polymer chains, the adsorption kinetics following the full imbibition of *cis*-1,4-polyisoprenes in AAO was systematically studied as a function of pore size (*i.e.*, diameters of 20, 40, and 100 nm) and molar mass (*i.e.*, PI 5k, 12k, 21k). **Figure 35a** depicts the evolution of the dielectric loss curves during and after the full imbibition of PI 5k into AAO nanopores having pores with a diameter of 20 nm at 303.15 K. We observed an increasing dielectric loss curves for the longest normal mode during imbibition until after 12000 s when the trend reversed and the dielectric loss curves start to decrease in intensity. The same Figure compiles the evolution in the dielectric strength, $\Delta\varepsilon$, of the normal mode for the same PI following imbibition in AAO with different pore diameters. This trend is more evident in the smaller pores. Note the very long time scales, that in the case of the 20 nm pores is in the order of (several) days. We will return to this point below.

In **Figure 35b** the dielectric strength is normalized to the maximum value. The maximum, $\Delta\varepsilon_n$, coincides with the full imbibition of the polymer as evidenced by independent measurements by reflection optical microscopy (ROM). At subsequent times, the strength of the normal mode is decreasing due to increasing adsorption. Polymer adsorption gives rise to train and loop chain configurations that are dielectrically inactive because part of the chain cannot fluctuate in space and time. The decrease in dielectric strength can be parameterized by an exponential function as: $\Delta\varepsilon = \Delta\varepsilon_{max}\left(exp^{-\frac{t}{\tau_{ads}}}\right)$, where τ_{ads} is the characteristic adsorption time. A single exponential is the simplest approach to describe the desorption process as rate-limited by the energetics of surface detachment. At the same time, we can record the position (frequency of maximum loss, f_{max}) of the normal mode, that relates to the longest relaxation time as $\tau_{max} = 1/(2\pi f_{max})$.

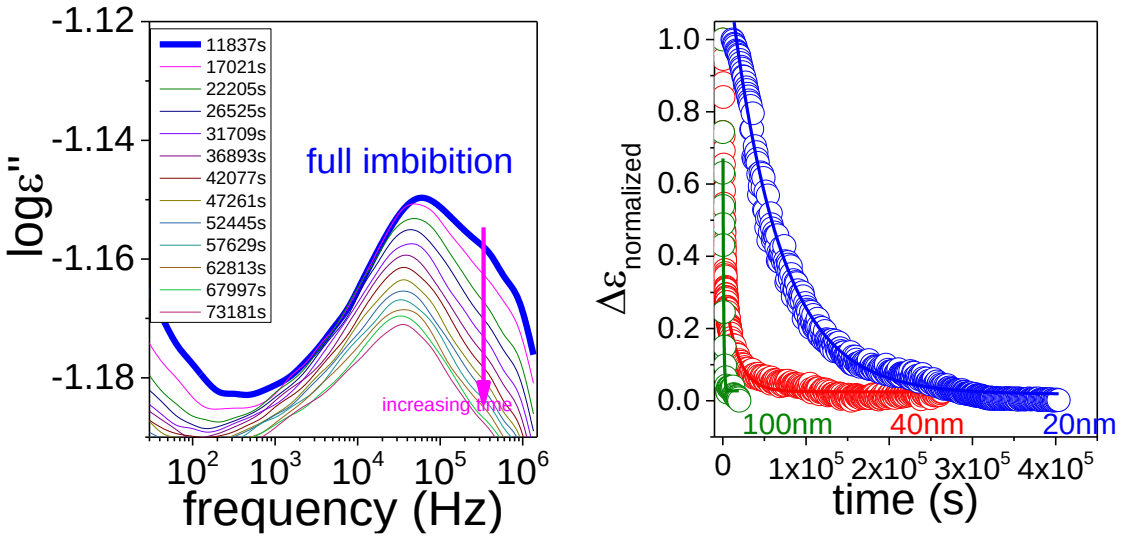

Figure 35. (left) Evolution of dielectric loss curves at the late stages of imbibition of PI 5k within AAO templates having 20 nm diameter pores at *T*=303.15K. (right) Evolution of the normalized dielectric intensity during the *in situ* imbibition and subsequent adsorption within AAO nanopores with different pore diameters; (green):100 nm, (red): 40 nm, and (blue): 20 nm all at the same temperature (303.15 K). Lines represent the result of the fit to an exponential decay function (see text).

The results of the adsorption kinetics of PI 5k can be discussed with the help of **Figure 36**. The figure depicts the characteristic adsorption time, $\log(\tau_{ads}/\mathrm{s})$ as a function of the inverse pore diameter (**Fig. 36a**) and as a function of the degree of confinement (**Fig. 36b**), the latter defined by the ratio of the polymer coil size ($2R_g$) to the pore diameter (D). In addition, the figure contains the time required for the full imbibition of the pores (in green) extracted by ROM (this time coincides with the $\Delta\varepsilon_{max}$). The adsorption time follows the dependencies as: $log(\tau_{ads}/s) = 2.2 \pm 0.2 + \frac{62\pm8}{D}$, $(D \ in\ nm)$ and $log(\tau_{ads}/s) = 2.2 \pm 0.2 + (13.5 \pm 1.8) \times \frac{2R_g}{D}$, $(D\ in\ nm)$, *e.g.*, strongly increasing with confinement. The characteristic relaxation times of the longest normal mode obtained from the dielectric loss maximum at the end of the imbibition process are also shown. Notably, this time scale is somewhat longer than in the bulk especially within the smaller pores. This finding could reflect an increasing density of topological constraints as a result of the loop/train configurations of the adsorbed chains (**Figure 34**). Loop/train configurations are expected to reduce the critical molecular weight for entanglements for chains in the vicinity to the

pore walls. The results presented here are consistent with the notion of surface-enhanced entanglements that "propagate" in the direction normal to the surface.[10]

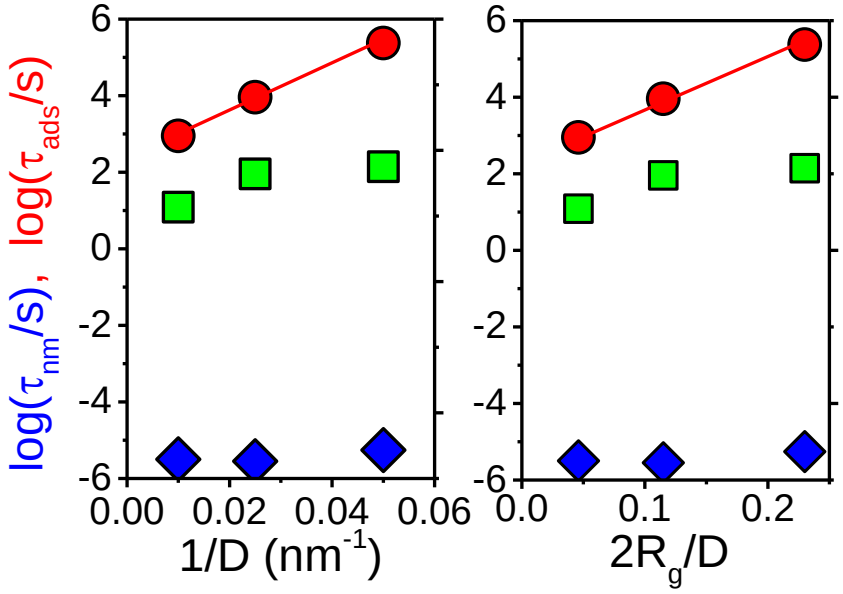

Figure 36. Dependence of the characteristic adsorption time, $\log(\tau_{ads}/s)$ on (left) the inverse pore diameter and (right) the degree of confinement, defined by the ratio of polymer size ($2R_g$) to the pore diameter for PI 5k: (red spheres): characteristic adsorption times obtained from the fits shown in Figure 35. The lines represent the result of a linear fit. The time scale of the longest normal mode (blue solid rhombi) is also plotted at the end of the adsorption process. The time of full imbibition is plotted with the green solid squares.

The chain length dependence of the adsorption process is examined next. **Figure 37** provides the evolution of dielectric strength for three PIs with molar masses of 5 kg·mol^{-1}, 12 kg·mol^{-1} and 21 kg·mol^{-1} within AAO templates with pore size of 100 nm at 303.15 K. The normalized dielectric strength was again fitted to an exponential function and the characteristic adsorption times are plotted in **Figure 38**. Evidently, adsorption times become much longer with increasing molar mass.

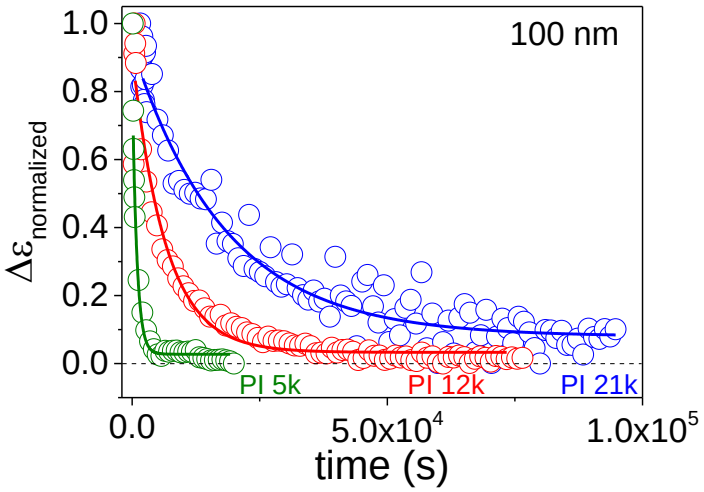

Figure 37. Evolution of dielectric intensity ($\Delta\varepsilon$) of **PI** with different molar masses during the *in situ* imbibition (and subsequent adsorption) within AAO nanopores with diameter of 100 nm at a temperature 303.15 K. Lines represent fits to an exponential decay function.

The different time scales can be discussed with the help of **Figure 38**. The figure contains in total four timescales: The faster (~ *n*s) is the segmental relaxation obtained from the Vogel-Fulcher-Tammann (VFT) equation at the imbibition temperature (303.15 K). The latter was obtained immediately following the kinetic experiments by fast cooling to below T_g and slow heating to higher temperatures. As expected, this time scale is the fastest without a significant dependence on molar mass. The second time scale is the longest normal mode obtained at the end of the imbibition process as $\tau_{max} = 1/(2\pi f_{max})$. The critical molar mass, M_c, for PI is ~ 10800 g·mol^{-1} (the entanglement molecular weight is M_e ~ 5400 g·mol^{-1}) meaning that PI 5k is unentangled, PI 21k is entangled whereas PI 12k is in the border region. Despite the limited data points two slopes can be obtained with exponents of approximately 2 and 3.4 below and above M_c. The third time-scale corresponds to the time needed for the full imbibition and has a clear molar mass dependence. Lastly, the fourth time-scale reflects the adsorption times that strongly depend on both the molar mass and the pore size. Adsorption times are (i) some 8 orders of magnitude slower than the terminal relaxation times (*e.g.*, the relaxation of the chain as a whole) and (ii) display a similar molar mass dependence with the terminal times.

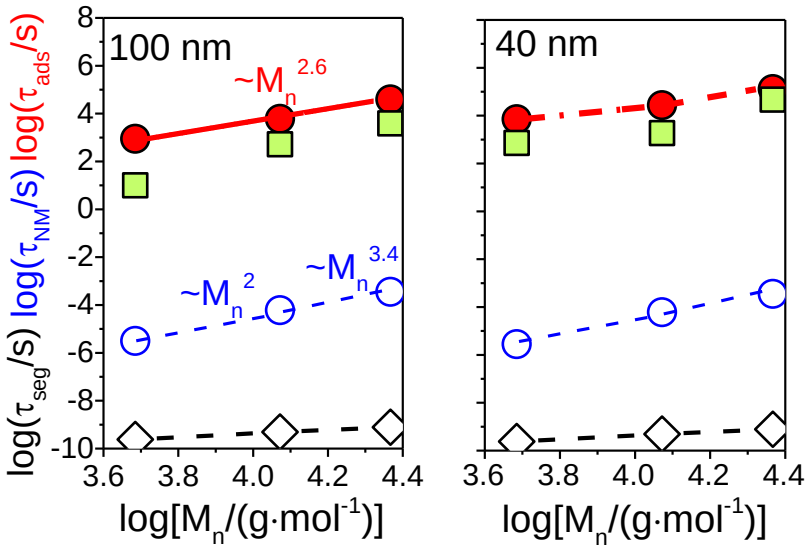

Figure 38. Molar mass dependence of the characteristic time scales within AAO nanopores with pore diameters (left) 100 nm and (right) 40 nm. (green squares): full imbibition time, (red spheres): characteristic adsorption time following imbibition, (blue solid/empty circles) peak position of longest normal mode of polyisoprene under confinement (at the end of adsorption process). Dashed and dash-dotted lines are linear fits.

The very long time scale of adsorption can be discussed in view of a scaling theory developed by de Gennes[44,45] that accounts for the formation of adsorbed layers in a good solvent. At early stages, a uniform polymer layer was considered on the (flat) surface as a result of bulk diffusion. Subsequent formation of an adsorbed layer was considered as a two-step process. At a first step, any new chain in order to be adsorbed needs to overcome the potential barrier due to the excluded volume of the already adsorbed chains. At a second step, the incoming chain replaces the already adsorbed chains by spreading on the surface whereas the previously adsorbed chain unfolds by the formation of long loops. As outgoing (and incoming) chains have to pass through several unfavorable configurations the latter process was predicted to be very slow. As for the molar mass dependence, by considering entangled polymers, de Gennes suggested that the longest relaxation time scales as $\tau \sim \tau_s N^3$, where τ_s is the relaxation time of an adsorbed monomer. Subsequently, Semenov and Joanny,[46] considered explicitly the structure of tails and loops within the adsorbed layer (the chain ends are effectively repelled from the surface) and further assumed Rouse-Zimm dynamics to predict the molar mass dependence of two characteristic times scales, the adsorption and the exchange times, with respective scaling as $\tau \sim N^{2.24}$ and $\tau \sim N^{2.42}$. Both of these

dependencies are in line with the experimental results over the limited range of molar masses investigated. Extending the range of molar masses is a formidable task due to limitations associated with the experimental frequency window and imbibition temperature.

Motivated by the earlier studies of polymer blend imbibition (PEO and PnBMA), we further investigated the effect of blending on the imbibition and adsorption kinetics for two symmetric PI blends (B1 (5k/21k) and B2 (5k/42k)). The question is whether the two components penetrate and adsorb on the pores simultaneously or consecutively. The results for the blend B2 with respect to the evolution of the dielectric loss curves during and following the full imbibition are shown in **Figure 39**. The evolution of the dielectric loss curves corresponding to the shorter and longer chains in the blend reveals distinct differences that will be discussed below with respect to **Figure 40**. We should point out here that the choice of the blend components in B1 and B2 is based on the existence of two separate normal modes in the blends both relaxing within the experimental window: a slower (faster) one reflecting the dynamics of the longer (shorter) chains in the blend. The results from blend B2 is mainly dsicussed here.

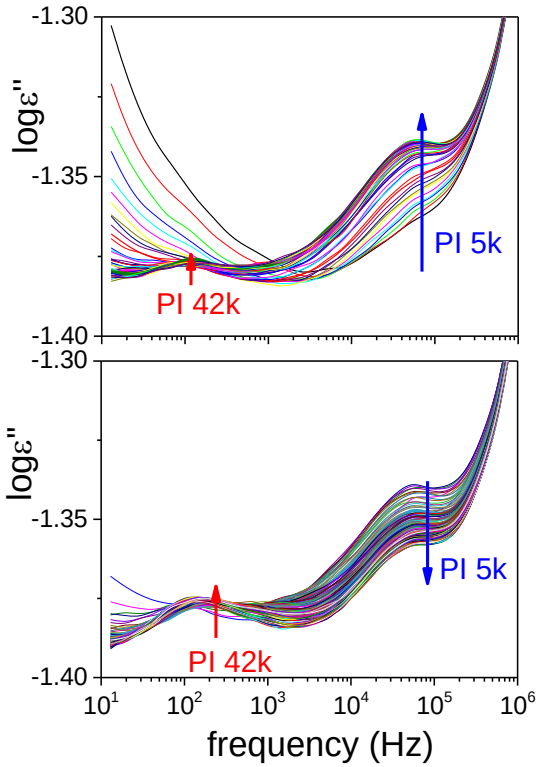

Figure 39. Evolution of dielectric loss curves corresponding to the two separate normal modes of PI in the blend B2 (5k/42k) during imbibition and subsequent long time adsorption within AAO with pore diameter of 40 nm at 303.15K. Early (top) and late (below) stages are shown. Arrows are indicative trends for the evolution of the dielectric loss curves corresponding to the normal modes of PI 5k (blue) and PI 42k (red) components in the blend.

Evidently, the results of the blend B2 (**Figure 40**) show that the blend components have very different imbibition speeds. Note that the imbibition lengths of the homopolymers calculated from the LWE based on the measured (**Table 3**) zero-shear viscosities (solid lines in **Fig. 40b**) are at variance from the measured lengths. While for the homopolymer PI 5k the extracted effective viscosity from the imbibition length and the use of the LWE is approximately the bulk zero-shear viscosity, for the PI 42k homopolymer there exist two slopes during imbibition with effective viscosities of 4660 Pa·s and 910 Pa·s, *i.e.*, much higher than bulk (**Table 3**). This finding reveals that the dead-layer effect is dominant. For the blend, the results from the ROM study (**Fig. 40b**) suggest that the imbibition length, d_1, is in proximity to the PI 5k homopolymer revealing a clear preference for the shorter chains to penetrate the pores. The emerging picture from these results is that the PI 5k chains are enter first and only later some PI 42k are dragged into the pores.

These results on the "static" imbibition length obtained *ex situ* (ROM) can be compared with the results from dynamic experiment performed *in situ* (*n*DS). In accordance with the static measurement revealing the faster imbibition of the shorter chains, the dielectric strength of the PI 5k blend component (**Fig. 39** and **Fig. 40a**) first increases during imbibition and reaches a maximum at a time scale that nicely corresponds to the full imbibition (as obtained from ROM). It is only at the late stages of the pore filling that the shorter chains drag along some of the longer chains in the pores as evidenced by the slow rise in the dielectric strength of the PI 42k component. At the same time, the normal mode of the PI 5k blend component starts to decrease as a result of increasing adsorption. Hence at the late stages of imbibition two effects take place: first the shorter chains are adsorbed onto the AAO pore surface, and at the same time, some of the longer chains are entering the pores. This further suggests that long-time adsorption in the blend is dominated by an exchange mechanism involving primarily the shorter chains.

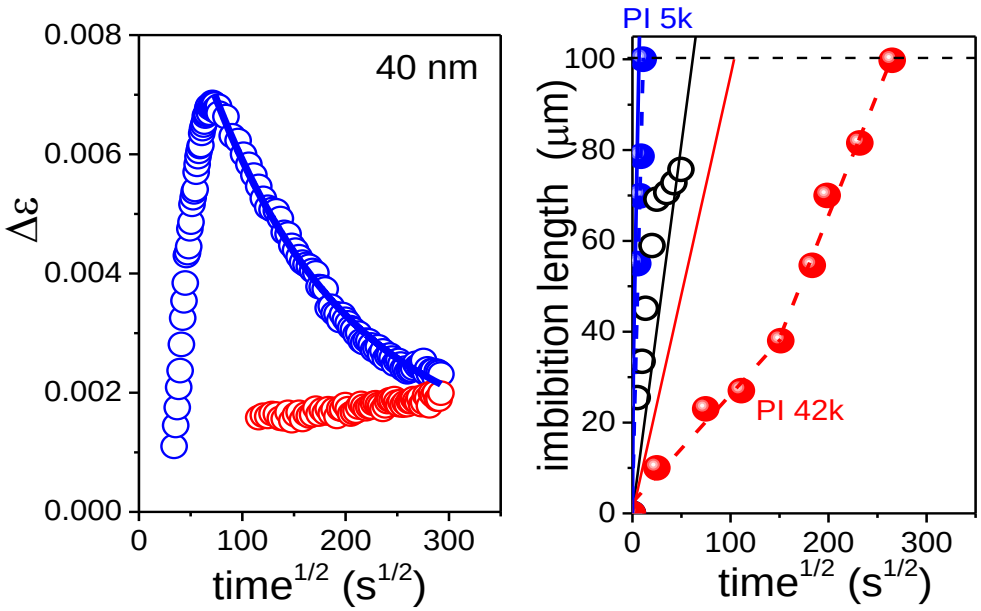

Figure 40. (left) Evolution of dielectric intensity for the PI blend B2 (5k/42k) during imbibition and subsequent long adsorption within AAO with pore diameter of 40 nm at T = 303.15K. (right) Imbibition length measured *ex situ* by ROM for three systems: homopolymer PI 5k (blue spheres), homopolymer PI 42k (red spheres), and B2 blend (black circles). Blue, red and black solid lines are the predictions of the imbibition length based on the LWE and the measured zero-shear viscosity (Table 3).

1.3.6. *In situ* imbibition of the solid polymer electrolyte — poly(ethylene oxide) /LiTFSI

The well-known polymer electrolyte PEO/LiTFSI was employed in this study. The polymer electrolytes were prepared following three steps (**Figure 41**): first, 3 w/v % solution of the PEO homopolymers (see **Table 4**) were prepared in THF. Second, the same concentration 3 w/v % of LiTFSI solutions were prepared also in THF. In a last step, the two solutions were mixed in different molar ratios $[EO^-]:[Li^+]$. For the PEO(8k)/LiTFSI, three composition ratios $[EO^-]:[Li^+]$=16:1, 8:1, and 4:1 were prepared. In a second series, the salt doping ratio $[EO^-]:[Li^+]$ was fixed to 4:1 and different molar masses of PEO (2k, 11k, 29k, and 44k) were investigated. The solutions were performed with an oil bath set at temperature of 50 ºC under continuous stirring to ensure homogeneity. The thus prepared polymer electrolyte solutions were stored in a vacuum oven for complete removal of the solvent.

Table 4. Molecular characteristics of the PEO.

Sample	$\overline{M_n}$ (g·mol^{-1})	$\overline{M_w}$ (g·mol^{-1})	$Đ$
PEO 2k	2005	2403	1.23
PEO 8k	8090	9155	1.13
PEO 11k	8793	10509	1.20
PEO 29k	29767	31425	1.06
PEO 44k	39615	49876	1.26

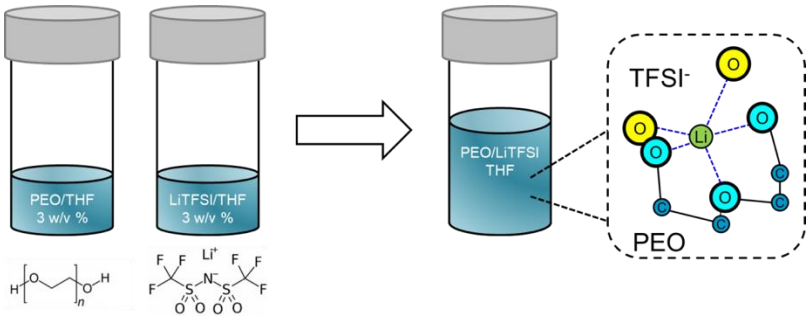

Figure 41. Schematic showing the preparation of polymer electrolytes based on PEO/LiTFSI.

Main findings

We first establish the phase diagram of the polymer electrolytes by using DSC. The cooling and subsequent heating traces for bulk PEO and different [EO^-]:[Li^+] ratios are shown in **Figure 42**. In the cooling curves, the strong crystallization exotherm of bulk PEO at ~38ºC is completely suppressed for the higher salt concentrations. For the [EO^-]:[Li^+]=16:1 there is some crystallization of PEO at ~ 0 ºC, suggesting the limiting chain length for PEO crystallization. In the absence of crystallization, the glass temperature of PEO segments enriched by [Li^+] are at -55 ºC, -50 ºC and -52 ºC for the [16:1], [8:1] and [4:1], respectively. On heating the polymer electrolytes with the higher salt content there is only a T_g that can be observed (completely amorphous). On the other hand, heating the electrolyte with [16:1] ratio from the glassy state results to cold crystallization at -2 ºC followed by a very broad melting at 34 ºC. The above data on the T_c, T_m and T_g are included in the phase diagram of **Figure 43**. Subsequently, in our investigation of the ion/polymer dynamics we concentrate on the [4:1] ratio that is completely amorphous and is expected to have the higher conductivity.

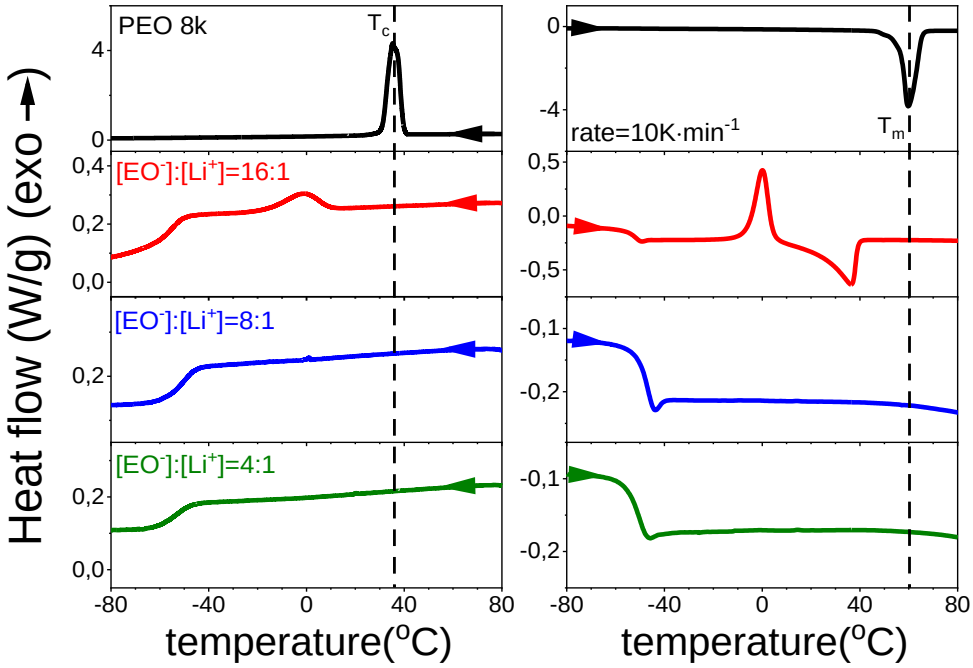

Figure 42. DSC traces of the bulk polymer electrolytes PEO8k/LiTFSI with salt concentration [EO^-]:[Li^+] with ratios ranging from 4:1 to 16:1, on cooling (left) and subsequent heating (right)

with a rate of 10 K·min^{-1}. The vertical dashed lines indicate the bulk crystallization temperature (T_c) and melting temperature (T_m), respectively.

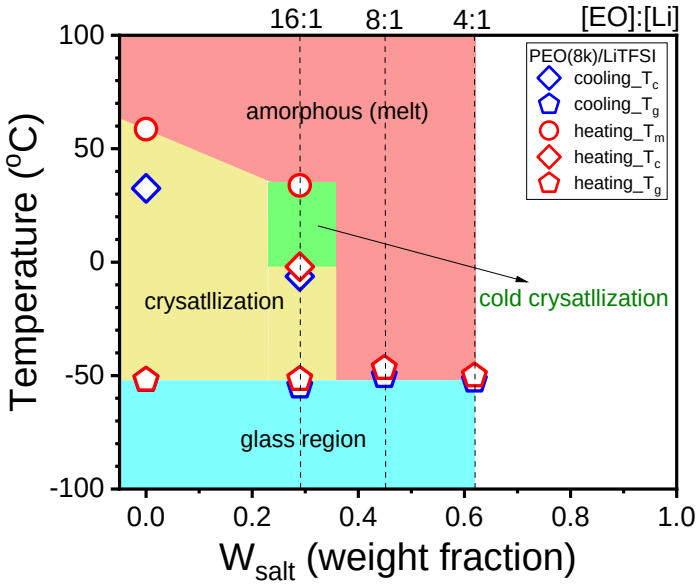

Figure 43. Phase diagram of the polymer electrolyte PEO8k/LiTFSI with salt concentration [EO$^-$]:[Li$^+$] ranging from 4:1 to 16:1. The crystallization, melting and glass temperatures were determined from DSC during the second cooling and heating scans.

The results of the ionic conductivity measurements for the bulk polymer electrolytes at two compositions can be discussed with respect to **Figure 44**. The Figure depicts the real (σ') and imaginary (σ'') parts of ionic conductivity as a function of frequency for different temperatures at two compositions (4:1 and 16:1). The σ' curves show a plateau at intermediate frequencies associated with the dc-conductivity, an upturn at higher frequencies (ac-conductivity) and a decrease at lower frequencies (electrode polarization). The temperature dependence of the dc-conductivity is depicted also in **Figure 44**. The two salt-doped electrolytes display a different behavior. For the completely amorphous electrolyte (4:1), $\sigma'_{dc}(T)$ exhibits a Vogel-Fulcher-Tammann (VFT) behavior as:

$$\sigma_{dc}(T) = \sigma_0^{\neq} exp\left(-\frac{B}{T - T_0}\right) \tag{72}$$

Here, $\sigma_0^{\neq}$=1.99 ± 0.3 S·cm^{-1} is the dc-conductivity in the limit of very high temperature, B=1321 ± 35 K is the activation parameter for ion migration and T_0 =183 ± 1 K is the "ideal" glass temperature. For the polymer electrolyte with [EO$^-$]:[Li$^+$]=16:1 that undergoes cold crystallization

and melting, the $\sigma'_{dc}(T)$ shows discontinuous changes at the respective T_c and T_m. PEO crystallization clearly impedes ion transport due to the increased effective viscosity.

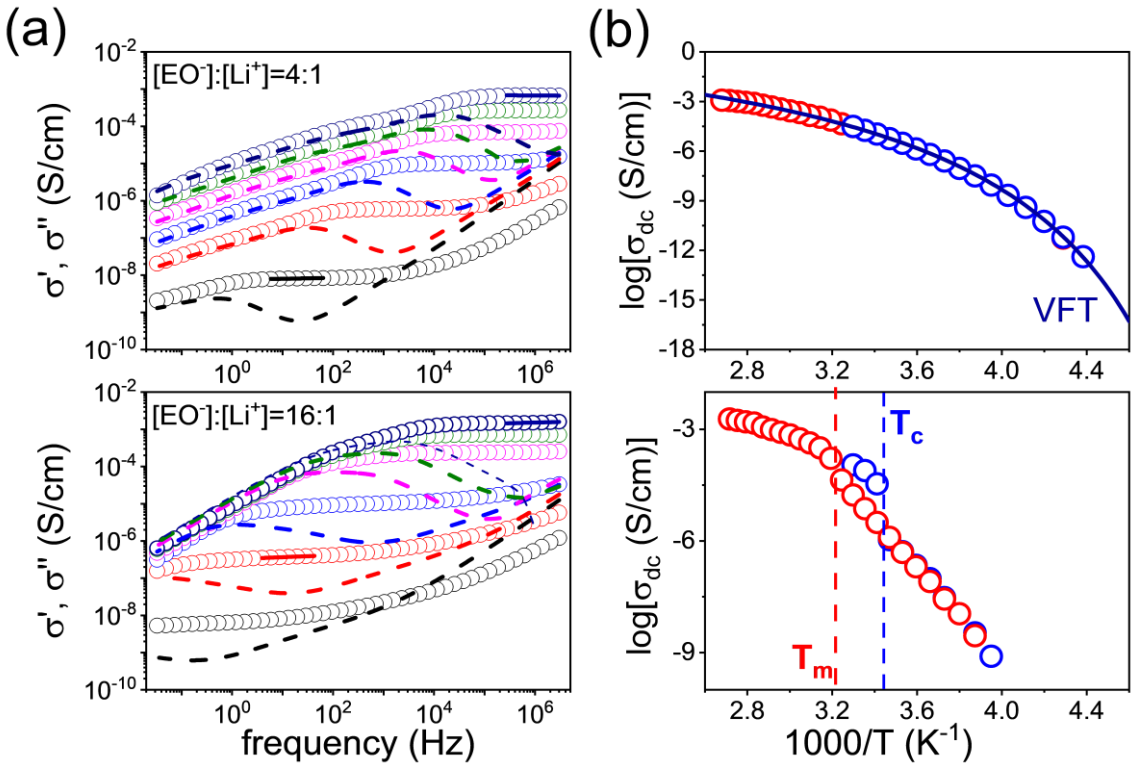

Figure 44. (a) Real (symbol) and imaginary (dashed lines) parts of the complex conductivity for PEO8k/LiTFSI with different salt concentrations [EO$^-$]:[Li$^+$]=4:1 (top) and 16:1 (bottom) at selected temperatures: 253 K (black), 273 K (red), 293 K (blue), 313 K (magenta), 333 K (green), and 353 K (dark blue). (b) Extracted dc conductivities from cooling and subsequent heating scans of DS measurements. Vertical dashed lines indicate the melting (red) and crystallization temperatures (blue) obtained, respectively, from DSC.

The evolution of dc-conductivity of the polymer electrolytes during imbibition within AAO nanopores is monitored by the *in situ* nanodielectric spectroscopy (*n*DS). **Figure 45** provides *in situ* dielectric curves of the real (σ') and the imaginary (σ'') parts of complex conductivity for the PEO8k/LiTFSI=4/1 electrolyte located inside AAO nanopores with diameter of 20 nm. The evolution of σ' and σ'' reveals two time regimes. For time intervals in the range for 0 to 50 $s^{1/2}$, conductivity increases without showing a clear plateau. It is only at later times that a plateau develops. Hence the dc conductivity can only be extracted at the late stage of the first regime. At times longer than 50 $s^{1/2}$, surprisingly, the dc conductivity starts to decrease. To understand this

phenomenon, independent calibration measurements were made in order to determine the imbibition length of the polymer electrolyte.

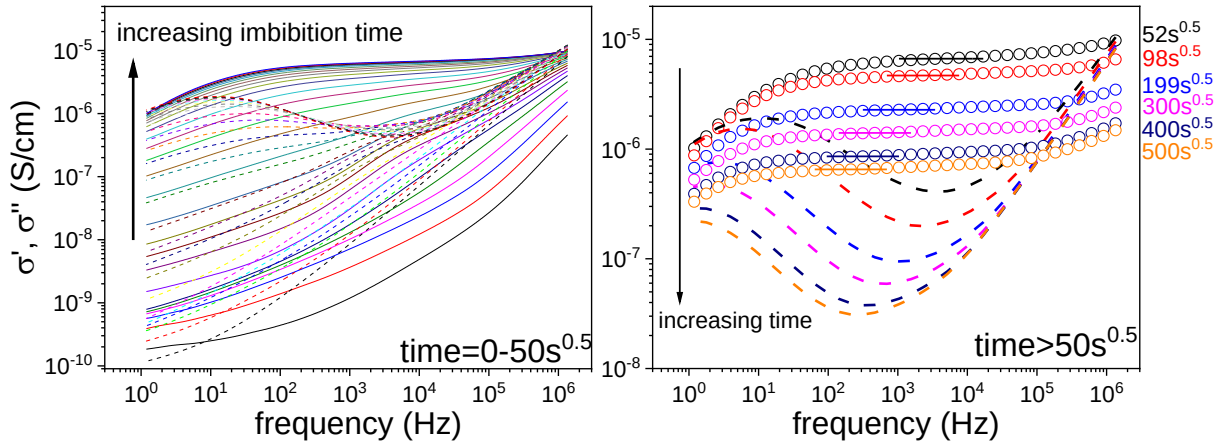

Figure 45. Evolution of the real (solid lines) and imaginary (dashed lines) parts for PEO8k/LiTFSI with salt concentration [EO^-]:[Li^+]=4:1 entering AAO 20nm nanopores at 303K in different time periods: from 0 to 50 $s^{0.5}$ (left) and beyond 50 $s^{0.5}$(right).

The evolution of σ_{dc} for the [EO^-]:[Li^+]=4:1 during imbibition in AAO pores with diameter 100 nm, 40 nm and 20 nm is depicted in **Figure 46**. These results are compared with *ex situ* ROM measurements of the imbibition length measured at different time intervals. We discuss first the ROM results. Independent of pore size they show a higher slope for the imbibition length vs $t^{\frac{1}{2}}$ as predicted by the LWE equation (the LWE predictions using the bulk viscosity of η_0 = 21 Pa·s, γ_L = 38.5 mN/m, cosθ = 0.61 are shown with the solid lines). This, within the context of the LWE, is interpreted as corresponding to a lower effective viscosity; from a bulk viscosity of 21 Pa·s to 5.7 Pa·s, 2.9 Pa·s and 14.3 Pa·s, respectively, within 100 nm, 40 nm and 20 nm pores. Evidently, on entering the nanopores the polymer electrolyte experiences a lower effective viscosity. This is expected to affect the dc-conductivity values. Indeed, the dc-conductivity at the early stages attain higher σ_{dc} values than in bulk (the latter is shown in **Fig. 46** with the dashed line). The ROM results also point to the time needed for a full imbibition. In the case of the polymer electrolyte within 20 nm pores this time nicely coincides with the maximum in $\sigma_{dc}(t)$ at $t^{1/2} \sim 30$ $s^{1/2}$. At shorter times the $\sigma_{dc}(t)$ increases as more of the polymer electrolyte fills the nanopores. However, the maximum is not evident in the larger pores because the process is faster as evidenced by ROM. The most intriguing feature of **Fig. 46** is the strong decrease in $\sigma_{dc}(t)$ at later times.

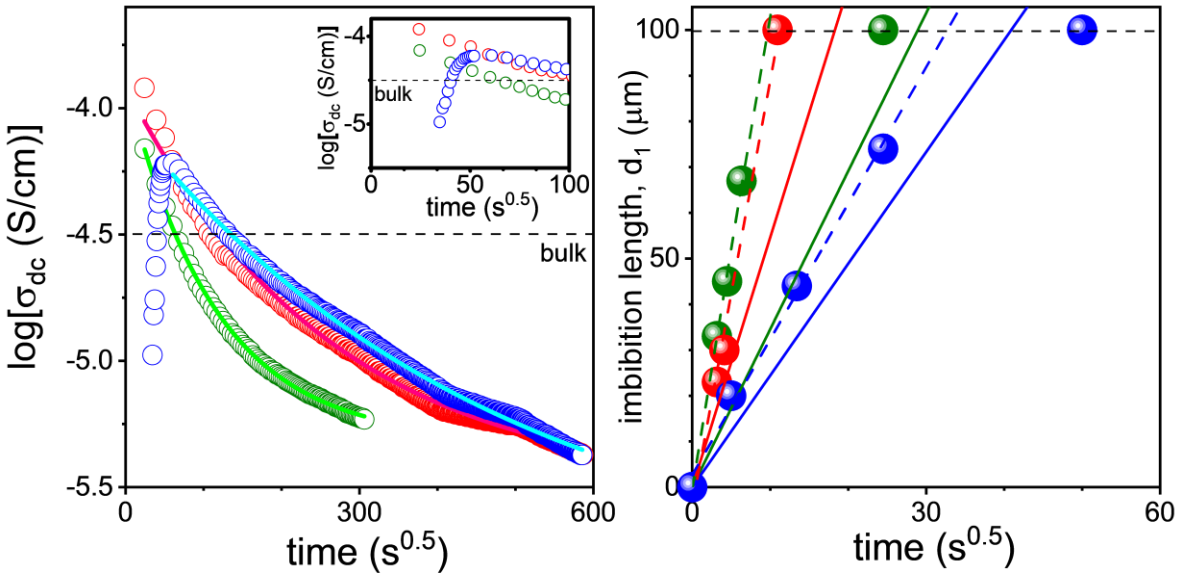

Figure 46. (Left) The extracted ionic conductivity from *in situ n*DS for PEO8k/LiTFSI with salt concentration [EO^-]:[Li^+]=4:1 inside the AAO nanopores of different pore size at 303 K: (green) 100 nm, (red) 40 nm, and (blue) 20 nm plotted as a function of the square root of imbibition time. (Right) Imbibition lengths extracted via optical reflection microscopy at selected times. The solid lines in the right plot are the theoretical predictions of Lucas-Washburn equations (LWE) with parameters as: bulk viscosity $\eta_0(bulk)$ = 21 Pa·s; γ_L=38.5 mN/m; $cos\theta$=0.61; R=50 nm.

The decreasing dc-conductivity can be related to the adsorption of polymer chains to the pore walls. Dc-conductivity is always a product of the number density with the mobility of ions. Due to the coupled dynamics of the polymer chains with the lithium ions, polymer adsorption inevitably drives some ions at the pore walls where they are immobilized. The characteristic adsorption times can be obtained via fitting the $\sigma_{dc}(t)$ with a stretched exponential function, known as Kohlraush-Williams-Watts function (KWW) as σ_{dc}= $(\sigma_{dc})_{max}\cdot \exp[-(\frac{t}{\tau^*})^{\beta}]$, where the τ* is the stretched exponential time, and β is the stretched exponential factor (~ 0.6) (**Figure 47a**). The characteristic adsorption time is obtained as $<\tau_{ads}> = \frac{\tau^*}{\beta}\Gamma(\frac{1}{\beta})$, where Γ is the gamma function. The thus obtained adsorption times are plotted in **Figure 47** as a function of inverse pore diameter and degree of confinement as $2R_g/D$, where R_g and D refer to the bulk polymer chain dimensions and pore diameter, respectively. The adsorption times follow the dependencies as (**Figure 47b**) $log(\tau_{ads}/s) = 2.9 \pm 0.4 + \frac{43\pm13}{D}$, $(D\ in\ nm)$ and $log(\tau_{ads}/s) = 2.9 \pm 0.4 + (6.5 \pm 2) \times \frac{2R_g}{D}$, $(D\ in\ nm)$. Evidently, adsorption takes longer time to reach the equilibrium in the smaller

pores and for higher degrees of confinement. This is reminiscent to the dependence found in a type-A polymer *cis*-1,4-polyisoprene.

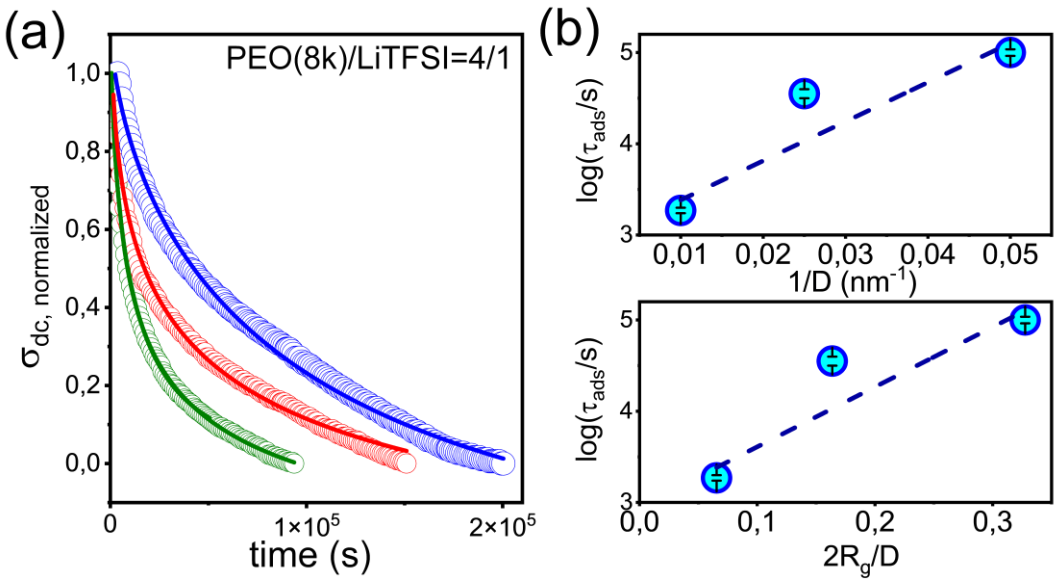

Figure 47. (a) Evolution of normalized dc conductivity as a function of the square root of time during the imbibition of PEO8k/LiTFSI with salt concentration [EO^-]:[Li^+]=4:1, at 303K, within different pores: (green) 100 nm, (red) 40 nm, and (blue) 20 nm. Solid lines represent fits to a stretched exponential function. (b) Dependence of the characteristic adsorption time log(τ_{ads}/s) on the (top) inverse pore diameter and (bottom) the degree of confinement, defined by the ratio of polymer size ($2R_g$) to the pore diameter. The dashed lines represent linear fits. Error bars are typically smaller than the symbol size.

Next we discuss the effect of polymer molar mass (2k, 8k, 11k, 29k, and 44 kg/mol) on the evolution of conductivity for a single pore diameter (100 nm). The results are depicted in **Figure 48**. They show a reduction in $\sigma'_{dc}(t)$ for the lower molar masses. However, a different behavior is seen for molar masses of 29 kg/mol and 44 kg/mol. In the case of 29 kg/mol an increase in $\sigma'_{dc}(t)$ is followed by a long plateau (from 300 to 500 $s^{1/2}$) and then by a decrease in conductivity. The characteristic time of full imbibition is at ~300 $s^{1/2}$ as obtained by ROM. Hence the initial increase is due to the filling of the pore whereas the $\sigma'_{dc}(t)$ dependence at later times associated with the adsorption of polymer segments. As discussed with respect to the previous PI study, the adsorption can be discussed in view of scaling theory by De Gennes. The theory accounts for the formation of adsorbed layers as a two-step process. Following adsorption of the first chains, the new chains to be adsorbed require to overcome the potential barrier due to the excluded volume of the already adsorbed chains (**Figure 34**). Subsequently, the incoming chains effectively replace the already

adsorbed chains (outgoing chains) and spread on the surface whereas the displaced chain unfolds by forming long loops. Since this process involves passing of the incoming and outgoing chains through several unfavorable configurations, the adsorption/desorption process is predicted to be very slow. These features are reflected in the shape of the $\sigma'_{dc}(t)$ for the 29 kg/mol sample. In the case of the highly entangled 44 kg/mol polymer electrolyte the imbibition process is extremely slow.

The molar mass dependence of the characteristic adsorption times is plotted in **Figure 48** (right). The adsorption times where obtained by stretched exponential fits to the $\sigma'_{dc}(t)$ reduction that is clearly seen for 2 kg/mol, 8 kg/mol and 11 kg/mol (**Figure 48** left). For the higher molecular weight (29 kg/mol) the extracted time is only an approximation. As for the 44 kg/mol the characteristic adsorption time is very long being outside the measured time-window. The characteristic time $\tau_{ads}(M)$ shows a dependence as $\tau_{ads} \sim M^2$, but this should not be taken literally as the adsorption time for the 29 kg/mol is likely to be much longer than the estimated by the initial drop $\sigma'_{dc}(t)$. The theoretical prediction for entangled polymer is that $\tau_{ads} \sim \tau_s M^3$, where, τ_s, is the characteristic time for the adsorption of a monomer. Subsequently the theory was modified by Semenov and Joanny to account for the structure of tails and loops within the adsorbed layer. They assumed Rouse-Zimm dynamics and predicted the molar mass dependence of two characteristic time scales, namely the adsorption and the exchange time scales as $\tau \sim N^{2.24}$ and $N^{2.42}$, respectively. The experimentally obtained $\sim M^2$ dependence is in line with the theoretical prediction. The Figure includes the time scales corresponding to the terminal and segmental relaxation both determined by rheology in the bulk. As expected the characteristic adsorption times are some 11 decades slower than the segmental and some 9 decades slower than the terminal times, both consistent with the theoretical prediction.

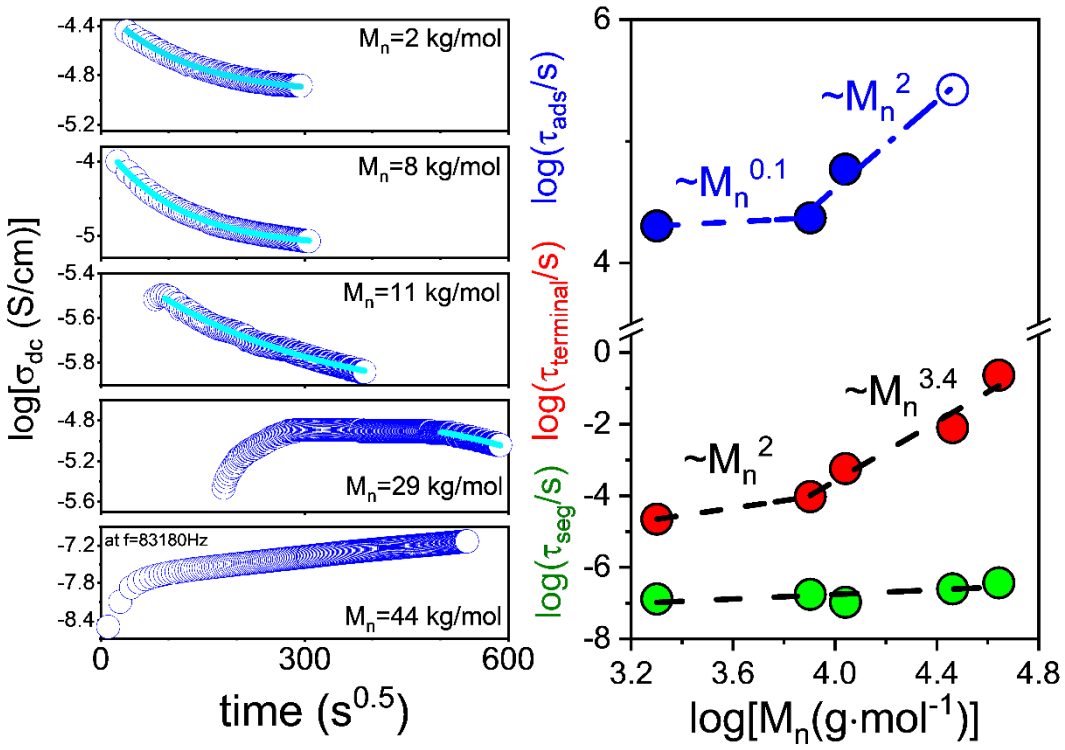

Figure 48. (Left) Evolution of dc-conductivity for PEO/LiTFSI=4/1 inside the AAO 100nm pores with different PEO molecular weights (2 kg/mol, 8 kg/mol, 11 kg/mol and 29 kg/mol). The data points for the case of 44 kg/mol are σ' values at frequency of 83180 Hz. The cyan lines represent the fits to a stretched exponential function. (Right) Molar mass dependence of the characteristic time scales within AAO nanopores with pore diameter of 100 nm: characteristic adsorption time following imbibition (blue), terminal (red) and segmental (green) relaxation times of the bulk determined from rheology. The empty blue circle is the estimated adsorption time for PEO29k/LiTFSI. Dashed and dash-dotted lines are linear fits.

Figure 49 (Left) shows the ionic conductivity as a function of inverse temperature for the bulk and confined polymer electrolytes. The latter is obtained from the cooling and heating scans following the in situ measurements. Overall, the temperature dependence of ionic conductivity follows the VFT behavior. The VFT parameters are shown in **Table 5**. However the ionic conductivity remains about two orders of magnitude lower than the bulk conductivity. The glass temperature associated to the ionic conductivity can be further extracted via extrapolating the VFT fits to σ_{dc} =10^{-14} S/cm (**Figure 49** right). As expected the extracted glass temperatures are found to be higher than in the bulk. Combining the observed higher T_g (reduced mobility) and lower σ_{dc}

suggest a correlation between the adsorption of polymer chains and the immobilization of ions at the pore walls.

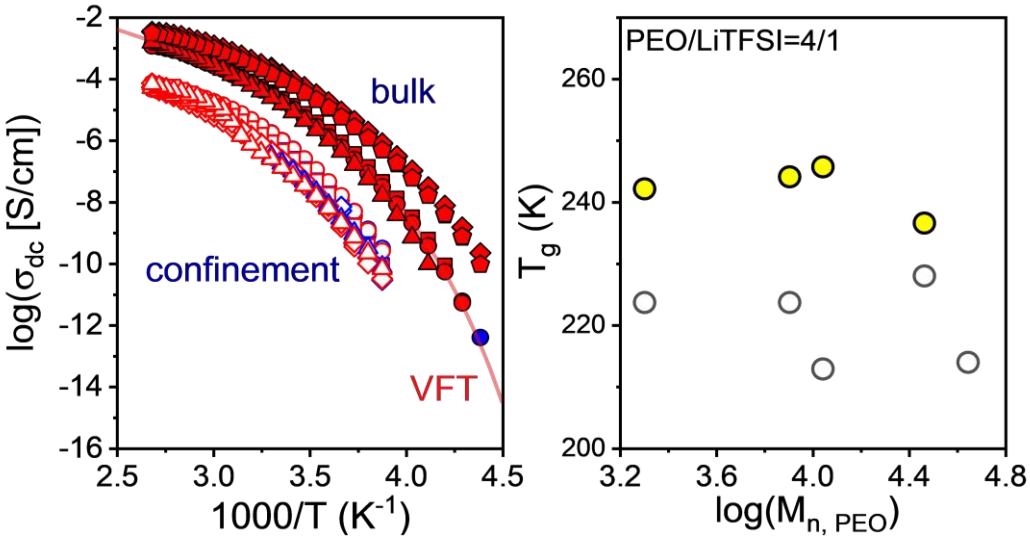

Figure 49. (Left) Temperature dependence of dc conductivity for bulk (solid symbols) and confined (empty symbols) polymer electrolytes at fixed $[EO^-]:[Li^+]=4:1$ with different molar masses of PEO: (square) PEO 2 kg/mol, (circle) PEO 8 kg/mol, (diamond) PEO 11 kg/mol, (triangle) PEO 29 kg/mol, and (pentagon) PEO 44 kg/mol. Red (blue) symbols represent data obtained from heating (cooling) scans. Red solid line represents VFT fits. (Right) Extracted glass temperatures T_g (obtained from the left plot by extrapolating the VFT to a dc conductivity value of 10^{-14} S/cm) are plotted as a function of $M_{w,\,PEO}$. Black empty symbols represent the T_g of the bulk polymer electrolytes, and the yellow solid circles refer to the confined polymer electrolytes.

Overall the results of the evolution of conductivity in the PEO/LiTFSI polymer electrolytes suggest that the $\sigma_{dc}(t)$ behavior is dictated by the adsorption of polymer chains at the pore walls. They further show that at the early stages of imbibition the effective viscosity is reduced below the bulk value. It seems that at such early stages the pore walls act as lubricants for the chain segments and ions. At much later stages, polymer adsorption takes place. The time scale of adsorption are very long—much longer than chain diffusion and certainly of monomer relaxation. Adsorption involves several unfavorable configurations of the polymer chains that inevitably affect the ion dynamics by (i) increasing the effective viscosity (higher T_g) and (ii) by reducing the number of mobile ions. These results are important in the design of confined polymer electrolytes.

Table 5. VFT parameters of the polymer electrolyte in the bulk and under confinement.

	Bulk			Confinement		
PEO(M_w)/LiTFSI	B (K)	T_0 (K)	$\log\sigma_0^{\neq}$ ($S\cdot cm^{-1}$)	B (K)	T_0 (K)	$\log\boldsymbol{\sigma_0^{\neq}}$ ($S\cdot cm^{-1}$)
M_w = 2 kg/mol	1254±25	184±0.8	0.2±0.05	1190±9.6	202±0.4	-1.1±0.02
M_w = 8 kg/mol	1352±31	182±0.9	0.3±0.07	740±37	216±2	-2.2±0.09
M_w = 11 kg/mol	1190±43	176±1.5	0.3±0.09	1197±11	205±0.4	-1.2±0.02
M_w = 29 kg/mol	1266±16	189±0.6	0.2±0.03	-	-	-
M_w = 44 kg/mol	1244±36	176±1.3	0.4±0.08	-	-	-

*These parameters are obtained from the VFT fits to the heating scan.

1.3.7. Imbibition of a semicrystalline polymer—poly(ethylene oxide) and poly(ε-caprolactone)

Two semicrystalline polymers were used in this study: poly(ethylene oxide) (PEO) and poly(ε-caprolactone) (PCL). They were synthesized in house. The molecular characteristics are shown in **Table 6**.

Table 6. Molecular characteristics of the PEO and PCL samples.

Sample	$\overline{M_n}$ (g·mol^{-1})	$\overline{M_w}$ (g·mol^{-1})	$Đ$	T_m (^{o}C)	ΔH_m [a]	X_c (%)[b]
PEO8k	8090	9155	1.13	62	139	70
PCL8.9k	5366	9723	1.81	56	72	49

[a]Heat of fusion determined from the second heating DSC thermograph.
[b]The crystallinity (X_c) was evaluated based on the heat of fusion as X_c (%)=($\Delta H_m/\Delta H^o_m$)×100%. Here, ΔH^o_m represents the heat of fusion of the perfect crystal (196 J/g for linear PEO and 148 J/g for linear PCL).[47]

Prior to infiltration, all AAO templates were annealed in a vacuum oven at T = 423 K for 8-10 h. Two thin films of PEO8k and PCL8.9k are prepared by hot pressing method. The thin films were subsequently deposit on top of AAO template and put into a vacuum oven with preset temperatures of 57^{o}C and 50^{o}C for PEO8k and PCL8.9k, respectively. The imbibition proceeded under vacuum for a period of 28 days for PEO8k and 51 days for PCL8.9k.

1.3.7.2 Main findings

The main results shown here relate to PEO8k (corresponding results for PCL8.9k can be found in Supporting Information). **Figure 50** compiles the thermodynamic, structured and rheological properties of bulk PEO8k. The DSC heating curve (**Figure 50a**) shows a major melting peak at temperate around 62^{o}C. Some minor melting peak can be seen at T = 57^{o}C corresponding to the melting of a minor lamellae. The degree of crystallinity of PEO was estimated to 70% from DSC. **Figure 50b** shows the viscoelastic behavior of PEO8k measured at the imbibition temperature of 57^{o}C. The measured bulk viscosity is frequency-dependent, and the storage modulus is always higher than loss modulus as expected for a crystalline sample (**Figure 50b**). From this result, we can ensure that PEO8k film on top of AAO template is in its crystalline state. The domain spacing, *d*, of PEO8k crystals obtained from SAXS (**Figure 50c**) are in the range from 15 to 18 nm

(depending on the cooling rate). Evidently, crystalline lamellae are far smaller than the pore size. The superstructure formation in PEO8k was also studied by POM. We used polarized optical microscopy (POM) to follow the crystallization of PEO8k under thermal conditions similar to that used for the long-imbibition specimen. **Figure 50d** shows the expected spherulitic superstructure with the typical maltese morphology.

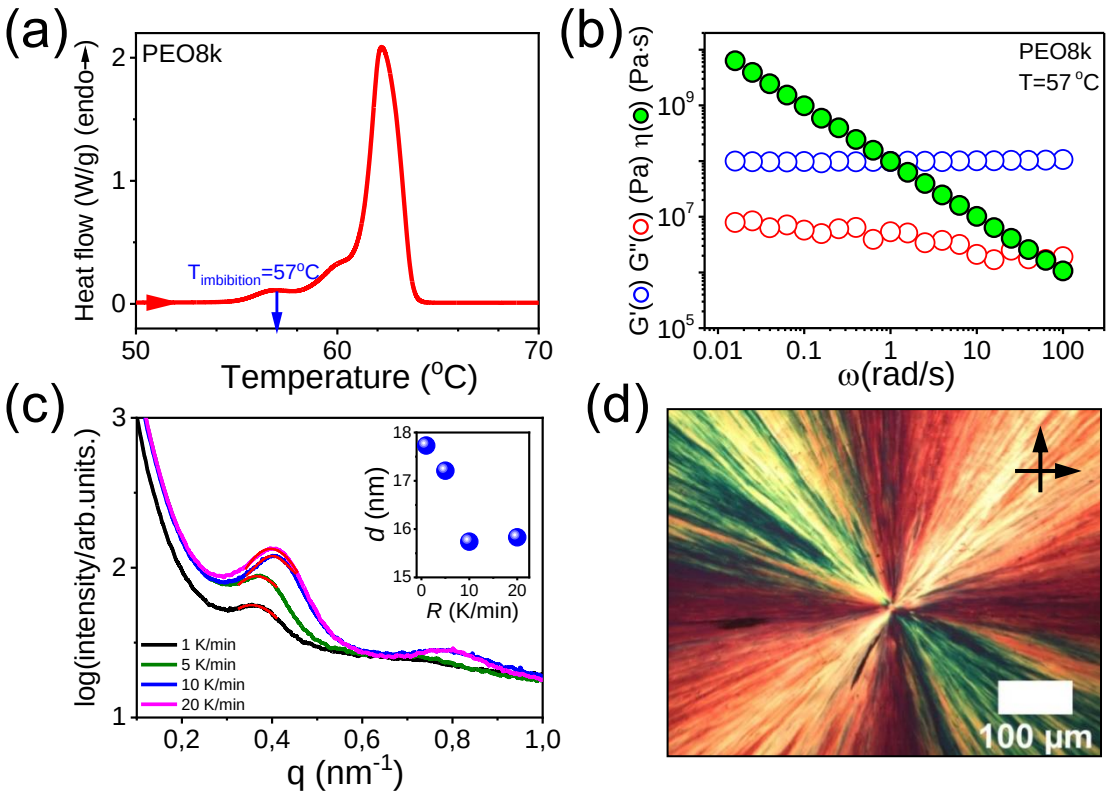

Figure 50. Thermodynamic, rheological and crystallization behavior of bulk is PEO8k. (a) DSC heating curve (rate = 2 K/min). The imbibition temperature is at 57 °C. (b) Storage and loss moduli and viscosity measured at the imbibition temperature (T = 57 °C). (c) SAXS curves indicating the domain spacing (d) under different cooling rates. (d) Spherulitic superstructure at room temperature after annealing at T = 75 °C for 2 minutes.

Following a 28-days imbibition at 57 °C, the PEO8k sample was cooled fast to room temperature. Subsequently, scanning electron microscopy (SEM) was employed to characterize the cross-section of the AAO templates. **Figure 51** shows the SEM images for the fractured surface of AAO 400 nm template. There are two important findings from SEM: (1) PEO8k clearly enters into the nanopores at a temperature located some 5°C below the melting temperature (*i.e.*, $T_{imbibition}$ = 57°C < T_{melt} = 62°C) with an approximate imbibition length of 800 nm. (2) There exists a

meniscus at the growth front of PEO 8k. The meniscus provides a direct proof of capillary force. Besides, the concave meniscus implies that the adhesion force between polymer and AAO wall is stronger than the cohesive force between the polymer chains. The successful imbibition was demonstrated for PCL8.9k as well (**Figure S2**). Both cases prove that capillary force is strong enough to drag the polymer crystals in the nanopores at a temperature below T_m. (To characterize the morphology of infiltrated polymers, atomic force microscopy (AFM) with nanometer resolution was employed.)

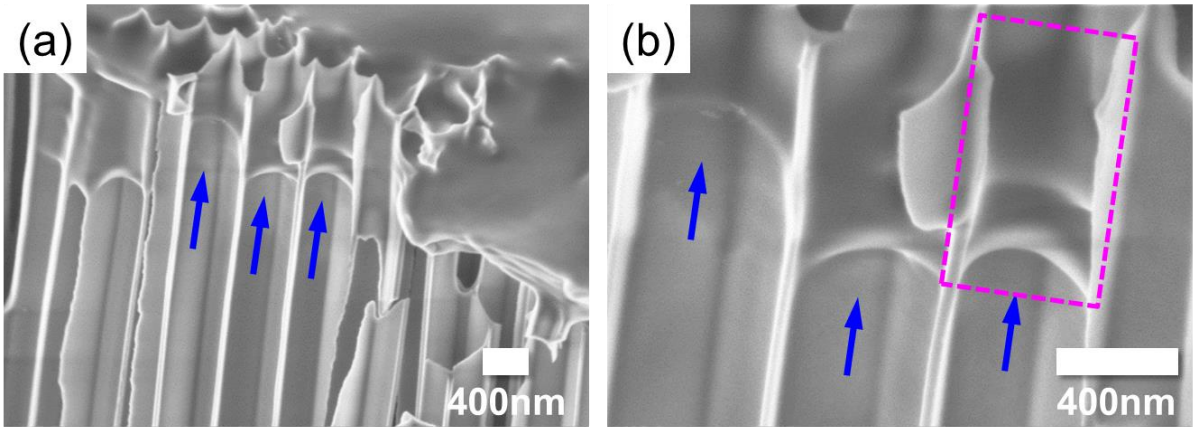

Figure 51. Scanning electron microscopy (SEM) pictures for the fractured surface of AAO 400nm nanopores with PEO8k infiltrated at T = 57 ºC for 28 days. (b) is zoom-in for (a). Blue arrows indicate the meniscus of PEO8k inside the nanopores.

We can obtain an estimate of the effective viscosity during imbibition, η_{eff}, of PEO by employing the Lucas-Washburn equation applicable to Newtonian liquids. We use $h(t)$ is the imbibition length (h = 800 nm), γ (~0.029 N/m), and an advancing contact angle of $\theta \sim 44^o$, R is the pore radius (200nm) and t is the imbibition time ($t \sim 2\times10^6$ s). This results to an effective viscosity of 8×10^9 Pa·s. This should be contrasted with the PEO8k bulk viscosity in crystalline and melt states, respectively. At a shear rate of $\dot{\gamma} = v/R \cong 10^{-6}$ s^{-1} (v is the imbibition speed obtained as $v = dh/dt \sim 3\times10^{-13}$ m/s) applicable during imbibition, the bulk viscosity at 57ºC (crystalline state) is higher (10^{10} Pa·s). On the other hand, the zero-shear viscosity in the melt state, η_0, has a much lower value (2×10^3 Pa·s). Evidently, the semicrystalline polymer flows within the nanotubes with a viscosity between the bulk values of crystalline and melt states, *i.e.*, η_{melt} (2×10^3 Pa·s) < η_{eff} (8×10^9 Pa·s) < $\eta_{crystal}$ (above 10^{10} Pa·s). The result suggests that during imbibition part of the semicrystalline chains are molten and show a lower overall viscosity.

This unanticipated point needs further investigation by other techniques. For example AFM on fractured surface combined with FTIR that can probe the stretching vibrational bands of PEO is required. This is expected to address the question of the state of polymer morphology (crystalline vs. amorphous) within the nanopores. Experiments in this direction are planned for the near future in our laboratory.

Supporting Information

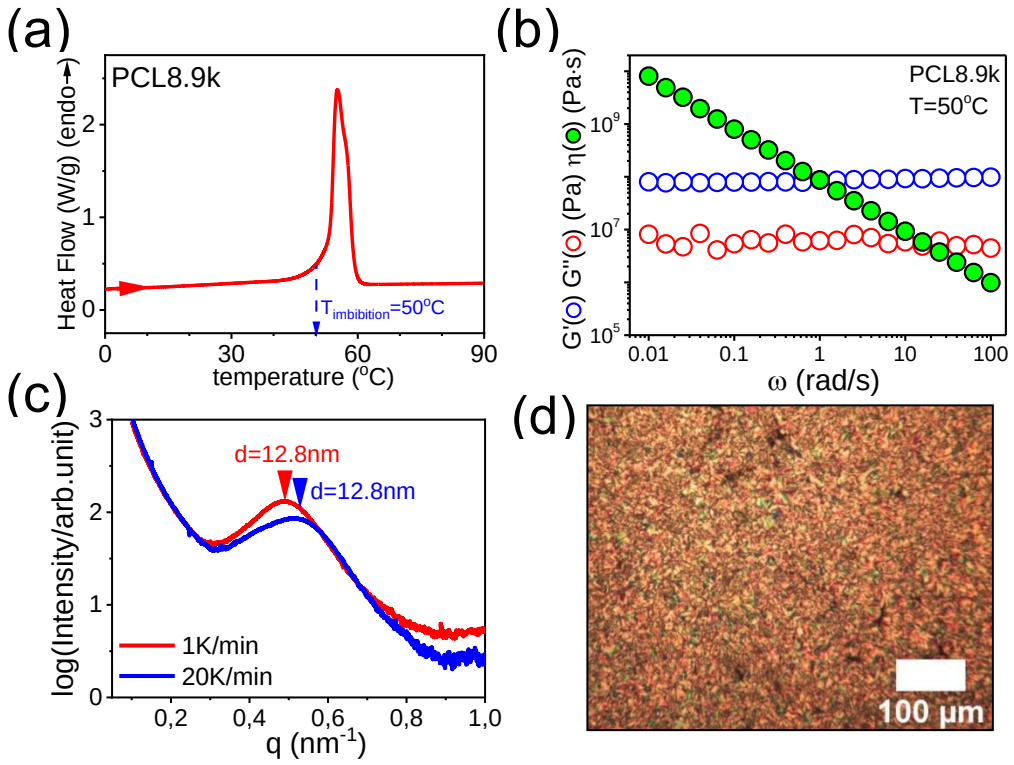

Figure S1. Thermodynamic, rheological and crystallization behavior of bulk is PCL8.9k. (a) DSC heating curve (rate = 2 K/min). The imbibition temperature is at 50 ºC. (b) Storage and loss moduli and viscosity measured at the imbibition temperature (T = 50 ºC). (c) SAXS curves indicating the domain spacing (d) under different cooling rates. (d) Spherulitic superstructure at room temperature after annealing at T = 75 ºC for 2 minutes.

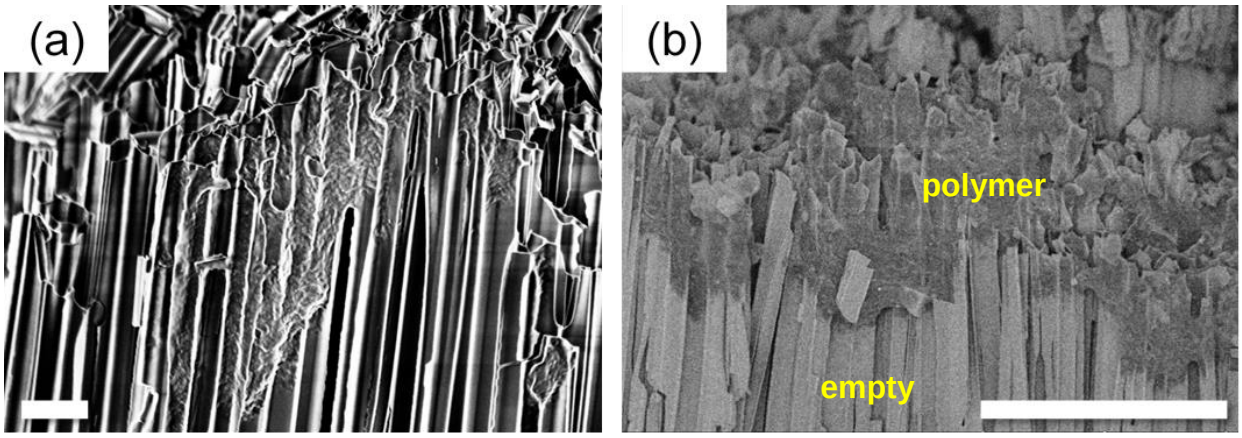

Figure S2. (a) SEM and (b) high-angle back scattering electron (HA-BSE) pictures for the cross-section of AAO 400nm nanopores with PCL8.9k infiltrated at T = 50 ^{o}C for 51days. White scale bar is 1 μm.

1.4 References

(1) Staudinger, H. Ueber Polymerisation. *Ber.Dtsch. Chem. Ges.* **1920**, *53*, 1073-1085.

(2) Doi, M.; Edwards, S.F. *The Theory of Polymer Dynamics*. Oxford University Press: **1988**.

(3) Rubinstein, M. and Colby, R.H. *Polymer Physics*. New York: Oxford University Press: **2003**.

(4) De Gennes, P.-G.; Gennes, P.-G. *Scaling Concepts in Polymer Physics*; Cornell university press: **1979**.

(5) Vaca Chávez, F.; Saalwächter, K. Time-domain NMR observation of entangled polymer dynamics: Universal behavior of flexible homopolymers and applicability of the tube model. *Macromolecules* **2011**, *44* (6), 1549-1559.

(6) Ferry, J.D. *Viscoelastic Properties of Polymers*. John Wiley & Sons: **1980**.

(7) Kremer, F.; Schönhals, A. (eds.) *Broadband Dielectric Spectroscopy*. Springer Science & Business Media: **2003**.

(8) Watanabe, H. Viscoelasticity and dynamics of entangled polymers. *Prog. Polym. Sci.***1999**, *24* (9), 1253-1403.

(9) Scheutjens, J.M.H.M.; Fleer, G.J. Statistical theory of the adsorption of interacting chain molecules. 2. Train, loop, and tail size distribution. *The Journal of Physical Chemistry* **1980**, *84* (2), 178-190.

(10) Granick, S. Perspective: kinetic and mechanical properties of adsorbed polymer layers. *Eur. Phys. J.E.* **2002**, *9*, 421−424.

(11) Kremer, F. (Ed.) *Dynamics in Geometrical Confinement*. Springer: **2016**.

(12) Alexandris, S.; Papadopoulos, P.; Sakellariou, G.; Steinhart, M.; Butt, H. J.; Floudas, G. Interfacial energy and glass temperature of polymers confined to nanoporous alumina. *Macromolecules* **2016**, *49* (19), 7400-7414.

(13) Talik, A.; Tarnacka, M.; Grudzka-Flak, I.; Maksym, P.; Geppert-Rybczynska, M.; Wolnica, K.; Kaminska, E.; Kaminski, K.; Paluch, M. The role of interfacial energy and specific interactions on the behavior of poly (propylene glycol) derivatives under 2D confinement. *Macromolecules* **2018**, *51* (13), 4840-4852.

(14) Politidis, C.; Alexandris, S.; Sakellariou, G.; Steinhart, M.; Floudas, G. Dynamics of entangled cis-1, 4-polyisoprene confined to nanoporous alumina. *Macromolecules* **2019**, *52* (11), 4185-4195.

(15) Alexandris, S.; Sakellariou, G.; Steinhart, M.; Floudas, G. Dynamics of unentangled cis-1, 4-polyisoprene confined to nanoporous alumina. *Macromolecules* **2014**, *47* (12), 3895-3900.

(16) Tarnacka, M.; Wojtyniak, M.; Brzózka, A.; Talik, A.; Hachuła, B.; Kamińska, E.; Sulka, G.D.; Kaminski, K.; Paluch, M. Unique behavior of poly (propylene glycols) confined within alumina templates having a nanostructured interface. *Nano letters* **2020**, *20* (8), 5714-5719.

(17) Tarnacka, M.; Kaminski, K.; Mapesa, E. U.; Kaminska, E.; Paluch, M. Studies on the Temperature and Time Induced Variation in the Segmental and Chain Dynamics in Poly (propylene glycol) Confined at the Nanoscale. *Macromolecules* **2016**, 49 (17), 6678-6686.

(18) Tarnacka, M.; Madejczyk, O.; Kaminski, K.; Paluch, M. Time and temperature as key parameters controlling dynamics and properties of spatially restricted polymers. *Macromolecules* **2017**, 50 (13), 5188-5193.

(19) Tarnacka, M.; Talik, A.; Kamińska, E.; Geppert-Rybczyńska, M.; Kaminski, K.; Paluch, M. The Impact of Molecular Weight on the Behavior of Poly (propylene glycol) Derivatives Confined within Alumina Templates. *Macromolecules* **2019**, 52 (9), 3516-3529.

(20) Adrjanowicz, K.; Winkler, R.; Chat, K.; Duarte, D.M.; Tu, W.; Unni, A.B.; Paluch, M.; Ngai, K.L. Study of increasing pressure and nanopore confinement effect on the segmental, chain, and secondary dynamics of poly (methylphenylsiloxane). *Macromolecules* **2019**, *52* (10), 3763-3774.

(21) Li, L.; Zhou, D.; Huang, D.; Xue, G. Double glass transition temperatures of poly (methyl methacrylate) confined in alumina nanotube templates. *Macromolecules* **2014**, *4* (1), 297-303.

(22) Li, L.; Chen, J.; Deng, W.; Zhang, C.; Sha, Y.; Cheng, Z.; Xue, G.; Zhou, D. Glass transitions of poly (methyl methacrylate) confined in nanopores: conversion of three-and two-layer models. *The Journal of Physical Chemistry B* **2015**, *119* (15), 5047-5054.

(23) Martin, J.; Krutyeva, M.; Monkenbusch, M.; Arbe, A.; Allgaier, J.; Radulescu, A.; Falus, P.; Maiz, J.; Mijangos, C.; Colmenero, J.; Richter, D. Direct observation of confined single chain dynamics by neutron scattering. *Physical review letters* **2010**, *104* (19), 197801.

(24) Krutyeva, M.; Wischnewski, A.; Monkenbusch, M.; Willner, L.; Maiz, J.; Mijangos, C.; Arbe, A.; Colmenero, J.; Radulescu, A.; Holderer, O.; Ohl, M. Effect of nanoconfinement on polymer dynamics: surface layers and interphases. *Physical review letters* **2013**, *110* (10), 108303.

(25) Krutyeva, M.; Pasini, S.; Monkenbusch, M.; Allgaier, J.; Maiz, J.; Mijangos, C.; Hartmann-Azanza, B.; Steinhart, M.; Jalarvo, N.; Richter, D. Polymer dynamics under cylindrical confinement featuring a locally repulsive surface: A quasielastic neutron scattering study. *The journal of chemical physics* **2017**, *146* (20), 203306.

(26) Franz, C.; Lange, F.; Golitsyn, Y.; Hartmann-Azanza, B.; Steinhart, M.; Krutyeva, M.; Saalwächter, K. Chain dynamics and segmental orientation in polymer melts confined to nanochannels. *Macromolecules* **2016**, *49* (1), 244-256.

(27) Lucas, R. Ueber das Zeitgesetz des Kapillaren Aufstiegs von Flüssigkeiten. Colloid Polym. Sci. **1918**, *23*, 15-22.

(28) Shin, K.; Obukhov, S.; Chen, J.T.; Huh, J.; Hwang, Y.; Mok, S.; Dobriyal, P.; Thiyagarajan, P.; Russell, T.P. Enhanced mobility of confined polymers. *Nature materials* **2007**, *6* (12), 961-965.

(29) Yao, Y.; Alexandris, S.; Henrich, F.; Auernhammer, G.; Steinhart, M.; Butt, H.-J.; Floudas, G. Complex dynamics of capillary imbibition of poly(ethylene oxide) melts in nanoporous alumina. *J. Chem. Phys.* **2017**, *146* (20), 203320.

(30) Yao, Y.; Butt, H.-J.; Floudas, G.; Zhou, J.; Doi, M. Theory on capillary filling of polymer melts in nanopores. *Macromol. Rapid Commun.* **2018**, *39*, 1800087.

(31) Yao, Y.; Butt, H.-J.; Zhou, J.; Doi, M.; Floudas, G. Capillary imbibition of polymer mixtures in nanopores. *Macromolecules* **2018**, *51*, 8755-8764.

(32) Serghei, A.; Chen, D.; Lee, D. H.; Russell, T. P. Segmental dynamics of polymers during capillary flow into nanopores. *Soft Matter* **2010**, 6, 1111-1113.

(33) Serghei, A.; Lutkenhaus, J. L.; Miranda, D. F.; McEnnis, K.; Kremer, F.; Russell, T. P. Density fluctuations and phase transitions of ferroelectric polymer nanowires. *Small* **2010**, *6* (16), 1822-1826.

(34) Serghei, A.; Zhao, W.; Wei, X.; Chen, D.; Russell, T. P. Nanofluidics with phase separated block-copolymers: glassy dynamics during capillary flow. *Eur. Phys. J. Special Topics* **2010**, *189*, 95-101.
(35) Serghei, A.; Zhao, W.; Miranda, D.; Russell, T. P. Curie transitions for attograms of ferroelectric polymers. *Nano Lett.* **2013**, *13*, 577-580.
(36) Adachi K.; Kotaka, T. Dielectric normal mode relaxation. *Prog. Polym. Sci.* **1993**, *18*, 585.
(37) Adachi K.; Kotaka, T. Dielectric normal mode process in undiluted cis-polyisoprene, *Macromolecules* **1985**, *18*, 466.
(38) Boese, D.; Kremer, F.; Fetters, L.J. Molecular dynamics in linear and multiarmed star polymers of cis-polyisoprene as studied by dielectric spectroscopy. *Macromolecules* **1990**, *23*, 1826.
(39) Boese, D.; Kremer, F. Molecular dynamics in bulk cispolyisoprene as studied by dielectric spectroscopy. *Macromolecules* **1990**, *23*, 829.
(40) Schönhals, A. Relation between main and normal mode relaxations for polyisoprene studied by dielectric spectroscopy. *Macromolecules* **1993**, *26*, 1309.
(41) Floudas, G.; Gravalides, C.; Reisinger, T.; Wegner, G. Effect of pressure on the segmental and chain dynamics of polyisoprene. Molecular weight dependence, *J. Chem. Phys.* **1999**, *111*, 9847.
(42) Floudas, G.; Paraskeva, S.; Hadjichristidis, N.; Fytas, G.; Chu, B.; Semenov, A.N. Dynamics of polyisoprene in star block copolymers confined in microstructures: A dielectric spectroscopy study. *J. Chem. Phys.* **1997**, *107*, 5502.
(43) Petychakis, L.; Floudas, G.; Fleisher, G. Chain dynamics of polyisoprene confined in porous media. A dielectric spectroscopy study, *Europhys. Lett.* **1997**, *40*, 685.
(44) De Gennes, P. G. Polymer solutions near an interface. Adsorption and depletion layers. *Macromolecules* **1981**, *14*, 1637− 1644.
(45) De Gennes, P. G. Polymers at an interface; a simplified view. *Adv. Colloid Interface Sci.* **1987**, *27*, 189−209.
(46) Semenov, A. N.; Joanny, J.-F. Kinetics of adsorption of linear homopolymers onto flat surfaces: Rouse dynamics. *J. Phys. II* **1995**, *5*, 859−876.
(47) Mark, J.E. ed. *Physical Properties of Polymers Handbook*. New York: Springer: **2007**.

Chapter 2. *In Situ* Monitoring the Imbibition of Poly(*n*-butyl methacrylate) in Nanoporous Alumina by Dielectric Spectroscopy.

This chapter has been published as a research paper in *Macromolecules*.

Chien-Hua Tu, Martin Steinhart, Hans-Jürgen Butt, and George Floudas
Macromolecules 52, 8167-8176 (2019)
DOI: 10.1021/acs.macromol.9b01383

Abstract

The imbibition dynamics of poly(*n*-butyl methacrylate) (PnBMA) in nanoporous alumina is studied by *in situ* dielectric spectroscopy at temperatures in the range 30-50 K above the glass temperature. A model provides the imbibition length from the measured dielectric strength of the segmental process. The relaxation times of the segmental process during imbibition are isochronal, except at early stages where a speed-up is observed. Furthermore, as polymer segments flow inside the pores, the distribution of relaxation times remain constant (Havriliak-Negami shape parameters similar to the bulk). Imbibition at longer length scales associates with the effective viscosity of the chains and provides a stringent test of the Lucas-Washburn equation applicable to Newtonian liquids. The equation fails to describe the imbibition process because the prefactor to the $t^{1/2}$ (t; time) dependence does not adequately describe the process. Imbibition of polymer blends composed of long and short chains reveals the enrichment of the pores by the shorter chains by their faster imbibition with possible application in fractionation.

2.1. Introduction

The behavior of polymer chains moving inside porous materials is important for many applications, ranging from gel permeation chromatography, filtration, heterogeneous catalysis, oil recovery, and so on. When a polymer melt gets into contact with the opening of a narrow pore, the capillary force is strong and drags the chains into the pore. The imbibition process for Newtonian liquids penetrating a cylindrical capillary is relatively simple and follows the Lucas-Washburn equation (LWE)[1,2]:

$$h(t) = \left(\frac{\gamma R cos\theta}{2\eta}\right)^{\frac{1}{2}} \sqrt{t} \qquad (1)$$

Here, $h(t)$ is the penetration depth/length of the liquid meniscus, R is the capillary radius, γ is the surface tension, θ is the advancing contact angle, η is the viscosity and t is the wetting time. Experiments, however, have shown that capillary imbibition of polymer melts into narrow pores deviate from the LWE.[3-6] In this endeavor, self- ordered nanoporous aluminum oxide (AAO) templates that contain arrays of discrete-isolated, parallel cylindrical nanopores that are uniform in length and diameter offer an ideal confining medium for testing the LWE predictions.[7-10]

Concerted efforts by theory[11,12] and experiment[3-6] have addressed the way that entangled polymers penetrate in nanopores. Deviations from the LWE were found when the nanopores were infiltrated with entangled polystyrene (PS)[3], polyethylene (PE)[4] and poly(ethylene oxide) (PEO)[5]. In the former *in situ* investigation an enhanced mobility was concluded on the basis of changes in the X-ray scattering invariant during capillary flow, resulting in a weak molecular weight dependence for the viscosity ($\eta \sim N^{1.4}$). More recent experiments from our group[5] performed on entangled PEO with *ex situ* reflection optical microscopy demonstrated the validity of $t^{1/2}$ dependence (in fact, any process that starts fast and slows down subsequently could be described by the law) but contradicted the prediction of the classical Lucas–Washburn equation with respect to the prefactor. A reversal in imbibition dynamics with polymer molecular weight was found. Shorter chains (with 50 entanglements or fewer) showed a *slower* capillary rise than theoretically predicted as opposed to chains with more entanglements that display a *faster* capillary rise. The net effect was to produce an effective viscosity that scaled as $\eta \sim N^1$ (instead of the expected $\eta \sim N^{3.4}$ for entangled polymers).[5] Subsequently, a unified theory[12] for the imbibition dynamics of entangled polymer melts into nanopores was proposed. The theory considered the

competition between two mechanisms: one is the standard hydrodynamic flow, resulting in a parabolic flow profile. Under conditions of strong attractions between the walls and the polymer, a layer of immobile chains is created (dead layer), resulting in an increase of the effective viscosity and hence to slower imbibition. The other is the reptation model, leading to a plug flow profile and to the reduction in the effective viscosity (faster imbibition). Subsequent studies[13,14] explored the possibility of separating long from short polymer chains by the difference in imbibition speeds within narrow pores. It was demonstrated that the faster imbibition of shorter chains in miscible blends is an effective mechanism for separating long from short polymer chains (*e.g.*, fractionation) with possible application as separation membranes.

An advancement in studying polymer imbibition *in situ* has been the so-called, *nanofluidic* method.[15-19] The method employs the same AAO templates sputtered with a thin gold layer to transform the membranes into capacitors where an ac field is applied along the pore axes. As the capillary force drives the polymer chains into the pores it increases the capacitance, *C*, by way of the dielectric permittivity of the penetrating polymer ($C = \varepsilon\varepsilon_f A/d$; where ε is the permittivity of the polymer, ε_f is the permittivity in free space, A is the area, and d the polymer thickness). The method offers simultaneous access to (i) the molecular dynamics during flow at the segmental and possibly the chain length scales and (ii) the kinetics of imbibition. The first report on polymer imbibition by the nanofluidic method concerned the segmental dynamics of poly(2-vinyl pyridine) in AAO with pore diameters from 200 nm down to 18 nm at imbibition temperatures from 40 to 63 K above T_g.[19] On the basis of the absence of any shift in the segmental process relative to the bulk, the authors concluded that any change in the dynamics due to interfacial interactions should take place on length scales much shorter than the pore diameter. Similar conclusions were obtained for the poly(4-vinylpyridine) segmental relaxation in the diblock copolymer polystyrene-*b*-poly(4-vinylpyridine) (PS-*b*-P4VP).[17] These observations are not in line with literature – some with polymers confined within the same AAO templates – revealing moderate to larger shifts in the glass temperature.[20,21] These shifts were discussed in terms of the variable polymer/AAO wall interfacial energy.[22] Evidently, this point needs clarification.

On the other hand, the kinetics of capillary imbibition into AAO nanopores are much less investigated by the nanofluidic approach. Two reports examined a PS homopolymer and a block copolymer based on poly(vinylidenefluoride-*co*-trifluoroethylene) (P(VDF-*b*-TrFE))[19]. In both

cases the imbibition length was found to scale as $t^{1/2}$. However, the effective viscosity experienced by the polymer during flow was not extracted, and this precluded a stringent test of the applicability of the Lucas-Washburn equation at the nanoscale.

The present study explores the details of the imbibition process by the nanofluidic approach by employing poly(*n*-butyl methacrylate) (PnBMA). The polymer has a convenient T_g, around ambient temperature, and a strong dipole moment at the segmental level.[23] The aim of the study is threefold: first, to construct a model that provides the imbibition length directly from the dielectric measurements; secondly, to access the segmental dynamics (relaxation times and distribution of relaxation times) during flow as a function of pore size and temperature; third, to provide a stringent test of the Lucas-Washburn equation by extracting the effective viscosity during the flow process in comparison to the bulk. In a separate investigation, we followed the imbibition of PnBMA blends composed of short and long chains, aiming at fractionation. The results demonstrate the potential of the method to extract *quantitative* information about the imbibition process *in situ* both on the segmental length scale and at longer length scales associated with the viscosity experienced by the polymer during flow.

2.2. Experimental

AAO Templates. Self-ordered AAO (pore diameters of 25, 35, 65, and 400 nm; pore depth about 100 μm) was prepared by following previously reported procedures.[7-9] In addition, the templates were characterized for conicity. Experiments using the focused ion beam method revealed a small decrease in pore diameter from the top to the bottom. For investigating the effect of trapped air within the AAO nanochannels two types of AAO templates were investigated. The first type of AAO templates had pores with closed ends. The AAO layers were attached to 900 μm thick aluminum substrates that served as the lower electrode. As second type we used freestanding AAO membranes with pores open at the top and bottom surfaces. We etched the aluminium substrates, to which the as-anodized AAO layers were attached, with a solution of 1.7 g $CuCl_2 \cdot 2\ H_2O$ in 50 mL 37 % HCl and 50 mL of deionized water cooled to 0° C. Then, the pore bottoms, which were still closed by the so-called barrier oxide, were opened by treatment with 10 % H_3PO_4 at 30° C. All etching steps were performed in such a way that the interior of the AAO pores was protected from the etching solutions. Prior to infiltration, all AAO templates were placed in an oven under

vacuum at a temperature of 443 K for 8-10 h. This procedure is essential here as it removes the majority of OH groups from the AAO surface.

Samples. Two poly(*n*-butyl methacrylate) homopolymers with narrows polydispersities were purchased from PSS Polymer Standards Service GmbH and used without further purification. Their molecular characteristics as obtained by GPC/SEC are shown in Table 1. Blends of the two homopolymers as PnBMA 5.5k/PnBMA 100k, with compositions B1 (75/25), B2 (50/50), B3 (25/75), were prepared and investigated in the second part of this study.

Table 1. Molecular characteristics of the poly(*n*-butyl methacrylate) samples.

Sample	M_n (g/mol)	M_w (g/mol)	$Đ$ (M_w/M_n)
PnBMA 5.5k	4950	5490	1.11
PnBMA 100k	104000	110000	1.06

Differential Scanning Calorimetry (DSC). DSC measurements were made with a Mettler Toledo (DSC-822) calorimeter. The glass temperatures of the homopolymer and their blends were obtained from the second heating run with a rate of 10 K/min.

Surface tension. Literature values of surface tension for a PnBMA sample with a viscosity-average molecular weight of 37000 g/mol measured by the pendant drop method were employed ($\gamma = 31.2 - 0.059\ (t - 20)$; γ in mN/m; t in ^{0}C).[24] Another report for a PnBMA sample with weight-averaged molecular weight of 180000 g/mol suggested $\gamma = 28.8 \pm 0.5$ mN/m.[25]

Contact angle. The advancing contact angles of the solid polymers were measured by placing nearly spherical polymer particles of ~ 1mm diameter onto the substrate and heating to 343 K. To form spherical particles, around 1 mg of sample was placed on a soot-templated superamphiphobic surface. The sample was heated and kept at 343 K for 24 h under vacuum to form a spherical shape caused by the surface tension of the polymer. Subsequently, the polymer sphere was slowly cooled and transferred onto an electropolished Al disk coated by a thin native oxide layer. The latter comprises a flat model surface that mimics the AAO surface. XPS was used to determine the

surface composition, and the results are shown in **Figure S1**, **Supporting Information**. The advancing contact angle of the homopolymer PnBMA 5.5k and the blends B1 and B2 was measured during spreading onto the substrate at different temperatures in the range from 323- 343 K with a commercial goniometer (OCA35, Dataphysics). For the PnBMA 100k and the blend B3 the advancing contact angle was very high at 343 K.

Dielectric Spectroscopy (DS). DS measurements in the bulk were performed at different temperatures in the range from 273 K to 413 K, at atmospheric pressure, and for frequencies in the range from 10^{-2} to 10^{7} Hz. Measurements were made with a Novocontrol Alpha frequency analyzer composed of a broadband dielectric converter and an active sample hand. For bulk PnBMA, the DS measurements were performed in the usual parallel plate geometry with electrodes of 20 mm in diameter and a sample thickness of 50 μm maintained by Teflon spacers. For the imbibition kinetic experiments a gold layer (diameter 8.4 mm; thickness 35 nm) was sputtered on top of the AAO template serving as the upper electrode whereas the aluminum substrate of AAO templates served as the lower electrode.[20-22] Additional experiments were made on templates with both ends open. In this case, a gold layer was sputtered on both surfaces. In the kinetic experiments the investigated frequency range was limited to 1-10^6 Hz to facilitate probing of the faster kinetics. In all cases, the complex dielectric permittivity $\varepsilon^* = \varepsilon' - i\varepsilon''$, where ε' is the real and ε'' is the imaginary part, was obtained as a function of frequency ω and temperature T, *i.e.*, $\varepsilon^*(T, \omega)$. **Figure S2**, **Supporting Information** provides fitting examples for bulk PnBMA by using the empirical equation of Havriliak and Negami (HN):[26,27]

$$\varepsilon^*_{HN}(\omega, T) = \varepsilon_\infty(T) + \sum_{k=1}^{2} \frac{\Delta\varepsilon_k(T)}{\left[1+\left(i\omega\tau_{HN,k}(T)\right)^{m_k}\right]^{n_k}} + \frac{\sigma_0(T)}{i\varepsilon_f\omega} \qquad (2)$$

Here, k indicates the process under investigation, $\Delta\varepsilon_k(T)$ is the relaxation strength, $\tau_{HN,k}$ is the relaxation time of the equation, m_k and n_k ($0 < m_k$, $m_k n_k \leq 1$) describe the symmetrical and asymmetrical broadening of the distribution of relaxation times, and ε_∞ is the dielectric permittivity at the limit of high frequencies. The relaxation times at maximum loss (τ_{max}) are presented herein and have been analytically obtained from the Havriliak−Negami equation as follows:

$$\tau_{max,k} = \tau_{HN,k} \sin^{-1/m}\left(\frac{\pi m_k}{2(1+n_k)}\right) \sin^{1/m}\left(\frac{\pi m_k n_k}{2(1+n_k)}\right) \qquad (3)$$

At lower frequencies, ε'' rises due to the conductivity ($\varepsilon'' = \sigma/(\omega\varepsilon_f)$, where σ is the dc conductivity and ε_f the permittivity of free space). The conductivity contribution has also been taken into account during the fitting process.

Rheology. The viscosities of the homopolymers and their blends were measured by a shear rheometer (ARES). Measurements were made with the environmental test chamber as a function of temperature in the respective ranges from 288 to 353 K (PnBMA 5.5k), from 298 K to 393 K (PnBMA 100k), 338 K to 403 K (B1), 333 K to 403 K (B2) and 303 K to 403 K (B3). Samples were prepared on the lower plate of the 8 and 25 mm diameter parallel plate geometry. The upper plate was brought into contact, the gap thickness was adjusted, and the sample was cooled. The storage (G') and loss (G'') shear moduli were monitored as a function of frequency, ω, for frequencies in the range from $10^{-2} < \omega < 10^{2}$ rad/s. All measurements refer to the linear viscoelastic range. Subsequently, the complex viscosity (η^*) follows as $\eta^* = G''/\omega - iG'/\omega$. Master curves at the same reference temperature (the imbibition temperature, T = 343 K) were made by use of the time-temperature superposition principle (tTs). The latter allows the frequency ω dependence of the complex modulus G^* at any temperature T to be determined from a master curve at a reference temperature. At each temperature T, a single frequency-scale shift factor a_T allow superposition of all viscoelastic data at temperature T with the data at the reference temperature, T_{ref}, as: $G^*(\omega;T) = G^*(a_T\omega;T_{ref})$. Master curves of the storage, the loss moduli, and the shear viscosity are shown in **Figure S3**, all at the same reference temperature of 343 K. The shift factors a_T and WLF coefficients (C_1^0, C_2^0 at the reference temperature) are shown in **Figure S4**. The zero shear viscosities at the reference temperature are included in **Table 3**.

2.3. Results and discussion

Extracting the imbibition length from dielectric measurements

For *in situ* monitoring the imbibition process, AAO templates were sputtered with a gold layer (thickness ~ 35 nm) serving as the upper electrode. Following sputtering, the AAO templates were characterized by SEM, indicating a uniform gold layer on the top surface. This procedure inevitably produced some small gold aggregates deposited below the pore openings in a maximum depth of about 380 nm (SEM image shown in **Figure S6**). Given the long pores, any inhomogeneities in the field lines are minor for the long nanochannels employed herein. An ac

field is applied between the two electrodes within a frequency/temperature range suitable to the specific polymer. Figure 1 shows the geometry of the Au-sputtered AAO templates with the infiltrated polymer and trapped air at the bottom of the channels.

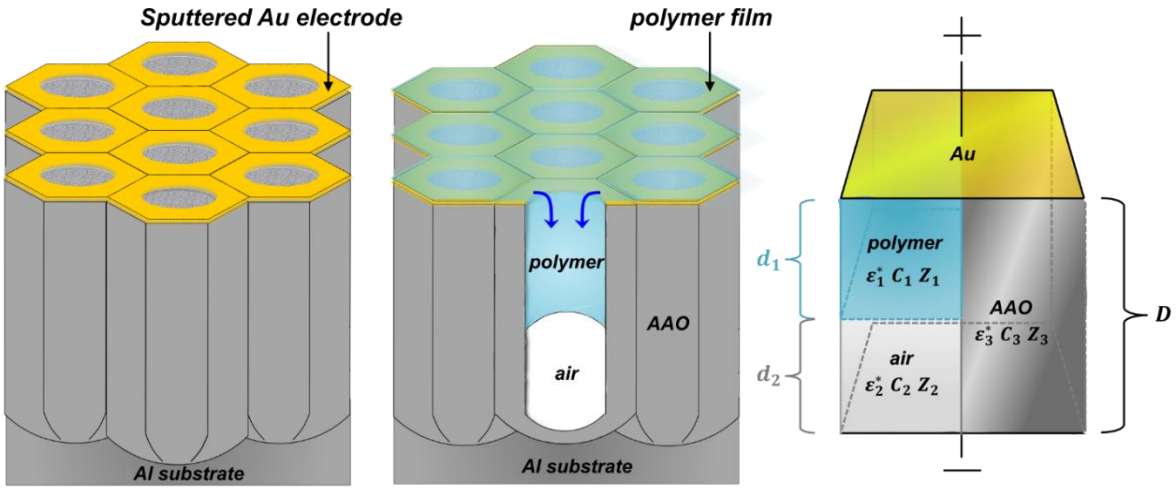

Figure 1. Schematic illustration of the experimental setup showing (left) an empty AAO template (sputtered with a gold layer on top). (middle) On top of the sputtered electrode a polymer film is placed (shown in blue) at the preselected temperature, and the imbibition process is initiated. (right) The corresponding equivalent circuit. Parameters ε_1^*, ε_2^*, ε_{12}^*, and ε_3^* refer respectively to the permittivities of the polymer layer, the entrapped air, the polymer/air composite and the AAO; C_1, C_2, C_{12},and C_3 are the respective capacitances and d_1, d_2, and D are the lengths of the pores comprising the polymer, air and AAO.

The scheme depicts the polymer melt advancing into the pores by pure capillary action (without the presence of a precursor film) as evidenced by independent SEM images of intermediate stages of the imbibition process (**Figure S7**, **Supporting Information**). The image shows the presence of a meniscus at the tip of the advancing polymer signifying the presence of a contact angle between the polymer melt and the inner cylindrical pore.

The experimental setup offers two ways of extracting the imbibition length, d_1, *in situ*. The first one is based on the growing dielectric strength of the segmental process. As an example, **Figure 2** shows the evolution of the dielectric loss curves and the associated Havriliak-Negami parameters (shape parameters, relaxation time at maximum loss, and dielectric strength, all associated with the segmental process) when a PnBMA 5.5 film is placed on top of an empty AAO template. Here the dielectric loss curve of the empty template is used as a background and is

subtracted from all other curves. Applying a single HN function to the dielectric loss curves results to the parameters plotted in the Figure 2. The dielectric strength increases fast in the beginning and later slows down typically as $t^{1/2}$. Subsequently, values of $\Delta\varepsilon$ are converted into imbibition lengths by *ex situ* measurement of the capillary height by reflection optical microscopy. This is conceivable as the dielectric strength is proportional to the number density of dipoles that is increasing with imbibition time ($\Delta\varepsilon = \varepsilon'_S - \varepsilon_\infty \sim \frac{1}{3\varepsilon_o}\frac{\mu^2}{k_B T}\frac{N_0}{V}$, where N_o/V is the number density of dipoles and μ is the dipole moment).

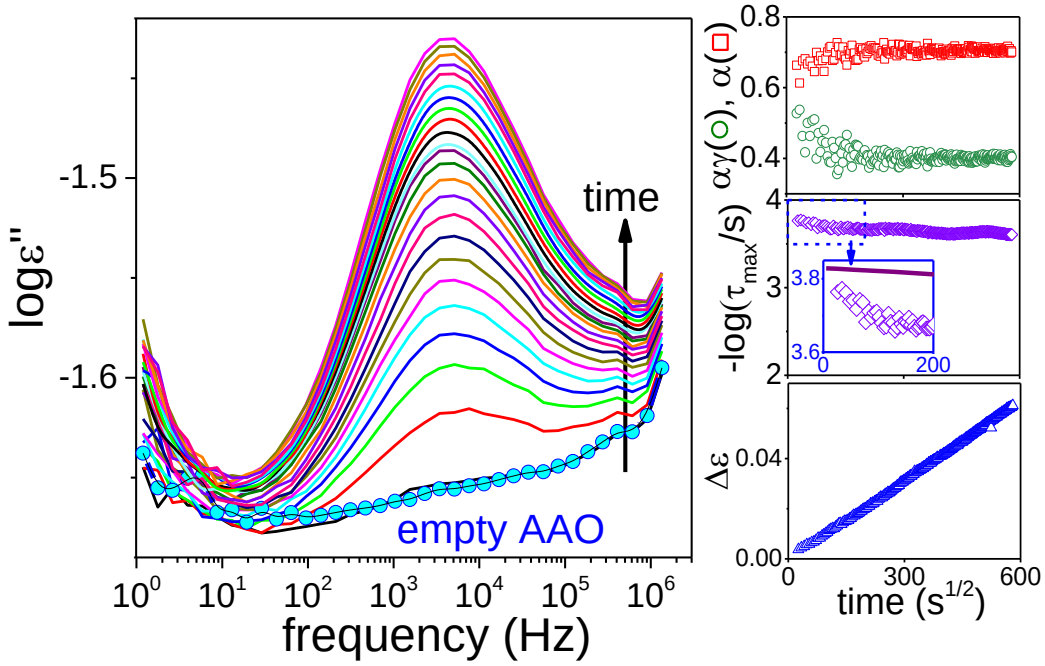

Figure 2. (left) Evolution of the dielectric loss curves for PnBMA 5.5k entering AAO nanopores with pore diameter of 65 nm at 333 K. The signal from the empty AAO template is shown under the same conditions with blue spheres. The vertical arrow indicates increasing time of imbibition. (right) Evolution of the HN shape parameters (top), of the relaxation time at maximum loss (middle), and of the dielectric strength (bottom) during the experiment plotted as a function of the square root of imbibition time. The inset in the middle shows the relaxation times at maximum loss corresponding to the initial stages of imbibition in comparison to the model predictions (Eq.6, magenta line).

The second method is based on the equivalent circuit. The geometry shown in Figure 1 can be treated equivalently as an electric circuit composed of three layers; polymer, air and AAO layers, each with its own permittivity, capacitance and length. Moreover, the polymer layer (indicated as

C_1) is connected with the air layer (indicated as C_2) in series, and this composite layer (polymer-air, C_{12}) is arranged in parallel to the AAO (C_3). In terms of the equivalent circuit,

$$\frac{1}{C_{12}} = \frac{1}{C_1} + \frac{1}{C_2} \tag{4}$$

$$\text{and} \quad C_{123} = C_{12} + C_3$$

or equivalently

$$\frac{1}{\left(\frac{\varepsilon_{12}^* A}{D}\right)} = \frac{1}{\left(\frac{\varepsilon_1^* A}{d_1}\right)} + \frac{1}{\left(\frac{\varepsilon_2^* A}{d_2}\right)} \tag{5}$$

$$\frac{\varepsilon_{123}^* A}{D} = \frac{\varepsilon_{12}^* \varphi_{12} A}{D} + \frac{\varepsilon_3^* \varphi_3 A}{D}$$

where C_{123} refers to the total capacitor. After some arrangements, we acquire the following expressions used to derive the imbibition length of the polymer as a function of time:

$$\varepsilon'_{123} - i\varepsilon''_{123} = \left\{\left[\frac{D\varepsilon'_1 d_1 + Dd_2[(\varepsilon'_1)^2 + (\varepsilon''_1)^2]}{(d_1 + d_2\varepsilon'_1)^2 + (d_2\varepsilon''_1)^2}\right]\varphi_{12} + \varepsilon'_3\varphi_3\right\} - i\left[\frac{Dd_1\varepsilon''_1\varphi_{12}}{(d_1 + d_2\varepsilon'_1)^2 + (d_2\varepsilon''_1)^2} + \varepsilon''_3\varphi_3\right] \tag{6}$$

and

$$d_1 = D\left(\frac{\varphi_{12} b}{(a)^2 + (b)^2}\right)\left(\frac{(\varepsilon'_1)^2 + (\varepsilon''_1)^2}{\varepsilon''_1}\right) \tag{7}$$

$$\text{with } a = \varepsilon'_{123} - (\varepsilon'_3)\varphi_3, \quad \text{and} \quad b = \varepsilon''_{123} - (\varepsilon''_3)\varphi_3.$$

Eq. 7 provides the polymer imbibition length, d_1, as a function of the dielectric properties of the bulk polymer (ε_1^*), the pure AAO (ε_3^*), the measured dielectric function of the composite cell (ε_{123}^*), and the porosity. The method is sensitive to the presence of a background in the pure AAO. Some simplification can result by subtracting the background contribution and subsequently employing the properties of alumina (ε_3' = 2.6; ε_3'' = 0). As for the porosity, φ_{12} ($\varphi_3 = 1 - \varphi_{12}$), we use the values obtained earlier as 0.375 (400 nm), 0.175 (65 nm), 0.0073 (35 nm) and 0.111 (25 nm).[28,29] The second method does not need a calibration measurement but requires knowledge of porosities. In general, a good agreement can be found by extracting the imbibition lengths with

the two methods (**Figure S8**) provided that the background contribution is subtracted and the porosities are known independently.

Homopolymer imbibition

Investigating the imbibition kinetics by DS requires a judicious choice of a polymer with a suitable glass temperature, T_g, and with a viscosity that is neither too low nor too high at the imbibition temperature so that the process under investigation (the segmental dynamics in this case) falls well within the experimental frequency window. PnBMA is a polymer with a convenient T_g bearing a strong dipole moment at the segmental level.[23] These dipoles are responsible for the local β-process below the dynamic T_g and the segmental α-process at higher temperatures. The former conforms to an Arrhenius T-dependence as

$$\tau = \tau_0 exp\left(\frac{E}{RT}\right) \quad (8)$$

where τ_o (= 10^{-14} s) is the relaxation time in the limit of very high temperatures and E is the activation energy. The latter conform to the Vogel-Fulcher-Tammann (VFT) dependence as

$$\tau = \tau_0 exp\left(\frac{B}{T-T_0}\right) \quad (9)$$

Here, τ_o is the relaxation time at very high temperatures, B is the activation parameter and T_o is the "ideal" glass temperature located below the conventional glass temperature. The relaxation times for these processes in the two homopolymers are depicted in **Figure 3**. At higher temperatures the two processes merge to a single process named the $\alpha\beta$-process. The relaxation times corresponding to the $\alpha\beta$-process display a temperature dependence intermediate to the β- and α-processes and have a VFT behavior.[23,30] The VFT parameters for the $\alpha\beta$-process pertinent to the current experiments are summarized in **Table 2**. The chosen temperature range used in the imbibition experiments for the PnBMA 5.5k and the blends is indicated in the Figure 3. In general, the imbibition temperature is located some 30-50 K above T_g. With this choice of temperatures the frequency range of the loss peak is positioned in the middle of the experimental frequency range.

The results of the imbibition experiments for the homopolymers can be discussed with the help of **Figure 2**. To extract the pertinent parameters to the segmental dynamics, *e.g.*, the two

shape parameters, the dielectric strength, $\Delta\varepsilon$, and the relaxation time at maximum loss, individual loss curves were corrected for the background (the latter was obtained by measuring the empty AAO template before the placement of the polymer film on top, otherwise under identical conditions). The Figure 2 shows low- and high-frequency shape parameters as well as relaxation times at longer times nearly identical to the bulk polymer. This effect, *e.g.*, the faster relaxation times at the beginning of the imbibition process, is anticipated by the equivalent circuit model. The predictions of the model (eq. 6) is included in **Figure 2** by a solid line and compared to the experimental times. Evidently, the measured segmental relaxation times exhibit a steeper dependence at short imbibition times than the theoretically predicted by the equivalent circuit. The fact that at the end of the process the segmental relaxation times are identical to the bulk might lead to the erroneous conclusion that there is little or even no effect of confinement on the polymer dynamics at the segmental level. Such a conclusion would not be in line with several experiments that have shown a speed-up of dynamics under confinement[20,22,31-36] or even a bimodal glass temperature.[21,37] Here this result is not unexpected as the imbibition temperature is located far above (typically 30-50 K) the glass temperature. On the other hand, imbibition at temperatures in the vicinity of T_g is extremely slow.

Table 2. Parameters of the VFT equation corresponding to the segmental ($\alpha\beta$) process for the two homopolymers and their blends pertinent to the imbibition experiments; T_g extracted from the α-process is also shown.

Sample	-log(τ_{max}/s)	B (K)	T_o (K)	T_g (K) (at τ=100 s)
PnBMA 5.5k	12.8	3430±10	170±1	285±1
PnBMA 100k	12.8*	3560±10	179±1	300±3
B1 (75/25)	12.8*	3480±10	172±1	288±1
B2 (50/50)	12.8*	3500±10	174±1	292±2
B3 (25/75)	12.8*	3490±10	178±1	297±2

*: value held fixed

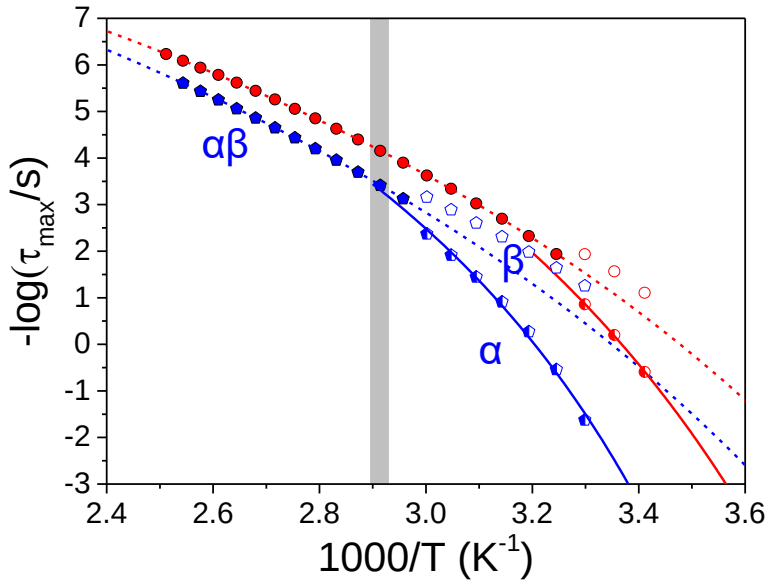

Figure 3. DS Segmental relaxation times of PnBMA 5.5k (red) and of PnBMA 100k (blue) plotted in an Arrhenius diagram. The *α*-, *β*- and *αβ*-processes are shown by half-filled, open and filled symbols, respectively. The marked area in gray indicates the temperature range used in the imbibition experiments.

To further obtain the imbibition length and extract the effective viscosity experienced by the polymer in nanopores, two parameters are needed in the LWE; the surface tension, γ, and the advancing contact angle, θ. Dynamic contact angles of PnBMA 5.5k and of the polymer blends (B1, B2 and B3) were measured at temperatures corresponding to the imbibition experiments (at 323, 333, and 343 K for the PnBMA 5.5k and at 343 K for the blends). Contact angles of highly viscous liquids need long times to equilibrate. Dynamic contact angles depend on the velocity of the three-phase contact line. In addition, the contact line velocity is strongly depending on polymer molecular weight as demonstrated by comparing the homopolymer PnBMA 5.5k with its the blends with the higher molecular weight polymer PnBMA 100k. In our imbibition experiments the relevant contact angle is the dynamic contact angle (DCA), θ_d, instead of the equilibrium one (ECA), θ_e, for the pertinent contact line velocities, v. As for the $\theta(v)$ dependence, we employed the thermodynamic theory proposed by Cox.[38] The theory emphasizes the viscous energy dissipation in the bulk and removes the singularities at the triple line by employing a microscopic slip boundary length, δ, according to:

$$\theta_d = \left(\theta_e^3 + 9A\frac{\eta}{\gamma}\upsilon\right)^{1/3} \quad (10)$$

where A=ln(R/δ), θ is expressed in rad, and υ in m/s. Representative fits to the DCA data for PnBMA 5.5k at the different temperatures investigated are given in **Figure S9**. In extracting the relevant dynamic contact angles, we have assumed $\upsilon = \partial d_1/\partial t$, where d_1 is the imbibition length. From the measured $d_1(t)$ dependence we extract the initial (υ_i) and final (υ_f) slopes and calculate the corresponding DCA from eq. 10. In comparing the experimental results with the LWE, we employ $\langle\cos\theta_d\rangle = (\cos\theta_{d,i}+\cos\theta_{d,f})/2$. Dynamic contact angles for the PnBMA 5.5k at different pore diameters and for the blends B1 and B2 at 343 K are provided in **Table 3**. Typical images of PnBMA 5.5k at three temperatures are shown in **Figure 4**.

Table 3. Parameters entering the LWE together with terminal relaxation times at 343 K.

Sample	γ ($\times10^{-3}$ N/m)	θ_d (°)	θ_e (°)	η_o (Pa·s)
		34.8 (400 nm)	21	
PnBMA 5.5k	28.2	23.2 (65 nm)	21	3.1×10^3
		21.4 (25 nm)	21	
PnBMA 100k	28.2			7.8×10^7
B1 (75/25)	28.2	43.5 (65 nm)	43	8.7×10^4
B2 (50/50)	28.2	72.0 (65 nm)	69	7.9×10^5
B3 (25/75)	28.2	- (65 nm)	-	1.6×10^7

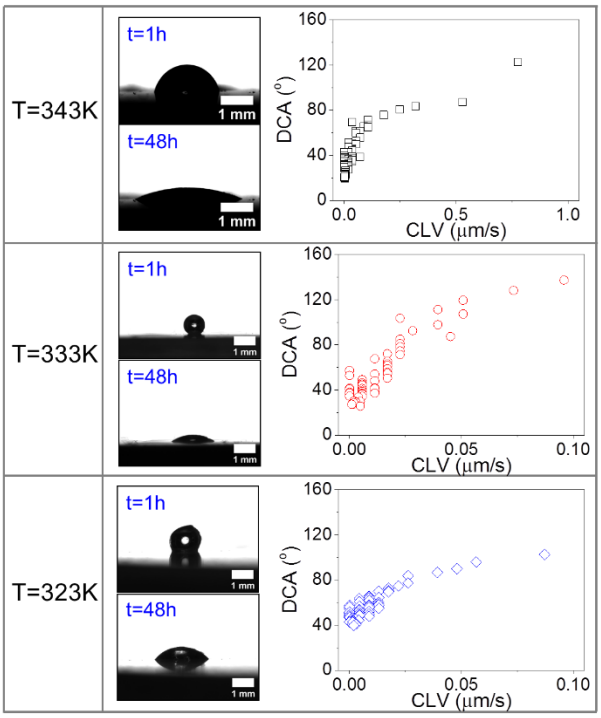

Figure 4. Optical images (left) and dynamic contact angles (right) of PnBMA 5.5k at three temperatures as indicated. The advancing contact angle pertinent to the velocity during the imbibition process is estimated as explained in the text.

The results of the imbibition experiments for PnBMA 5.5k are shown for different temperatures at two pore diameters in **Figure 5** and for different pore diameters at two temperatures in **Figure 6**. At early times the rise of the imbibition length, d_1, is linear with the square root of time. At longer times, however, deviations from linearity were observed. In **Figure S11**, the imbibition lengths are compared for a template with one end closed and a template with both ends open. The figure confirms the notion that the origin of the nonlinear dependence at long times is the pressure exerted by the trapped air at the bottom of nanotubes.[39] Imbibition lengths based on the LWE are calculated based on the $<\cos\theta_d>$ values and are shown by the solid lines. As has been observed earlier, the LWE fails to describe the experimental data nearly at all temperatures and for all pore diameters. The deviations from LWE are more pronounced at lower temperatures and for the smaller pore diameters. The experimental data suggest a higher effective viscosity for **PnBMA 5.5k** within the smaller nanopores in line with earlier results.[5,12] According to a recent theory,[12] the imbibition of entangled polymer melts is governed by the competition between two mechanisms. The first is the standard hydrodynamic flow. Under conditions of strong

adsorption between the walls and the polymer a layer of immobile surface layer is formed (dead layer), reducing the pore radius, and leading to an increase in the effective viscosity. The second mechanism is the reptation of chains under a pressure gradient. The latter mechanism under strong confinement enhances the mobility of chains, leading to a faster imbibition (plug flow). We have applied the same model for PnBMA 5.5k in AAO at 343 K (**Fig. 6**), and the results for the effective viscosity relative to the bulk are included in **Figure S12**. Evidently, the dead-layer effect is dominant for this molecular weight. From the fit to the model a dead-layer thickness of about 2 nm was estimated.

The solid lines give the predictions of the LWE equation using $\langle \cos \theta_d \rangle$, whereas $\cos \theta_{id}$ and $\cos \theta_{fd}$ values were also used in the LWE and plotted with dashed and dash-dotted lines, respectively. The horizontal dashed lines provide the template thickness (different for each template).

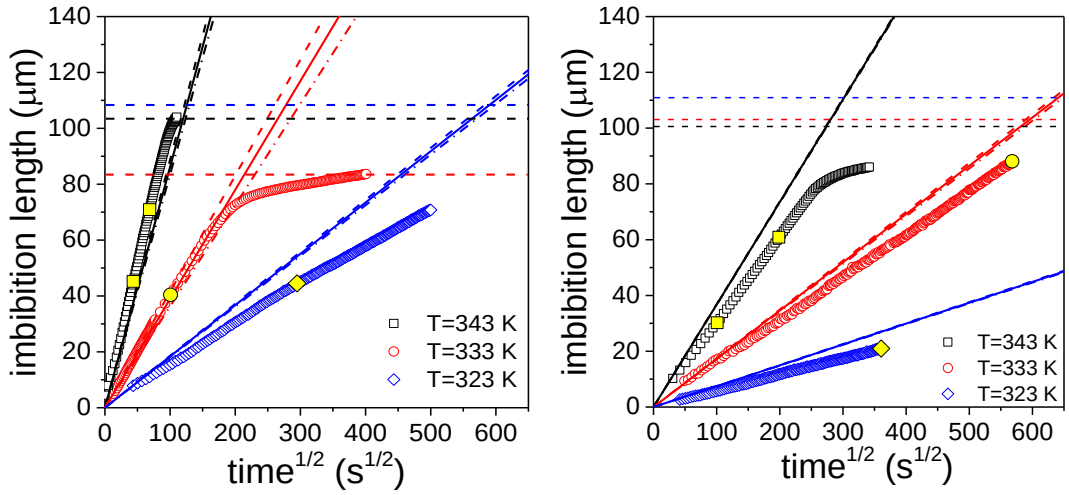

Figure 5. Imbibition length d_1, as a function of $t^{1/2}$ for the PnBMA 5.5k at different temperatures T = 343 K (squares), T = 333 K (circles), and T = 323 K (rhombi) and for two AAO pore diameters of 400 nm (left) and 65 nm (right). Symbols in yellow indicate the calibration points used from reflection optical microscopy.

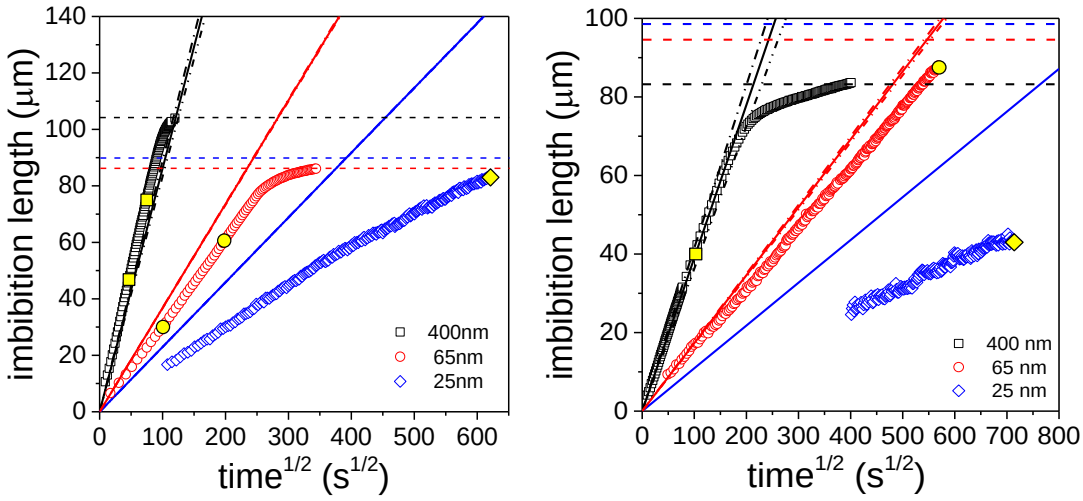

Figure 6. Imbibition length, d_1, as a function of $t^{1/2}$ for the PnBMA 5.5k for different AAO pore diameters of 400 nm (squares), 65 nm (circles), and 25 nm (rhombi) at two temperatures of (left) T = 343 K and (right) T = 333 K. The solid lines give the predictions of the LWE equation using $\langle\cos\theta_d\rangle$, whereas $\cos\theta_{id}$ and $\cos\theta_{fd}$ values were also used in the LWE and plotted with dashed and dash-dotted lines, respectively. The horizontal dashed lines provide the template thickness (different for each template).

Imbibition of polymer blends

Recent imbibition experiments on blends of PS[13] and PEO[14] within the same AAO templates indicated that the blend composition under confinement can differ from the bulk composition. The experiments were based on *ex situ* reflection microscopy and demonstrated the enrichment of the pores by the shorter chains due to their faster imbibition. Herein we apply DS to follow the imbibition kinetics *in situ* for three PnBMA blends (B1, B2 and B3) by following the evolution of the segmental process. The dynamics of the three blends were first studied in the bulk as a function of temperature. The VFT parameters of the single $\alpha\beta$-process are provided in **Table 2**. **Figure 7** compares the dielectric loss curves of the homopolymers and the blends in the bulk at the imbibition temperature (343 K). The relaxation times at maximum loss in the bulk follows a linear concentration dependence (**Fig. 7c**) anticipated by the proximity of the glass temperatures of the individual homopolymers.[40] This is to be contrasted with the segmental dynamics at the end of the imbibition process (**Fig. 7b**); the segmental process does not follow the same linear dependence.

As shown in **Fig. 7b,c** the segmental process of B2 (50/50) and of B3 (25/75) deviate (are faster) from the expected bulk relaxation times.

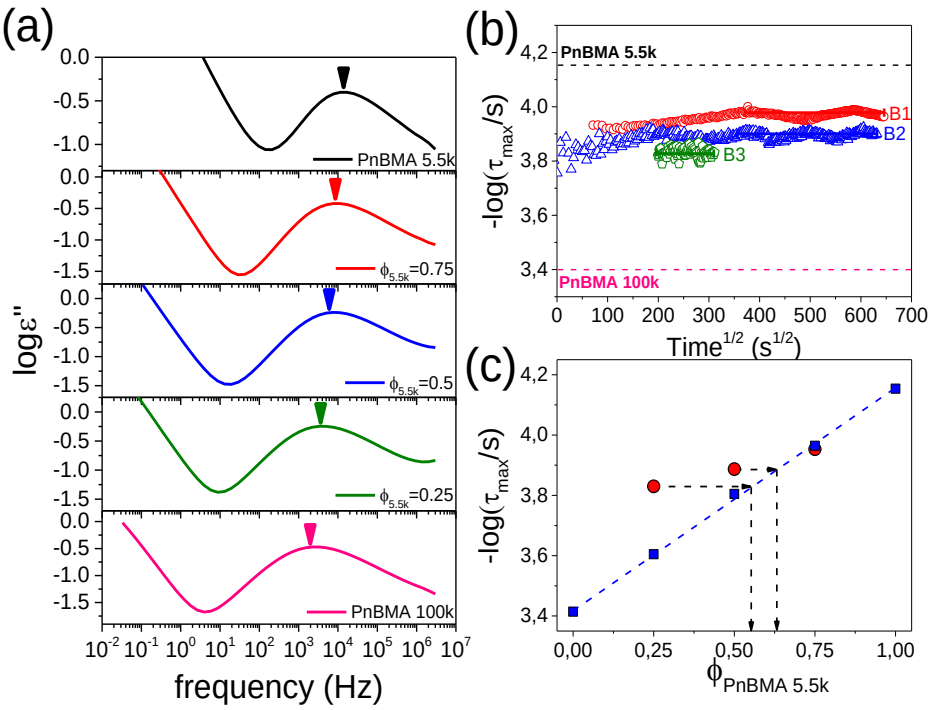

Figure 7. (a) Dielectric loss spectra of the homopolymers and their blends at 343 K. Arrows indicate the frequency of maximum loss. (b) Evolution of the relaxation time at maximum loss for the three blends (circles) B1, (squares) B2 and (up triangles) B3 during their imbibition within AAO with a pore diameter of 65 nm at 343 K. Dashed and dash-dotted lines give the respective times for the PnBMA 5.5k and PnBMA 100k homopolymers. (c) Relaxation times at maximum loss as a function of blend composition (blue squares) at 343 K. The corresponding times for the blends located inside AAO following imbibition are also shown (red circles). Dashed lines with arrows indicate projections to the composition in the bulk that provides estimates of the effective blend composition within the nanopores.

Evidently, the B2 and B3 blend composition inside AAO is enriched by segments from the shorter chains (PnBMA 5.5k) and hence become faster. By projecting isochronally the relaxation times in confinement to the composition dependence in the bulk, we estimate an effective composition of 55/45 instead of 25/75 for B3. Similarly, for B2 the estimated blend composition is 63/37 instead of 50/50. Because the segmental relaxation times in the blends is independent of imbibition time (Fig. 7b) this suggests that already at short time scales polymer chains entering the nanopores are enriched by PnBMA 5.5k. This result is supported by recent SCFT calculations[14] showing the enrichment of the pores by the shorter chains. From an entropic point of view, ends

of polymer chains have equal probability to be found near the pore surface. Consequently, shorter chains enrich the pore surface. In effect, shorter chains enter first the nanopores and "lubricate" the inner pore surface. In the case of B3, rich in the longer chains, this effect is minor but becomes dominant in B2 and B3 because of the majority of shorter chains.

This enrichment by segments of the shorter chains should alter the imbibition dynamics at longer length scales as probed by the evolution of the dielectric strength and the associated imbibition length. This is depicted in **Figure 8** for the three blends in comparison to the homopolymer PnBMA 5.5k at 343 K. We should mention that the imbibition dynamics of PnBMA 100k is too slow at this temperature. The extracted imbibition lengths are compared with the expectations from the LWE. In the latter, the bulk viscosities and the measured dynamic contact angles are employed. Dynamic contact angle measurements in the blends are depicted in **Figure 9**. Representative fits to the Cox model for the blends B1 and B2, at 343 K are provided in **Figure S10**. Finally, the results on the DCA for B1 and B2 are included in Table 3.

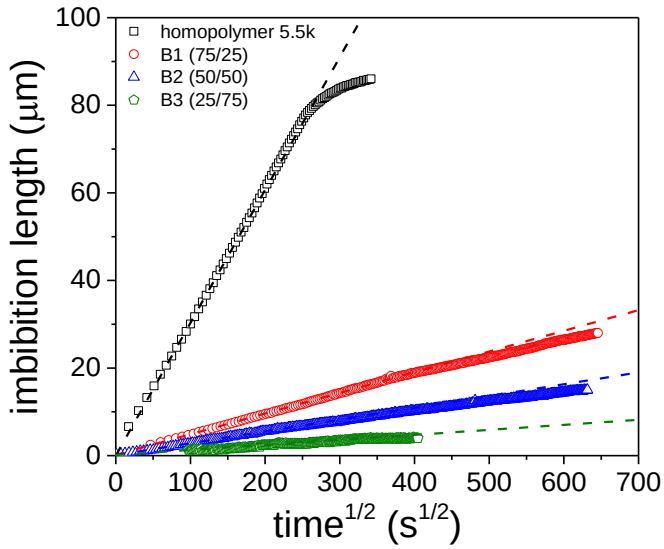

Figure 8. Imbibition length as a function of $t^{1/2}$ for the PnBMA 5.5k homopolymer (squares) and its blends with PnBMA 100k for AAO pore diameter of 65 nm at 343 K: B1 (circles) , B2 (triangles), and B3 (rhombi). The dashed lines represent linear fits to the initial imbibition process (for PnBMA 5.5k up to 250 $s^{1/2}$ and for the blends to 350 $s^{1/2}$).

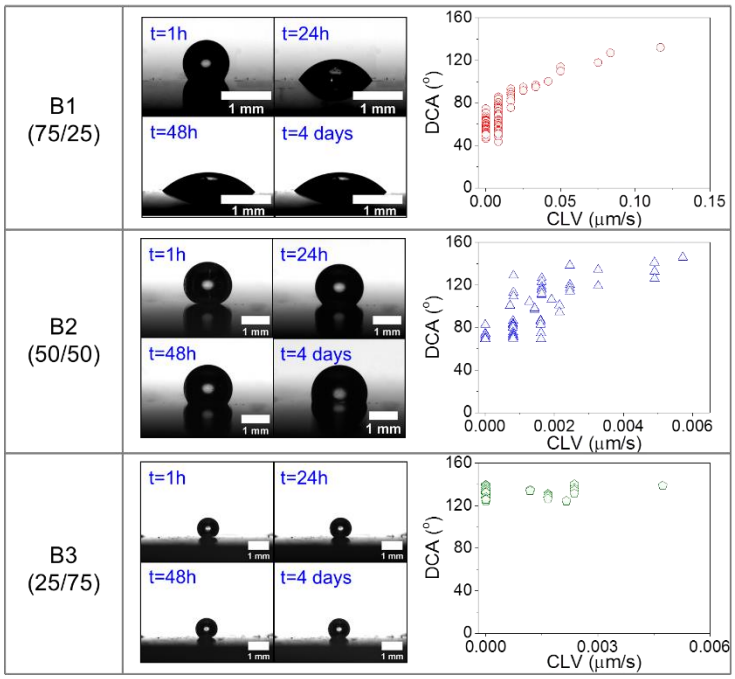

Figure 9. Dynamic contact angles of B1 (top), B2 (middle) and B3 (bottom) at 343 K. The advancing contact angle pertinent to the velocity during the imbibition process is estimated as explained in the text.

Interestingly, the blend imbibition lengths exhibit some curvature with $t^{1/2}$, suggesting that the effective viscosity is a function of time as well (**Figure 8**). We have employed the initial slopes and within the context of the LWE we extracted the corresponding effective viscosities. There is a reversal of the imbibition dynamics in going from the homopolymer to B1 and B2. In B1 the effective viscosity is higher than the bulk viscosity as with the PnBMA 5.5k homopolymer, meaning that the dead-zone effect is the dominant. However, in B2 the effective viscosity is lower than the corresponding η_0. This finding is in line with the enrichment of the blends by the shorter chains, found by exploring the segmental dynamics. This can better be visualized in **Figure 10** where the bulk zero shear viscosities in the blends are compared with the effective viscosities extracted from the LWE (**Figure 8**). The dependence of the zero shear viscosity in the blends under confinement is less steep ($\eta_{\text{eff}} \sim \varphi^{0}$) as compared to the bulk ($\eta_0 \sim \varphi^{-6}$). There are two reasons for this dependence: In the blend rich in the smaller molecular weight (B1), the effective viscosity is somewhat higher than in the bulk mainly because of the dead-layer effect. In the symmetric blend B2, the dead-layer effect is overtaken by the enrichment by the shorter chains. This effect is

expected to become stronger in B3 in view of the results from the segmental relaxation times. However, extracting the DCA for B3 (as well as in PnBMA 100k) is a difficult task.

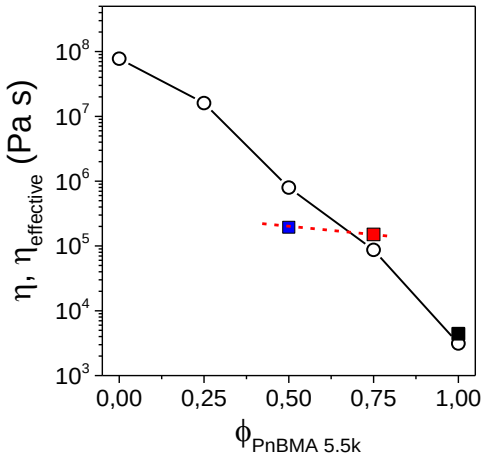

Figure 10. Zero-shear viscosity of the homopolymers and their blends at 343 K (open circles) and effective shear viscosity during the imbibition process for the homopolymer PnBMA 5.5k (black square), the blend B1 (red square), and the blend B2 (blue square). The line for the zero-shear viscosity data is to guide the eye.

Overall, the blend study confirmed the potential of the method to fractionate polymers with different molecular weights. This was demonstrated at two length scales; at the segmental length scale by following the evolution of the segmental process in the blends and at the chain length scale by extracting the effective viscosity. Both resulted in a weak composition dependence of the relaxation times and of the effective viscosity revealing the enrichment of nanopores with the shorter chains. More efforts are needed to obtain the microscopic details of the imbibition process (changes in entanglement density, adsorption *etc*.).

2.4. Conclusion

The nanofluidic method was employed to study the details of PnBMA imbibition in AAO nanopores. The method is capable of providing quantitative information of the imbibition process at the segmental and chain length scales *in situ*. Imbibition at the segmental level is isochronal except at the initial stages where a speed-up is observed, with shape parameters that are independent of imbibition time. This result is not surprising given that the imbibition temperature is located some 30-50 K above T_g. At such temperatures any contribution to the segmental dynamics by interfacial effects will diminish. Imbibition at longer length scales associated with the effective viscosity provided a stringent test of the Lucas-Washburn equation. For PnBMA 5.5k the effective viscosity in the smaller pores is higher than in bulk suggesting that the dead-layer effects dominate.

Imbibition of polymer blends composed from short and long chains confirmed the potential of the nanofluidic method to fractionate polymers with different molecular weights. The effective viscosity - extracted within the context of Lucas-Washburn equation - and the segmental relaxation times during the imbibition process, both show a weak composition dependence consistent with the enrichment of nanopores by the shorter chains, revealing that shorter chains first enter the nanopores followed by the longer chains. This result is supported by recent SCFT calculations[14] showing the enrichment of pores by the shorter chains and by the entropy argument.

Future works will explore the potential of the nanofluidic method to follow *in situ* polymer dynamics directly at the chain length scale by studying the evolution of normal modes in type-A polymers, like *cis*-1,4-Polyisoprene.

2.5 References

(1) Lucas, R. Ueber das zeitgesetz des kapillaren aufstiegs von flüssigkeiten. *Colloid Polym. Sci.* **1918**, 23, 15-22.

(2) Washburn, E. W. The dynamics of capillary flow. *Phys. Rev.* **1921**, 17 (3), 273-283.

(3) Shin, K.; Obukhov, S.; Chen, J.-T.; Huh, J.; Hwang, Y.; Mok, S.; Dobriyal, P.; Thiyagarajan, P.; Russell, T. P. Enhanced mobility of confined polymers. *Nat. Mater*. **2007**, 6, 961.

(4) Cao, B.-Y.; Yang, M.; Hu, G.-J. Capillary filling dynamics of polymer melts in nanopores: Experiments and rheological modelling. *RSC Adv.* **2016**, 6, 7553.

(5) Yao, Y.; Alexandris, S.; Henrich, F.; Auernhammer, G.; Steinhart, M.; Butt, H.-J.; Floudas, G. Complex dynamics of capillary imbibition of poly(ethylene oxide) melts in nanoporous alumina. *J. Chem. Phys.* **2017**, 146 (20), 203320.

(6) Yao, Y.; Suzuki, Y.; Seiwert, J.; Steinhart, M.; Frey, H.; Butt, H.-J.; Floudas, G. Capillary Imbibition, crystallization, and local dynamics of hyperbranched poly(ethylene oxide) confined to nanoporous alumina. *Macromolecules* **2017**, 50, 8755-8764.

(7) Masuda, H.; Fukuda, K., Ordered metal nanohole arrays made by a two-step replication of honeycomb structures of anodic alumina. *Science* **1995**, 268, 1466-1468.

(8) Masuda, H.; Hasegawa; F.; Ono, S. Self-ordering of cell arrangement of anodic porous alumina formed in sulfuric acid solution. *J. Electrochem. Soc.* **1997**, 144, L127-L130.

(9) Masuda, H.; Yada, K.; Osaka, A., Self-ordering of cell configuration of anodic porous alumina with large-size pores in phosphoric acid solution. *Jpn. J. Appl. Phys.* **1998**, 37, L1340.

(10) Steinhart, M., Supramolecular organization of polymeric materials in nanoporous hard templates. *Adv. Polym. Sci.* **2008**, 220, 123-187.

(11) Johner, A.; Shin K.; Obukhov, S. Nanofluidity of a polymer melt: Breakdown of Poiseuille's flow model. *Europhysics Letters* **2010**, 91, 38002.

(12) Yao, Y.; Butt, H.-J.; Floudas, G.; Zhou, J.; Doi, M. Theory on capillary filling of polymer melts in nanopores. *Macromol. Rapid Commun.* **2018**, 39, 1800087.

(13) Zhang, M.; Dobriyal, P.; Chen, J.-T.; Russell, T. P.; Olmo, J.; Merry, A. Wetting transition in cylindrical alumina nanopores with polymer melts. *Nano Lett.* **2006**, 6, 1075-1079.

(14) Yao, Y.; Butt, H.-J.; Zhou, J.; Doi, M.; Floudas, G. Capillary imbibition of polymer mixtures in nanopores. *Macromolecules* **2018**, 51, 8755-8764.

(15) Serghei, A.; Chen, D.; Lee, D. H.; Russell, T. P. Segmental dynamics of polymers during capillary flow into nanopores. *Soft Matter* **2010**, 6, 1111-1113.

(16) Serghei, A.; Lutkenhaus, J. L.; Miranda, D. F.; McEnnis, K.; Kremer, F.; Russell, T. P. Density fluctuations and phase transitions of ferroelectric polymer nanowires. *Small* **2010**, 6 (16), 1822-1826.

(17) Serghei, A.; Zhao, W.; Wei, X.; Chen, D.; Russell, T. P. Nanofluidics with phase separated block-copolymers: Glassy dynamics during capillary flow. *Eur. Phys. J. Special Topics* **2010**, 189, 95-101.

(18) Serghei, A.; Zhao, W.; Miranda, D.; Russell, T. P. Curie transitions for attograms of ferroelectric polymers. *Nano Lett.* **2013**, 13, 577-580.

(19) Houachtia, A.; Alcouffe, P.; Boiteux, G.; Seytre, G.; Gérard, J.-F.; Serghei, A. Nanofluidics approach to separate between static and kinetic nanoconfinement effects on the crystallization of polymers. *Nano Lett.* **2015**, 15, 4311-4316.

(20) Alexandris, S.; Sakellariou, G.; Steinhart, M.; Floudas, G., Dynamics on unentangled cis-1,4-polyisoprene confined to nanoporous alumina. *Macromolecules* **2014**, 47, 3895-3900.
(21) Politidis, C.; Alexandris, S.; Sakellariou, G.; Steinhart, M.; Floudas, G., Dynamics of entangled cis-1,4-polyisoprene confined to nanoporous alumina. *Macromolecules* **2019**, 52, 4185-4195.
(22) Alexandris, S.; Papadopoulos, P.; Sakellariou, G.; Steinhart, M.; Butt, H.-J.; Floudas, G. Interfacial energy and glass temperature of polymers confined to nanoporous alumina, *Macromolecules*, **2016**, 49, 7400-7414.
(23) Deres, A.; Floudas, G. A.; Müllen, K.; Van der Auweraer, M.; De Schryver, F.; Enderlein, J.; Uji-i, H.; Hofkens, J. The origin of heterogeneity of polymer dynamics near the glass temperature as probed by defocused imaging. *Macromolecules* **2011**, 44, 9703-9709.
(24) Wu, S. Surface and interfacial tensions of polymer melts. II. Poly(methyl methacrylate), poly(n-butyl methacrylate) and polystyrene. *J. Phys. Chem.* **1970**, 74, 632-638.
(25) Kwok, D. Y.; Leung, A.; Li, A.; Lam, C. N. C.; Wu, R.; Neumann, A.W. Low-rate dynamic contact angles on poly(n-butyl methacrylate) and the determination of solid surface tensions. *Colloid Polym. Sci.*, **1998**, 276, 459-469.
(26) Kremer, F.; Schönhals, A. in Broadband Dielectric Spectroscopy, Springer, Berlin, **2002**.
(27) Floudas, G.; Paluch, M.; Grzybowski, A.; Ngai, K.L. in *Molecular Dynamics of Glass-Forming Systems. Effects of Pressure*; Springer **2011**.
(28) Suzuki, Y.; Duran, H.; Steinhart, M.; Kappl, M.; Butt, H.-J.; Floudas, G. Homogeneous Nucleation of Predominantly Cubic Ice Confined in Nanoporous Alumina. *Nano Lett.* 2015, 15, 1987−1992.
(29) Suzuki, Y.; Steinhart, M.; Graf, R.; Butt, H.-J.; Floudas, G. Dynamics of Ice/Water Confined in Nanoporous Alumina. *J. Phys. Chem. B* **2015**, 119, 14814−14820.
(30) Mpoukouvalas, K.; Floudas, G. Williams, G. Origin of the α, β, (βα), and "Slow" Dielectric Processes in Poly(ethyl methacrylate). *Macromolecules* **2009**, 42, 4690-4700.
(31) Schönhals, A.; Rittig, F.; Kärger, J., Self-diffusion of poly(propylene glycol) in nanoporous glasses studied by pulsed field gradient NMR: A study of molecular dynamics and surface interactions. *J. Chem. Phys.* **2010**, 133, 094903.
(32) Mapesa, E.U.; Tress, M.; Schulz, G.; Huth, H.; Schick, C.; Reiche, M.; Kremer F., Segmental and chain dynamics in nanometric layers of poly(cis-1,4-isoprene) as studied by broadband dielectric spectroscopy and temperature-modulated calorimetry. *Soft Matter* **2013**, 9, 10592-10598.
(33) Kipnusu, W.K.; Elmahdy, M.M.; Mapesa, E.U.; Zhang, J.; Böhlmann, W.; Smilgies, D.-M.; Papadakis, C.M.; Kremer, F. Structure and dynamics of asymmetric poly(styrene-b-1,4-isoprene) diblock copolymer under 1D and 2D nanoconfinement. *ACS Appl. Mater. Interfaces* **2015**, 7, 12328-12338.
(34) Tarnacka, M.; Kaminski, K.; Mapesa, E.U.; Kaminska, E.; Paluch, M. Studies on the temperature and time induced variation in the segmental and chain dynamics in poly(propylene glycol) confined at the nanoscale. *Macromolecules* **2016**, 49, 6678-6686.
(35) Talik, A.; Tarnacka, M.; Grudzka-Flak, I.; Maksym, P.; Geppert-Rybczynska, M.; Wolnica, K.; Kaminska, E.; Kaminski, K.; Paluch, M. The role of interfacial energy and specific interactions on the behavior of poly(propylene glycol) derivatives under 2D confinement. *Macromolecules* **2018**, 51, 4840-4852.

(36) Schönhals, A.; Goering, H.; Schick, C.; Frick, B.; Zorn, R., Glassy dynamics of polymers confined to nanoporous glasses revealed by relaxational and scattering experiments. *Eur. Phys. J.E.* **2003**, 12, 173-178.

(37) Li, L.; Zhou, D.; Huang, D.; Xue, G. Double glass transition temperatures of poly(methyl methacrylate) confined in alumina nanotube templates. *Macromolecules* **2014**, 47, 297-303.

(38) Cox, G. The dynamics of the spreading of liquids on a solid surface. Part 1. Viscous flow. *J. Fluid Mech.* **1986**, 168, 169.

(39) Cencha, L.G.; Huber, P.; Kappl, M.; Floudas, G.; Steinhart, M.; Berli, C.L.A.; Urteaga, R. Nondescructive high-throughput screening of nanopore geometry in porous membranes by imbibition. *Appl. Phys. Lett.* **2019**, 115, 113701.

(40) Lodge, T. P.; McLeish, T. C. B. Self-concentrations and effective glass transition temperatures in polymer blends. *Macromolecules* **2000**, 33, 5278-5284.

2.6 Supporting information

I. Surface characterization (XPS)

XPS measurements were made to determine the surface characteristics of the electropolished Al disks coated with the thin native oxide layer in comparison to the AAO templates. An Axis Ultra DLD imaging X-ray photoelectron spectrometer was used utilizing a MgKα X-ray source (15 kV, 30mA (450W)). Spectra were recorded at an angle of 90 º to the surface.

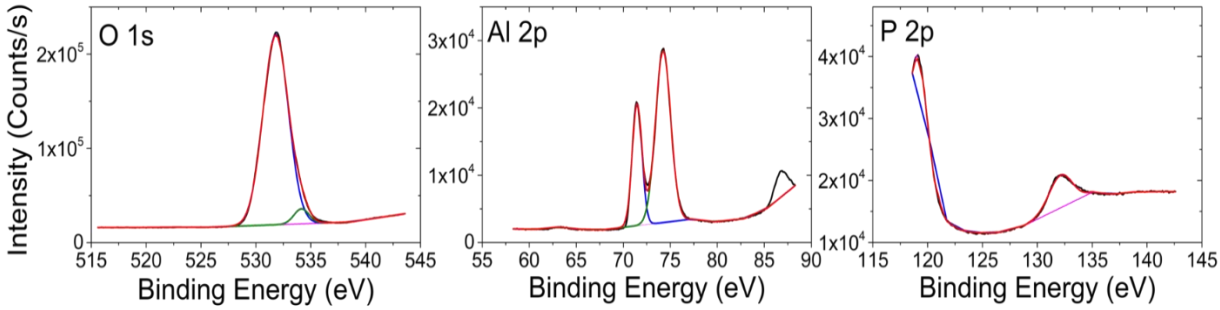

Figure S1. XPS high-resolution spectra from the electropolished Al disks coated with the thin native oxide layer. Spectra refer to oxygen (left), aluminum (center) and phosphorous (right) concentrations.

Figure S1 gives the oxygen, aluminum and phosphorous concentrations in the electropolished Al disks coated with the thin native oxide layer. The relative contributions of oxygen, aluminum and phosphorous is 69%, 9% and 1.5%, respectively. The O 1s spectrum provides information on the possible type of alumina. The main oxygen contribution is from oxidic oxygen (531.3 eV) (e.g., Al_2O_3) with a minor contribution from aluminum hydroxide (*e.g.*, Boehmite AlO(OH), Gibbsite $Al(OH)_3$ or Augelite $Al_2(PO_4)(OH)_3$)).[1] On the other hand, the Al 2p spectrum shows two distinct contributions at 71.8 eV and 74.5 eV, corresponding to aluminum metal and aluminum oxide and/or aluminum hydroxides. Given the small contribution of hydroxide in the oxygen spectrum we conclude that the main contribution is from aluminum oxide.[2] Lastly a small contribution from phosphorous is found. These results on the surface characterization of the electropolished Al disks coated with the thin native oxide layer indicate similarities to surface properties of native AAO membranes.[3]

II. Dielectric Spectroscopy

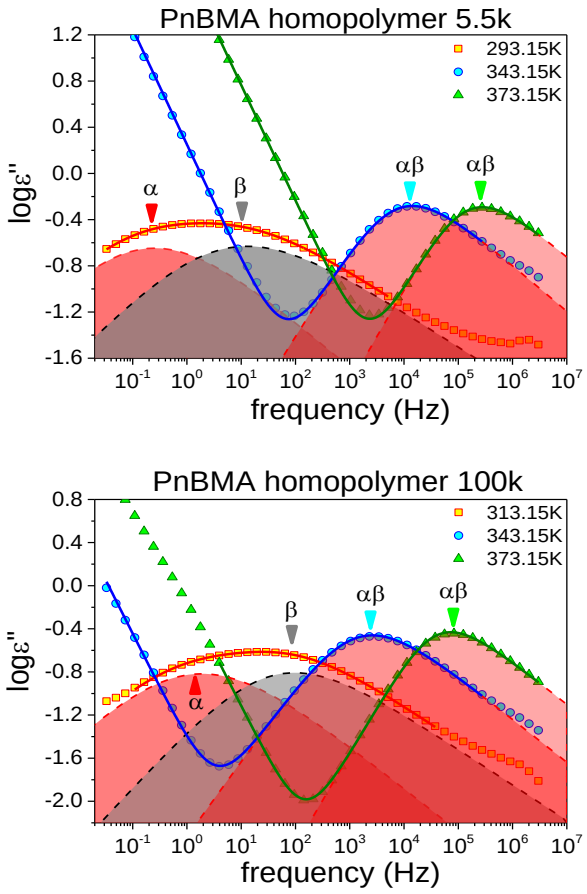

Figure S2. Dielectric loss curves at three temperatures for the two homopolymers (top): PnBMA 5.5k and (bottom): PnBMA 100k. The curves correspond to the separate α- and β-processes at the lower temperatures (293 K, 313 K) and to the merged $\alpha\beta$-process at the higher temperatures (343 K, 373 K).

III. Rheology

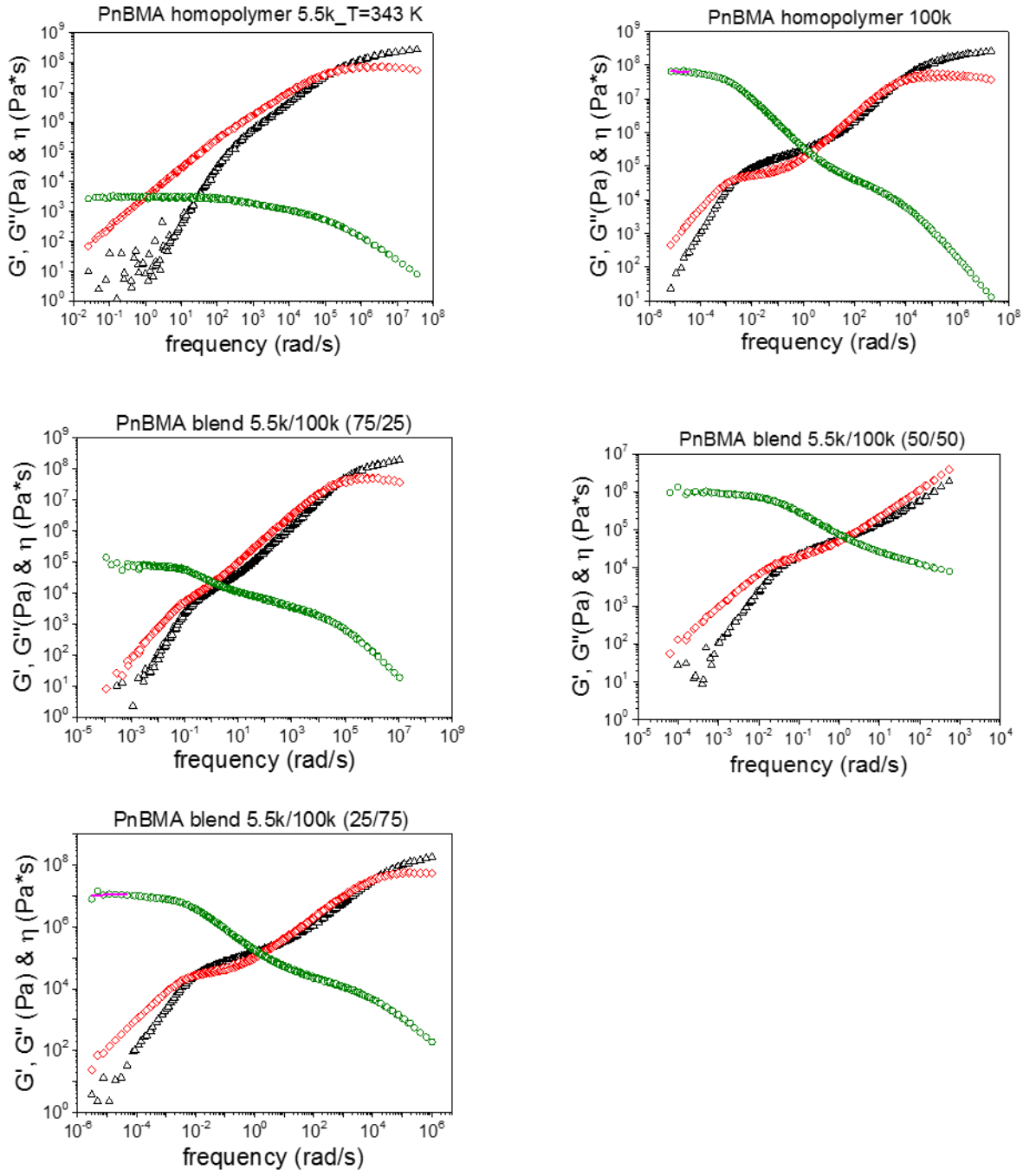

Figure S3. Master curves for the storage (black triangles), the loss (red rhombi) moduli and the shear viscosity (green circles) all constructed at the same reference temperature (343 K).

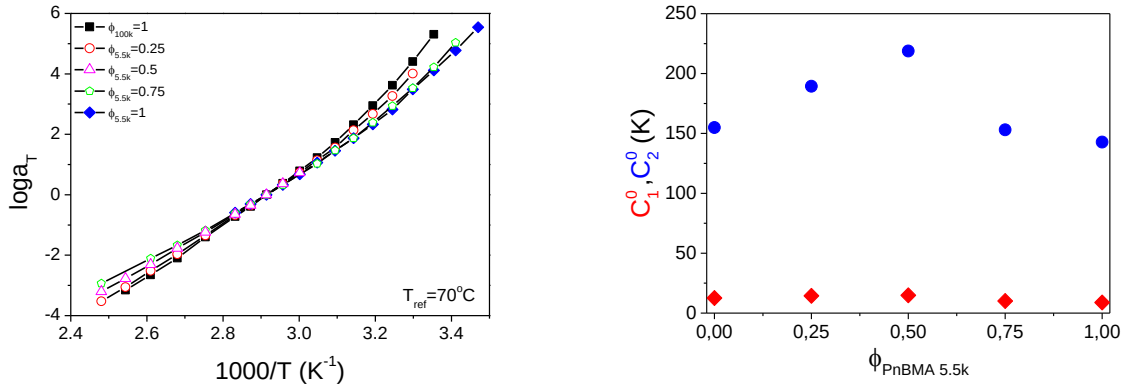

Figure S4. (left) Shift factors for the homopolymers and their blends at the reference temperature (343 K). Solid lines represent fits to the WLF equation. (right) WLF coefficients as a function of blend composition, $\varphi_{\text{PnBMA 5.5k}}$, at the reference temperature.

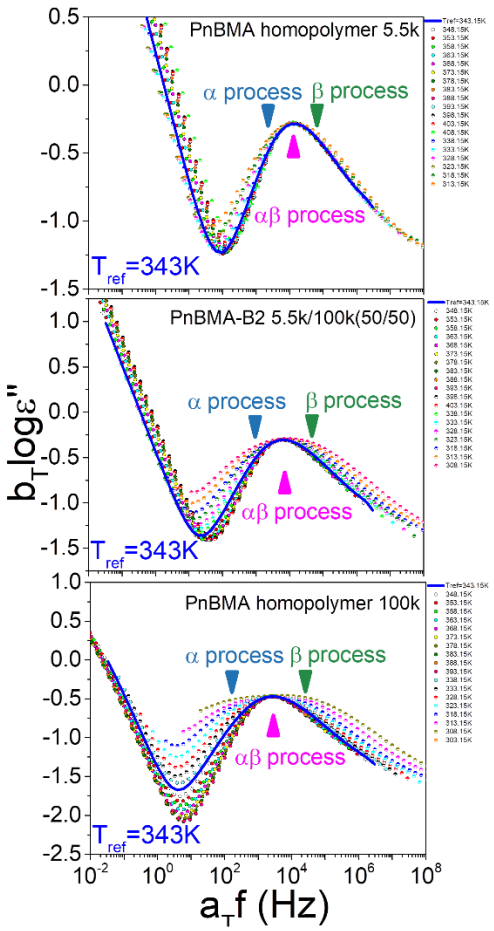

Figure S5. Attempted use of time-temperature superposition for the PnBMA 5.5k (top) and PnBMA 100k (bottom) homopolymers and their symmetric blend (middle) at the same reference

temperature. t*T*s does work because of overlapping processes with different temperature dependencies.

IV. SEM

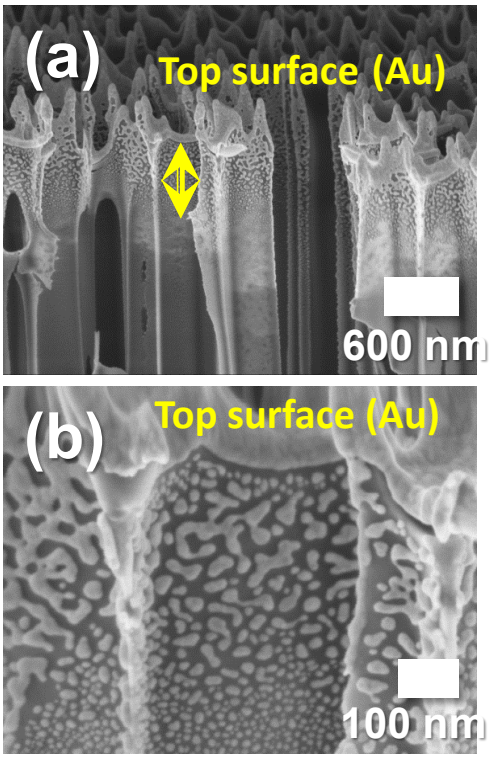

Figure S6. SEM images of a cross section from an AAO template with a 65 nm pore diameter showing a gold layer on the top surface and small gold particles in a maximum depth of 380 nm. (b) is a magnification of (a).

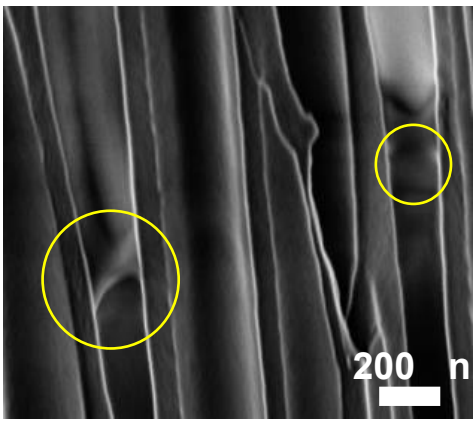

Figure S7. SEM image showing the presence of a meniscus (in yellow circles) at the tip of the advancing PnBMA 5.5k melt within an AAO template with a 400 nm pore diameter. The image refers to 5625 s of imbibition at 343 K.

V. Reflection optical microscopy (length calibration)

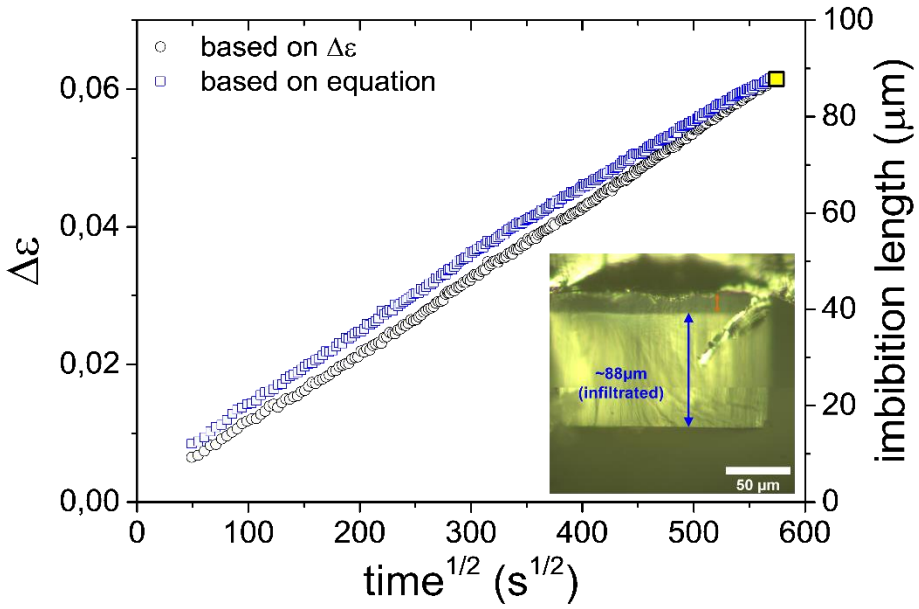

Figure S8. Imbibition lengths extracted by the two differed methods: (circles) from the evolution of the dielectric strength, (squares) from the equivalent circuit. The polymer is PnBMA 5.5 k, the templates have a diameter of 65 nm and the imbibition temperature is at 333 K. The image from reflection optical microscopy (inset) is obtained at the end of the imbibition process (corresponding yellow square point at 88 μm).

VI. Dynamic contact angle

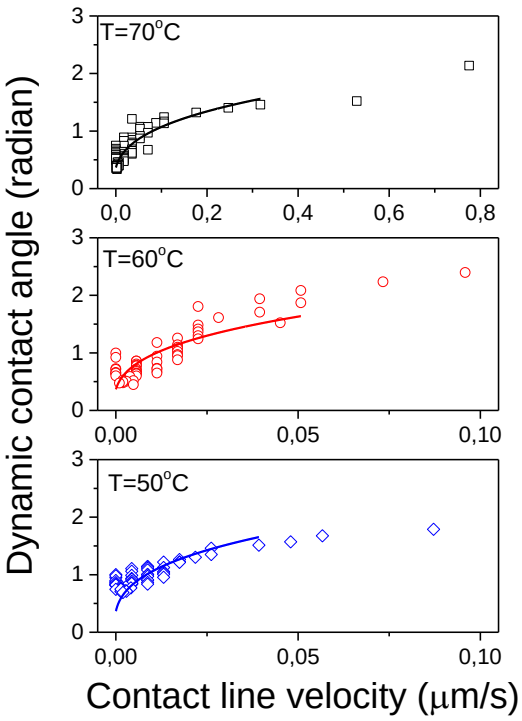

Figure S9. Fits of the dynamic contact angles of PnBMA 5.5k to the Cox model at three different temperatures; (top) T = 343 K, (middle) T = 333 K and (bottom) T = 323 K.

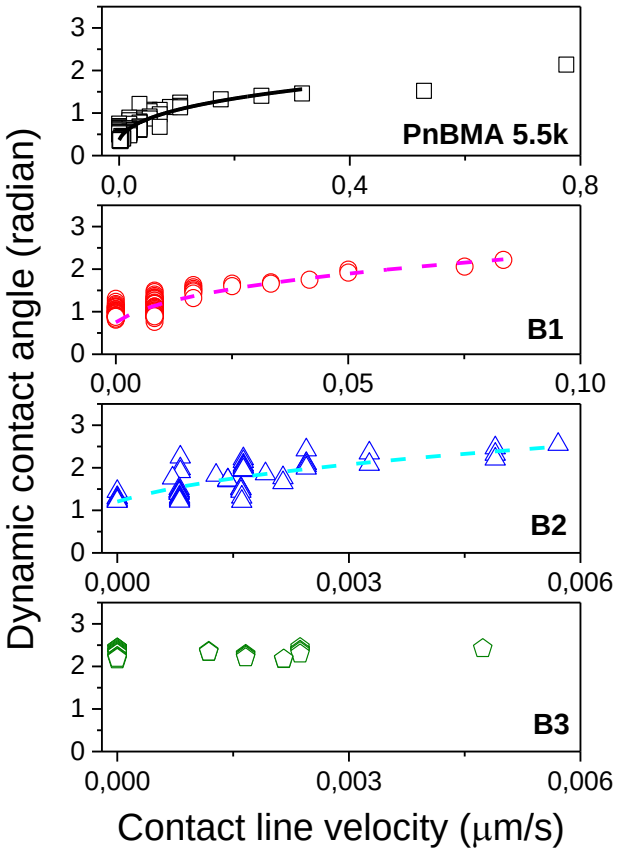

Figure S10. Fits of the dynamic contact angle of the blends B1 (top) and B2 (middle) to the Cox model at T = 343 K.

VII. AAO templates closed from one end vs open in both ends (free standing). Effect of trapped air.

The effect of trapped air was studied in AAO templates with nominal pore size of 65 nm. Figure S11, provides the imbibition length at 343 K for an AAO template with only one open end. It shows the expected increase as $t^{1/2}$ followed by a bending at longer times due to the pressure exerted by trapped air. To compare this with an AAO template with two open ends the following procedure was used. A 10% H_3PO_4 water solution was employed and the AAO template was put on top. In this way the closed side -which appears glossy- was in contact with the acid. As soon as the pore bottoms are opened, the solution flows through the pores to the upper AAO surface with the initial pore openings. Subsequently, the AAO template was removed from the acid solution and rinsed with water. As we can see from Fig. S11, this procedure inevitably results in pore widening especially from the template side in contact with the solution. This is shown in consecutive SEM images taken along the pore length indicating that the pore widening starts already from the middle region (B) all the way to the bottom (C). The pore widening process makes the comparison with the templates with one open end a difficult task especially for the longer imbibition times. The comparison of the two templates, one with one open end vs two open ends, is shown in Fig.S11. It shows comparable imbibition lengths at the beginning of the process. However, at longer times pore widening results to a further increase of the imbibition length without showing the bend over characteristic of trapped air. The Figure confirms that the origin of the non-linear dependence at long times for AAO templates with one open end is the pressure exerted by the trapped air at the bottom of nanotubes.

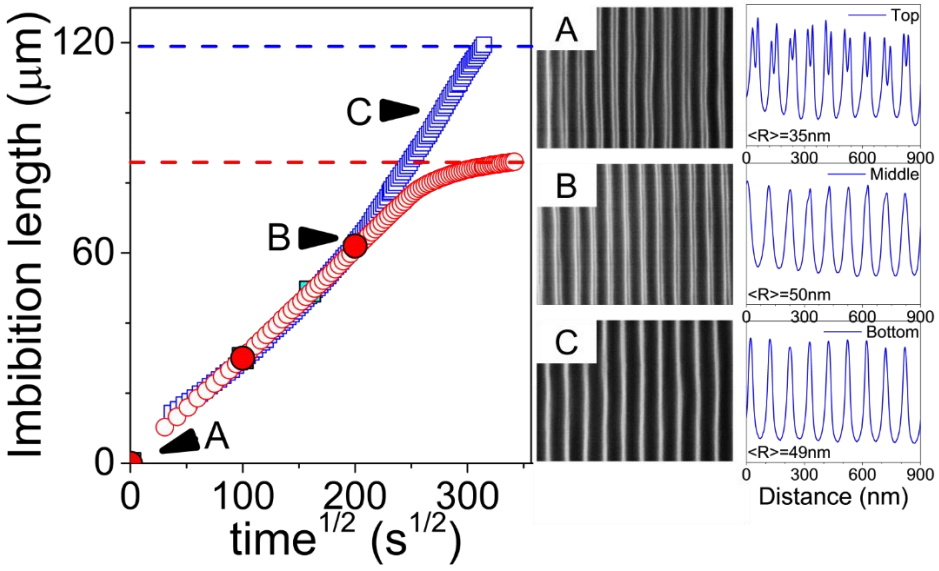

Figure S11. (Left) Comparison of the imbibition lengths at a temperature of 343 K for a template with one open end (red circles) and a template with two open ends (blue squares). The AAO template with the one open end had pore diameters (2*R*) of 65 nm. Calibration points from reflection microscopy are shown with respective filled symbols. (Right) SEM images of the AAO template with two open ends taken at various positions along the nanopores: (A) 1.5 μm, (B) 65 μm and (C) 100 μm from the top opening. The corresponding analysis with *ImageJ* reveals a widening of pores at the bottom.

VIII. Effective viscosity and dead layer thickness

According to a recent theory by M. Doi, the imbibition of entangled polymer melts is governed by the competition between two mechanisms. The first is the standard hydrodynamic flow. Under conditions of strong adsorption between the walls and the polymer a layer of immobile surface layer is formed (dead layer) reducing the pore radius, and leading to an increase in the effective viscosity. The second mechanism is the reptation of chains under a pressure gradient. The latter mechanism under strong confinement enhances the mobility of chains, leading to a faster imbibition (plug flow). According to the model the effective viscosity (η_{eff}) experienced by the polymer in confinement relative to the bulk (η_0) is:

$$\frac{\eta_{eff}}{\eta_0} = \left[\left(\frac{R_{eff}}{R}\right)^4 + \varphi\frac{8N_e^{\alpha}b^3\eta_0}{3\zeta NR^2}\right]^{-1},\ \eta_0 \approx \frac{\zeta b^2}{V_0}\frac{N^3}{N_e^2} \tag{S.1}$$

The effective viscosity is of the form:

$$\frac{\eta_{eff}}{\eta_0} = [f(\Delta R, R) + g(\phi, N, R)]^{-1} \tag{S.2}$$

where the first function, f, is related to the dead-zone with thickness ΔR,

$$f(\Delta R, R) = \begin{cases} \left(1 - \frac{\Delta R}{R}\right)^4 & if\ R > \Delta R \\ 0 & if\ R < \Delta R \end{cases} \quad \text{(S.3)}$$

The second function, g, is from the reptation model,

$$g(\phi, N, R) = \varphi \frac{8 N_e^{\alpha} b^3 \eta_0}{3\zeta N R^2} = \varphi \frac{8 N_e^{\alpha-2} b^5}{3 V_0} \frac{N^2}{R^2} = \phi \frac{N^2}{R^2} \quad \text{(S.4)}$$

Here φ is the fraction of free chains and N is the degree of polymerization. We have applied the model for PnBMA 5.5k in AAO at 343 K (**Fig. 6**) and the results for the effective viscosity relative to the bulk are included in **Figure S11**. Evidently, the dead layer effect is dominant for this molecular weight. From the fit to the model a dead layer thickness of about 2 nm was estimated.

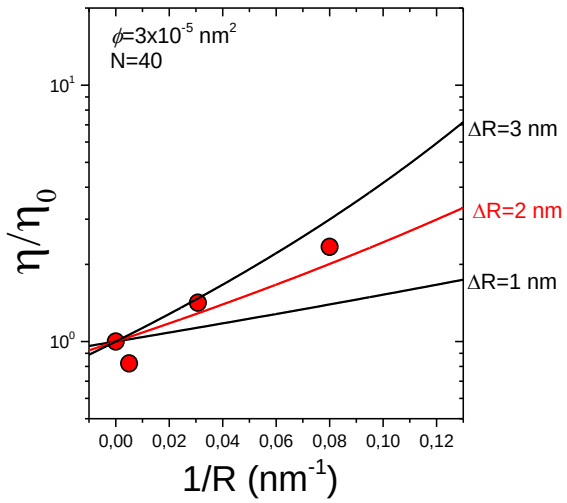

Figure S12. The ratio η_{eff}/η_0 for the PnBMA 5.5k within AAO with different pore diameters ($2R$) plotted as a function of $1/R$ extracted. The effective viscosity is extracted from the slopes of Figure 6 (at 343 K). Lines are theoretical predictions (fraction of free chains $\varphi = 3\times10^{-5}$ nm^2, degree of polymerization, $N = 40$) plotted for different values of the dead-zone thickness, ΔR. A dead zone thickness of approximately 2 nm is obtained.

Rerefences

(1) Thissen, P.; Valtiner, M.; Grundmeier, G. Stability of phosphonic acid self-assembled monolayers on amorphous and single-crystalline aluminum oxide surfaces in aqueous solution. *Langmuir* **2010**, *26*, 156-164.

(2) Strohmeir, B.R. An ESCA method for determining the oxide thickness of aluminum alloys. *Surface and Interface Analysis* **1990**, *15*, 51-56.

(3) Selevou, A.; Papamokos, G.; Yildirim, T.; Duran, H.; Steinhart, M.; Floudas, G. Eutectic Liquid crystal mixture E7 in nanoporous alumina. Effects of confinement on the thermal and concentration fluctuations. *RSC Advances* (submitted).

Chapter 3. Interfacial Interactions During *In Situ* Polymer Imbibition in Nanopores

This chapter has been published as a research paper in *Physical Review Letters*.

Chien-Hua Tu, Jiajia Zhou, Masao Doi, Hans-Jürgen Butt, and George Floudas,
Phys. Rev. Lett. 125, 127802 (2020)
DOI: 10.1103/PhysRevLett.125.127802

Abstract

Using *in situ* nanodielectric spectroscopy we demonstrate that the imbibition kinetics of *cis*-1,4-polyisoprene in native alumina nanopores proceeds in two time regimes both with higher effective viscosity than bulk. This finding is discussed by a microscopic picture that considers the competition from an increasing number of chains entering the pores and a decreasing number of fluctuating chain ends. The latter is a direct manifestation of increasing adsorption sites during flow. At the same time, the longest normal mode is somewhat longer than in bulk. This could reflect an increasing density of topological constraints of chains entering the pores with the longer loops formed by other chains.

3.1. Main text

Understanding that way that polymers penetrate in narrow pores is important for applications including separation of proteins with relevance in cell biology and the development of inkjet printing for commercial xerography. In general, placing macromolecules close to interfaces alter their conformational and dynamic properties[1,2]. Much of this behavior stems from polymer-substrate interactions[3-6]. Taming the strength of interfacial interactions especially under non-equilibrium conditions (*e.g.*, during flow), will enable the design of polymer interfaces with controlled physical properties (viscosity, glass temperature as well as wettability and adhesion) of importance in applications (organic electronic devices, coatings, membranes).

A recent advancement in this field have been experiments by the so-called, *nanofluidic* method.[7-10] The method employs self-ordered nanoporous aluminum oxide (AAO) templates sputtered with a thin gold layer to transform the nanoporous membranes into capacitors where an ac field is applied along the pore axes (**Fig. 1**). When the openings of the pores are brought into contact with a polymer melt, capillary forces drive the polymer chains into the pores. The polymer increases the capacitance C by way of the dielectric permittivity ε of the penetrating polymer ($C \sim \varepsilon$). The method offers simultaneous access to the kinetics of imbibition and to the molecular dynamics during flow at the segmental and possibly the chain length scales. Results have demonstrated the potential of the method to extract *quantitative* information on the viscosity experienced by the polymer during flow.[7] However, despite profound importance in applications, the pertinent polymer chain dynamics during flow have not been addressed either in theory or in experiment.

In this Letter we employ the nanofluidic method to follow the *in situ* polymer dynamics directly at the chain length scale by studying the evolution of normal modes in *cis*-1,4-polyisoprene (PI) during imbibition in AAO nanopores. The scientific question we address is, *if* and *how*, adsorption affects the imbibition kinetics of polymers. This question, despite being of importance in the design of membranes and devices, has not been addressed so far. The reason is that it requires precise measurements of polymer dynamics *during* flow. Results show that polymer imbibition proceeds in two time regimes with distinct changes in the dielectric strength of normal modes. We discuss this finding with the help of a microscopic picture that considers the competition from an

increasing number of chains entering the pores and a decreasing number of fluctuating chains with time. The latter provide unambiguous evidence for increasing adsorption sites during flow.

The studied polyisoprene (PI) homopolymer had M_n = 42410 g·mol^{-1} and M_w = 44000 g·mol^{-1} (PI-42k). AAO templates[11] with both ends open and thickness of 100 μm were purchased from InRedox (Longmont, USA). Pore diameters and corresponding porosities were 100 (24 ± 3%), 40 (12 ± 2%) and 20 nm (11 ± 2%), respectively. Two types of AAO surfaces were examined. One (the untreated) where templates were placed in an oven under vacuum at a temperature of 443 K for 8-10 h in order to remove the majority of OH groups from the AAO surface. Another one (the silanized) with a treated surface with trichloro(1H,1H,2H,2H-perfluorooctyl)silane (for 5 min under vacuum followed by heating to 423 K in order to remove any excess silane). Dielectric spectroscopy (DS) measurements were carried out at different temperatures in the range from 183 K to 393 K, at atmospheric pressure, and for frequencies in the range from $10^{-2} - 3\times10^{6}$ Hz. For the *in situ* imbibition kinetic experiments, a gold layer (thickness 35 nm) was sputtered on both sides of the AAO templates as top and bottom electrodes (**Figure 1**). More details on material and methods can be found in the Supporting Information.[12]

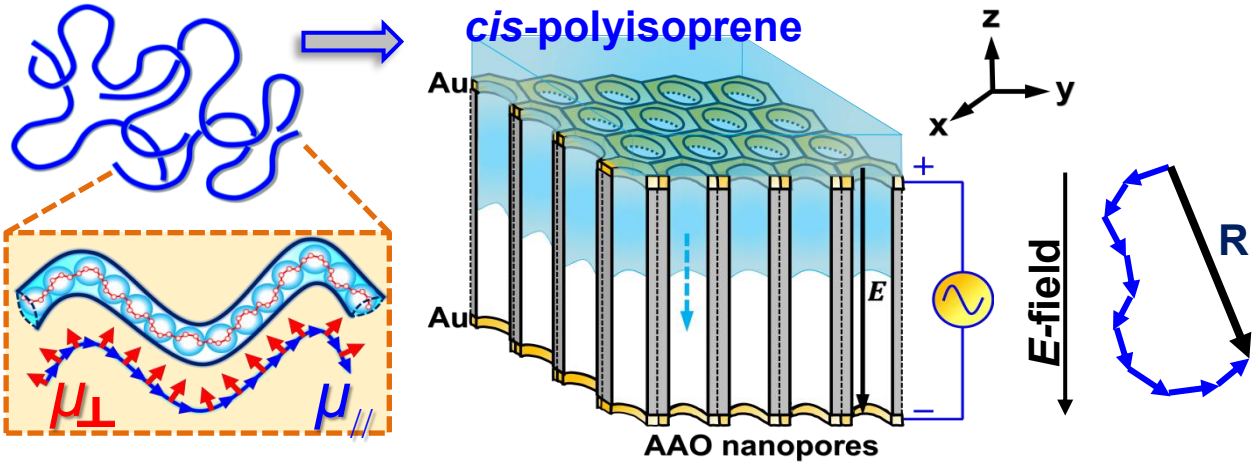

FIG. 1. Schematic of the AAO-sample geometry for the *in situ* imbibition of *cis*-1,4-polyisoprene. In the upper part the dipole moment components along ($\mu_{\parallel}$) and perpendicular ($\mu_{\perp}$) to the chain contour are indicated. The direction of the *E* field with respect to the end-to-end vector (thick arrow) is shown in the right. The electric filed is applied in the *z* direction (flow direction), hence the *z* component of the polarization is detected.

Figure 2a provides fitting examples for bulk PI using a summation of two Havriliak and Negami (HN) functions[13,14] following imbibition. The slower one corresponds to the longest normal mode whereas the faster to the summation of all higher (shorter) modes. We first note that the higher normal modes seem to approach the longest normal mode and second, the longest normal mode is longer than in the bulk. We will return to this point later.

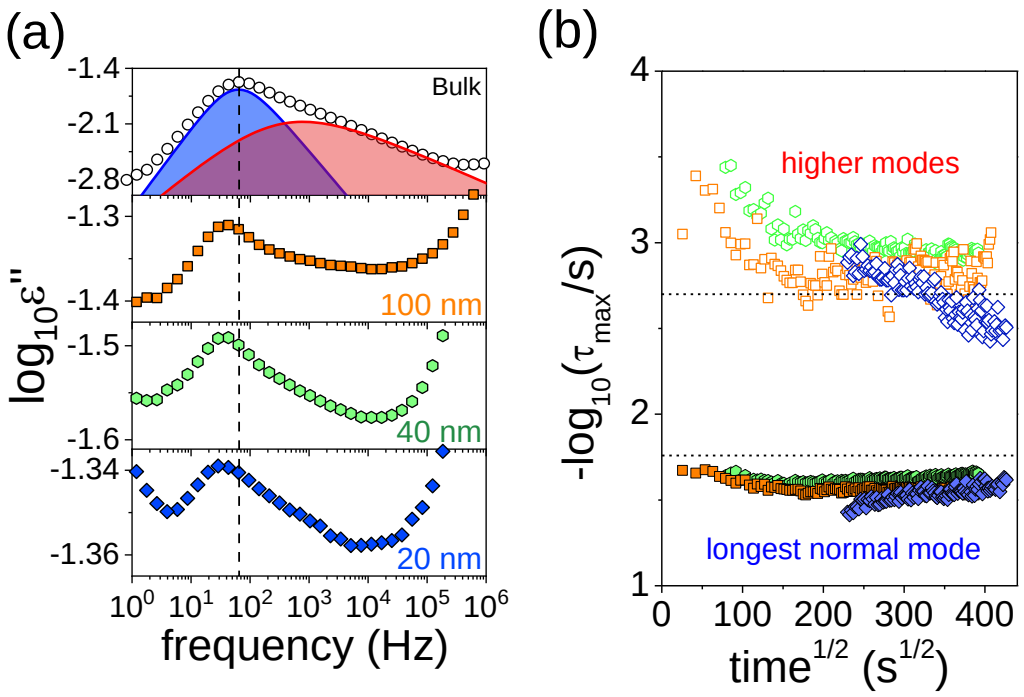

FIG. 2 (a) Dielectric loss curves of bulk and confined PI-42k within AAO pores with pore diameters of 100, 40, and 20 nm at T = 303 K. The black dashed line indicates the peak position of the longest normal mode in bulk PI. Representative fit of the dielectric loss curve for the bulk PI-42k with a summation of two HN functions corresponding to the longest normal mode (blue shaded area) and the summation of shorter normal modes (red shaded area). (b) Evolution of the relaxation times for PI-42k during imbibition inside AAO nanopores as a function of the square-root of time. Same color codes as in (a): 100 nm (orange circles), 40 nm (green squares), and 20 nm (blue rhombi). The short dash lines give the position of the longest normal mode and of the internal modes in the bulk polymer at the same imbibition temperature.

The evolution of the dielectric loss curves at the length scale of the normal modes is depicted in **Figure 3a** for AAO pores with diameter of 40 nm. The radius of gyration of the polymer, R_g, is smaller than the diameter of the pore, d, ($2R_g/d$ = 0.35). The analysis of the dielectric loss curves provides the dielectric strength of the slower (longest normal mode) and faster (higher normal modes) (**Figure 3b**). It shows an initially increasing dielectric strength for both modes, scaling as

$t^{1/2}$, up to 17000 s. This increase is followed by a plateau at longer times (for the slower mode) or even a decrease (for the higher normal modes). Notably, the plateau is absent in the case of the silanized pores (**Figure S2,** Supplemental Material[12]). In parallel, the imbibition lengths, *L*, was measured *ex situ* by optical reflection microscopy and the result is shown in **Figure 3c**. Based on the Lucas - Washburn equation (LWE) developed for Newtonian liquids penetrating a cylindrical capillary of radius *R,* the imbibition length should scale as:[15,16]

$$L(t) = \left(\frac{\gamma R cos\theta}{2\eta}\right)^{\frac{1}{2}} \sqrt{t} \qquad (1)$$

Here, γ is the surface tension, θ is the advancing contact angle, *R* is the pore diameter, η is the viscosity and *t* is the wetting time. Employing the bulk viscosity η_0 = 285 Pa·s (from rheology measurements), the measured surface tension γ_L = 30.1 mN/m and the measured advancing contact angle, θ = 28° we obtain the solid line in **Figure 3c**. The experimental results deviate from the LWE predictions. The *L*-versus-√t plots (**Fig. 3c**) also show the two regimes. Up to *t*=17000 s the polymer melt imbibes like a liquid with the effective viscosities of 4660 Pa·s. For longer times the imbibition can be described by an effective viscosity of 910 Pa·s. This suggests that the polymer penetrates the pores with a 16-fold and threefold higher viscosity than in the bulk. At the same time, the characteristic relaxation time corresponding to the longest normal mode (**Fig. 2b**) is slightly *longer* than in the bulk.

Higher effective viscosities than the bulk are not uncommon during polymer imbibition in nanopores.[17-19] Recently, Doi *et al*[19] constructed a unified theory to describe the imbibition behavior of polymer melts in nanopores. Two different mechanisms were proposed: one is the dead-layer effect due to the adsorption of polymer segments. Strongly adsorbed polymer chains create a smaller effective pore radius ($R_{effective} < R_{AAO}$) giving rise to a higher effective viscosity ($\eta_{effective} > \eta_{bulk}$). The other mechanism relies on the reptation of polymer chains under a pressure gradient. As pores reduce to a size comparable to the thickness of the dead layer (extreme confinement), polymer chain transport is achieved mainly by the reptation of free polymer chains in a network driven by the pressure gradient originating from the capillary force. This mechanism leads to the lower effective viscosity ($\eta_{effective} < \eta_{bulk}$). The nonmonotonic behavior of the effective

viscosity on pore size is the result of the competition between the two mechanisms. This effect found experimentally[17] was well-captured by theory[19].

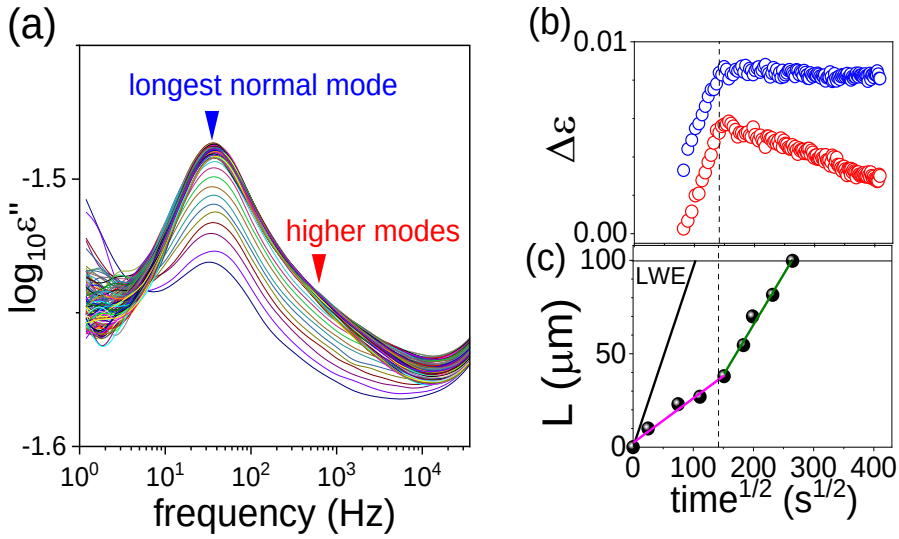

FIG. 3. (a) Evolution of the dielectric loss spectra of PI 42k during imbibition within AAO nanopores with pore diameter of 40 nm at 303 K. (b) The extracted dielectric intensity as a function of the square root of imbibition time. (c) Imbibition lengths extracted via the optical reflection method at selected times. The dashed line is a guide for the eye. The extracted effective viscosity, η_{eff}, in the two regimes is 4660 Pa·s (magenta) and 910 Pa·s (green) for regimes I and II, respectively. The solid black line is the prediction of LWE. The calculation is based on the bulk viscosity η_0 (bulk) = 285 Pa·s; γ_L = 30.1 mN/m; cosθ = 0.88; R = 20 nm.

By contrasting the growing imbibition lengths (**Figure 3c**) with the evolution of dielectric loss (**Figure 3b**) we come to, at a first site, a surprising finding: Although in regime I the polymer advances within the pores following the LWE (albeit with a higher effective viscosity), in regime II, the polymer continues to advance under a *constant* (or even slightly decreasing) dielectric strength. To better understand this result we need to comment on the microscopic factors that influence the dielectric strength for the segmental and normal mode processes. The corresponding $\Delta\varepsilon$'s for the segmental and normal mode processes are[20-27]:

$$\Delta\varepsilon_{segmental} = \frac{1}{3\varepsilon_0} F g \frac{\mu_s^2}{k_B T} \frac{N_A}{V} \tag{2}$$

$$\Delta\varepsilon_{longest\ n.m.} = \frac{4\pi N_A \mu_{NM}^2}{3k_B T} \frac{\langle r^2 \rangle}{M_{PI}} \tag{3}$$

In Eq. 2, for the segmental relaxation, F is the local field, g the Kirkwood-Fröhlich correlation factor, μ_s the dipole moment per molecule and N_A Avogadro's number. Evidently, the dielectric strength for the segmental mode being proportional to the number density of dipoles, is an increasing function of imbibition time up to the complete pore filling. This has been confirmed by following the evolution of the segmental process in PI (at a lower temperature) and in another polymer (poly(*n*-butyl methacrylate)[7]). Hence, the evolution of the segmental process follows approximately the predictions from Eq. 2.

In contrast, the dielectric strength of the chain modes relates to the relaxation of the end-to-end vector, $<r^2>$, the dipole moment per contour length, μ_{NM}, and the chain molecular weight, M_{PI}. The former is prone to chain configurations next to the pore wall (**Figure 4**). For example, adsorbed polymer segments with a fixed train configuration next to the walls do not fluctuate in time and hence do not contribute to the dielectric strength of the chain relaxation. Likewise, segments in looped configurations do not contribute to the dielectric strength as both ends are fixed at the pore walls. Only segments located in the tails can fluctuate in time and hence contribute to the dielectric strength of the chain relaxation. The data shown in **Figure 3** provide unambiguous evidence than only a *portion* of chains (*i.e.*, sub-chains) fluctuate in time during the imbibition process. This should be contrasted with the silanized pores where the dielectric strength is increasing up to complete pore filling. Surface treatment reduces adsorption sites effectively acting as lubricant for the chains [see **Fig. S2,** Supplemental Material[12]]. However, it is puzzling that the obtained relaxation time of the chain relaxation (**Fig. 2**) is not faster – as it would be expected for shorter chain configurations associated with the free ends[27].

Below we provide a plausible *microscopic* scenario (with the help of **Figure 4**) that attempts to reconcile all experimental findings. The figure depicts only a few chains and shows the imbibition process at the beginning (corresponding to regime I) and at later stages (regime II) of the imbibition process. At the beginning, only a small portion of chains are in contact with the pore walls forming trains, loops and some tails (*e.g.*, chain in red). Despite the small fraction of adsorbed segments, the effective pore diameter is reduced and the overall viscosity is increased reflecting the effect of the dead layer. However, the majority of chains are not in contact with the pore walls and hence there exist fluctuations of the end-to-end vector (*e.g.*, chains in green, blue

and yellow). As time progresses within regime I ($t^{1/2} < 150$ $s^{1/2}$) more polymer chains enter the pores and the dielectric strength increases (Eq. 3). At longer times, within regime II, more segments are adsorbed at the pore walls creating more train and longer loop configurations that have as an effect the reduction in the dielectric strength for the normal modes.

The kinetics of irreversible adsorption were first studied theoretically for functionalized polymers in solution[3] and subsequently generalized for thin polymer films (where confinement is one dimensional) by evaluating the thickness of the adsorbed layer[4-6]. It was found that adsorption follows two time regimes; at short annealing times, the thickness (h_{ads}) increases linearly with time due to the available substrate surface scaling as ($h_{ads} \sim N^{1/2} \sim R_g$, N is the degree of polymerization). At longer times, the available surface sites are reduced and chains adsorb by loops with a length that increases in time. The thickness of the adsorbed layer in this case increases slower with time with a logarithmic dependence. As the subchains forming the loops cannot fluctuate, the loops inevitably become dielectrically inactive. As a result, the dielectric strength of normal modes will decrease with time[4]. These effects, obtained under quasiequilibrium conditions, will also affect the dielectric strength of the normal modes in the present case, *e.g.*, during polymer flow. Interestingly, the fast-growing initial dependence and the final slower logarithmic dependence is reminiscent to the square-root time dependence of the imbibition length (Eq. 1) but this point needs to be explored further.

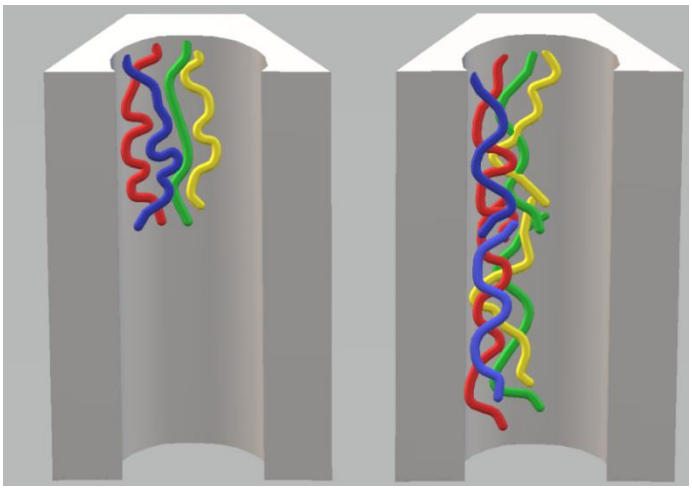

FIG. 4. Schematic of PI imbibition in native nanopores. Four colored chains are shown at initial (left) and additional chains at later stages (right). Initially only a small number of segments corresponding to the red chain are adsorbed to the walls forming some trains, loops and tails. At

latter stages, additional chains have segments in the vicinity of the pore walls and inner chains (*e.g.*, yellow chain) are more entangled with the loops of the adsorbed chains (red or blue chains).

Despite the similarities with 1D confinement there exist, however, a fundamental difference. In the present case, the near constancy of the dielectric strength is a composite effect owing to an increasing number of chains within the pores and a decreasing number of fluctuating chains (**Figure 3b**). Interestingly, the crossover time from **Fig. 3b** corresponds to a timescale much longer than the terminal relaxation time of the bulk polymer [see **Figure S7,** Supplemental Material[12]]. This provides additional support to the fact that other – longer - timescales are involved in the adsorption process. Adsorption, apart from chain diffusion towards the interphase, involves continuous conformational pathways of the chains towards minimizing their free energy.

The existence of a somewhat slower longest normal mode (**Figure 2**) within regime II in the native AAO nanopores is more difficult to explain. It could associate with an increasing density of topological constraints (entanglements). New chains entering the pores (*e.g.*, yellow chains in **Figure 4**) are topologically constrained by the increased numbers of longer loops. This can explain the longer characteristic time for the normal modes during polymer flow (**Fig. 2**). Notably, this effect is absent in the case of silanized AAO (see **Fig. S3,** Supplemental Material[12]). In the absence of adsorption sites long loops are not formed, the chains do not experience extra topological constraints and imbibe with the same time scale as in bulk.

These results will depend on the degree of confinement (*e.g.*, $2R_g/d$). For the same PI-42k entering 100 nm pores [see **Fig. S3,** Supplemental Material[12]] where $2R_g/d \sim 0.14$, the imbibition process has also two regimes with enhanced viscosity than in bulk, however, stage II has now the higher viscosity. In addition, part of the findings could be attributed to changes in glass temperature, T_g, under confinement[28-33]. Having this in mind we studied the segmental dynamics following the *in situ* imbibition (by cooling and subsequent heating runs [see **Fig. S4,** Supplemental Material[12]]). In agreement with earlier studies the segmental dynamics become bimodal below some "critical" temperature ($T_c \sim 226$ K)[31-33]. The high T_g is near (slightly above) the bulk T_g whereas the lower T_g depends on the degree of confinement. The shift in T_g from the bulk value in the latter case can be parameterized as $\Delta T_g \sim -54(2R_g/d)$ [see **Fig. S5,** Supplemental Material[12]] for a range of PI

molecular weights and degrees of confinement. Changes in T_g under confinement have been discussed in terms of increasing interfacial energy for a number of different polymers[28, 29].

Lastly, we compare the current findings with the results from a rheodielectric experiment on the same polymer[34] where the dielectric response was followed during shear. It was shown that the latter is much less sensitive to shear as compared to the strong shear-thinning behavior in the viscoelastic response. Differences in the viscoelastic and dielectric responses were discussed in terms of isochronal orientational cross-correlation of segments under fast shear. We note two differences from the present case. First, viscoelasticity is less important for flow within channels. From the data depicted in **Fig. 3c**, we can extract effective shear rates as $\dot{\gamma} = v/R$ (~ 0.5 rad/s), v is the velocity, R is the pore radius. At such low shear rates, the viscosity that is experienced by the polymer during flow is the zero-shear viscosity [see **Fig. S7,** Supplemental Material[12]]. Second, the measured dielectric strength ($\Delta\varepsilon$) reflects the chain dimension $\langle R_z^2 \rangle$ in the flow direction (**Fig. 1**) as opposed to the shear gradient direction probed in rheodielectrics.

In conclusion, the imbibition kinetics of entangled *cis*-1,4-PI was studied, for the first time during flow, by *in situ* nanodielectric spectroscopy, under conditions of confinement ($0.14 < 2R_g/d < 0.35$) and as a function of pore surface treatment. For native AAO pores, imbibition follows two time regimes both with increased effective viscosity relative to bulk. Within the later stages the dielectric strength of the longest normal mode remains constant despite the fact that more chains are entering the pores. We have discussed this finding by a microscopic picture that considers the competition from an increasing number of chains entering the pores (that increases the dielectric strength) and a decreasing number of fluctuating chains (that decreases the dielectric strength). At the same time, the longest normal mode is somewhat longer than in bulk within native pores but not in silanized pores. This could reflect an increased density of topological constraints with time in the former case.

In situ dielectric spectroscopy provides us with access to length scales and timescales (from the local segmental to internal chain modes, and to the longest normal mode) under nonequilibrium conditions (during flow) never considered before. The method and current results provided unambiguous evidence for growing interfacial interactions. Taming the strength of interfacial interactions under such nonequilibrium conditions could help towards designing polymer interfaces with controlled physical properties.

3.5 References

(1) S. Granick, *Science* **253**, 1374 (1991).

(2) Advances in Dielectrics. *Dynamics in Geometrical Confinement* F. Kremer (Ed.), (Springer, Berlin, 2014).

(3) C. Ligoure and L. Leibler, *J. Phys.* **51**, 1313 (1990).

(4) S. Napolitano and M. Wübbenhorst, *Nature Communications* **2**, 260 (2011).

(5) C. Housmans, M. Sferrazza and S. Napolitano, *Macromolecules* **47**, 3390 (2014).

(6) D.N. Simavilla, A. Panagopoulou and S. Napolitano, *Macromol. Chem. Phys.* **219**, 1700303 (2018).

(7) C.-H. Tu, M. Steinhart, H.-J. Butt and G. Floudas, *Macromolecules* **52**, 8167 (2019).

(8) A. Serghei, D. Chen, D.H. Lee and T. P. Russell, *Soft Matter* **6**, 1111 (2010).

(9) A. Serghei, J.L. Lutkenhaus, D.F. Miranda, K. McEnnis, F. Kremer and T. P. Russell, *Small* **6**, 1822 (2010).

(10) A. Serghei, W. Zhao, X. Wei, D. Chen and T. P. Russell, *Eur. Phys. J.: Spec. Top.* **189**, 95 (2010).

(11) H. Masuda and K. Fukuda, *Science* **268**, 1466 (1995).

(12) See Supplemental Materials at http://link.aps.org/supplemental/ for further details on the technique, sample preparation and data evaluation, additional in situ data as a function of surface treatment, results on the segmental dynamics following imbibition and the T_g-dependence on confinement.

(13) F. Kremer and A. Schönhals, *Broadband Dielectric Spectroscopy* (Springer, Berlin, 2002).

(14) G. Floudas, M. Paluch, A. Grzybowski and K.L. Ngai, *Molecular Dynamics of Glass-Forming Systems: Effects of Pressure* (Springer, Berlin, 2011).

(15) R. Lucas, *Colloid Polym. Sci.* **23**, 15 (1918).

(16) E.W. Washburn, *Phys. Rev.* **17**, 273 (1921).

(17) Y. Yao, S. Alexandris, F. Henrich, G. Auernhammer, M. Steinhart, H.-J. Butt and G. Floudas, *J. Chem. Phys.* **146**, 203320 (2017).

(18) Y. Yao, Y. Suzuki, J. Seiwert, M. Steinhart, H. Frey, H.-J. Butt and G. Floudas, *Macromolecules* **50**, 8755 (2017).

(19) Y. Yao, H.-J. Butt, G. Floudas, J. Zhou and M. Doi, *Macromol. Rapid Commun.* **39**, 1800087 (2018).

(20) K. Adachi and T. Kotaka, *Prog. Polym. Sci.*, **8**, 585 (1993).

(21) K. Adachi and T. Kotaka, *Macromolecules* **18**, 466 (1985).

(22) D. Boese, F. Kremer and L.J. Fetters, *Macromolecules* **23**, 1826 (1990).

(23) D. Boese and F. Kremer, *Macromolecules* **23**, 829 (1990).

(24) A. Schönhals, *Macromolecules* **26**, 1309 (1993).

(25) G. Floudas, G., C. Gravalides, T. Reisinger and G. Wegner, *J. Chem. Phys.* **111**, 9847 (1999).

(26) G. Floudas, G., S. Paraskeva, N. Hadjichristidis, G. Fytas, B. Chu and A.N. Semenov, *J. Chem. Phys.* **107**, 5502 (1999).

(27) L. Petychakis, G. Floudas and G. Fleisher, *Europhys. Lett.* **40**, 685 (1997).
(28) S. Alexandris, P. Papadopoulos, G. Sakellariou, M. Steinhart, H.-J. Butt and G. Floudas, *Macromolecules* **49**, 7400 (2016).
(29) A. Talik, M. Tarnacka, I. Grudzka-Flak, P. Maksym, M. Geppert-Rybczynska, K. Wolnica, E. Kaminska, K. Kaminski and M. Paluch, *Macromolecules* **51**, 4840 (2018).
(30) S. Alexandris, G. Sakellariou, M. Steinhart and G. Floudas, *Macromolecules* **47**, 3895 (2014).
(31) C. Politidis, S. Alexandris, G. Sakellariou, M. Steinhart and G. Floudas, *Macromolecules* **52**, 4185 (2019).
(32) M. Tarnacka, K. Kaminski, E.U. Mapesa, E. Kaminska and M. Paluch, *Macromolecules* **49**, 6678 (2016)
(33) E.C. Glor, G.V. Angrand and Z. Fakhraai, *J. Chem. Phys.* **146**, 203330 (2017).
(34) H. Watanabe, S. Ishida and Y. Matsumiya, *Macromolecules* **35**, 8802 (2002).

3.6 Supporting material

Reflection Optical Microscopy.

The infiltration process was followed for specific time intervals. Subsequently, the top layer was removed, the AAO templates were cross sectioned and the imbibition length was determined from the cross sections by reflection optical microscopy (ROM) (Zeiss Axiotech vario). **Figure S1**, provides representative images of cross-sectioned AAO templates for different time intervals. In ROM, the optical contrast originates from the change in the index of refraction between the empty nanopores and the polymer infiltrated part. Typically for each cross section the imbibition lengths were obtained at 10 different positions.

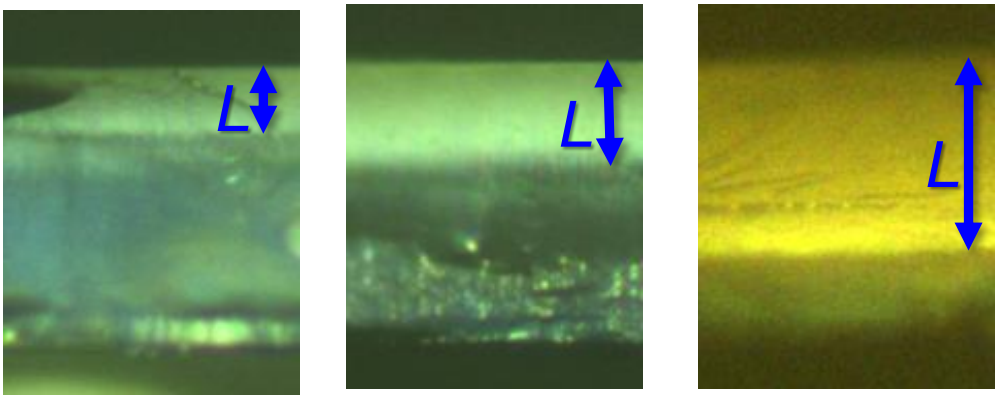

FIG. S1. Optical images showing the imbibition length of PI 42k within AAO with pore diameter of 40 nm at 30 ºC for different time periods: (left) 111 $s^{1/2}$, L = 27 μm, (center) 150 $s^{1/2}$, L = 38 μm, and (right) 199 $s^{1/2}$, L = 70 μm. The regions specified by blue arrows represent the areas filled with PI 42k.

Dielectric Spectroscopy.

Dielectric spectroscopy (DS) measurements were performed at different temperatures in the ranges from 183 K to 393 K, at atmospheric pressure, and for frequencies in the range from $10^{-2} - 10^{7}$ Hz. Measurements were made with a Novocontrol Alpha frequency analyzer composed of a broadband dielectric converter and an active sample cell. For the bulk material, DS measurements were carried out in the usual parallel plate geometry with electrodes of 20 mm in diameter and a sample thickness of 50 μm maintained by Teflon spacers. For the *in situ* imbibition kinetic

experiments, a gold layer (thickness 35 nm) was sputtered on both sides of the AAO templates as top and bottom electrodes (**Figure 1**). Two types of AAO surfaces were examined. One (the untreated) where templates were placed in an oven under vacuum at a temperature of 443 K for 8-10 h in order to remove the majority of OH groups from the AAO surface. Another one (the silanized) with a treated surface with trichloro(1H,1H,2H,2H-perfluorooctyl)silane (for 5 min under vacuum followed by heating to 423 K in order to remove any excess silane). In the kinetic experiments the investigated frequency range was restricted in the range 1-10^6 Hz to facilitate probing the faster kinetics. In all cases, the complex dielectric permittivity $\varepsilon^* = \varepsilon' - i\varepsilon''$, where ε' is the real and ε'' is the imaginary part, was obtained as a function of frequency ω and temperature T, *i.e.*, $\varepsilon^*(T, \omega)$. **Figure 2a** provides fitting examples for bulk PI using the empirical equation of Havriliak and Negami (HN):

$$\varepsilon^*_{HN}(\omega, T) = \varepsilon_\infty(T) + \sum_{k=1}^{2} \frac{\Delta\varepsilon_k(T)}{\left[1 + \left(i\omega\tau_{HN,k}(T)\right)^{m_k}\right]^{n_k}} + \frac{\sigma_0(T)}{i\varepsilon_f\omega} \quad \text{(S1)}$$

Here, k indicates the process under investigation, $\Delta\varepsilon_k(T)$ is the relaxation strength, $\tau_{HN,k}$ is the relaxation time of the equation, m_k, n_k ($0 < m_k$, $m_k n_k \leq 1$) describe the symmetrical and asymmetrical broadening of the distribution of relaxation times and ε_∞ is the dielectric permittivity at the limit of high frequencies. The relaxation times at maximum loss (τ_{max}) are presented herein and have been analytically obtained from the Havriliak–Negami equation as follows:

$$\tau_{max,k} = \tau_{HN,k} \sin^{-1/m}\left(\frac{\pi m_k}{2(1+n_k)}\right) \sin^{1/m}\left(\frac{\pi m_k n_k}{2(1+n_k)}\right) \quad \text{(S2)}$$

At lower frequencies, ε'' rises due to the conductivity ($\varepsilon'' = \sigma/(\omega\varepsilon_f)$, where σ is the dc conductivity and ε_f the permittivity of free space). The conductivity contribution has also been taken into account during the fitting process.

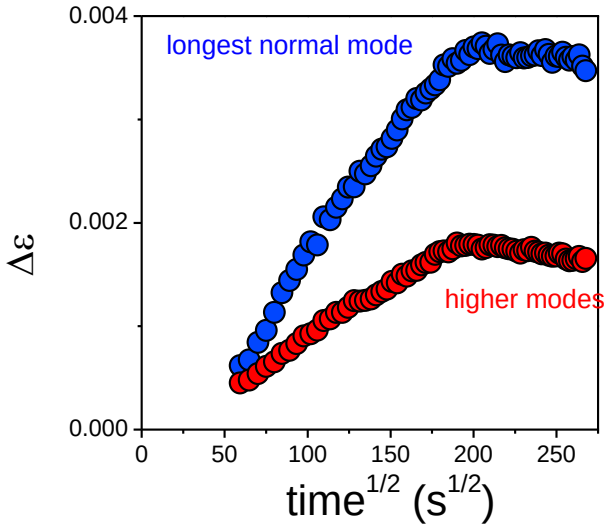

Figure S2. Imbibition of PI 42k in treated (silanized) pores. Evolution of the dielectric loss at the peak frequency during imbibition within AAO nanopores with pore diameter of 40 nm at 303 K as a function of the square root of imbibition time.

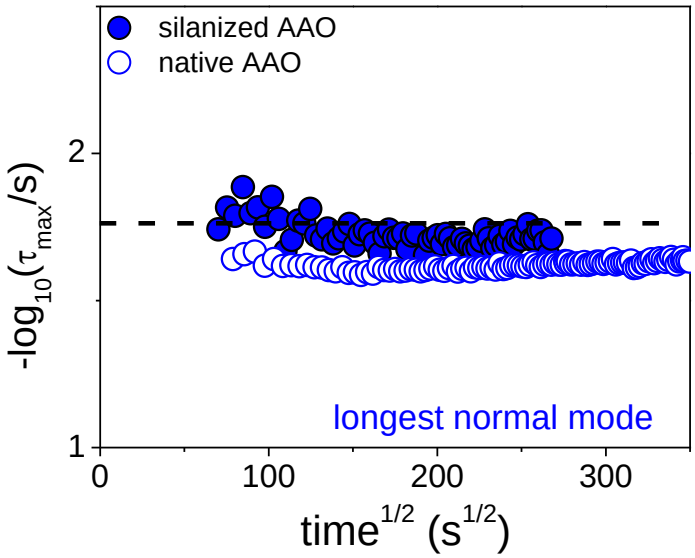

Figure S3. Evolution of relaxation times corresponding to the longest normal mode for PI 42k in silanized (filled circles) and native (open circles) AAO pores with pore diameter of 40 nm at 303 K as a function of the square root of imbibition time. The dashed line gives the relaxation time of the longest normal mode in the bulk polymer.

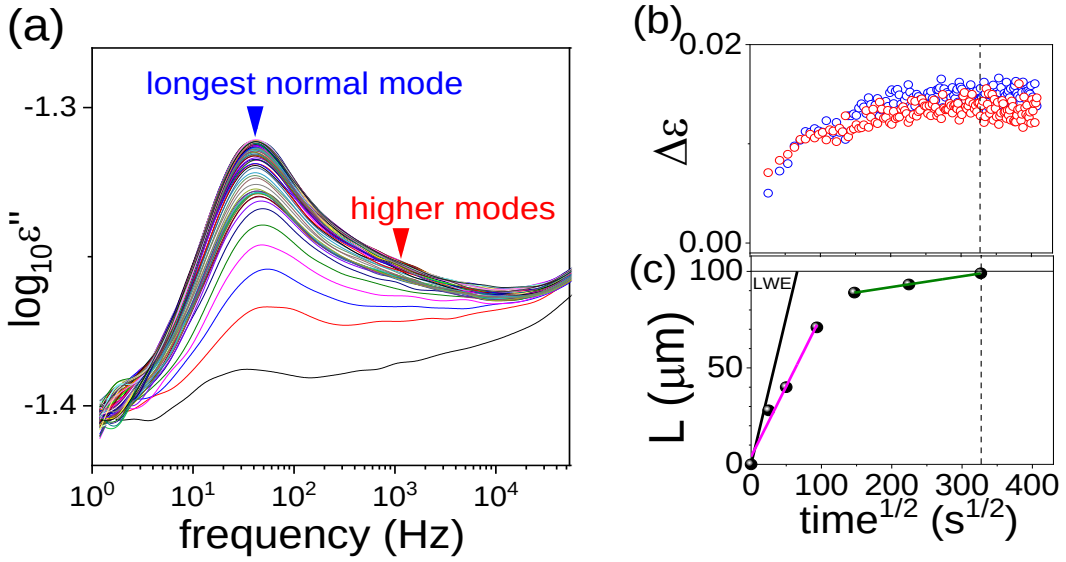

Figure S4. (a) Evolution of the dielectric loss curves of PI 42k during imbibition within AAO nanopores with pore diameter of 100 nm at 303 K. (b) Evolution of the dielectric loss at the peak frequency and pf the extracted dielectric intensity (inset) as a function of the square root of imbibition time. (c) Imbibition lengths extracted via the optical reflection method (yellow points) at selected times. The dashed line is a guide for the eye. The solid black line is the prediction of LWE. The calculation is based on the bulk viscosity η_0 (bulk) = 285 Pa·s; γ_L = 30.1 mN/m; cosθ = 0.88; R = 50 nm.

Segmental dynamics following imbibition

Subsequent cooling/heating scans following the *in situ* imbibition can provide the state of the segmental dynamics under confinement. The results are discussed with respect to **Figure S5**. In the larger pores (100 nm) there exists a single segmental process that is faster than in bulk PI (*i.e.*, lower glass temperature). In the smaller pores however (40 nm), the dielectric loss curves are clearly bimodal (**Figure S5a**) giving rise to a "lower" and a "higher" glass temperature, respectively. It is noteworthy that the bimodal distribution only displays on cooling/heating scans below a "critical" temperature T_c ~ 226 K (**Figure S5**). The bimodal character of the PI segmental dynamics has been discussed earlier.

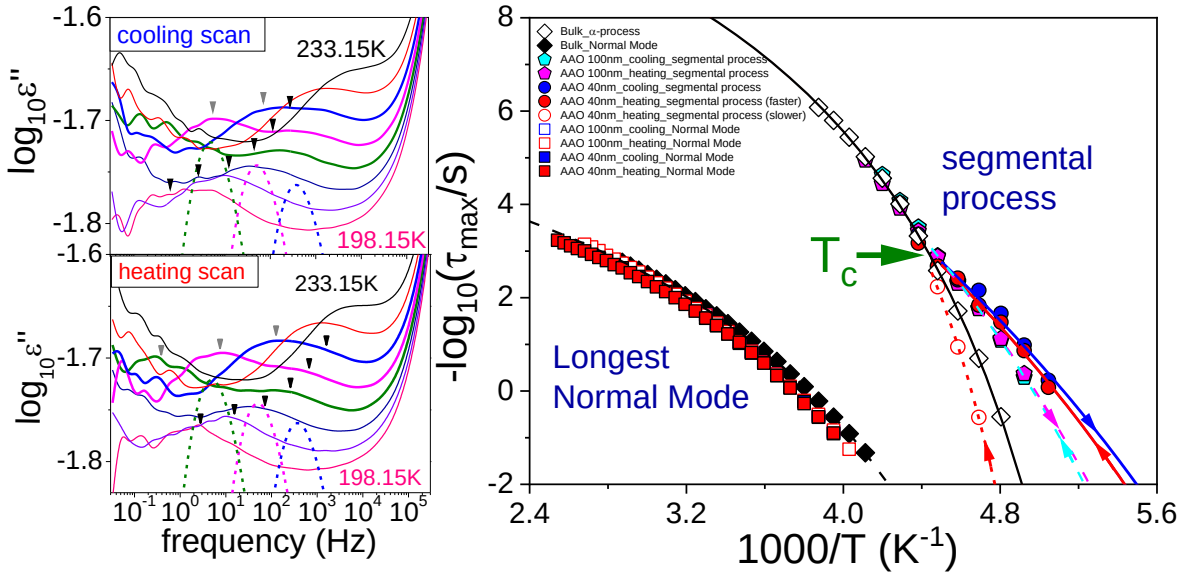

Figure S5. (a) Representative dielectric loss curves of bulk (dashed lines) and cooling/heating loss curves of PI 42k located inside AAO with pore diameter of 40 nm following imbibition (solid lines). Selected temperatures range from 198.15 K to 233.15 K with a step of 5 K. The same color code in curves of bulk and confined PI 42k is used: 223.15K (blue), 218.15K (magenta), and 213.15K (orange). The loss curves are bimodal and the *faster* (*slower*) segmental processes are indicated by black (gray) arrows. The rise of the dielectric loss at high frequencies comes from the AAO background. (b) Relaxation diagram showing the temperature dependence of the segmental and longest chain relaxation times for the bulk (rhombi) and under confinement within different pore sizes: (pentagons): 100 nm pores; (circles): 40 nm pores.

Figure S6 shows the change in glass temperature in confinement from the bulk T_g as a function of inverse pore diameter ($1/d$) and degree of confinement ($2R_g/d$) for PI-42k in comparison to other entangled PIs. In the case of PI-42k and for the smaller pore diameters only the lower glass temperature is depicted. All data nicely collapse onto a single curve that can be parameterized as $\Delta T_g \sim -54 \times (2R_g/d)$ (**Figure S6b**). The reduced glass temperature under confinement has been discussed in terms of an increasing interfacial energy for a number of polymers.

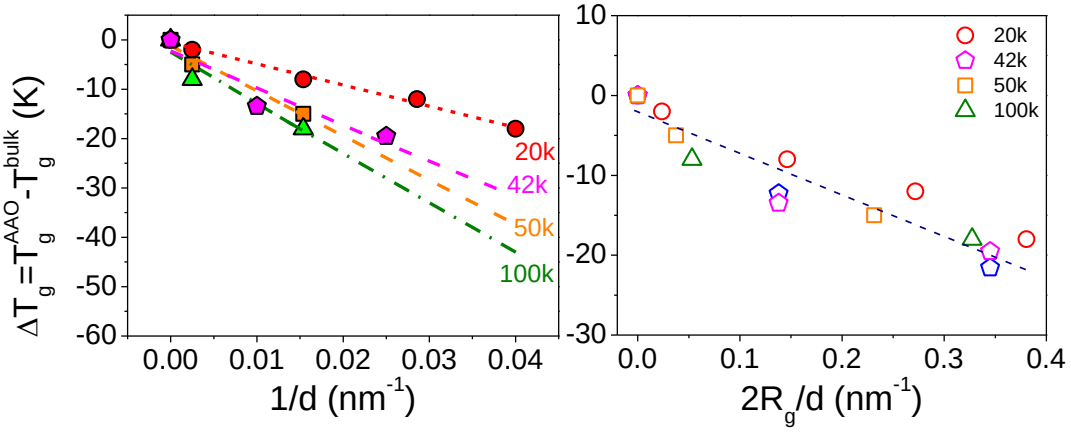

Figure S6. Dependence of ΔT_g ($=T_g^{AAO}- T_g^{bulk}$) on (left) inverse pore diameter and (right) the degree of confinement, defined by the ratio of molecular size ($2R_g$) to the pore diameter for entangled PIs. The T_g value of PI 42k refers to the lower glass temperature extracted from Figure S5. T_g is defined as the temperature where the segmental relaxation time is at time ~ 10^2 s. The T_g values of other entangled PIs (*i.e.*, 20 kg·mol^{-1}, 50 kg·mol^{-1} and 100 kg·mol^{-1}) are from literature.

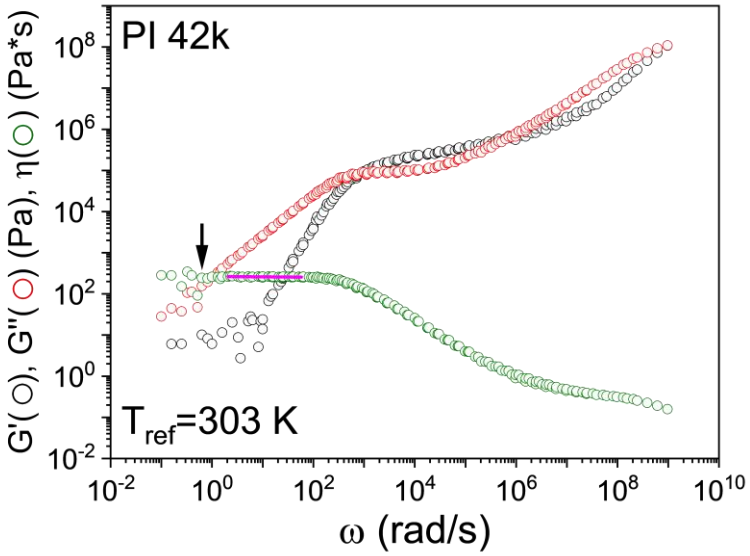

Figure S7. Master curve construction for PI 42k at a reference temperature of 303 K. The vertical arrow indicates the average shear rate experienced by the polymer during flow (corresponding to the zero-shear viscosity plateau indicated by the magenta line).

Chapter 4. Polymers under 2-D Confinement: Flow of Polymer Melts at the Nanoscale

This chapter has been published as a chapter in ACS Symposium Book — Broadband Dielectric Spectroscopy: A Modern Analytical Technique.

Chien-Hua Tu, Martin Steinhart, Hans-Jürgen Butt, and George Floudas
ACS Symposium Series, 1375(9), 203-221
DOI: 10.1021/bk-2021-1375.ch009

Abstract

With the recently developed nanofluidic method one is able to follow *in situ* the imbibition of polymers into nanotubes. Therefore, pieces of nanoporous anodic aluminum oxide (AAO) are coated with gold electrodes on the top and bottom face. The dielectric response is recorded while the polymer imbibes into the cylindrical nanopores of ≈100 μm length and 12 - 200 nm radius. The method provides simultaneous access to the imbibition kinetics and the associated polymer dynamics (at the segmental and chain length scales) during polymer flow. Two models- a parallel and a series model- with different interactions between the polymer/AAO are investigated with respect to the evolution of the dielectric strength and of the characteristic relaxation times. The model predictions are compared and tested against existing results from two polymers: a polar polymer (poly(*n*-butyl methacrylate), PnBMA) and a non-polar polymer (*cis*-1,4-polyisoprene, PI). In the case of PI, where the longest normal mode was probed, it was shown that the dielectric strength during imbibition deviates from the usual dependence. The results are discussed in terms of increasing adsorption sites with time. We further discuss the potential of the method in current polymer physics problems of interest.

4.1 Introduction

Polymer properties may deviate from bulk when the polymer is confined into sizes close to or even below the radius of gyration. Most of these deviations originate from the interactions between the polymer and the confining medium at the vicinity of the interface[1]. Discerning these effects can bring forth certain advantages in the design and eventually fabrication of nanostructured devices. Several confining geometries (1D, 2D, and 3D) have been employed to address the issue of confinement[1]. A relatively recent development in this direction has been the construction of model 2D confining tubes based on self-ordered nanoporous anodic aluminum oxide, better known as AAO[2, 3]. AAO templates contain arrays of parallel cylindrical nanopores uniform in length and diameter where polymers can be infiltrated by capillary action[2, 3].

Our concern here is the exact process of polymer imbibition in AAO. For Newtonian liquids, nearly a century ago, Lucas and Washburn proposed an equation (known as LWE) to describe the capillary imbibition[4, 5]:

$$h(t) = \sqrt{\frac{\gamma R \cos\theta}{2\eta}}\sqrt{t} \qquad (1)$$

Here, $h(t)$ is the imbibition length (up to ~ 100 μm in the present system), R is the capillary radius (200 nm and 20 nm in the present study), γ is the surface tension, θ is the advancing contact angle, η is the viscosity and t is the imbibition time. Although successfully capturing the imbibition of Newtonian liquids, eq. 1 fails to describe the capillary imbibition of complex liquids like polymers. Recently, a unified theory constructed by Doi[6] proposed that the imbibition of polymer melts inside nanopores can be described via two mechanisms: one is the *dead-layer* effect due to the strong adsorption of polymer chains. This effect creates a smaller effective pore radius ($R_{effective} < R_{AAO}$) and gives rise to a higher effective viscosity ($\eta_{effective} > \eta_{bulk}$) during flow. The other mechanism relies on the *reptation* model under a pressure gradient. As pores reduce to a size comparable to the thickness of the dead zone (extreme confinement), polymer transport proceeds by the *reptation* of free polymer chains in a network. It is driven by the pressure gradient originating from the capillary pressure at the front. This mechanism leads to a lower effective viscosity ($\eta_{effective} < \eta_{bulk}$). The competition of the two mechanisms gives rise to a non-monotonic behavior for the dependence of the effective viscosity on inverse pore size. Compared with the

experimental results[6,7], the reversal in imbibition of melts of poly(ethylene oxide) was qualitatively captured by the theory.

Despite several studies of polymer dynamics under 2D confinement (including shifts in the glass temperature and the global chain motion) little is known on how polymers flow within narrow pores. Comprehensive understanding of the imbibition process requires not only knowledge of the effective viscosity but also the relevant polymer dynamics *during* flow. The only problem is that in such experiments the polymer chains are away from equilibrium. However, most processes in our daily life are away from equilibrium and certainly the design of nanomaterials and nanostructures requires a deep understanding of how polymers flow next to surfaces and in the presence of strong boundary interactions. One possible method of following polymer imbibition *in situ* was proposed recently[8]. The method is based on an interferometric technique by detecting changes of the refractive index of the polymer/AAO[8]. However, despite its simplicity, it requires several calibration steps with liquids of known viscosity.

An important step in this direction has been the development of a nanofluidic method, based on dielectric spectroscopy (DS)[9-15]. The principle of the method is based on measuring the capacitance. The top and bottom side of a piece of AAO are coated with a metal and form the electrodes of a plate capacitor, C ($C=\varepsilon\varepsilon_0 A/d$; where ε is the dielectric permittivity of the polymer, ε_0 the vacuum permittivity, A the area and d is the polymer thickness) during flow. As more polymer is dragged into the pores, the capacitance is increased by virtue of the dielectric permittivity. The method provides access to the imbibition length through the measured dielectric strength. The latter can be compared with independent *ex situ* measurements with *e.g.*, reflection optical microscopy. At the same time, DS is capable of measuring the polymer dynamics at the segmental or chain lengths during flow. Despite the obvious importance of the method, there exist only a few studies on polymer imbibition: mainly on poly(2-vinyl pyridine)[9], and poly(vinylidene fluoride-*co*-trifluoroethylene) (PVDF-TrFE)[12]. In these studies the imbibition kinetics were found to scale as $t^{1/2}$, as predicted by the LWE. However, the effective viscosity was not extracted, which precluded a stringent test of the LWE.

In the present investigation, we employ different models that take into account the interactions of the polymer with the AAO surface and discuss the evolution of the dielectric strength and of the characteristic times during flow. The model predictions are compared and tested against

existing results from two polymers. For this purpose we employ a polar and a non-polar polymer based, respectively, on poly(*n*-butyl methacrylate) (PnBMA) and *cis*-1,4-polyisoprene (PI) and discuss the different possibilities and limitations of the technique. At the end we provide an outlook of the potential of the method to address some important polymer physics questions.

4.2 The Materials

A poly(*n*-butyl methacrylate) (PnBMA) homopolymer with M_n = 4.9 kg·mol^{-1}, M_w = 5.4 kg·mol^{-1}, T_g=285 K and narrow dispersity *Đ* (M_w/M_n)=1.11 was purchased from PSS Polymer Standards Service GmbH and used without further purification. A *cis*-1,4-polyisoprene (PI) homopolymer with M_n = 42 kg·mol^{-1}, M_w = 43 kg·mol$^{-1,}$ and narrow dispersity *Đ* (M_w/M_n) = 1.04, T_g = 203 K was synthesized in house. Two types of AAO templates were used (**Figure 1**) as these are used from various research groups: (i) self-ordered AAO (pore diameters of 25, 35, 65 and 400 nm; pore depth about 100 μm) with one closed end (the other was attached to an Al substrate) prepared following previously reported procedures[2, 3]. (ii) AAO templates with both-ends open purchased from InRedox (Longmont, USA). Pore diameters and corresponding porosities were 100 nm (24±3%), 40 nm (12±2%) and 20 nm (11±2%), respectively. Prior to infiltration, all AAO templates were placed in an oven under vacuum at a temperature of 443 K for 8-10 h. This procedure is essential as it produces reproducible surface properties and removes the majority of OH groups from the AAO surface.

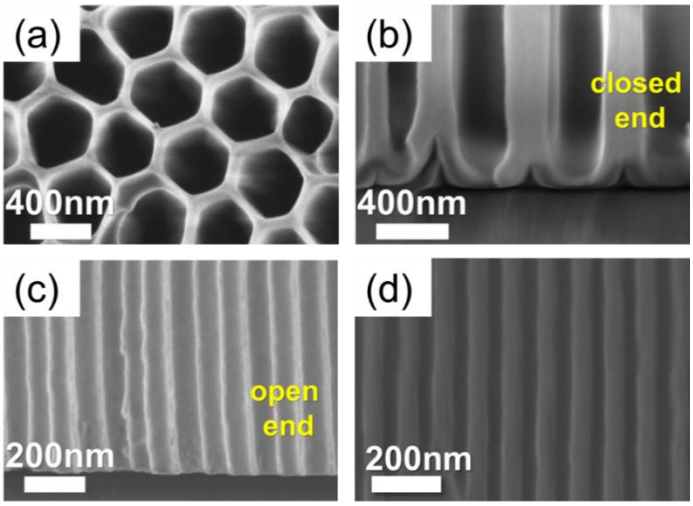

Figure 1. SEM figures showing the (a) top surface of AAO 400 nm pores and cross sections of AAO pores with diameter of (b) 400 nm, (c) 65 nm, and (d) 40 nm. (d) represents the template from InRedox.

4.3 The Method – Nanodielectric Spectroscopy

Dielectric spectroscopy (DS) is employed to determine the dynamics of bulk and confined PnBMA and PI. The instrument is equipped with a Novocontrol Alpha frequency analyzer composed of a broadband dielectric converter and an active sample head. For bulk samples, polymers are embedded between two stainless steel electrodes with a diameter of 20 mm accompanied with a Teflon spacer of 50 μm to maintain the thickness. The sample preparation for *in situ* nanodieletric spectroscopy is more complicated (**Figure 2**). First, the AAO templates are sputtered with a gold layer with a thickness of 35 nm on the top side (or even rear side for templates from InRedox templates). The aim of the sputtered Au layers is to serve as electrodes, which can build a complete circuit across the template. Sputtering was made under high vacuum (better than 2×10^{-5} Pa) by Bal-tec MED 020 with a current density of 40 mA. The high vacuum environment is to ensure the uniformity of the sputtered Au layer. The current density is optimized to produce Au grains with appropriate size (too big will block the AAO pores; too small will hinder the current transport). Following sputtering, scanning electron microscopy (SEM) is used to determine the distribution of Au grains on the inner surface of the AAO templates (**Figure 2**). In addition to a uniform film deposited on top of AAO templates, Au particles are inevitably found to fall within pores (depth of about 380 nm). However, given the high aspect ratio (> 10^3) of nanopores, any inhomogeneities in the field lines can be neglected. Subsequently, a thin film or a drop of polymer is deposited on the top of the template. The frequency range also needs to be selected. A broad frequency range from $10^{-2} - 10^7$ Hz is normally used in bulk DS measurements. In contrast, a narrower frequency range, from $10{-}10^6$ Hz, is applied to probe the faster imbibition kinetics since a shorter time is needed. Typically, the applied voltage is below 1 Volt. The dielectric function depends on frequency, temperature and time. At a given time and temperature, it can be fitted by the empirical equation of Havriliak and Negami (HN):

$$\varepsilon^*_{HN}(\omega,T,t) = \varepsilon_\infty(T,t) + \sum_{k=1}^{2} \frac{\Delta\varepsilon_k(T,t)}{\left[1+\left(i\omega\tau_{HN,k}(T,t)\right)^{\alpha(t)}\right]^{\gamma(t)}} + \frac{\sigma_0(T,t)}{i\varepsilon_0\omega} \qquad (2)$$

Here, k indicates the process under investigation, $\Delta\varepsilon_k(T,t)$ is the relaxation strength, $\tau_{HN,k}$ is the Havriliak-Negami relaxation time, α, γ ($0 < \alpha$, $\alpha\gamma \leq 1$) are shape parameters describing the symmetric and asymmetric broadening of dielectric function (with the high frequency slope in a log-log representation being $\alpha\gamma$), and ε_∞ is the dielectric permittivity at the limit of high

frequencies. At lower frequencies, ε'' rises due to the conductivity ($\varepsilon'' = \sigma_0/(\omega\varepsilon_0)$, where σ_0 is the dc conductivity and ε_0 the vacuum permittivity).

There are also certain limitations in following the imbibition kinetics by Nanodielectric Spectroscopy. It requires a judicious choice of a polymer with a suitable glass temperature, T_g, and with a bulk viscosity that is neither too low nor too high at the imbibition temperature, so that, the process falls within the experimental frequency window. The frequency window may also be limited by fast kinetics. These are parameters that need to be considered in designing any experiment.

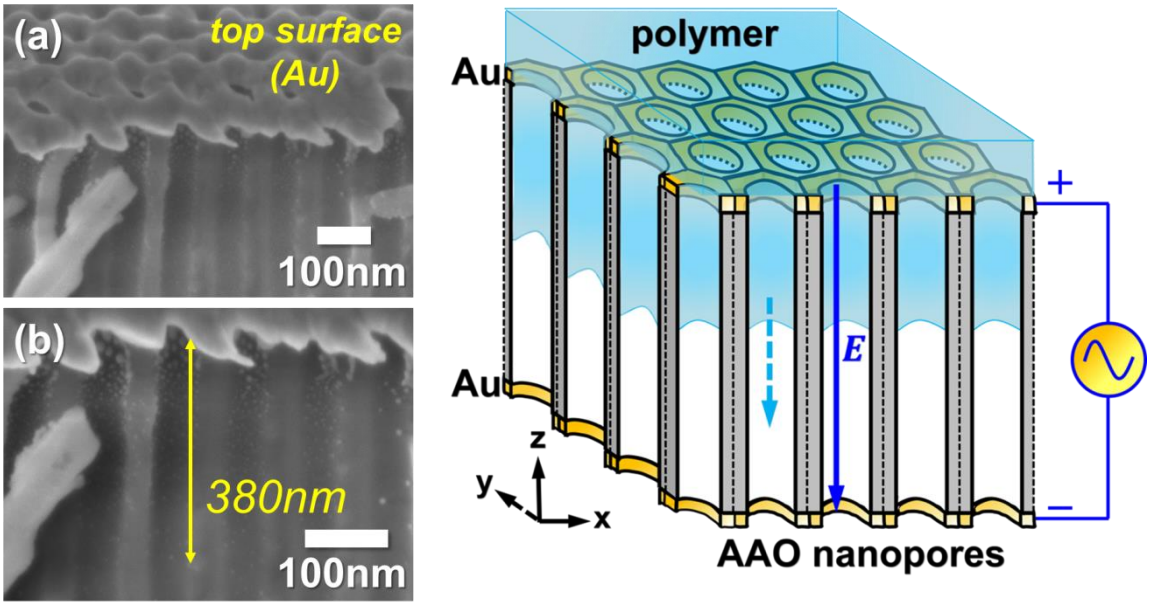

Figure 2. (Left top and bottom) SEM figures showing the top surface and cross section of AAO pores with a dimeter of 65nm after Au sputtering. The left bottom figure is a zoom-in picture. Au particles are distributed at the top of the nanopores within a distance of 380 nm. (Right) Schematic of the experimental setup of in-situ nanodielectric spectroscopy. The blue arrow indicates the direction of the applied electric field, E (along the nanopores, z-axis). The cyan dashed arrow indicates the flow direction of the polymer meniscus within the AAO nanopores. The *xyz* coordinate represent the laboratory axis.

4.4 Simulation of the Imbibition Process

Despite the simplicity of the method several factors need to be considered, including the porosity of the templates, the presence of closed ends and the possibility of entrapped air, the background signal from the AAO, the polarity of the polymer and the interactions between the polymer and

the AAO walls. The Debye model function is used to simulate the frequency dependence of complex dielectric permittivity ($\varepsilon^* = \varepsilon' - i\varepsilon''$) of a polar and a nonpolar polymer:

$$\varepsilon^*_{polymer} = \Delta\varepsilon_{polymer} \frac{1}{1 + i\omega\tau_D} + \varepsilon_{polymer,\infty} \tag{3}$$

with real (ε') and imaginary (ε'') parts

$$\varepsilon'_{polymer} = \frac{\Delta\varepsilon_{polymer}}{1 + (\omega\tau_D)^2} + \varepsilon_{polymer,\infty} \tag{4}$$

$$\varepsilon''_{polymer} = \Delta\varepsilon_{polymer} \frac{\omega\tau_D}{1 + (\omega\tau_D)^2} \tag{5}$$

Here, $\Delta\varepsilon_{polymer}$ is the dielectric strength of the polymer, $\varepsilon_{polymer,\infty}$ is the dielectric permittivity at very high frequencies, and τ_D is a characteristic relaxation time (here set to 1s). For the polar (nonpolar) polymer cases, the following exemplary values were employed: $\Delta\varepsilon_{polymer}$=1 (0.1), and $\varepsilon^*_{polymer,\infty}$ = 2.25 for both cases. To provide a comprehensive analysis the equivalent capacitance representation is necessary. Here, two models are considered with respect to the interaction of the polymer/AAO (*e.g.*, by "interaction" we mean the area of contact and the strength of polymer/AAO interaction at the interface: (i) a parallel model with weak interactions in the horizontal direction (*e.g.*, the direction perpendicular to the nanotubes), and (ii) a series model with strong interactions in the horizontal direction. In the parallel model, the capacitance of the polymer (C_1) and air (C_2) are connected in series, and the combinational capacitance of polymer/air (C_{12}) connects in parallel with AAO (C_3) (**Figure 3a**). In the series model, the combinatorial capacitance of the polymer (C_1) and AAO (C_3), C_{13} connect in series with the combined air/AAO capacitance (C_{23}) (**Figure 3b**).

Parallel Model: Weak Interaction between Polymer and AAO in the Horizontal Direction

In terms of the equivalent circuit, we have the following equations,

$$\frac{1}{C_{12}} = \frac{1}{C_1} + \frac{1}{C_2} \tag{6}$$

$$C_{123} = C_{12} + C_3 \tag{7}$$

From the definition of capacitance (*i.e.*, $C = \varepsilon A/d$) it follows that,

$$\varepsilon^*_{12} = \frac{D\varepsilon^*_1}{d_1 + d_2\varepsilon^*_1} \tag{8}$$

$$\varepsilon_{123}^{*} = \varepsilon_{12}^{*}\varphi_{12} + \varepsilon_{3}^{*}\varphi_{3} \tag{9}$$

φ_{12} represents the porosity of AAO templates, $\varphi_3 (= 1 - \varphi_{12})$ is the remaining area of the template, and *D* is the full length of AAO nanopores. After some arrangements, we can obtain the following equation for the complex dielectric permittivity:

$$\varepsilon_{123}^{*} = \left[\frac{D\varepsilon_{1}^{*}}{d_1 + d_2\varepsilon_{1}^{*}}\right]\varphi_{12} + \varepsilon_{3}^{*}\varphi_{3} \tag{10}$$

Therefore, the imaginary part is

$$\varepsilon_{123}'' = \frac{d_1\varepsilon_{1}''\varphi_{12}}{(d_1 + d_2\varepsilon_{1}')^2 + (\varepsilon_{1}''d_2)^2} \tag{11}$$

Series Model: Strong Interaction between Polymer and AAO in the Horizontal Direction

In terms of the equivalent circuit,

$$\frac{1}{C_{123}} = \frac{1}{C_{13}} + \frac{1}{C_{23}} \tag{12}$$

$$C_{13} = C_1 + C_3 \tag{13}$$

$$C_{23} = C_2 + C_3 \tag{14}$$

From the definition of capacitance (*i.e.*, $C = \varepsilon A/d$),

$$\frac{D}{\varepsilon_{123}^{*}} = \frac{d_1}{\varepsilon_{13}^{*}} + \frac{d_2}{\varepsilon_{23}^{*}} \tag{15}$$

$$\varepsilon_{13}^{*} = \varepsilon_{1}^{*}\varphi + \varepsilon_{3}^{*}(1 - \varphi) \tag{16}$$

$$\varepsilon_{23}^{*} = \varepsilon_{2}^{*}\varphi + \varepsilon_{3}^{*}(1 - \varphi) \tag{17}$$

After some arrangements, we can obtain the following equation for the complex dielectric permittivity:

$$\varepsilon_{123}^{*} = \frac{[\varepsilon_{1}^{*}\varphi + \varepsilon_{3}^{*}(1 - \varphi)][\varepsilon_{2}^{*}\varphi + \varepsilon_{3}^{*}(1 - \varphi)]}{[\varepsilon_{1}^{*}\varphi + \varepsilon_{3}^{*}(1 - \varphi)] + x\varphi(\varepsilon_{2}^{*} - \varepsilon_{1}^{*})} \tag{18}$$

Here, $x = d_1$ (imbibition length of polymer). The imaginary part is

$$\varepsilon_{123}'' = \frac{BC - AG}{C^2 + G^2} \tag{19}$$

$$B \rightarrow \varepsilon_{1}''\varphi^2 + a\varphi\varepsilon_{1}'' \tag{20}$$

$$C \rightarrow \varepsilon_{1}'\varphi(1 - x) + a + x\varphi \tag{21}$$

$$A \rightarrow \varepsilon_{1}'\varphi^2 + a\varphi(\varepsilon_{1}' + 1) + a^2 \tag{22}$$

$$G \rightarrow \varepsilon_{1}''\varphi(1 - x) \tag{23}$$

$$a \rightarrow \varepsilon_3^*(1-\varphi) \tag{24}$$

For the real and imaginary parts of dielectric constant of AAO we have employed typical values $\varepsilon_3' = \varepsilon_{AAO}' = 2.6$ and $\varepsilon_3'' = \varepsilon_{AAO}'' = 0$.[14] The latter involves the subtraction of the empty cell (*e.g.*, background) signal.

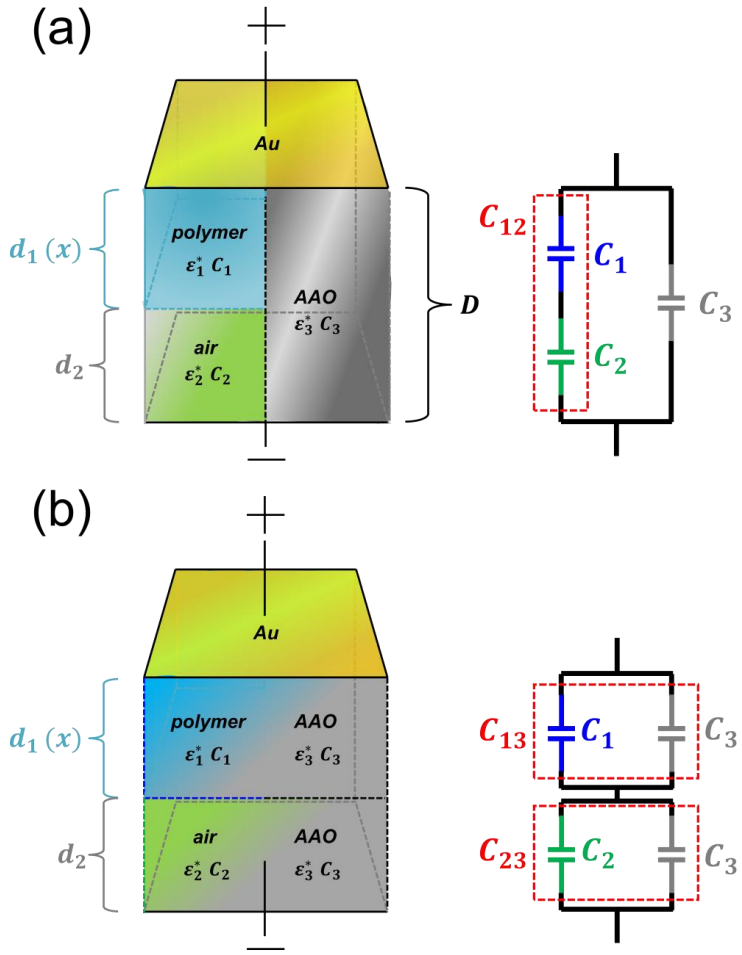

Figure 3. Schematics illustrating the equivalent capacitance of the (a) parallel and (b) series models. Parameters are defined as follows: ε_1^*, ε_2^*, ε_3^*, ε_{12}^*, ε_{13}^*, and ε_{23}^* are, respectively, the permittivity of the polymer layer, air, AAO, polymer/air composite, the polymer/AAO composite, and air/AAO composite; C_1, C_2, C_3, C_{12}, C_{13}, and C_{23} are the respective capacitances; d_1, and d_2 are the lengths of the pores comprising the polymer and air. D is the full length of nanopores.

Three issues are addressed for two polymers (polar and apolar): (i) the effect of porosity (φ) on the evolution of ε", (ii) the variation of the dielectric strength ($\Delta\varepsilon$) with the imbibition length (d_1 or x), and (iii) the variation of the relaxation time during imbibition. The results of the parallel and the series model for the nonpolar and polar polymers (**Figures 4-7**) are discussed with respect

to the growing dielectric loss versus the imbibition length. Independent of polarity, at low porosities (*i.e.*, $\varphi = 0.1$), $\Delta\varepsilon$ shows a linear increase with d_1 in the series model (**Figure 4b** and **5b**). In contrast, within the parallel model a linearity applies only at the initial stages of the imbibition process turning rapidly nonlinear at late stages. At intermediate (*i.e.*, φ=0.5), and high (*i.e.*, φ=0.9) porosities even the series model (**Fig. 4, 5**) deviates from linearity.

On the other hand, polarity affects mainly the relaxation times *during* imbibition. For the nonpolar polymer (*e.g.*, *cis*-1,4-polyisoprene), the position of the relaxation peak stays nearly constant during imbibition and this is independent from the model; by contrast, for the polar polymer [*e.g.*, poly(*n*-butyl methacrylate)] a faster relaxation process at shorter imbibition lengths is followed by a gradual slowing-down at longer imbibition lengths (**Figure 6**). Notice that the molecular dynamics obtained from the series model are always slower than the parallel model and closer to bulk behavior. This phenomenon reflects on the extensive interactions between polymer and AAO in the series model.

The effects of porosity on the relaxation times during imbibition are shown in **Figure 7** for the polar and nonpolar polymer. Within the series model increasing porosity results in faster times whereas porosity plays no role within the parallel model. As expected, these changes are more prominent in the more polar polymer and rather insignificant for the nonpolar polymer. More realistic applications of the models can be made for the two particular polymers to be examined here: PI and PnBMA. The results of the two models for the actual experimental porosities are provided in **Figure 8**. The figure depicts a minor effect on the PI relaxation times and some effect (faster dynamics at the initial stages of imbibition) for the more polar PnBMA. Additional examples are discussed in the appendix (**Figures A1**-**A4**).

Overall simulation results show stronger effects on the evolution of the characteristic times and the dielectric strength for the polar polymers and nearly no effect for the nonpolar polymer. Hence, such effects should be considered at the initial stages of imbibition for polar polymers.

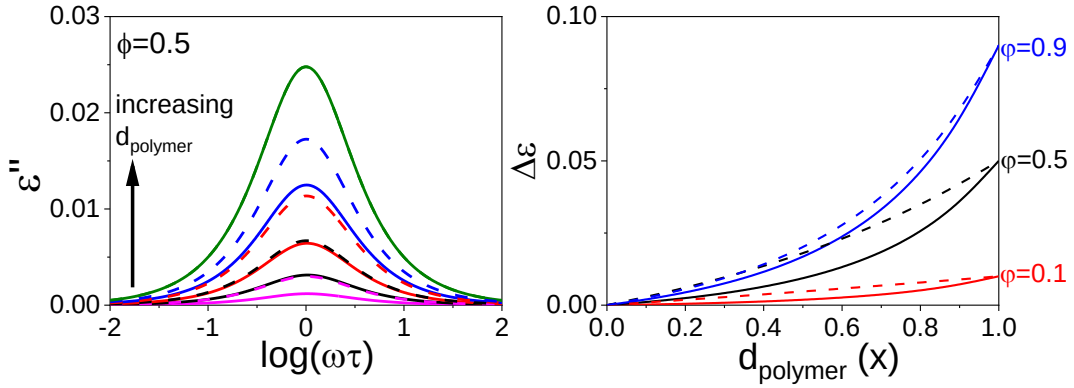

Figure 4. (Left) Comparison in simulated growing ε" of a nonpolar polymer ($\Delta\varepsilon$ = 0.1) as a function of imbibition length (x) via two different models (solid lines: parallel model; dashed lines: series model) for porosity (φ) equal to 0.5. Color codes are as following: (magenta) x = 0.2, (black) x = 0.4, (red) x = 0.6, (blue) x = 0.8, and (olive) x = 1. (Right) Comparison in extracted dielectric intensity ($\Delta\varepsilon$) as a function of x for different porosity: (red) φ=0.1, (black) φ=0.5, and (blue) φ=0.9. Solid (dashed) lines represent the parallel (series) model.

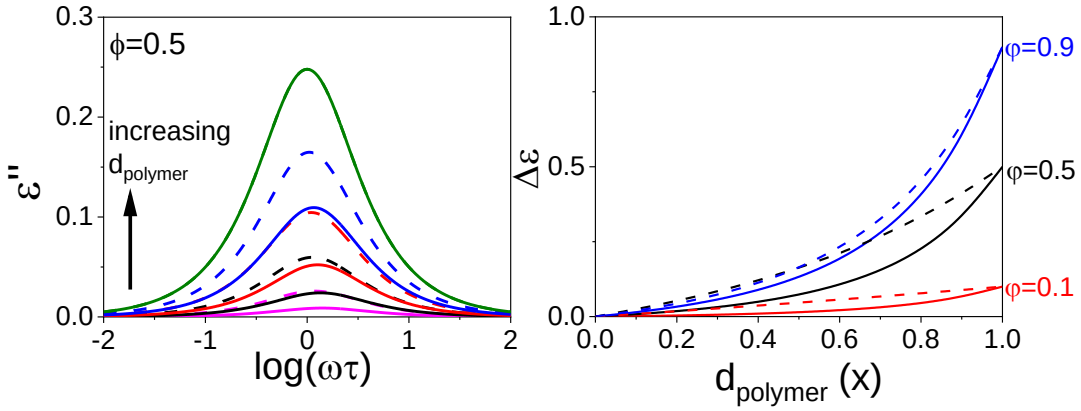

Figure 5. (Left) Simulated ε" of a polar polymer ($\Delta\varepsilon$ = 1) as a function of imbibition length (x) via two different models (solid lines: parallel model; dashed lines: series model) for porosity (φ) equal to 0.5. Color codes are as following: (magenta) x = 0.2, (black) x = 0.4, (red) x = 0.6, (blue) x = 0.8, and (olive) x = 1. (Right) Comparison in extracted dielectric intensity ($\Delta\varepsilon$) as a function of x for different porosity: (red) φ = 0.1, (black) φ = 0.5, and (blue) φ = 0.9. Solid (dashed) lines represent the parallel (series) model.

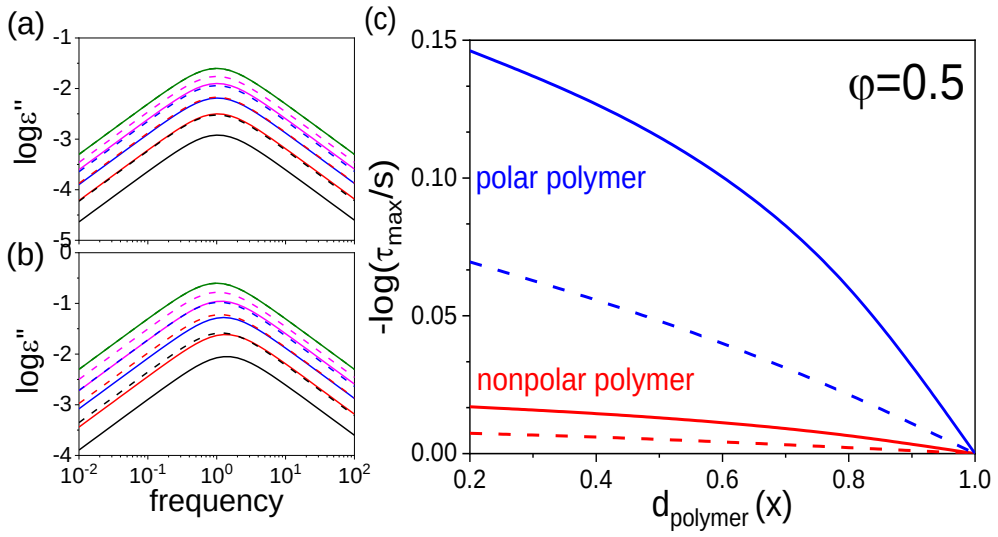

Figure 6. Representative simulated DS loss curves during imbibition for (a) nonpolar and (b) polar polymers. (c) Comparison in extracted relaxation times as a function of imbibition length (x) is plotted. Solid (dashed) lines represent the parallel (series) model. Color codes in (a) and (b): (black) x = 0.2, (red) x = 0.4, (blue) x = 0.6, (magenta) x = 0.8, and (olive) x = 1.0. Color codes in (c): (blue) polar polymer and (red) nonpolar polymer. The selected porosity (φ) for all cases here is 0.5.

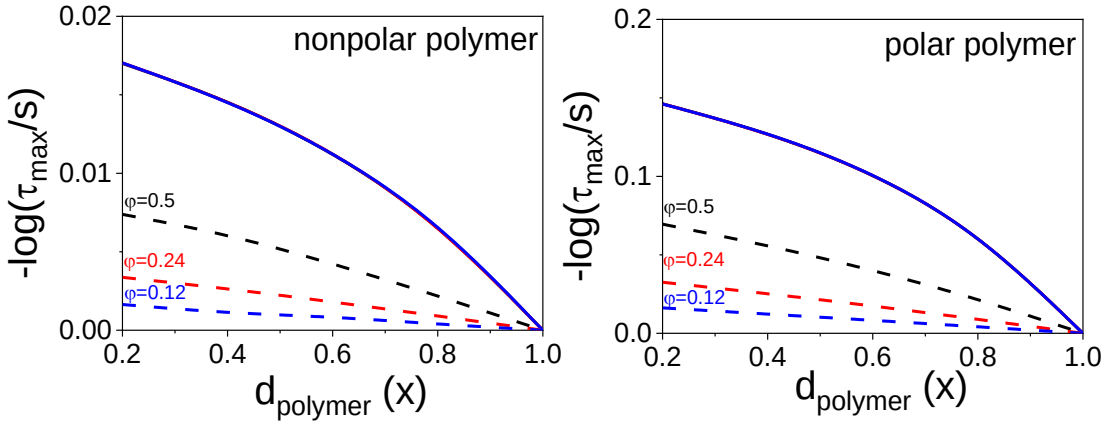

Figure 7. Comparison of the relaxation times for a (left) nonpolar and (right) a polar polymer during imbibition. Porosity: (blue) 0.12, (red) 0.24, and (black) 0.5. Simulation models: (dashed lines) series model and (solid lines) parallel model.

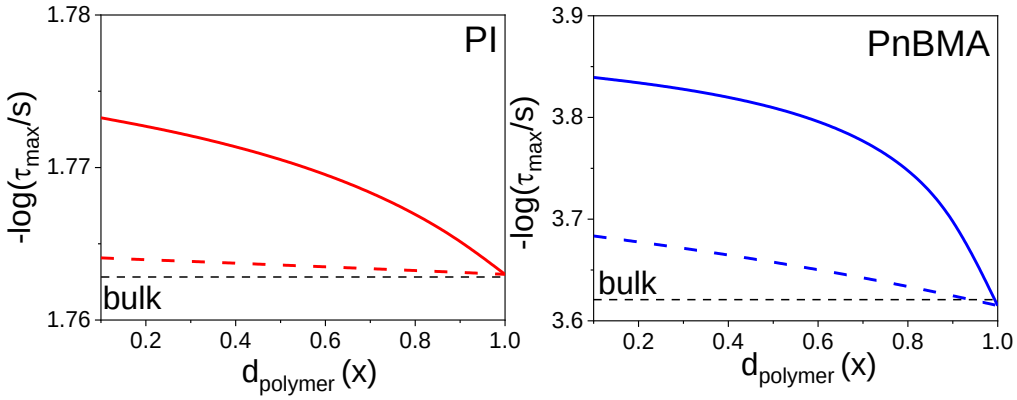

Figure 8. Comparison of the relaxation times of (left) polyisoprene (PI) and (right) poly(*n*-butyl methacrylate) (PnBMA) during imbibition at temperatures of 303 K and 333 K, respectively. Simulation models: (dashed lines) series model and (solid lines) parallel model. Porosity: 0.12 (Left, AAO with pore dimeter of 40 nm) and 0.175 (Right, AAO with pore diameter of 65 nm). Black dashed line in the left (right) plot indicates the longest normal mode relaxation (α-relaxation) time in bulk polymers.

4.5 In Situ DS Measurements of a Polar (PnBMA) and a Non-polar (PI) Polymer

Herein, in an effort to explore the different possibilities and limitations of the nanofluidic method we compare two polymers with different dielectric properties (*i.e.*, polarity and dielectric relaxation processes) – PnBMA and PI. PnBMA, as a member of alkyl methacrylate polymers has a high polarity due to strong electric dipole located in the side group. For this reason, different processes can be detected dielectrically: From the faster β-process in the glassy state, to the segmental α-process at and above T_g to the merged $\alpha\beta$-processes at higher temperatures[14,16,17]. Because of the high viscosity near T_g, the segmental process (practically the merged $\alpha\beta$-process) can only be followed at elevated temperatures (a temperature $T = T_g + 58$ K is shown in **Figure 9**).

PI is a type-A polymer (according to the classification by Stockmayer[18]), and as such has components of the dipole moment both perpendicular and parallel to the contour of the polymer chain. The former contributes to the local segmental relaxation, and the latter provides the dynamics of the end-to-end vector as well as of the internal modes (normal mode relaxation). Because of experimental difficulties in observing the fast kinetics of imbibition – during the cooling process – we have followed the imbibition kinetics at a temperature of 303 K (*i.e.*, at T_g + 96 K) and at the length scale of the normal modes. **Figure 9** depicts typical dielectric loss curves for the two polymers together with the respective fits to a single (PnBMA) or dual (PI) Havriliak-

Negami processes. With respect to the latter, it is known that a single HN cannot capture the "spectrum" of normal modes in type-A polymers and that a summation of two HN functions is necessary.

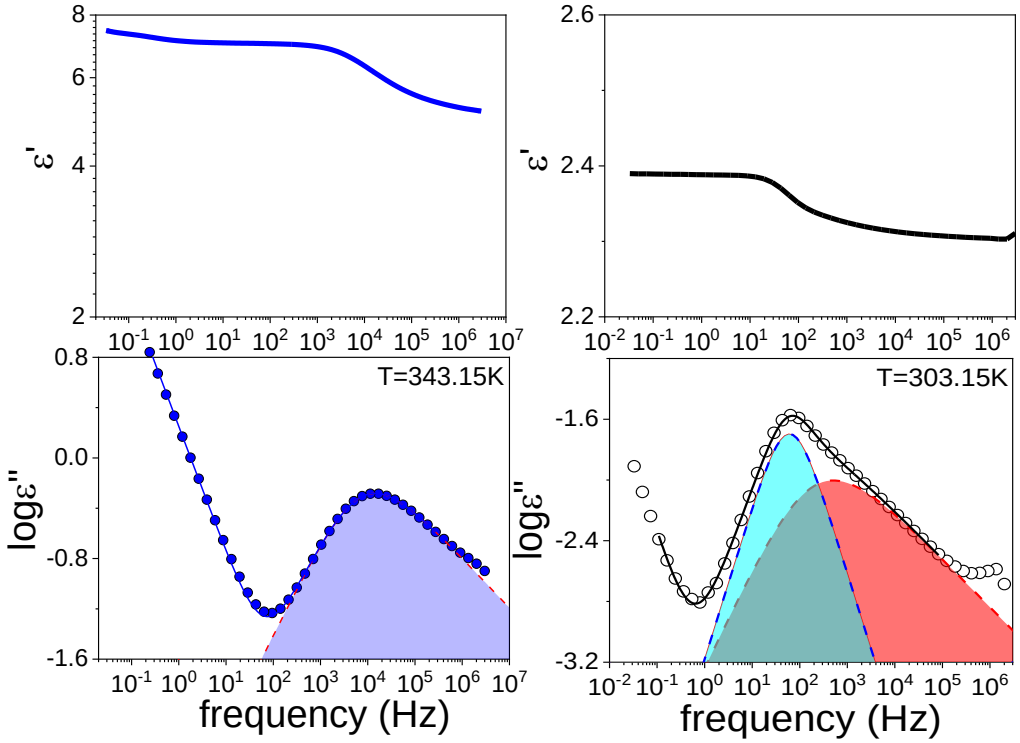

Figure 9. Real (ε') and imaginary (ε'') part of complex dielectric function of (Left column) PnBMA 5.5k and (Right column) PI 42k at selected temperatures. The shaded area in left plot represents the segmental relaxation. The cyan (red) shaded area in right plot represents the longest normal mode relaxation (higher normal modes).

Based on the dynamics shown in **Figure 9**, we can probe the way that PnBMA penetrates AAO nanopores by following the segmental process whereas in the case of PI we can follow the imbibition at the length scale of the chain (normal) modes. The results of the *in situ* imbibition are discussed with respect to **Figures 10-12**.

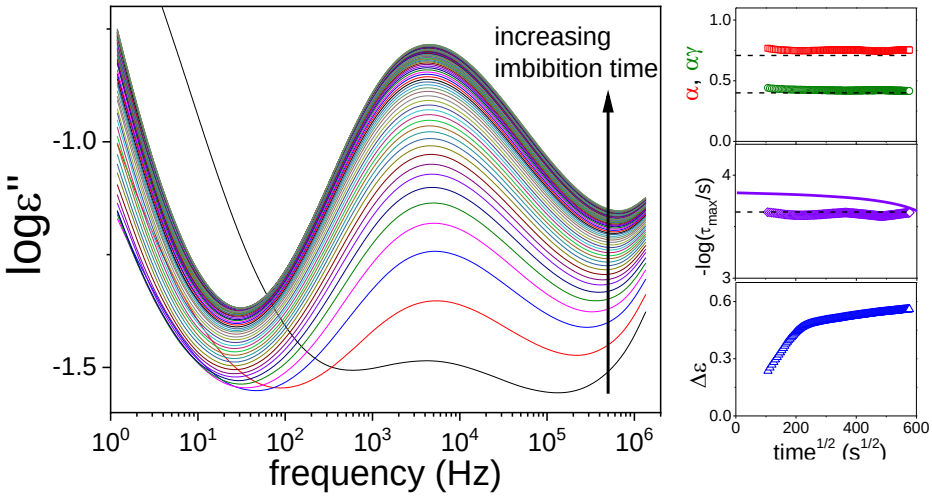

Figure 10. (Left) Evolution of the dielectric loss curves for PnBMA 5.5k entering AAO nanopores with pore diameter of 400 nm at 333 K. The vertical arrow indicates increasing time of imbibition. (Right) Evolution of the HN shape parameters (top), of the relaxation time at maximum loss (middle) and of the dielectric strength (bottom) during the experiment plotted as a function of the square root of imbibition time. The solid line for the characteristic times gives the parallel model predictions. Dashed lines give the parameters corresponding to the bulk polymer.

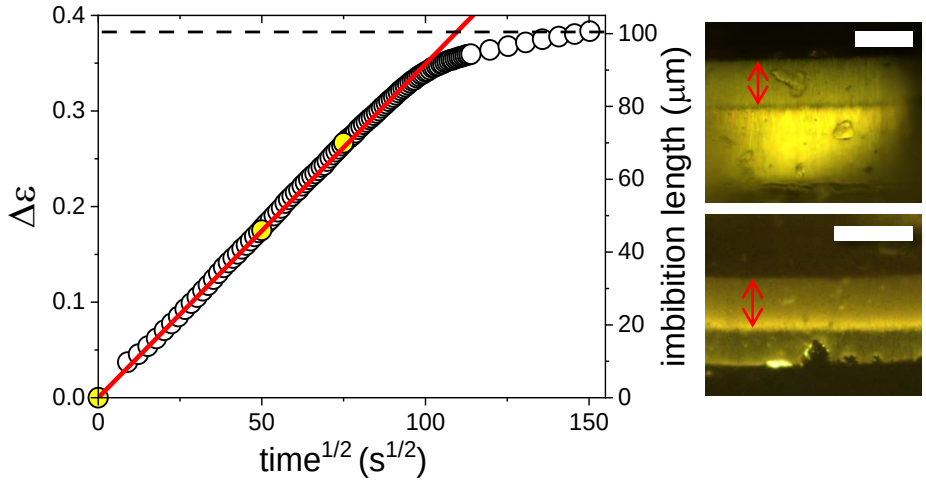

Figure 11. Imbibition length d_1 and dielectric intensity versus imbibition time $t^{1/2}$ for the PnBMA (5.5k) within AAO pores with a diameter of 400 nm at 343 K extracted from the parallel model. Black dashed line indicates the thickness of AAO template. Red line represents the theoretical prediction based on Lucas-Washburn equation. The yellow points represent the calibration points via reflection optical microscopy (ROM). The insets are ROM pictures for selected imbibition periods. The white scale bar indicates 100 μm (top) and 50 μm (bottom).

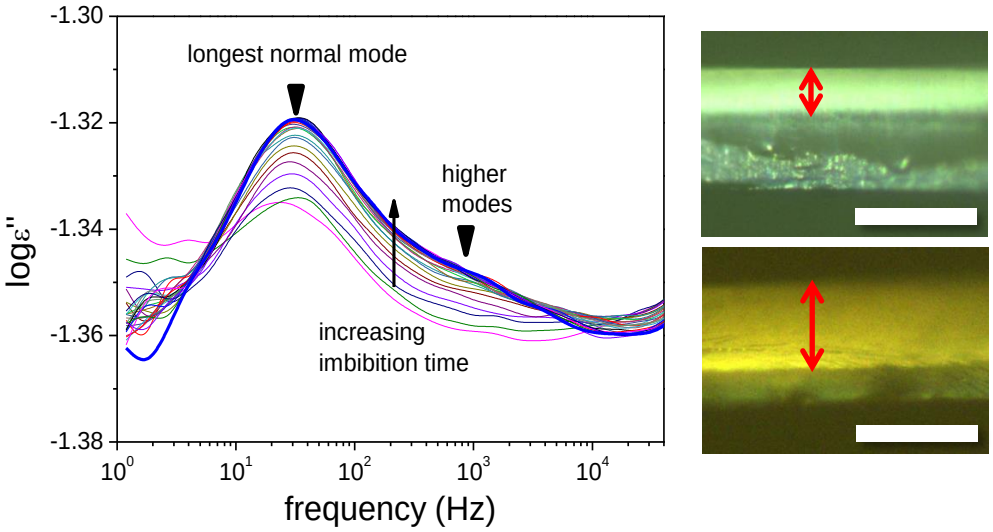

Figure 12. (Left) Evolution of DS curves of PI 42k within AAO 40 nm at temperature of 303 K. The dielectric loss curve with the thick blue color corresponds to imbibition time of 200 $s^{0.5}$. (Right) Representative ROM images for imbibition times of 150 $s^{0.5}$ (top) and 199 $s^{0.5}$ (bottom) respectively. The areas specified by red arrows indicate the filled regions. The white scale bar indicates 100 μm.

Figure 10 depicts the growing dielectric loss curves as PnBMA 5.5k penetrates the pores. It provides details with respect to the dielectric strength, the distribution of relaxation times and the relaxation times at maximum loss. The low- and high- frequency slopes of the segmental process (*i.e.*, α and $\alpha\gamma$) and relaxation times during imbibition are found to be nearly identical to the bulk value (except for the somewhat faster relaxation at the early times, discussed in the simulations part). This observation may sound contradictory to literature data revealing faster dynamics (compared with bulk) under confinement[19]. However, there is *no* contradiction if we consider the fact that the selected imbibition temperature is much above T_g where these effects are diminished ($T = T_g + 96$ K).

Interestingly, the dielectric intensity shows a two stage growth. In the initial part the dielectric strength grows as $t^{1/2}$, whereas at longer times it bends over. The extremely slow imbibition at late stage results from the trapped-air at the nanopore bottom (AAO templates with one close end were employed in the PnBMA case). This is a general feature of all templates with one closed end. To further examine the imbibition kinetics, the information on the effective viscosity that the polymer experiences during flow needs to be extracted. This can be made by *ex situ* measurements of the

actual imbibition length by reflection optical microscopy. As an example, the imbibition kinetics of PnBMA within the larger pores (*i.e.*, 400 nm) is well captured by Lucas-Washburn equation (**Figure 11**). However, the LWE fails to predict the effective viscosity in the smaller nanopores as documented by measurements reported [14]. In addition, the imbibition length can be obtained from the dielectric strength and the use of the parallel model discussed earlier (**Figure 11**). The PnBMA results clearly show the potential of the method to extract precise information of the polymer dynamics at the segmental length scale as well as the potential to extract the effective viscosity during flow.

The case of PI where we probe the imbibition at the longer lengthscales (*i.e.*, the chain dynamics) is substantially different than in the segmental case of PnBMA (**Figure 12**). Herein, the initial continuous growth of normal modes is followed by a longer time regime where the dielectric loss curves remain unchanged or even reduced in dielectric strength. In parallel, the exact imbibition lengths were measured *ex situ* by optical reflection microscopy. A direct comparison of the two experiments provides the following scenario: while at the beginning of the process PI penetrates the pores resulting in the increase of the dielectric strength for the chain modes, at longer times the polymer penetrates the pores but at constant or even decreasing dielectric strength for the chain modes. Note that none of proposed models (*i.e.*, parallel and series model) can explain this behavior. The results suggest increasing adsorption of chain segments at the pore walls. Such adsorbed segments give rise to loops that are de-activated dielectrically as their chain-ends are fixed at the pore walls and cannot fluctuate in space and time. Increasing adsorption sites result to the decrease of the intensity of normal modes as observed experimentally[15].

4.6 Conclusion — Emerged Physical Picture of Polymer Imbibition in Nanopores

In situ nanodielectric spectroscopy has the capacity to explore not only confinement effects but also polymer/substrate interactions during polymer flow. Following some theoretical considerations, we provided here two examples: one for a polar polymer where the imbibition was followed at the segmental process and for a nonpolar polymer where imbibition was followed at the lengthscale of normal modes. Results demonstrate the possibility to extract important information on the relaxation times and distribution of relaxation times during flow for both length scales. At the same time, and within the context of the LWE, the effective viscosity during polymer flow can be obtained and compared to the bulk. We are not aware of another technique that can

access these dynamic properties *during* polymer flow. In addition, imbibition of type-A polymers is expected to provide quantitative information on the role of the adsorption both during and at the end of the filling process (including the kinetics). These results can be compared with the adsorption in polymer films where confinement is 1D[20].

Several additional polymer physics problems can be addressed with the method. While in-situ monitoring the imbibition process of PI, we observed that the (rather low) ionic conductivity was a decreasing function of imbibition time. It implies that certain ions are entering preferentially at the early stage of imbibition process followed by the polymer segments. This point requires further studies that include systems of higher ion content (ionic liquids, polymer electrolytes) and to further explore the role of the charged AAO surface[21]. Experiments in this direction are currently in progress in our laboratory. On another issue, we can employ the same method to study the imbibition process of a biomacromolecule possessing an intrinsic secondary structure (*e.g.*, poly(γ-benzyl-L-glutamate), PBLG[22]). With PBLG several issues can be addressed: (i) Can we infiltrate an ordered α-helical secondary structure directly into the nanopores? (ii) Can we follow in-situ the segmental and slower dynamics of polypeptides and proteins during imbibition? It is noted that the slower process in bulk PBLG resembles the normal modes of polyisoprene owing to its dipoles arranged along the α-helical structure (PBLG is also a type-A polymer)[22]. If successful, these studies will have implications to the problem of protein translocation, *e.g.*, to the motion of a protein through narrow pores.

4.7 References

(1) Kremer, F. (Ed.) *Dynamics in Geometrical Confinement*; Springer: Berlin, **2014**.

(2) Masuda, H.; Hasegawa; F.; Ono, S. Self-ordering of cell arrangement of anodic porous alumina formed in sulfuric acid solution. *J. Electrochem. Soc.* **1997**, 144, L127-L130.

(3) Steinhart, M., Supramolecular organization of polymeric materials in nanoporous hard templates. *Adv. Polym. Sci.* **2008**, 220, 123-187.

(4) Lucas, R. Ueber das zeitgesetz des kapillaren aufstiegs von flüssigkeiten. *Colloid Polym. Sci.* **1918**, 23, 15-22.

(5) Washburn, E. W. The dynamics of capillary flow. *Phys. Rev.* **1921**, 17 (3), 273-283.

(6) Yao, Y.; Butt, H. J.; Floudas, G.; Zhou, J.; Doi, M. Theory on capillary filling of polymer melts in nanopores. *Macromolecular rapid communications* **2018**, 39(14), 1800087.

(7) Yao, Y.; Alexandris, S.; Henrich, F.; Auernhammer, G.; Steinhart, M.; Butt, H.-J.; Floudas, G. Complex dynamics of capillary imbibition of poly(ethylene oxide) melts in nanoporous alumina. *J. Chem. Phys.* **2017**, 146 (20), 203320.

(8) Cencha, L. G.; Urteaga, R.; Berli, C. L. *Macromolecules* **2018**, 51(21), 8721-8728.

(9) Serghei, A.; Chen, D.; Lee, D. H.; Russell, T. P. Segmental dynamics of polymers during capillary flow into nanopores. *Soft Matter* **2010**, 6, 1111-1113.

(10) Serghei, A.; Lutkenhaus, J. L.; Miranda, D. F.; McEnnis, K.; Kremer, F.; Russell, T. P. Density fluctuations and phase transitions of ferroelectric polymer nanowires. *Small* **2010**, 6 (16), 1822-1826.

(11) Serghei, A.; Zhao, W.; Wei, X.; Chen, D.; Russell, T. P. Nanofluidics with phase separated block-copolymers: Glassy dynamics during capillary flow. *Eur. Phys. J. Special Topics* **2010**, 189, 95-101.

(12) Serghei, A.; Zhao, W.; Miranda, D.; Russell, T. P. Curie transitions for attograms of ferroelectric polymers. *Nano Lett.* **2013**, 13, 577-580.

(13) Houachtia, A.; Alcouffe, P.; Boiteux, G.; Seytre, G.; Gérard, J.-F.; Serghei, A. Nanofluidics approach to separate between static and kinetic nanoconfinement effects on the crystallization of polymers. *Nano Lett.* **2015**, 15, 4311-4316.

(14) Tu, C.-H.; Steinhart, M.; Butt, H.-J.; Floudas, G. In situ monitoring of the imbibition of poly (n-butyl methacrylates) in nanoporous alumina by dielectric spectroscopy. *Macromolecules* **2019**, 52(21), 8167-8176.

(15) Tu, C.-H.; Zhou, J.; Doi, M.; Butt, H.-J.; Floudas, G. Interfacial interactions during *in situ* polymer imbibition in nanopores. *Phys. Rev. Lett.* **2020**, 125, 127802.

(16) Mpoukouvalas, K.; Floudas, G. Williams, G. Origin of the α, β, ($\beta\alpha$), and "slow" dielectric processes in poly(ethyl methacrylate). *Macromolecules* **2009**, 42, 4690-4700.

(17) Deres, A.; Floudas, G. A.; Müllen, K.; Van der Auweraer, M.; De Schryver, F.; Enderlein, J.; Uji-i, H.; Hofkens, J. The origin of heterogeneity of polymer dynamics near the glass temperature as probed by defocused imaging. *Macromolecules* **2011**, 44, 9703-9709.

(18) Stockmayer, W. H. Dielectric dispersion in solutions of flexible polymers. *Pure and Applied Chemistry* **1967**, 15(3-4), 539-554.

(19) Alexandris, S.; Papadopoulos, P.; Sakellariou, G.; Steinhart, M.; Butt, H.-J.; Floudas, G. Interfacial energy and glass temperature of polymers confined to nanoporous alumina, *Macromolecules* **2016**, 49, 7400.

(20) Napolitano, S.; Wübbenhorst, M. The lifetime of the deviations from bulk behaviour in polymers confined at the nanoscale, *Nat. Commun.* **2011**, 2, 260.

(21) Zardalidis, G.; Ioannou, E.; Pispas, S.; Floudas, G. Relating Structure, Viscoelasticity and local Mobility to Conductivity in PEO/LiTf Electrolytes, *Macromolecules* **2013**, 46, 2705-2714.

(22) Floudas, G.; Spiess, H.W. Self-assembly and dynamics of polypeptides, *Macromol. Rapid Commun.* **2009**, 30, 278.

4.8 Appendix

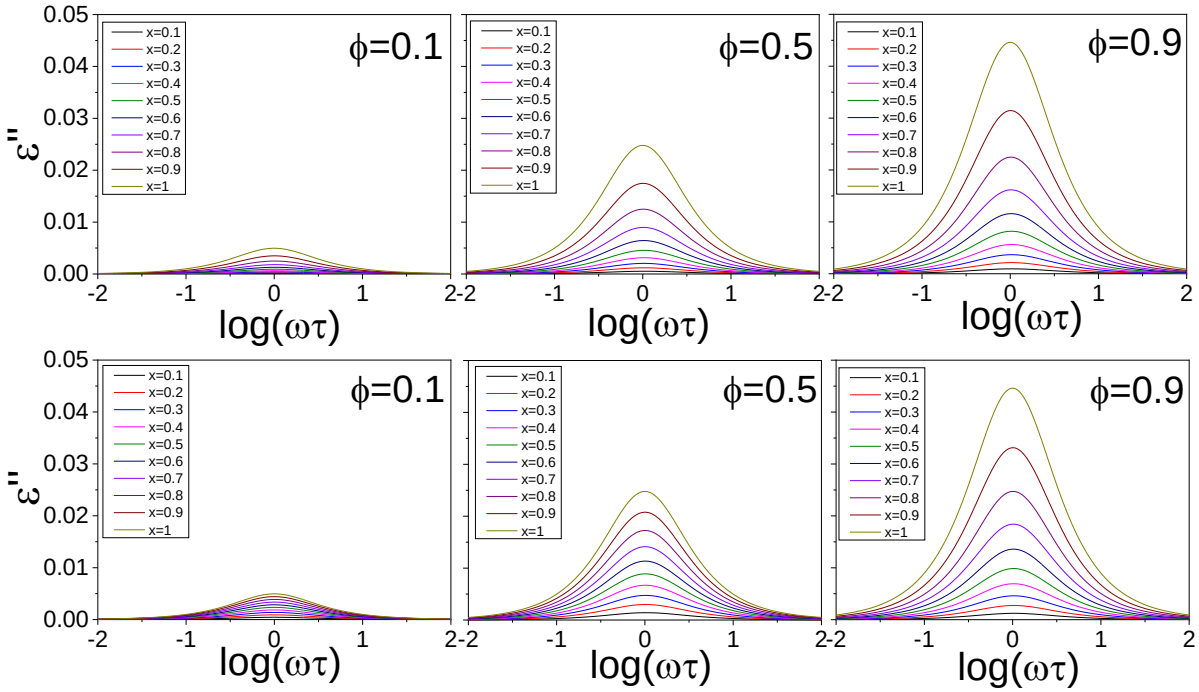

Figure A1. Simulated growing imaginary part of dielectric permittivity of a nonpolar polymer ($\Delta\varepsilon = 0.1$) as a function of imbibition length (x) based on the parallel model (top raw) and on the series model (bottom row) with different porosities: (left) 0.1, (middle) 0.5, and (right) 0.9.

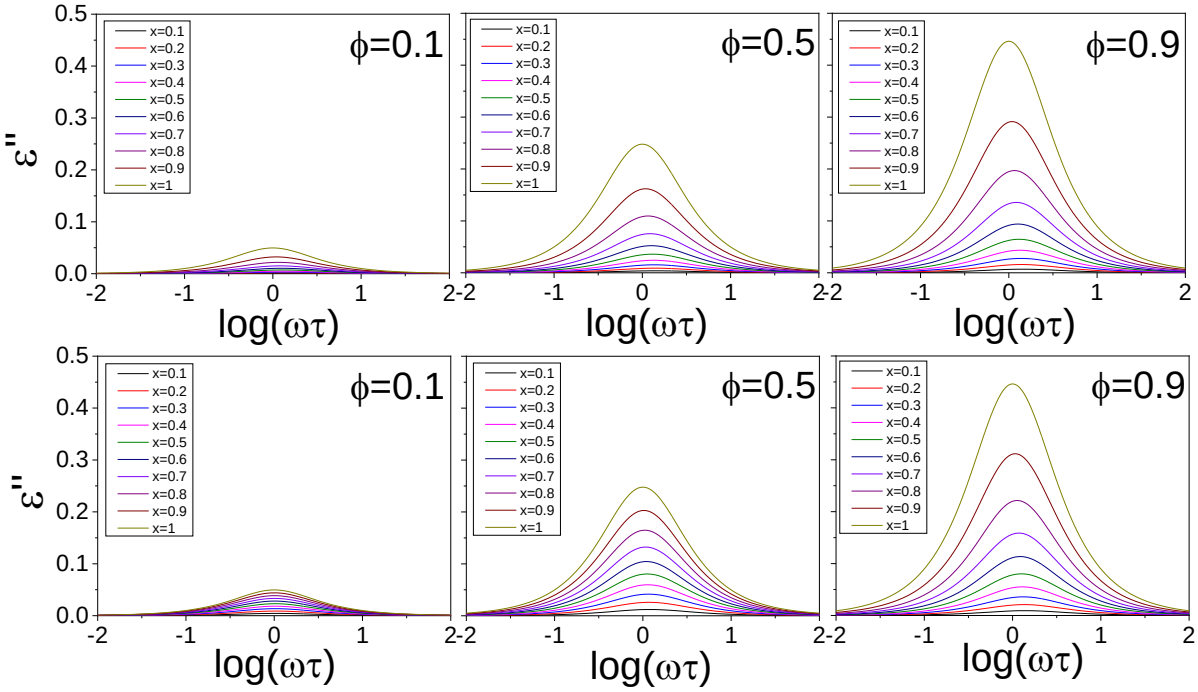

Figure A2. Simulated growing imaginary part of dielectric permittivity of a polar polymer ($\Delta\varepsilon$ = 1) as a function of imbibition length (x) based on the parallel model (top raw) and the series model (bottom row) with different porosities: (left) 0.1, (middle) 0.5, and (right) 0.9.

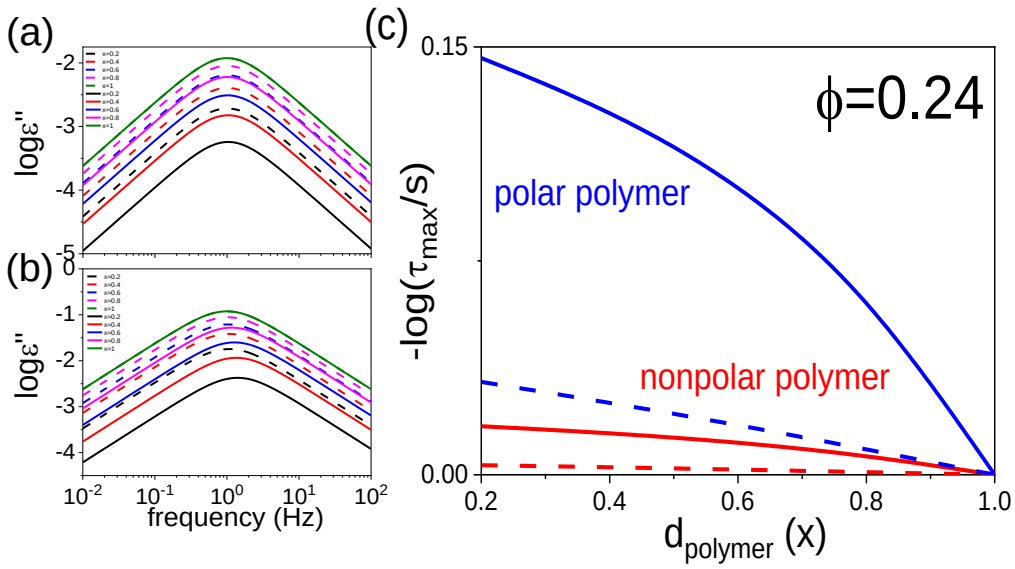

Figure A3. Representative simulated DS curves during imbibition for (a) nonpolar and (b) polar polymers. (c) Comparison in extracted relaxation times as a function of imbibition length (x) is plotted. Real (dashed) lines represent the parallel (series) model. Color codes in (a) and (b): (black) x = 0.2, (red) x = 0.4, (blue) x = 0.6, (magenta) x = 0.8, and (olive) x = 1.0. Color codes in (c): (blue) polar polymer and (red) nonpolar polymer. The selected porosity (φ) for all case here is 0.24 (same as InRedox AAO template with pore size of 100 nm).

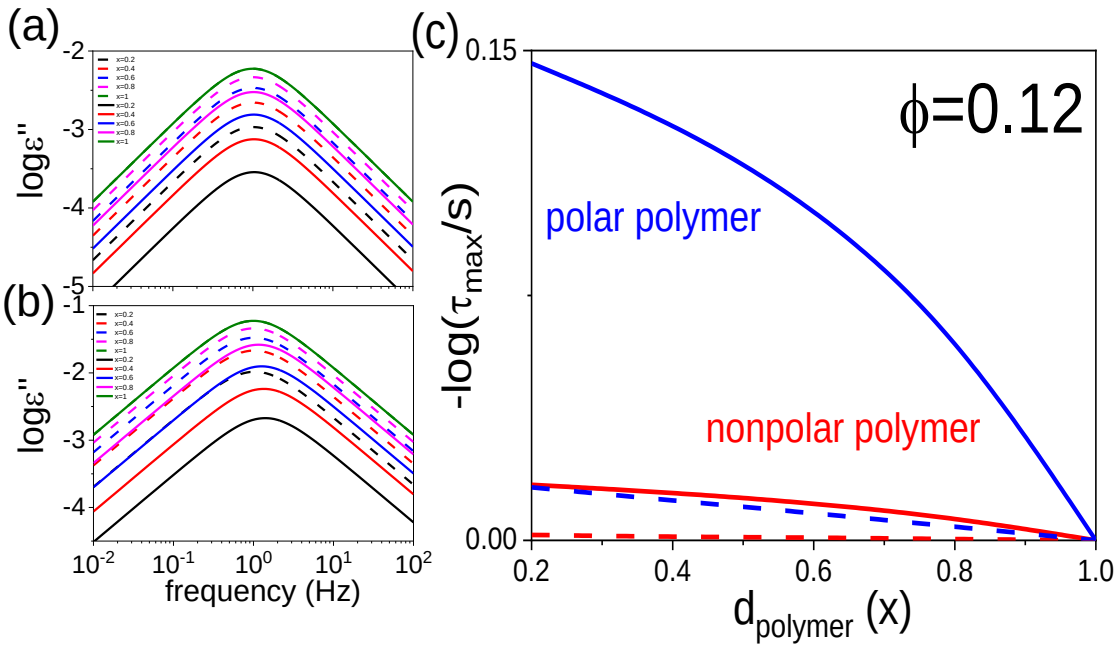

Figure A4. Representative simulated DS curves during imbibition for (a) nonpolar and (b) polar polymers. (c) Comparison in extracted relaxation times as a function of imbibition length (x) is plotted. Real (dashed) lines represent the parallel (series) model. Color codes in (a) and (b): (black) x = 0.2, (red) x = 0.4, (blue) x = 0.6, (magenta) x = 0.8, and (olive) x = 1.0. Color codes in (c): (blue) polar polymer and (red) nonpolar polymer. The selected porosity (φ) for all case here is 0.12 (same as InRedox AAO template with pore size of 40 nm).

Chapter 5. Adsorption Kinetics of *cis*-1,4-Polyisoprene in Nanopores by *In Situ* Nanodielectric Spectroscopy

This chapter has been published as a research paper in Macromolecules.

Chien-Hua Tu, Jiajia Zhou, Hans-Jürgen Butt, and George Floudas
Macromolecules 54(13), 6267-6274 (2021).
DOI: 10.1021/acs.macromol.1c00821

Abstract

Using *in situ* nanodielectric spectroscopy we studied the adsorption kinetics of *cis*-1,4-polyisoprene (PI) into porous alumina by following the evolution of the dielectrically active longest normal mode. We studied the influence of molar mass, nanopore diameter and surface functionalization. Adsorption times depend strongly on the ratio $2R_g/D$; R_g is the radius of gyration and D is the pore diameter. For a given pore diameter, the characteristic adsorption times are some 8 orders of magnitude slower than the terminal relaxation times and more than 12 orders of magnitude slower than the segmental times. The extremely slow kinetics reflect the fact that exchanging chains with the pore surface have to pass through several unfavorable configurations (*e.g.*, trains, loops). The molar mass dependence of the characteristic adsorption times ($\tau_{ads} \sim N^{2.6}$) is in good agreement with a scaling theory proposed by de Gennes and later refined by Semenov and Joanny. Subsequently, we investigated the imbibition of miscible PI blends by taking advantage of the difference in imbibition speeds of the respective homopolymers. We show that the shorter chains penetrate first the nanopores, whereas the longer chains enter only at the late stages of the filling process. Moreover, the long-time adsorption is dominated by an exchange mechanism involving primarily the shorter chains. The results from *in situ* nanodielectric

spectroscopy demonstrate the capacity of the technique to provide the imbibition length, the adsorption kinetics, and, at the same time, the chain dynamics.

5.1 Introduction

There is a growing interest in understanding the way that polymers penetrate narrow pores.[1,2] One example is sequencing DNA with nanopores,[3] a technique based on passing DNA through a nanopore in a membrane and reading off individual bases from the ion current passing through the pore. Another example involving synthetic macromolecules is inkjet printing. In both cases, it is essential to characterize the conformations of the macromolecules inside the pores as well as the polymer–wall interactions.[4-10] The latter is the key factor for the design of polymer interfaces with controlled physical properties (wettability, adhesion, viscosity, glass temperature, *etc.*) of importance in several applications including membranes, coatings and organic electronic devices.

In this endeavor, techniques that can provide simultaneous access to the kinetics of imbibition and to the molecular dynamics during and after flow are advantageous. A recent development in this direction has been the implementation of the nanodielectric spectroscopy (*n*DS) technique to follow the imbibition of polymers in nanopores.[11-14] In this technique, a capacitor is formed by the two surfaces of a nanoporous aluminum template and an ac field is applied along the pore axis. A polymer melt on the top surface of a template will penetrate the pores by capillary action. By recording the evolution of capacitance, C, it is possible to extract the complex dielectric permittivity ($C \sim \varepsilon$), where the details of the polymer dynamics during flow (*e.g.*, *in situ*) are encoded. With nanoporous alumina, the probing volumes are typically ~10^{-19} m^3 or smaller (~ 10^{-20} m^3 at the early stages of imbibition) and the polymer mass is ~ 10^{-15} g (*i.e.*, femtograms), hence the term *n*DS. The technique provides simultaneous access to the kinetics of imbibition and to the molecular dynamics during flow at the segmental and chain length scales.

In a recent study[14] we have employed a type A polymer, *i.e.*, a polymer having components of dipole moment both perpendicular and along the polymer backbone. We could show that interfacial interactions develop already during the polymer flow in nanopores. Herein, we study the adsorption kinetics of *cis*-1,4-polyisoprene as a function of polymer molar mass (M_n from 4840 g·mol^{-1} to 42412 g·mol^{-1}), nanopore diameter (from 100 nm to 20 nm) and surface treatment (native vs silanized nanopores) by following the evolution of the longest normal mode. For the confining medium we employ self-ordered nanoporous aluminum oxide (AAO) that contains arrays of parallel cylindrical nanopores uniform in length (pore depth = 100 μm) and diameter (pore diameters = 100, 40, and 20 nm) that can easily be infiltrated from the melt.[15] In contrast to the

earlier study,[14] here, we are interested in the long-time adsorption kinetics following the full imbibition. The aim is to establish scaling laws for the adsorption time as a function of the pore size and the molecular mass. We find that adsorption is an extremely slow process because it involves unlocking several unfavorable chain configurations. The characteristic time scale depends strongly on the degree of confinement and molar mass. The experimental findings on the molar mass dependence of the characteristic adsorption times are discussed in view of a scaling theory proposed by De Gennes[4,5] and later refined by Semenov and Joanny.[6]

As an extension of this work we explore how symmetric PI blends penetrate the same nanopores. This part requires a judicious choice of blend components so that both chains relax within the experimental window at the imbibition temperature. We find that shorter chains (i) penetrate first and (ii) adsorb first on the AAO walls. The longer chains are entering the pores only at the late stages of the filling process providing an example of polymer fractionation in the absence of solvent. The advantage of *n*DS over other - static – techniques is that it provides the pertinent time scales (chain relaxation) *in situ* and in parallel with the adsorption kinetics.

5.2 Experimental section

Samples. Four *cis*-1,4-polyisoprene homopolymers with narrow dispersities, *Đ*, were employed in the present study (Table 1). PI 12k and PI 21k were purchased from PSS Polymer Standards Service GmbH and used without further purification. PI 5k and PI 42k were synthesized in house (MPI-P). Two symmetric blends (composition 50/50 wt%) of PI 5k with PI 21k and of PI 5k with PI 42k (designated as B1 and B2, respectively) were prepared and investigated in the second part of this study.

Table 1. Molecular characteristics of the *cis*-1,4-polyisoprene homopolymers and their blends as obtained from GPC/SEC.

Sample	M_n (g·mol^{-1})	M_w (g·mol^{-1})	$Đ$	R_g (nm)[a]	η_o (Pa·s)
PI 5k	4840	5116	1.06	2.3	2.0
PI 12k	11800	12000	1.02	3.6	8.8
PI 21k	23300	23600	1.01	5.1	
PI 42k	42412	43997	1.04	6.9	259.0
B1 (5k/21k)					-
B2 (5k/42k)					50.0

[a]: The radius of gyration, R_g, was calculated according to $\langle {R_g}^2 \rangle_0 = \frac{1}{6}\langle R^2 \rangle_0$ by using $\frac{\langle R^2 \rangle_0}{M}$=0.679 (Å^2 mol/g).[16]

AAO Templates. Self-ordered nanoporous aluminum oxide (AAO) templates with both ends open were purchased from InRedox (Longmont, USA). Pore diameters and the corresponding porosities were 100 nm (24 ± 3%), 40 nm (12 ± 2%) and 20 nm (11 ± 2%), respectively, according to the manufacturer, and the pore length was 100 μm. Prior to infiltration, all AAO templates were annealed in a vacuum oven at T = 443 K for 8-10 h. This procedure removes the majority of OH groups from the AAO surface.

In situ **nanodielectric spectroscopy.** Dielectric spectroscopy (DS) and *in situ* nanodielectric spectroscopy (*n*DS) were employed to follow the dynamics of bulk and confined PI. In both cases, a Novocontrol Alpha frequency analyzer composed of a broadband dielectric converter and an active sample head was used. For bulk samples, polymers were embedded between two stainless steel electrodes with a diameter of 20 mm accompanied with a Teflon spacer of 50 μm to maintain a constant thickness. The sample configuration for *in situ n*DS is shown in **Figure 1**. First, the AAO templates were sputtered with a gold layer (thickness of 35 nm) on both sides. Sputtering was made under vacuum (lower than 2×10^{-5} Pa) by a Bal-tec MED 020 with a current density of 40 mA. The high vacuum environment is to ensure the uniformity of the sputtered Au layer. The current density during sputtering was optimized to produce Au grains with appropriate size (too big may block the AAO pores; too small may hinder the current transport). Scanning electron microscopy (SEM) was subsequently explored to determine the distribution of Au grains on the inner surface of the AAO templates (**Figure 1**). In addition to a uniform film deposited on top of the AAO templates, traces of gold are found also within the pores (down to a depth of about 400 nm). However, given the high aspect ratio (> 10^3) of nanopores, any inhomogeneities in the field lines can be neglected. A thin film of the polymer was then deposited on the top of the AAO template. For the kinetic studies, the polymer molar mass as well as the temperature and frequency ranges need to be wisely selected. A broad frequency range from $10^{-2} - 10^7$ Hz was employed for the bulk DS measurements. In contrast, a narrower frequency range, from $10 - 10^6$ Hz, is necessary to probe the imbibition kinetics by *n*DS. With this choice, the time needed for a single dielectric curve is around 2 min. In general, the dielectric function depends on the frequency, temperature, and time. At a given time and temperature, it can be fitted by the empirical equation of Havriliak and Negami (HN):[17]

$$\varepsilon^*_{HN}(\omega,T,t) = \varepsilon_\infty(T,t) + \frac{\Delta\varepsilon(T,t)}{[1+(i\omega\tau_{HN}(T,t))^{\alpha(t)}]^{\gamma(t)}} + \frac{\sigma_0(T,t)}{i\varepsilon_0\omega} \quad (1)$$

Here, $\Delta\varepsilon(T,t)$ is the relaxation strength, τ_{HN} is the Havriliak-Negami relaxation time, α and γ ($0 < \alpha$, $\alpha\gamma \leq 1$) are shape parameters describing the symmetric and asymmetric broadening of dielectric function (with the high-frequency slope in a log-log representation being $\alpha\gamma$), respectively, and ε_∞ is the dielectric permittivity at the limit of high frequencies. At lower frequencies, ε'' increases due to the conductivity ($\varepsilon'' = \sigma_0/(\omega\varepsilon_0)$, where σ_0 is the dc conductivity and ε_0 the vacuum permittivity). The upturn of ε'' at the higher frequencies is due to the background signal from the Au sputtered electrodes.

Simulation of the imbibition process. *n*DS provides precise information on the evolution of the imbibition length and the associated polymer dynamics.[11] Modeling the imbibition process requires the use of the equivalent capacitance model (**Figure 1**). In the parallel model, the capacitance of the polymer (C_1) and air (C_2) are connected in series, whereas the combinational capacitance of the polymer/air (C_{12}) connects in parallel with the capacitance of AAO (C_3). Therefore,

$$\frac{1}{C_{12}} = \frac{1}{C_1} + \frac{1}{C_2}, \text{and } C_{123} = C_{12} + C_3 \quad (2)$$

Since the capacitance is $C = \varepsilon A/L$, where L and A are the thickness and electrode area, respectively, it follows that,

$$\varepsilon^*_{12} = \frac{L\varepsilon^*_1}{d_1 + d_2\varepsilon^*_1} \quad (3)$$

$$\varepsilon^*_{123} = \varepsilon^*_{12}\varphi_{12} + \varepsilon^*_3\varphi_3 \quad (4)$$

In the last equation, φ_{12} represents the porosity of AAO templates, $\varphi_3(= 1 - \varphi_{12})$ is the AAO area, and L is full length of the AAO nanopores. After some arrangements, we can obtain the following equation for the complex dielectric permittivity:

$$\varepsilon^*_{123} = \left[\frac{L\varepsilon^*_1}{d_1 + d_2\varepsilon^*_1}\right]\varphi_{12} + \varepsilon^*_3\varphi_3 \quad (5)$$

Therefore, the imaginary part is

$$\varepsilon''_{123} = \frac{d_1 \varepsilon''_1 \varphi_{12}}{(d_1 + d_2 \varepsilon'_1)^2 + (\varepsilon''_1 d_2)^2} \quad (6)$$

For the real and imaginary parts of the dielectric function of AAO we employed $\varepsilon_3' = 2.6$ and $\varepsilon_3'' = 0$. The latter value involves the subtraction of the empty cell signal (*e.g.*, the background). Based on eq. 6, the presence of an air capacitor can influence the dielectric loss maximum for polar molecules.[18] For nonpolar substances, like PI, the shift of the frequency at maximum loss during imbibition is insignificant (see Supporting Information, **Fig. S1**).

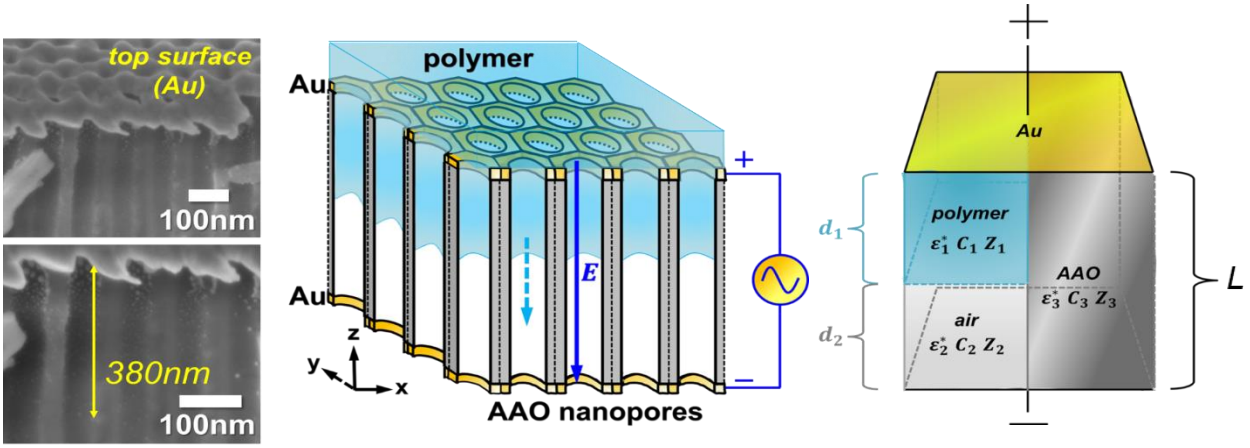

Figure 1. (Left) SEM images showing the top surface and cross section of AAO pores with a dimeter of 65 nm after Au sputtering. The left bottom figure is a zoom-in of part of the top image. Au particles are distributed at the top of the nanopores within a distance of 380 nm. (Middle) Schematic of the experimental setup employed for *n*Ds. The blue arrow indicates the direction of the applied electric field, *E* (along the nanopores, *z*-axis). The cyan dashed arrow indicates the flow direction of the meniscus within the AAO nanopores. The *xyz* coordinate represents the laboratory axis. (Right) The equivalent capacitor circuit with *Z* being the impedance.

Calibration experiments. Independent calibration measurements of the imbibition length were made by employing *ex situ* reflection optical microscopy (ROM). Measurements were made on fractured surfaces of AAO templates and for different imbibition times. Before fracturing, the templates were immersed into liquid nitrogen to prevent the further imbibition of PI into nanopores. For Newtonian liquids, the time dependence of imbibition length, d_1 (**Fig. 1**), can be obtained from the Lucas-Washburn equation (LWE):[19-21]

$$d_1(t) = \left(\frac{\gamma D \cos\theta}{2\eta}\right)^{1/2} \sqrt{t} \quad (7)$$

Here, γ is the surface tension, θ is the advancing contact angle, D is the pore diameter, η is the viscosity and t is the wetting time. For the surface tension and static contact angle, we have employed the reported values from a PI homopolymer (M_n = 800 g·mol^{-1} and M_w = 880 g·mol^{-1}).[22] The former was measured by the pendant drop method at T = 290 K (γ = 30 mN·m^{-1}) whereas the latter was measured by employing a customized setup on sessile drops at 290 K ($\cos\theta$ = 0.88 ± 0.02). Examples are provided in the Supporting Information **Figure S2**.

Rheology. The viscosities of the PI homopolymers and their blends were measured by a shear rheometer (ARES). Measurements were made with the environmental test chamber as a function of temperature ranging from 208.15 K to 303.15 K. The zero-shear viscosities at the reference temperature are included in Table 1. Details are provided in the Supporting Information section (**Fig. S3** and **Fig. S4**).

5.3 Results and discussion

Homopolymer adsorption. The adsorption kinetics following the full imbibition of *cis*-1,4-polyisoprenes in AAO was studied as a function of pore size and molar mass (**Figure 2**). **Figure 2** depicts the evolution of the dielectric loss curves during and after the full imbibition of PI 5k into AAO nanopores having pores with a diameter of 20 nm at 303.15 K. The technique requires a judicious choice of the parameters (temperature/molar mass) such that the spectrum of normal modes is contributing to the dielectric loss within the investigated (restricted) frequency window at the imbibition temperature. We observed an increasing dielectric loss curves for the longest normal mode during imbibition until after 12000 s when the trend reversed and the dielectric loss curves start to decrease in intensity. The same figure compiles the evolution in the dielectric strength, $\Delta\varepsilon$, of the normal mode for the same PI following imbibition in AAO with different pore diameters. This trend is more evident in the smaller pores. Note the very long-time scales, in the case of the 20 nm pores, in the order of (several) days. We will return to this point below.

In **Figure 2** the dielectric strength is normalized to the maximum value. The maximum, $\Delta\varepsilon_n$, coincides with the full imbibition of the polymer as evidenced by independent measurements by reflection optical microscopy (ROM). At subsequent times, the strength of the normal mode is decreasing due to increasing adsorption. In the figure, the dielectric strength is normalized (from max (1) to min (0) values) to make the comparison of the time scales more evident. Polymer

adsorption gives rise to train and loop chain configurations that are dielectrically inactive because part of the chain cannot fluctuate in space and time. This is evident, as the dielectric strength for the normal mode is given by[23-32]

$$\Delta\varepsilon = \frac{N_A \mu_{NM}^2}{3\varepsilon_0 k_B T} \frac{\langle r^2 \rangle}{M_{PI}} \tag{8}$$

Here, $\langle r^2 \rangle$ is the mean-square end-to-end distance, μ_{NM} is the dipole moment per contour length and M_{PI} is the chain molar mass. The decrease in dielectric strength can be parameterized by an exponential function as, $\Delta\varepsilon = \Delta\varepsilon_{max}\left(exp^{-\frac{t}{\tau_{ads}}}\right)$, where τ_{ads} is the characteristic adsorption time. A single exponential is the simplest approach to describe the desorption process as rate-limited by the energetics of surface detachment.[33] At the same time, we can record the position (frequency of maximum loss, f_{max}) of the normal mode, that relates to the longest relaxation time as $\tau_{max} = 1/(2\pi f_{max})$. Hence, *n*DS provides simultaneous access to the adsorption kinetics and to the chain dynamics during adsorption.

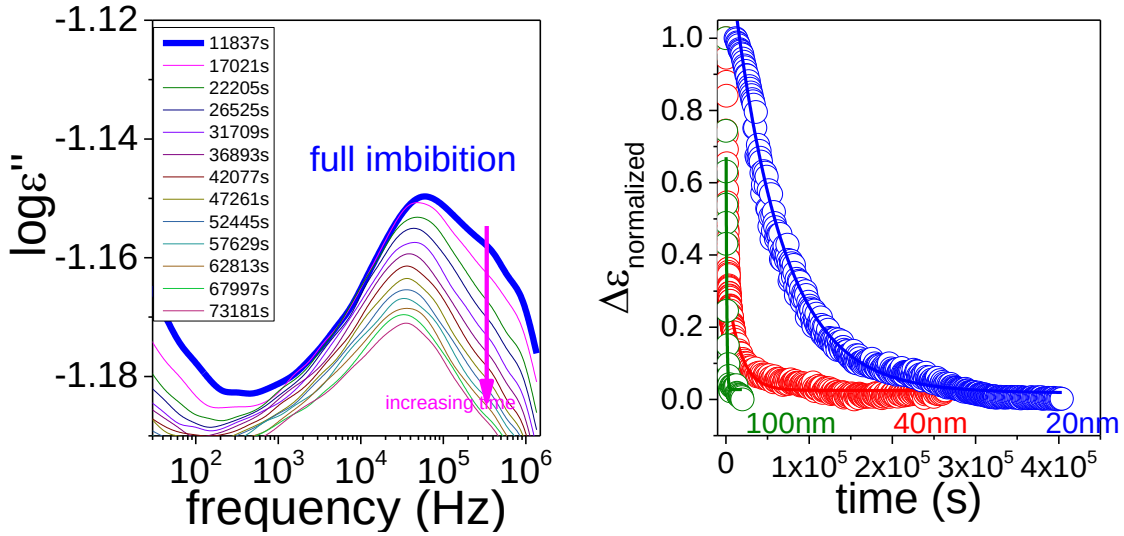

Figure 2. (left) Evolution of dielectric loss curves at the late stages of imbibition of PI 5k within AAO templates having 20 nm diameter pores at *T*=303.15K. (right) Evolution of the normalized dielectric intensity during the *in situ* imbibition and subsequent adsorption within AAO nanopores with different pore diameters; (green):100 nm, (red): 40 nm, and (blue): 20 nm all at the same temperature (303.15 K). Lines represent the result of the fit to an exponential decay function (see text).

The results of the adsorption kinetics of PI 5k can be discussed with the help of **Figure 3**. The figure depicts the characteristic adsorption time, $\log(\tau_{ads}/s)$ as a function of the inverse pore diameter (**Fig. 3a**) and as a function of the degree of confinement (**Fig. 3b**), the latter defined by the ratio of the polymer coil size ($2R_g$) to the pore diameter. In addition, the figure contains the time required for the full imbibition of the pores (in green) extracted by ROM (this time coincides with the $\Delta\varepsilon_{max}$). The adsorption time follows the dependencies as: $log(\tau_{ads}/s) = 2.2 \pm 0.2 + \frac{62\pm8}{D}$, $(D \ in\ nm)$ and $log(\tau_{ads}/s) = 2.2 \pm 0.2 + (13.5 \pm 1.8) \times \frac{2R_g}{D}$, $(D\ in\ nm)$, *e.g.*, strongly increasing with confinement. The characteristic relaxation times of the longest normal mode obtained from the dielectric loss maximum at the end of the imbibition process are also shown. Notably, this time scale is somewhat longer than in the bulk especially within the smaller pores (Supporting Information **Fig. S5**). This finding could reflect an increasing density of topological constraints as a result of the loop/train configurations of the adsorbed chains. Loop/train configurations are expected to reduce the critical molecular weight for entanglements for chains in the vicinity to the pore walls. The results presented here as well as in ref [11] are consistent with the notion of surface-enhanced entanglements that "propagate" in the direction normal to the surface.[34] On the other hand, the results on the time scale of chain relaxation obtained in situ by following the full imbibition are at variance from earlier results on 3-d as well as 1-d and 2-d confined PI that reported faster chain dynamics through the relaxation of terminal subchains.[27,35]

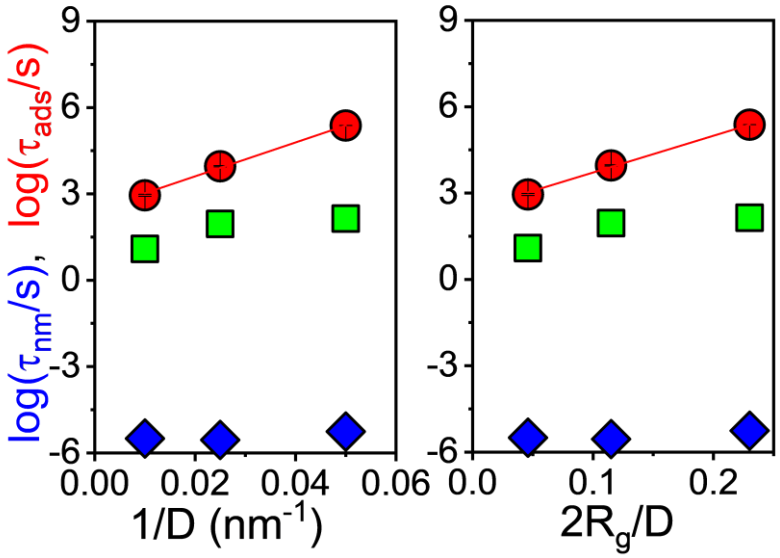

Figure 3. Dependence of the characteristic adsorption time, $\log(\tau_{ads}/s)$ on (left) the inverse pore diameter and (right) the degree of confinement, defined by the ratio of polymer size ($2R_g$) to the pore diameter for PI 5k: (red spheres): characteristic adsorption times obtained from the fits shown in Figure 2. The lines represent the result of a linear fit. The time scale of the longest normal mode (blue solid rhombi) is also plotted at the end of the adsorption process (see Fig. S5). The time of full imbibition is plotted with the green solid squares. Error bars give the uncertainties (typically smaller than the symbol size).

A direct proof that the decrease in the dielectric intensity of the longest normal mode is due to the adsorption of chains is provided by following the same kinetics but in a treated (silanized) AAO surface. The results between untreated and treated surfaces for a PI 21k within AAO templates having pores with diameter of 100 nm at 303.15 K are compared in **Figure 4**. Following the full imbibition, the dielectric strength in a silanized pore remains constant with time in sharp contrast to native AAO surface. Evidently, silanization is very effective in reducing adsorption sites acting as lubricant for the incoming chains.

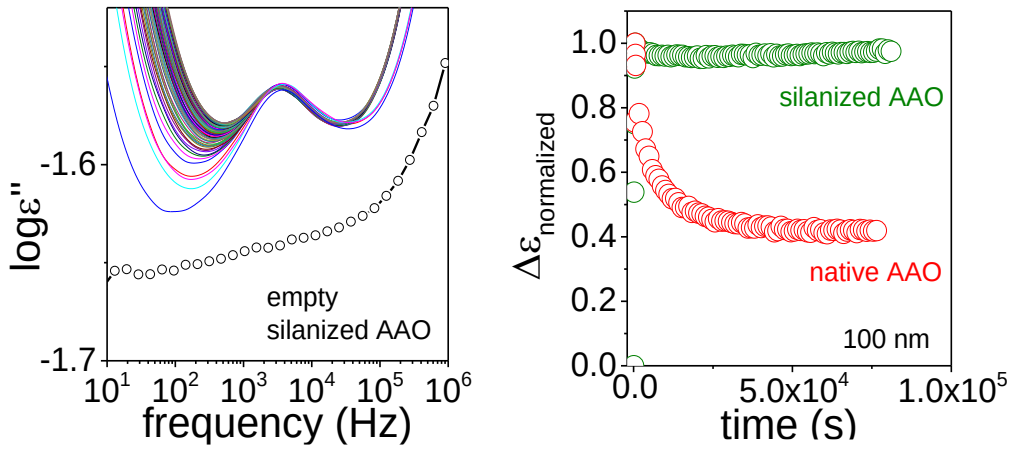

Figure 4. (a) Evolution of the dielectric loss curves during and following the complete imbibition of PI 12k within silanized AAO nanopores having pore diameters of 100 nm at T = 303.15 K. (b) Evolution of dielectric intensity ($\Delta\varepsilon$) of PI 12k during the *in situ* imbibition (and subsequent adsorption) within nanopores with a native (red) or silanized (green) inner pore surface.

Next, we discuss the evolution of the distribution of relaxation times during and following polymer imbibition. The data refer to PI 21k, where the maximum in the loss of the chain modes is well within the frequency window. In **Figure 5**, the evolution of the dielectric loss curves at the late stages of imbibition within AAO templates having 40 nm pores at 303.15 K are shown. The same figure depicts the low- and high-frequency HN parameters during the adsorption kinetics. The evolution of the high-frequency slope ($\alpha\gamma$) shows the narrowing of the distribution of

relaxation times with time. The broader distribution at the earlier stages reflects the continuous changes due to chain adsorption.

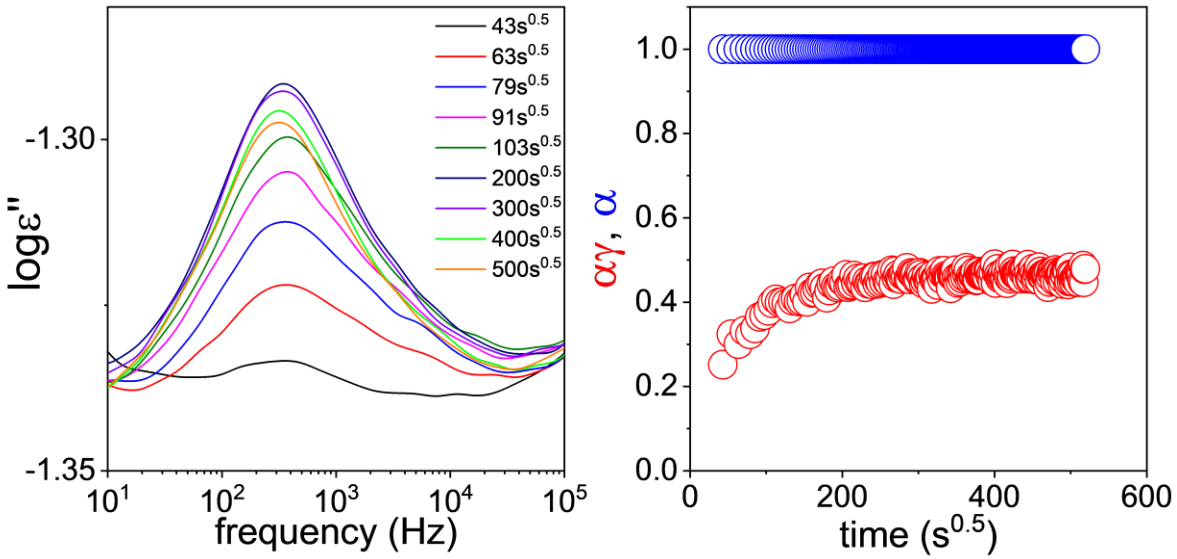

Figure 5. (Left) Evolution of the dielectric loss curves at the late stages of imbibition of PI 21k within AAO templates having 40 nm pores at 303.15 K. (Right) Evolution of the HN shape parameters.

The chain length dependence of the adsorption process is examined next. **Figure 6** provides the evolution of dielectric strength for three PIs with molar masses of 5 kg·mol^{-1}, 12 kg·mol^{-1} and 21 kg·mol^{-1} within AAO templates with a pore size of 100 nm at 303.15 K. The normalized dielectric strength was again fitted to an exponential function, and the characteristic adsorption times are plotted in **Figure 6**. Evidently, adsorption times become much longer with increasing molar mass. Additional data for a smaller pore diameter (40 nm) are provided in Supporting Information **Figure S6**.

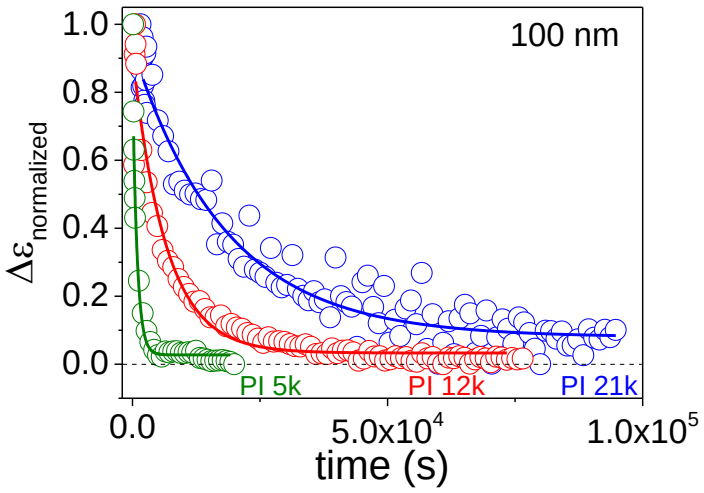

Figure 6. Evolution of dielectric intensity ($\Delta\varepsilon$) of PI with different molar masses during the *in situ* imbibition (and subsequent adsorption) within AAO nanopores with diameter of 100 nm at a temperature 303.15 K. Lines represent fits to an exponential decay function.

The different time scales can be discussed with the help of **Figure 7**. The figure contains in total four time scales: The faster (~ *n*s) is the segmental relaxation obtained from the Vogel-Fulcher-Tammann (VFT) equation at the imbibition temperature (303.15 K) (Supporting Information **Fig. S7**). The latter was obtained immediately following the kinetic experiments by fast cooling to below T_g and slow heating to higher temperatures. As expected, this time scale is the fastest without a significant dependence on molar mass. The second time scale is the longest normal mode obtained at the end of the imbibition process as $\tau_{max} = 1/(2\pi f_{max})$ (Supporting Information **Fig. S5**). The critical molar mass M_c for PI is ~ 10800 g·mol^{-1} (the entanglement molecular weight is M_e ~ 5400 g·mol^{-1}) meaning that PI 5k is unentangled, PI 21k is entangled, and PI 12k is in the border region.[16] Despite the limited data points two slopes can be obtained with exponents of approximately 2 and 3.4 below and above M_c. The third time scale corresponds to the time needed for the full imbibition and has a clear molar mass dependence. Finally, the fourth time scale reflects the adsorption times that strongly depend on both the molar mass and the pore size. Adsorption times are (i) some 8 orders of magnitude slower than the terminal relaxation times (*e.g.*, the relaxation of the chain as a whole) and (ii) display a similar molar mass dependence with the terminal times. Interestingly, annealing times were also found to scale with the chain relaxation times in confined poly(propylene glycol) within AAO templates (although through a different temperature protocol).[36,37]

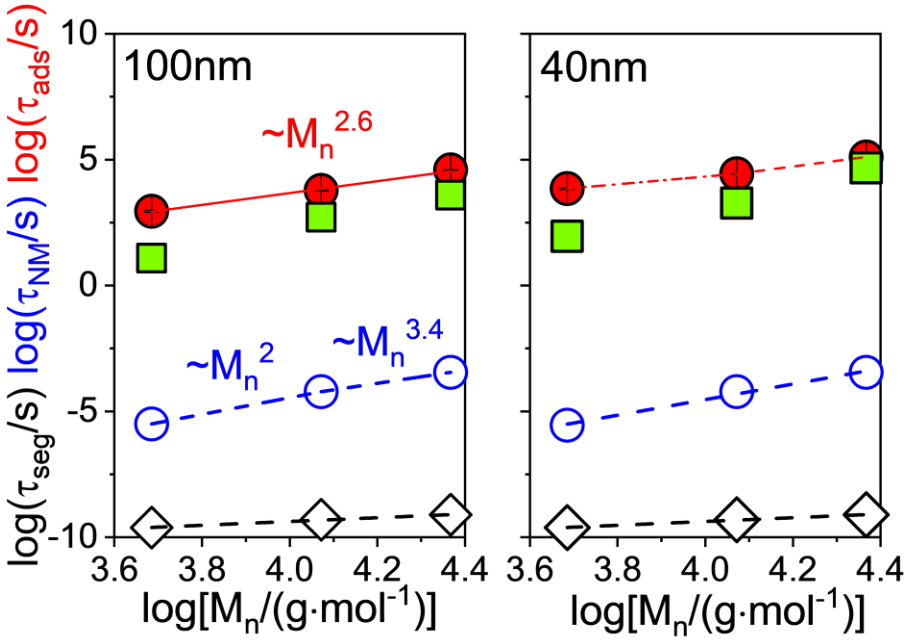

Figure 7. Molar mass dependence of the characteristic time scales within AAO nanopores with pore diameters (left) 100 nm and (right) 40 nm. (green squares): full imbibition time, (red spheres): characteristic adsorption time following imbibition, (blue solid/empty circles) peak position of the longest normal mode of polyisoprene under confinement (at the end of adsorption process). Dashed and dash-dotted lines are linear fits. Error bars give the uncertainties (typically smaller than the symbol size).

The very long time scale of adsorption can be discussed in view of a scaling theory developed by De Gennes[4,5] that accounts for the formation of adsorbed layers in a good solvent. At early stages, a uniform polymer layer was considered on the (flat) surface as a result of bulk diffusion. Subsequent formation of an adsorbed layer was considered as a two-step process. At a first step, any new chain to be adsorbed needs to overcome the potential barrier due to the excluded volume of the already adsorbed chains. At a second step, the incoming chain replaces the already adsorbed chains by spreading on the surface, whereas the previously adsorbed chain unfolds by the formation of long loops. As outgoing (and incoming) chains have to pass through several unfavorable configurations the latter process was predicted to be very slow. As for the molar mass dependence, by considering entangled polymers, de Gennes suggested that the longest relaxation time scales as $\tau \sim \tau_s N^3$, where τ_s is the relaxation time of an adsorbed monomer. Subsequently, Semenov and Joanny,[6] considered explicitly the structure of tails and loops within the adsorbed layer (the chain ends are effectively repelled from the surface) and further assumed Rouse-Zimm

dynamics to predict the molar mass dependence of two characteristic times scales, the adsorption and the exchange times, with respective scaling as $\tau \sim N^{2.24}$ and $\tau \sim N^{2.42}$. Both of these dependencies are in line with the experimental results over the limited range of molar masses investigated. Extending the range of molar masses is a formidable task due to limitations associated with the experimental frequency window and imbibition temperature.

Blend Imbibition and adsorption. We further investigated the effect of blending on the imbibition and adsorption kinetics for two symmetric PI blends (B1 (5k/21k) and B2 (5k/42k)). While the short chains do not entangle, the long chains are above the entanglement limit.[16] The question is whether the two components penetrate and adsorb on the pores simultaneously or consecutively. We mention here that earlier experiments using *ex situ* methods have demonstrated the ability of the AAO templates to effectively separate the components of miscible blends by taking advantage of the difference in the imbibition speeds of the respective homopolymers.[38,39] These techniques, however, have two shortcomings: First, they do not provide the respective time scales and second, they cannot follow the adsorption kinetics. The advantage of nanodielectric spectroscopy is that it simultaneously provides access to the imbibition length and the adsorption kinetics by following the change in the dielectric strength of the chain relaxation.

The results for the blend B2 with respect to the evolution of the dielectric loss curves during and following the full imbibition are shown in **Figure 8**. The evolution of the dielectric loss curves corresponding to the shorter and longer chains in the blend reveals distinct differences that will be discussed below with respect to **Figure 10**. We should point out here that the choice of the blend components in B1 and B2 is based on the existence of two separate normal modes in the blends both relaxing within the experimental window: a slower (faster) one reflecting the dynamics of the longer (shorter) chains in the blend. We will first discuss the results from blend B1.

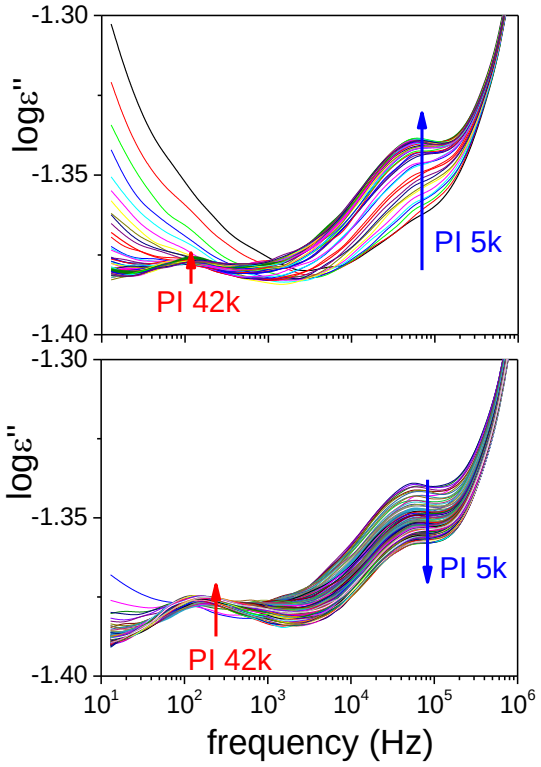

Figure 8. Evolution of dielectric loss curves corresponding to the two separate normal modes of PI in the blend B2 (5/42k) during imbibition and subsequent long-time adsorption within AAO with a pore diameter of 40 nm at 303.15K. Early (top) and late (below) stages are shown. Arrows are indicative trends for the evolution of the dielectric loss curves corresponding to the normal modes of PI 5k (blue) and PI 42k (red) components in the blend.

The evolution of the dielectric intensities of the two separate normal modes in blend B1 is provided in **Figure 9**. We point out that in the blend there exists a single local friction as obtained by temperature-dependent measurements of the (single) segmental process in the blends. The results are compared to independent ROM measurements of the imbibition length in comparison to the respective homopolymers (**Fig. 9b**). The imbibition lengths for blend B1 are located in between the corresponding lengths for the two homopolymers. It further suggests the complete imbibition of the blend in ~ 620 s. At this time, the increase of the dielectric strength of the normal mode for the PI 5k component in the blend reaches a maximum. Following the full imbibition, the dielectric strength of the PI 5k component decreases due to adsorption with a characteristic adsorption time of ~ 2.9 $\times 10^3$ s. The evolution of the dielectric strength of the PI 21k bears similarities to the lower-molecular-weight component albeit with one difference. The maximum

in the dielectric strength is attained somewhat later and the characteristic adsorption time increases to 1.5×10^4 s. The latter is in agreement with the characteristic adsorption times of the respective homopolymers discussed with respect to **Figure 6**. This suggests that in blend B1, imbibition of the two components proceeds with somewhat different rates; first, the shorter chains are entering the nanopores, and somewhat later, the longer chains penetrate together with the remaining short chains. The difference in imbibition speeds, however, is not dramatic. To enhance the difference in imbibition speeds of the two components we return to the blend B2 (5k/42k) (**Figure 8** and **Figure 10**).

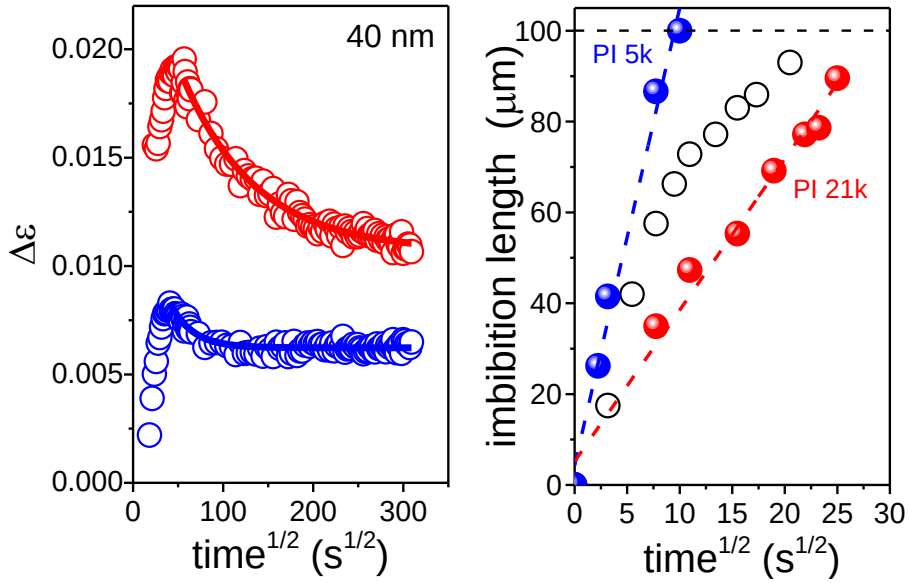

Figure 9. (left) Evolution of dielectric intensity for the PI blend B1 (5k/21k) during imbibition and subsequent long adsorption within AAO with a pore diameter of 40 nm at T = 303.15K. (Right) Imbibition lengths measured *ex situ* by ROM for three systems: homopolymer PI 5k (blue spheres), homopolymer PI 21k (red spheres), and B1 blend (black circles). Blue and red dashed lines represent linear fits to the homopolymer data. The horizontal dashed line indicates the length corresponding to full imbibition.

The results of the blend B2 (**Figure 10**) are distinctly different from those of B1. This is evident here as the blend components have very different imbibition speeds. Note that the imbibition lengths of the homopolymers calculated from the LWE based on the measured (**Table 1**) zero-shear viscosities (solid lines in **Fig. 10b**) are at variance from the measured lengths. While for the homopolymer PI 5k the extracted effective viscosity from the imbibition length and the use

of the LWE is approximately the bulk zero-shear viscosity, for the PI 42k homopolymer there exist two slopes during imbibition with effective viscosities of 4660 Pa·s and 910 Pa·s, *e.g.*, much higher than bulk (**Table 1**). This finding reveals that the dead-layer effect is dominant.[11] For the blend, the results from the ROM study (**Fig. 10b**) suggest that the imbibition length, d_1, is in proximity to the PI 5k homopolymer revealing a clear preference for the shorter chains to penetrate the pores. The emerging picture from these results is that the PI 5k chains are enter first, and only later, some PI 42k are dragged into the pores. This is more evident here because the two homopolymers have very different imbibition speeds.

These results on the "static" imbibition length obtained *ex situ* (ROM) can be compared with the results from dynamic experiment performed *in situ* (*n*DS). In accordance with the static measurement revealing the faster imbibition of the shorter chains, the dielectric strength of the PI 5k blend component (**Fig. 8** and **Fig. 10a**) first increases during imbibition and reaches a maximum at a time scale that nicely corresponds to the full imbibition (as obtained from ROM). It is only at the late stages of the pore filling that the shorter chains drag along some of the longer chains in the pores as evidenced by the slow increase in the dielectric strength of the PI 42k component. At the same time, the normal mode of the PI 5k blend component stars to decrease as a result of increasing adsorption. Hence, at the late stages of imbibition, two effects take place: first, the shorter chains are adsorbed onto the AAO pore surface, and at the same time, some of the longer chains are entering the pores. This further suggests that long-time adsorption in the blend is dominated by an exchange mechanism involving primarily the shorter chains.

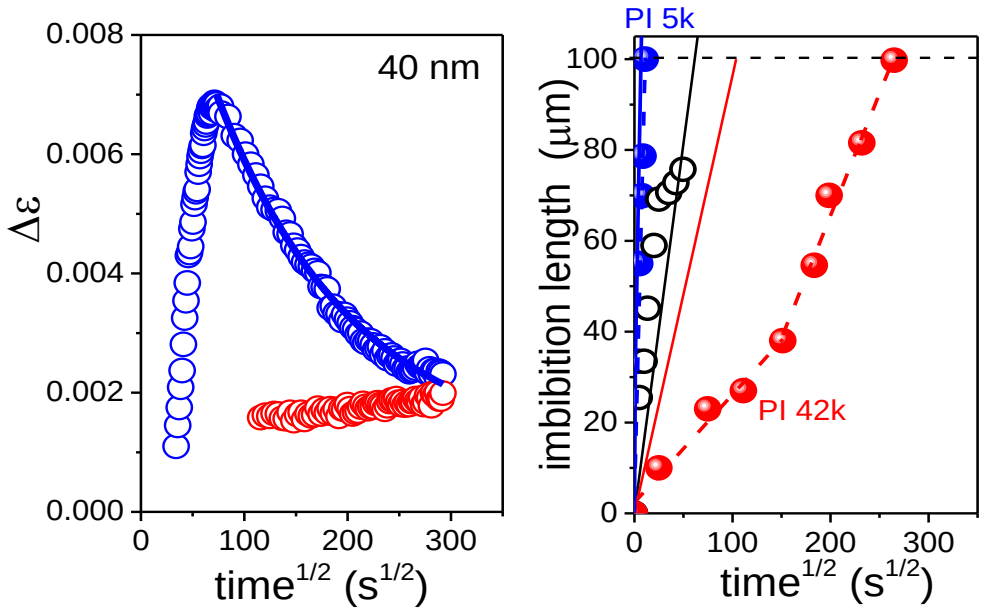

Figure 10. (left) Evolution of dielectric intensity for the PI blend B2 (5k/42k) during imbibition and subsequent long adsorption within AAO with a pore diameter of 40 nm at T = 303.15K. (Right) Imbibition lengthw measured *ex situ* by ROM for three systems: homopolymer PI 5k (blue spheres), homopolymer PI 42k (red spheres), and B2 blend (black circles). Blue, red and black solid lines are the predictions of the imbibition length based on the LWE and the measured zero-shear viscosity (Table 1).

Overall, results show an efficient separation of long/short chains in a miscible polymer blend by following the imbibition length and the associated dynamics of the longest normal modes. Although previous techniques[11,38,39] were able to show the potential of AAO templates in separating chains of different molar masses and in the absence of solvent, *n*DS has the advantage of providing the chain dynamics at the same time. When the blend components have drastically different molar masses (M_n (long)/M_n(short) ~ 8) the long-time adsorption kinetics is dominated by the shorter chains, otherwise (*i.e.*, M_n(long)/M_n(short) ~ 4) both chains participate in the adsorption process.

5.4 Conclusion

The adsorption kinetics of *cis*-1,4-polyisoprene was studied as a function of polymer molar mass, AAO pore diameter, and surface treatment by following the evolution of the dielectrically active longest normal mode by nanodielectric spectroscopy. Following the initial imbibition of polymer chains and the formation of an adsorbed layer, the adsorption of other chains is an extremely slow

process. For a given molar mass, the characteristic adsorption times strongly depend on the ratio $2R_g/D$. For a given pore diameter, adsorption times are some 8 orders of magnitude slower than the terminal relaxation times and more than 12 orders of magnitude slower than the segmental times. Nevertheless, the adsorption and terminal relaxation times display similar molar mass dependences. The extremely slow kinetics reflect the fact that incoming and outgoing chains from the pore surface have to pass through several unfavorable configurations (*e.g.*, trains, loops). The molar mass dependence of the characteristic adsorption times is in good agreement with a scaling theory proposed by de Gennes and later refined by Semenov and Joanny, to account explicitly the structure of tails and loops within the adsorbed layer. The latter suggested that the adsorption and exchange times scale as $\tau \sim N^{2.24}$ and $\tau \sim N^{2.42}$ not far from the experimental observations given the small molar mass range accessible by *n*DS.

As an extension of this work, we explored how symmetric PI blends penetrate the same nanopores. Of particular interest were blends where the imbibition speeds of the two homopolymers were very different. By taking advantage of the disparity in the imbibition speeds we were able to show that shorter chains penetrate first, and in addition, that they adsorb first on the AAO walls. The longer chains are entering the pores only at the late stages of the filling process providing an example of fractionation and in the absence of solvent. The results from *n*DS demonstrate the advantage of the technique to provide the imbibition lengths, the adsorption kinetics and chain dynamics.

In a broader context, the results suggest means of controlling the interfacial interactions in homopolymers and their blends of importance in the design of polymer interfaces with controlled physical processes.

5.5 References

(1) De Gennes, P. G. Scaling Theory of Polymer Adsorption. *Journal de Physique* **1976**, *37* (12), 1445-1452.

(2) Granick, S. Motions and Relaxations of Confined Liquids. *Science* **1991**, *253* (5026), 1374-1379.

(3) Aksimentiev, A.; Heng, J. B.; Timp, G.; Schulten, K. Microscopic Kinetics of DNA Translocation through Synthetic Nanopores. *Biophys. J.* **2004**, *87* (3), 2086-2097.

(4) De Gennes, P. G. Polymer Solutions near an Interface. Adsorption and Depletion Layers. *Macromolecules* **1981**, *14* (6), 1637-1644.

(5) De Gennes, P. G. Polymers at an Interface; a Simplified View. *Adv. Colloid Interface Sci.* **1987**, *27* (3-4), 189-209.

(6) Semenov, A. N.; Joanny, J.-F. Kinetics of Adsorption of Linear Homopolymers onto Flat Surfaces: Rouse Dynamics. *J. Phys. II* **1995**, *5* (6), 859–876.

(7) O'Shaughnessy, B.; Vavylonis, D. Non-equilibrium in Adsorbed Polymer Layers. *J. Phys.: Condens. Matter* **2004**, *17* (2), R63-R99.

(8) Ligoure, C.; Leibler, L. Thermodynamics and Kinetics of Grafting End-functionalized Polymers to an Interface. *J. Phys.* **1990**, *51* (12), 1313-1328.

(9) Kremer, F. (Ed.) *Dynamics in Geometrical Confinement*. Springer: Berlin, **2014**.

(10) Napolitano, S.; Wübbenhorst, M. The Lifetime of the Deviations from Bulk Behaviour in Polymers Confined at the Nanoscale, *Nat. Commun.* **2011**, *2* (1), 260.

(11) Tu, C.-H.; Steinhart, M.; Butt, H.-J.; Floudas, G. In Situ Monitoring of the Imbibition of Poly (*n*-butyl methacrylates) in Nanoporous Alumina by Dielectric Spectroscopy. *Macromolecules* **2019**, *52* (21), 8167-8176.

(12) Serghei, A.; Chen, D.; Lee, D. H.; Russell, T. P. Segmental Dynamics of Polymers during Capillary Flow into Nanopores. *Soft Matter* **2010**, *6* (6), 1111-1113.

(13) Serghei, A.; Lutkenhaus, J. L.; Miranda, D. F.; McEnnis, K.; Kremer, F.; Russell, T. P. Density Fluctuations and Phase Transitions of Ferroelectric Polymer Nanowires. *Small* **2010**, *6* (16), 1822-1826.

(14) Tu, C.-H.; Zhou, J.; Doi, M.; Butt, H.-J.; Floudas, G. Interfacial Interactions During In Situ Polymer Imbibition in Nanopores. *Phys. Rev. Lett.* **2020**, *125* (12), 127802.

(15) Masuda, H.; Fukuda, K. Ordered Metal Nanohole Arrays Made by a Two-step Replication of Honeycomb Structures of Anodic Alumina. *Science* **1995**, *268* (5216), 1466-1468.

(16) Fetters, L.J.; Lohse, D.J.; Colby, R.H. Chain Dimensions and Entanglement Spacings. *Physical Properties of Polymers Handbook.* Springer, New York, NY, **2007**, 447-454.

(17) Kremer, F. and Schönhals, A. (Eds.) *Broadband Dielectric Spectroscopy*. Springer Science & Business Media, **2002**.

(18) Tu, C-.H.; Steinhart, M.; Butt, H-.J.; Floudas, G. Polymers under 2-D Confinement: Flow of Polymer Melts at the Nanoscale. *Broadband Dielectric Spectroscopy: A Modern Analytical Technique.* American Chemical Society, **2021**, 203-221.

(19) Lucas, R. Ueber das Zeitgesetz des Kapillaren Aufstiegs von Flüssigkeiten. *Colloid Polym. Sci.* **1918**, 23, 15-22.

(20) Washburn, E. W. The Dynamics of Capillary Flow. *Phys. Rev.* **1921**, *17* (3), 273-283.

(21) Yao, Y.; Alexandris, S.; Henrich, F.; Auernhammer, *G.*; Steinhart, M.; Butt, H.-J.; Floudas, G. Complex Dynamics of Capillary Imbibition of Poly(ethylene oxide) Melts in Nanoporous Alumina. *J. Chem. Phys.* **2017**, *146* (20), *203320.*

(22) Alexandris, S.; Papadopoulos, P.; Sakellariou, G.; Steinhart, M.; Butt, H.-J.; Floudas, G. Interfacial Energy and Glass Temperature of Polymers Confined to Nanoporous Alumina. *Macromolecules* **2016**, *49* (19), 7400-7414.

(23) Adachi, K.; Kotaka, T. Dielectric Normal Mode Process in Undiluted Cis-polyisoprene. *Macromolecules* **1985**, *18* (3), 466-472.

(24) Boese, D.; Kremer, F.; Fetters, L. J. Molecular Dynamics in Linear and Multiarmed Star Polymers of Cis-polyisoprene as Studied by Dielectric Spectroscopy. *Macromolecules* **1990** *23* (6), 1826-1830.

(25) Schönhals, A. Relation between Main and Normal Mode Relaxations for Polyisoprene Studied by Dielectric Spectroscopy. *Macromolecules* **1993**, *26* (6), 1309-1312.

(26) Floudas, G.; Paraskeva, S.; Hadjichristidis, N.; Fytas, G.; Chu, B.; Semenov, A. N. Dynamics of Polyisoprene in Star Block Copolymers Confined in Microstructures: A Dielectric Spectroscopy Study. *J. Chem. Phys.* **1997**, *107* (14), 5502-5509.

(27) Petychakis, L.; Floudas, G.; Fleischer, G. Chain Dynamics of Polyisoprene Confined in Porous Media. A Dielectric Spectroscopy Study. *Europys. Lett.* **1997**, *40* (6), 685.

(28) Alexandris, S.; Sakellariou, G.; Steinhart, M.; Floudas, G. Dynamics of Unentangled Cis-1,4-polyisoprene Confined to Nanoporous Alumina. *Macromolecules* **2014**, *47* (12), 3895-3900.

(29) Tarnacka, M.; Kaminski, K.; Mapesa, E. U.; Kaminska, E.; Paluch, M. Studies on the Temperature and Time Induced Variation in the Segmental and Chain Dynamics in Poly (propylene glycol) Confined at the Nanoscale. *Macromolecules* **2016**, *49* (17), 6678-6686.

(30) Talik, A.; Tarnacka, M.; Grudzka-Flak, I.; Maksym, P.; Geppert-Rybczynska, M.; Wolnica, K.; Kaminska, E.; Kaminski, K.; Paluch, M. The Role of Interfacial Energy and Specific Interactions on the Behavior of Poly (propylene glycol) Derivatives under 2D Confinement. *Macromolecules* **2018**, *51* (13), 4840-4852.

(31) Politidis, C.; Alexandris, S.; Sakellariou, G.; Steinhart, M.; Floudas, G. Dynamics of Entangled Cis-1, 4-polyisoprene Confined to Nanoporous Alumina. *Macromolecules* **2019**, *52* (11), 4185-4195.

(32) Watanabe, H.; Ishida, S.; Matsumiya, Y. Rheodielectric Behavior of Entangled Cis-polyisoprene under Fast Shear. *Macromolecules* **2002**, *35* (23), 8802-8818.

(33) Douglas, J.F.; Johnson, H.E.; Granick, S. A Simple Kinetic Model of Polymer Adsorption and Desorption. *Science* **1993**, *262*, 2010-2012.

(34) Granick, S. Perspective: Kinetic and Mechanical Properties of Adsorbed Polymer Layers. *Eur. Phys. J.E.* **2002**, *9*, 421-424.

(35) Mapesa, E.U.; Popp, L.; Kipnusu, W.K.; Tress, M.; Kremer, F. Molecular dynamics in 1- and 2-D confinement as studied for the case of poly (*cis*-1, 4-isoprene). *Soft Materials* **2014**, 12, S22-S30.

(36) Tarnacka, M.; Talik, A.; Kamińska, E.; Geppert-Rybczyńska, M.; Kaminski, K.; Paluch, M. The Impact of Molecular Weight on the Behavior of Poly (propylene glycol) Derivatives Confined within Alumina Templates. *Macromolecules* **2019**, 52(9), 3516-3529.

(37) Tarnacka, M.; Madejczyk, O.; Kaminski, K.; Paluch, M. Time and temperature as key parameters controlling dynamics and properties of spatially restricted polymers. *Macromolecules* **2017**, 50(13), 5188-5193.

(38) Yao, Y.; Butt, H.-J.; Zhou, J.; Doi, M.; Floudas, G. Capillary Imbibition of Polymer Mixtures in Nanopores. *Macromolecules* **2018**, *51* (8), 3059-3065.

(39) Zhang, M.; Dobriyal, P.; Chen, J. T.; Russell, T. P.; Olmo, J.; Merry, A. Wetting Transition in Cylindrical Alumina Nanopores with Polymer Melts. *Nano letters* **2006**, *6*(5), 1075-1079.

5.6 Supporting information

I. Simulation of the imbibition process of PI

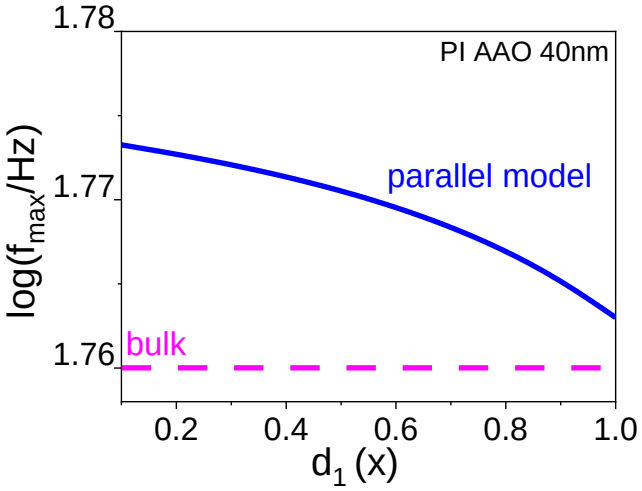

Figure S1. Evolution of the peak frequency for the non-polar polymer PI during imbibition as a function of polymer penetration depth, d_1, based on the parallel model.

II. Calibration experiments (Reflection Optical Microscopy)

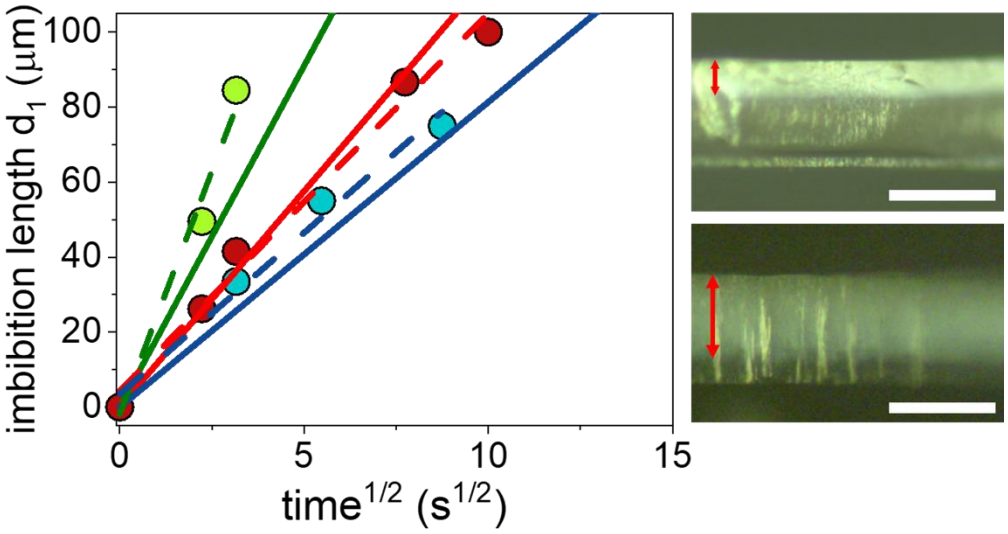

Figure S2. (Left) Calibration measurements for the imbibition of PI 5k within different AAO pores: 100 nm (green), 40 nm (red), and 20 nm (blue). Dashed lines are linear fits. Solid lines are theoretical predictions according to Lucas-Washburn equation with bulk viscosity. (Right) Representative ROM images obtained *ex situ* during the imbibition of PI 5k within AAO 20 nm at 303 K corresponding to different time periods: (top) $3.16 s^{1/2}$ and (bottom) $8.7 s^{1/2}$. The scale bar is 100 μm.

III. Rheology

Samples were prepared on the lower plate of the 8 and 25 mm diameter parallel plate geometry. The upper plate was brought into contact, the gap thickness was adjusted and the sample was cooled. The storage (G') and loss (G'') shear moduli were monitored as a function of frequency, ω, for frequencies in the range from $10^{-2} < \omega < 10^{2}$ rad/s. All measurements refer to the linear viscoelastic range. Subsequently, the complex viscosity (η^*) follows as $\eta^* = G''/\omega - iG'/\omega$. Master curves at the same reference temperature (the imbibition temperature, T = 303.15 K) were made by using the time-temperature superposition principle (tTs). The latter allows the frequency ω dependence of the complex modulus G^* at any temperature T to be determined from a master curve at a reference temperature. At each temperature T, a single frequency-scale shift factor a_T allow superposition of all viscoelastic data at temperature T with the data at the reference temperature, T_{ref}, as: $G^*(\omega;T) = G^*\left(a_T\omega;T_{ref}\right)$. Master-curves of the storage, the loss moduli and the shear viscosity are shown in **Figure S3** all at the same reference temperature of 303.15 K. The shift factors a_T and Williams-Landel-Ferry (WLF) coefficients (C_1^0, C_2^0 at T_{ref}) are shown in **Figure S4**.

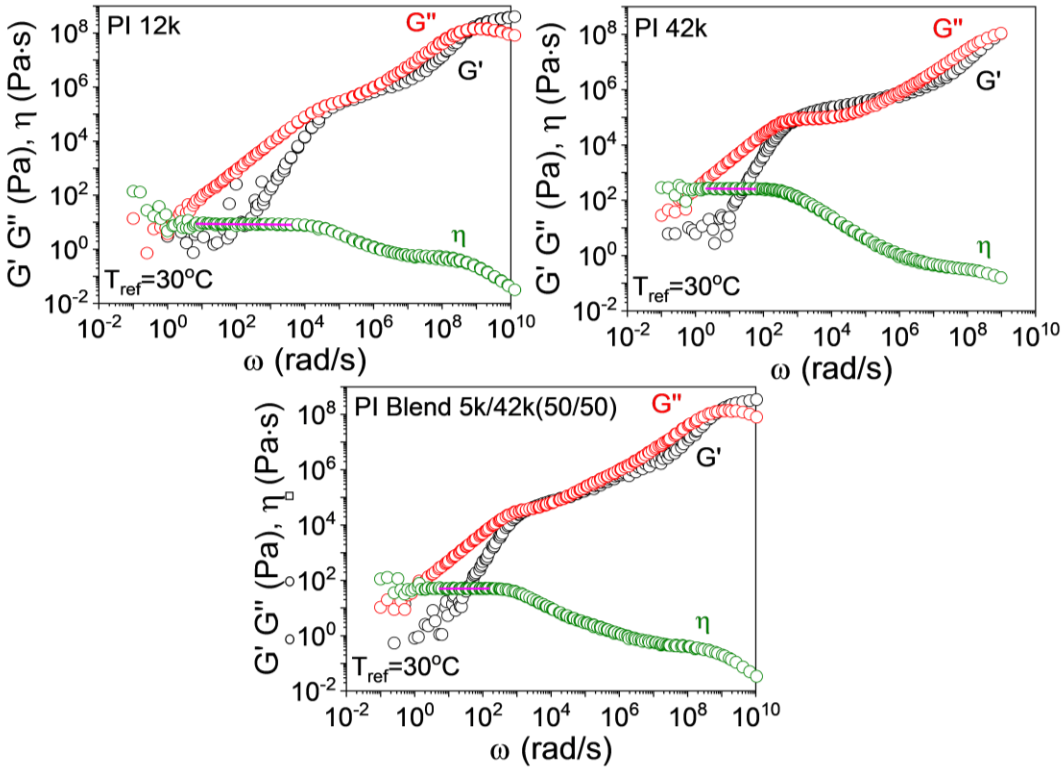

Figure S3. Master curves for the storage (black), the loss (red) moduli and the shear viscosity (green) all constructed at the same reference temperature (303.15 K).

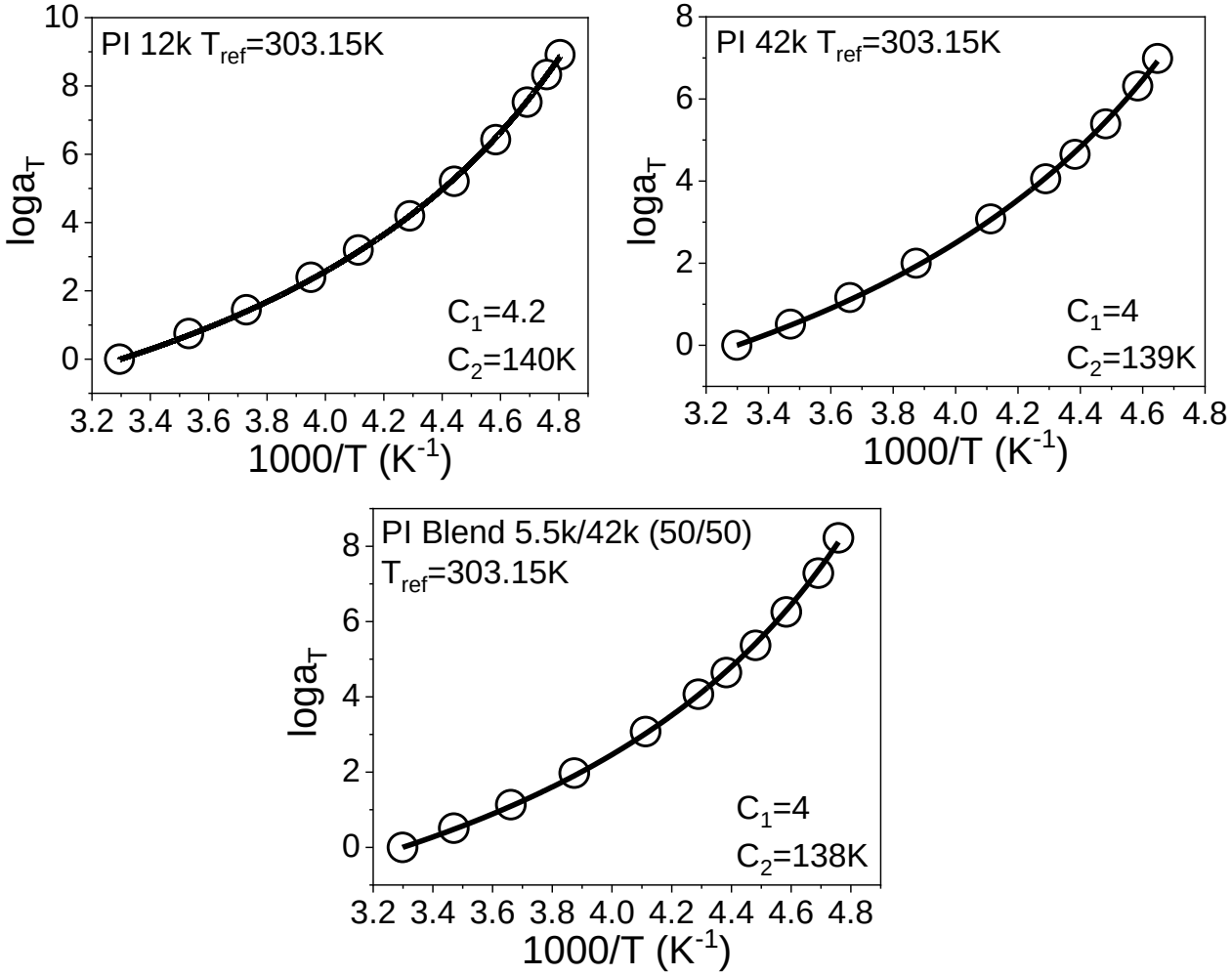

Figure S4. Shift factors for the homopolymers and the symmetric blend 5k/42k at the reference temperature (303.15 K). Solid lines represent fits to the WLF equation.

IV. Evolution of longest normal mode during and after imbibition

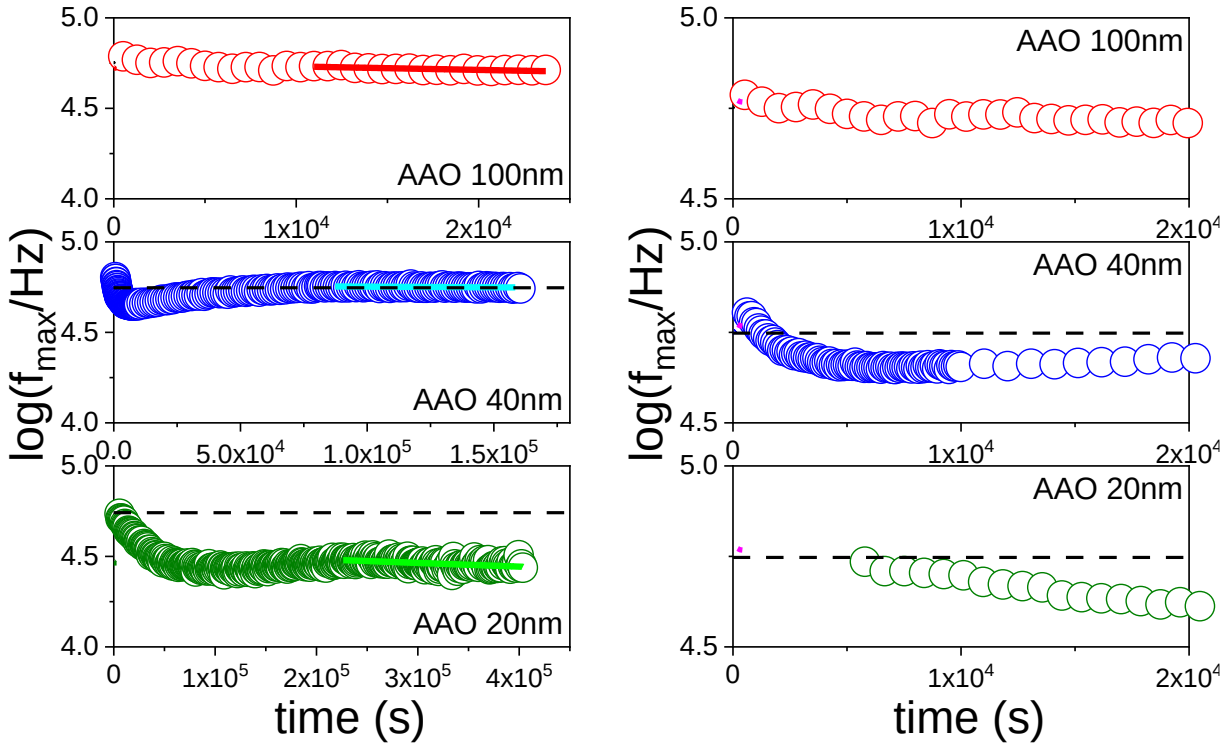

Figure S5. Evolution of peak position log(f_{max}/Hz) of the longest normal mode of PI 5k during in situ imbibition and adsorption process within different AAO templates with pore diameters (100 nm, 40 nm, and 20 nm): (left) entire imbibition and adsorption process and (right) zoom-in at the early stages. Black dashed lines indicate the frequency of the longest normal mode for the bulk polymer. Solid colored lines give the frequency of the peak position corresponding to the longest normal mode at the late stages. Notice the slower normal mode relaxation within the 20 nm pores as compared to the bulk.

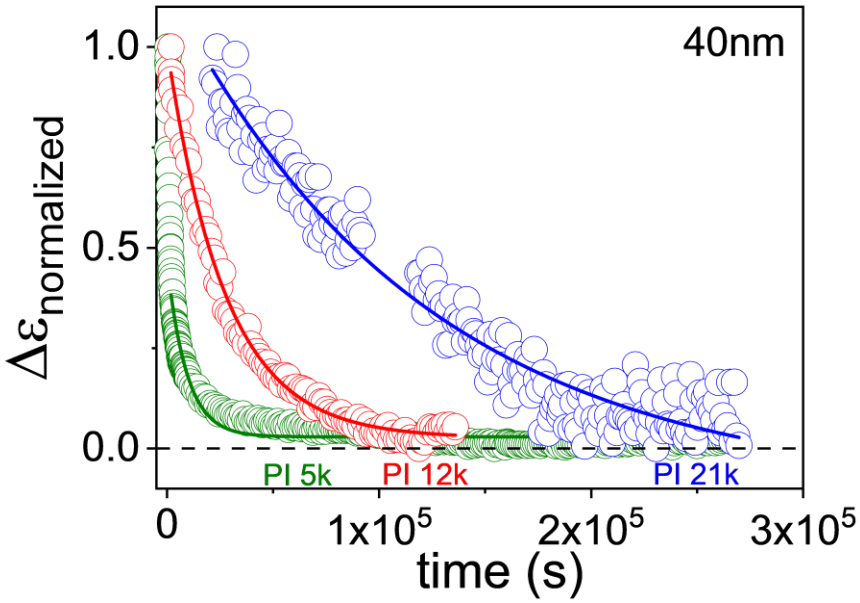

Figure S6. Evolution of dielectric intensity ($\Delta\varepsilon$) of PI with different molar masses during the *in situ* imbibition (and subsequent adsorption) within AAO nanopores with diameter of 40 nm at a temperature 303.15 K. Lines represent fits to an exponential decay function.

V. Polymer dynamics following imbibition

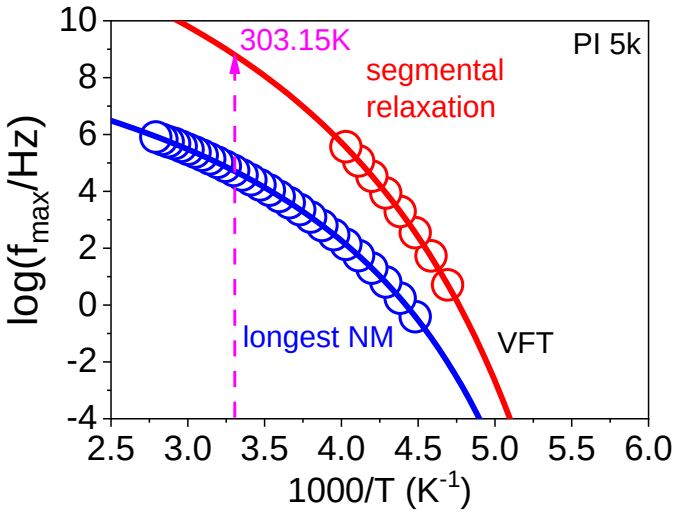

Figure S7. Arrhenius plot of the characteristic peak frequencies of PI 5k: longest normal mode (blue) and segmental relaxation (red). Solid lines are fits to the Vogel-Fulcher-Tammann equation. The vertical dashed line at 303.15 K indicates the peak frequencies of the normal mode and of the (extrapolated) segmental mode at the imbibition temperature.

Conclusion

In this Thesis the technique of *in situ* nanodielectric spectroscopy is used to address some important questions in polymer physics. The first topic is *if* and *how* the segmental and chain polymer dynamics are affected during imbibition. The second topic relates to the imbibition of a polymer electrolyte where both polymer segments and ions are transported at the nanoscale. The third topic explores the possibility to infiltrate a polymer directly from the semicrystalline state. In addition to the polymer (and ion) dynamics the technique provides access to the effective viscosity that a polymer experiences during flow in nanopores — that cannot easily be attained by other techniques. The main conclusions from each topic are summarized below:

(I) Segmental and chain polymer dynamics during imbibition

We first investigated the segmental dynamics of the polar polymer PnBMA. PnBMA has a strong dipole moment and a convenient T_g (~RT) for such studies. Imbibition at the segmental level was nearly isochronal, except at the initial stages, with shape parameters that were independent of imbibition time. This result was not surprising given that the imbibition temperature was located some 30-50 K above T_g. At such temperatures any contribution to the segmental dynamics by interfacial energy effects diminishes. Imbibition at longer length scales provided the effective viscosity and thus a stringent test of the LWE. For PnBMA 5.5k the effective viscosity in the smaller pores was higher than in bulk suggesting that the dead-layer effects dominates. The imbibition of polymer blends composed from short and long PnBMA chains confirmed the potential of the nanofluidic method to fractionate polymers with different molar masses and in the absence of solvent (directly from the bulk state).

Second, we employ the typical type-A polymer *cis*-1,4-polyisoprene to investigate the effect of imbibition on the chain modes. The imbibition kinetics were studied, for the first time during flow, by in situ nanodielectric spectroscopy, under conditions of confinement ($0.14 < 2R_g/D < 0.35$) and as a function of pore surface functionality. For native AAO pores, the imbibition of PI 42k followed two time regimes both with increased effective viscosity relative to the bulk. Within the later stages the dielectric strength of the longest normal mode remained constant despite the fact that more chains were entering the pores. We have discussed this finding by a microscopic

picture that considers the competition from an increasing number of chains entering the pores (that increases the dielectric strength) and a decreasing number of fluctuating chains (that decreases the dielectric strength). At the same time, the longest normal mode was somewhat longer than in bulk especially in the native pores. This could reflect an increased density of topological constraints with time. The adsorption kinetics of *cis*-1,4-polyisoprene was further studied as a function of polymer molar mass, AAO pore diameter, and surface treatment by following the evolution of the dielectrically active longest normal mode. Following the initial imbibition of polymer chains and the formation of an adsorbed layer, the adsorption of other chains was an extremely slow process. For a given molar mass, the characteristic adsorption times strongly depends on the ratio $2R_g/D$. For a given pore diameter, adsorption times were some 8 orders of magnitude slower than the terminal relaxation times and more than 12 orders of magnitude slower than the segmental times. Nevertheless, the adsorption and terminal relaxation times displayed similar molar mass dependences. The extremely slow kinetics reflect the fact that incoming and outgoing chains from the pore surface have to pass through several unfavorable configurations (*e.g.*, trains, loops). The molar mass dependence of the characteristic adsorption times is in good agreement with a scaling theory proposed by de Gennes and later refined by Semenov and Joanny, to account explicitly the structure of tails and loops within the adsorbed layer. The latter suggested that the adsorption and exchange times scale as $\tau \sim N^{2.24}$ and $N^{2.42}$, not far from the experimental observations, given the small molar mass range accessible by *n*DS. As an extension of this work, we explored how symmetric PI blends penetrate the same nanopores. Of particular interest were blends where the imbibition speeds of the two homopolymers were very different. By taking advantage of the disparity in the imbibition speeds, we were able to show that shorter chains penetrate first and, in addition, that they adsorb first on the AAO walls. The longer chains are entering the pores only at the late stages of the filling process providing a further example of polymer fractionation in the absence of solvent.

(II) Dc-conductivity and polymer dynamics during the imbibition of a polymer electrolyte

The investigatin of the PEO/LiTFSI polymer electrolyte suggested that the evolution of dc-conductivity is dictated by the adsorption of polymer chains at the pore walls. They further showed that at the early stages of imbibition the effective viscosity is reduced below the bulk value. It seems that at such early stages the pore walls act as lubricants for the chain segments and ions. At

much later stages, polymer adsorption takes place. The time scale of adsorption is very long—much longer than chain diffusion and certainly of the segmental relaxation. Adsorption involves several unfavorable configurations of the polymer chains that inevitably affect the ion dynamics by (i) increasing the effective viscosity (higher T_g) and (ii) by reducing the number of mobile ions. These effects should be considered when studing ionic systems within nanopores.

(III) Infiltration of a polymer from its semicrystalline state

There are two important findings from SEM: (1) PEO clearly enters the nanopores at a temperature located some 5°C below the melting temperature (*i.e.*, $T_{imbibition} = 57^{o}C < T_{melt} = 62^{o}C$) with an approximate imbibition length of 800 nm. (2) There exists a meniscus at the growth front of the polymer. The meniscus provides a direct proof of capillary force. From the LWE equation, the semicrystalline polymer flows within the nanopores with a viscosity between the bulk values of crystalline and melt states. This suggests that during imbibition part of the crystals are molten and flow with a lower overall viscosity. This unanticipated point needs further investigation by other techniques (like AFM-IR). The question of the state of polymer morphology (crystalline vs. amorphous) within the nanopores needs to be addressed in the near future.

Acknowledgements

This thesis would not have been possible without the tremendous support and motivation in all possible ways from my supervisors Prof. Dr. George Floudas and Prof. Dr. Hans-Jürgen Butt at the Max Planck Institute for Polymer Research. Thanks to the knowledge of wetting phenomena from Prof. Dr. Hans-Jürgen Butt, numerous insights into the imbibition of polymers have been obtained. I appreciate Prof. George Floudas for exposing me to a mulititude of projects relate to polymer phyics. His invaluable experiences in dielectric spectroscopy helped me a lot through the entire PhD research, especially at the early stage for developing the nanofluidic method based on nanodielectric spectroscopy. I also feel grateful for his patience for improving my English skills. It is truly one of my best luck to have a PhD supervisor like Prof. Dr. George Floudas!

I thank our external collaborators: Prof. Dr. Masso Doi and Prof. Dr. Jiajia Zhou (South China University of Technology) for scientific discussion in both theoretical and experimental; Prof. Dr. Martin Steinhart (University of Osnabrück) for providing the AAO templates. I also thank our internal collaborators (MPIP): Dr. Michael Kappl for the AFM measurements and for introducing me to the working principles of AFM; Dr. Lothar Veith for the ToF-SIMS measurements; Mr. Gunnar Glaßer for the SEM guidance (and interesting jokes); Mr. Andreas Hanewald for the rheological measurements and Mr. Andreas Best for sharing with me his knowledge of optics. I give my special thanks to the group members of Prof. Dr. George Floudas at the University of Ioannina. The fruitful discussion with all of you brings me much happiness and inspiration in science.

I want to thank my best friend in MPIP Pranav Sudersan for playing table soccer, cycling and having nice chats with me! My PhD journey will become much boring and less colorful without you, Pranav! I also want to give my thanks to Dr. Yang Yao and her husband Dr. Minghan Hu. They helped me a lot when I was just arriving in Germany. Special thanks to Dr. Yang Yao for sharing her experiences as a PhD student and helping me with the dielectric experiments. Many thanks to those lovely friends I met in badminton and table tennis!

Lastly, I am grateful to my family in Taiwan and my girlfriend—Shijiao You. Meeting all of you in my life is my best luck! You are the meaning for me to keep going ahead!

Chien-Hua Tu

Mainz

October 2021

Chien-Hua Tu

tu@mpip-mainz.mpg.de

EDUCATION

Ph.D. in Chemistry **07/2018 – 12/2021**

- Max Planck Institute for Polymer Research (MPIP), Mainz, Germany

Master of Science in Chemical Engineering (*summa cum laude*, GPA: 4.3/4.3) **07/2017**

- Dept. of Chemical Engineering, National Cheng-Kung University (NCKU), Taiwan

Bachelor of Science in Chemical Engineering (GPA: 3.91/4.0) **06/2015**

- Dept. of Chemical Engineering, National Cheng-Kung University (NCKU), Taiwan

WORKING EXPERIENCE

PhD researcher **07/2018 –12/2021**

Max Planck Institute for Polymer Research, Mainz, Germany

- *Supervisors:* Prof. George Floudas and Prof. Hans-Jürgen Butt
- *Project:* Soft matter under 2D confinement
- *Short description:* A nanofluidic method based on nanodielectric spectroscopy was employed to address three important questions in polymer physics. In first area we are interested how the segmental dynamics and chain dynamics are affected during imbibition. What is the effective viscosity that a polymer experiences during imbibition? In second area, we are interested how ions and polymer segments migrate in a polymer electrolyte during imbibition. In third area we explore the possibility that a semicrystalline polymer can penetrate into narrow pores from its crystal state.
- *Characterization techniques:* BDS, SEM, DSC, WAXS, POM, Rheometer, Contact angle measurement, Surface tension measurement, ToF-SIMS

Process Engineer **08/2017 - 06/2018**

Taiwan Semiconductor Manufacturing Company (TSMC), Tainan, Taiwan

- *Units*: Dept. of Diffusion Engineering, Sec. of Chemical Mechanical Polishing (CMP)

Graduate Researcher (Master) **09/2015 - 07/2017**

National Cheng-Kung University, Tainan, Taiwan

- *Supervisor*: Prof. Eamor Woo
- *Project*: 3-D Interior Lamellar Assembly in Dual Types of Ring-banded Spherulites of Poly(nonamethylene terephthalate) and Analyses of Crystal Packing Mechanisms
- *Short description*: Thorough microscopy analyses are done on dissecting 3D interiors of poly(nonamethylene terephthalate) (PNT) banded spherulites. 3D analysis exhibits that the banded spherulites possess a Janus-face morphology of compounded shell-and-kink lamellae assembly with dual discontinuities.

- *Characterization techniques:* POM, SEM, DSC, WAXD

Summer Intern
Taiwan Semiconductor Manufacturing Company (TSMC) 07/2015 - 08/2015
- *Units:* Dept. of Diffusion Engineering, Sec. of Ion Implantation

SCHOLARSHIPS/AWARDS and HONORS

- **Frank J. Padden Jr. Award**-Finalist (APS March Meeting) **2021**
- **Rank 6th**-TSMC TOEIC competition (Taiwan) **2018**
- **Honor Member (rank top 3%)**-Phi Tau Phi Scholastic Honor Society (Taiwan) **2017**
- **Travel Scholarship** (declined)-Ministry of Science of Technology (MOST)- EPF (European Polymer Federation) 2017 conference (Lyon) **2017**
- **Merit Award**-Oral presentation (English) Competition-Polymer Society (Taiwan) **2017**
- **TASCO Chemical Corporation Scholarship** (Taiwan) **2016**
- **Award of Outstanding Student in Graduate Program of Engineering College**-Advanced Semiconductor Engineering (ASE Group) Inc. (Taiwan) **2015**
- **Award of Outstanding Student for Academic Achievement (rank top 10%)** -National Cheng-Kung University (Taiwan) **2012-2013**
- **Award of Outstanding Student for Academic Achievement (rank top 10%)** -National Cheng-Kung University (Taiwan) **2011-2012**

PUBLICATIONS

1. **Tu, C.-H.**; Veith, L.; Butt, H.-J.; Floudas, G. " *In situ* imbibition of polymer electrolytes." In preparation.
2. **Tu, C.-H.**; Zhou, J.; Butt, H.-J.; Floudas, G. "Adsorption kinetics of *cis*-1,4-polyisoprene in nanopores by *in situ* nanodielectric spectroscopy." *Macromolecules* **2021**, *54* (13), 6267-6274. DOI: 10.1021/acs.macromol.1c00821
3. **Tu, C.-H.**; Steinhart, M.; Butt, H.-J.; Floudas, G. "Polymers under 2-D confinement: flow of polymer melts at the nanoscale." *ACS Symposium Series*; American Chemical Society: Washington, DC, **2021**, *1375* (9), 203-221. DOI: 10.1021/bk-2021-1375.ch009
4. **Tu, C.-H.**; Woo, EM.; Nagarajan, S.; Lugito, G. "Sophisticated dual-discontunity periodic bands of poly(nonamethylene terephthalate)." *CrystEngComm*, **2021**, *23*, 892-903. DOI: 10.1039/D0CE01329C
5. **Tu, C.-H.**; Zhou, J.; Doi, M.; Butt, H.-J.; Floudas, G. "Interfacial interactions during *in situ* polymer imbibition in nanopores." *Phys. Rev. Lett.* **2020**, *125* (12), 127802. DOI: 10.1103/PhysRevLett.125.127802
   => Spotlighted in official website of Max Planck Institute for Polymer Research (link: https://www.mpip-mainz.mpg.de/en/press/pr-2020-17)
6. **Tu, C.-H.**; Steinhart, M.; Butt, H. J.; Floudas, G. "*In situ* monitoring of the imbibition of poly(*n*-butyl methacrylate) in nanoporous alumina by dielectric spectroscopy." *Macromolecules* **2019**, *52* (21), 8167-8176. DOI: 10.1021/acs.macromol.9b01383
7. **Tu, C.-H.**; Woo, E. M.; Lugito, G. "Structured growth from sheaf-like nuclei to highly asymmetric morphology in poly(nonamethylene terephthalate)." *RSC Adv.* **2017**, *7* (75), 47614-47618. DOI: 10.1039/C7RA09170B

PRESENTATIONS

1. "*In Situ* Monitoring the Imbibition and Adsorption Kinetics of cis-1,4-polyisoprene in Nanopores by Nanodielectric Spectroscopy" IDS Online Workshop 2021 (Poster)
2. "*In Situ* Monitoring Polymer Imbibition in Nanopores by Nanodielectric Spectroscopy" APS March Meeting 2021 (Padden Award Symposium). 2021 APS March Meeting Website
3. "*In Situ* Monitoring the Imbibition of poly(*n*-butyl methacrylates) in Nanoporous Alumina by Nanodielectric Spectroscopy" ACS National Meeting, March 2020, Philadelphia (cancelled due to outbreak of corona virus).
4. "Interior Analyses on Lamellar Assembly in Dual Types of Ring-banded Spherulites of Poly(nonamethylene terephthalate)", Annual Meeting of Polymer Society, January 2017, Taichung, Taiwan (oral).

EXTRACURRICULAR ACTIVITY

- **Runner up**-Badminton Man Doubles-16th Hechtsheimer Badminton Tournament **2019**
- Volunteer Bilingual Translator (English-Mandarin Taiwanese) **2015**
- Department Team of Badminton and Table Tennis **2014-2017**